High-Throughput Platforms for Tumor Dormancy-Relapse and Biomolecule Binding Using Aminoglycoside-Derived Hydrogels

by

Taraka Sai Pavan Grandhi

A Dissertation Presented in Partial Fulfillment
of the Requirements for the Degree
Doctor of Philosophy

Approved April 2016 by the
Graduate Supervisory Committee:

Kaushal Rege, Co-Chair
Deirdre R. Meldrum, Co-Chair
Michael Caplan
Sarah Stabenfeldt
Yanqing Tian

ARIZONA STATE UNIVERSITY

May 2016

ABSTRACT

Relapse after tumor dormancy is one of the leading causes of cancer recurrence that ultimately leads to patient mortality. Upon relapse, cancer manifests as metastases that are linked to almost 90% cancer related deaths. Capture of the dormant and relapsed tumor phenotypes in high-throughput will allow for rapid targeted drug discovery, development and validation. Ablation of dormant cancer will not only completely remove the cancer disease, but also will prevent any future recurrence. A novel hydrogel, Amikagel, was developed by crosslinking of aminoglycoside amikacin with a polyethylene glycol crosslinker. Aminoglycosides contain abundant amount of easily conjugable groups such as amino and hydroxyl moieties that were crosslinked to generate the hydrogel. Cancer cells formed 3D spheroidal structures that underwent near complete dormancy on Amikagel high-throughput drug discovery platform. Due to their dormant status, conventional anticancer drugs such as mitoxantrone and docetaxel that target the actively dividing tumor phenotype were found to be ineffective. Hypothesis driven rational drug discovery approaches were used to identify novel pathways that could sensitize dormant cancer cells to death. Strategies were used to further accelerate the dormant cancer cell death to save time required for the therapeutic outcome.

Amikagel's properties were chemo-mechanically tunable and directly impacted the outcome of tumor dormancy or relapse. Exposure of dormant spheroids to weakly stiff and adhesive formulation of Amikagel resulted in significant relapse, mimicking the response to changes in extracellular matrix around dormant tumors. Relapsed cells showed significant differences in their metastatic potential compared to the cells that remained dormant after the induction of relapse. Further, the dissertation discusses the use of Amikagels as novel pDNA binding resins in microbead and monolithic formats for potential use in chromatographic purifications. High abundance of amino groups allowed their utilization as novel anion-exchange pDNA binding resins. This dissertation discusses Amikagel formulations for pDNA binding, metastatic cancer cell separation and novel drug discovery against tumor dormancy and relapse.

DEDICATION

To my mom, dad and my twin brother who have been a constant support throughout this journey.

ACKNOWLEDGMENTS

I would first like to acknowledge my dissertation committee members, Dr. Kaushal Rege, Dr. Deirdre R. Meldrum, Dr. Yanqing Tian, Dr. Sarah Stabenfeldt and Dr. Michael Caplan for their constant support and guidance throughout my journey.

I am very lucky to have had the resources of the Gold Water Center, Solid State Sciences Center, Life Sciences Building, and Center for Biosignatures Discovery Automation (CBDA) and Biodesign Institute available to me during my dissertation work. Dr. Rege's creative vision, strong leadership, dedicated mentorship and unrelenting focus have made this work a possibility. I am sure the spark he ignited to completely understand the underlying causes of observed phenomena will always guide me in my future ventures.

Also, behind the screen efforts of a number of SEMTE department's administrative staffs, April McCleary, Susan Baldi, Delilah Alirez, Gayla Ruark, Myrna Martinez, Mariah Pacey and Mia Kroeger have kept my work running smoothly and comfortably. I would also like to thank the amazing academic advisors and staffs from SBHSE, Laura Hawes, Keli Palmer, Tammie Cameron, and Tomi E. St John for providing their valuable support throughout my PhD term. I am very grateful to my current graduate academic advisor Laura Hawes who often went out of her way to help her students like myself. I am also grateful to Christine Willet, Carol Glaub, Maria Hanlin, Lauren Dempsey and Dr. Stephen Johnston for their help with my transition into ASU.

I would like to acknowledge excellent graduate, undergraduate and high-school students whom I've had the pleasure of mentoring and subsequently working aside in different projects during my PhD, Andrew Dobos, Indrani Deshpande, Kevin Lin, Amrita Mallik, Haley Gjertsen, Yifan Tian, Ananyaa Mahajan, Kailey Rumbo and Patrick Cao. Mentoring and inspiring my students was one of the best experiences in my PhD. I am very happy that all of them have found high paying jobs and satisfying careers after their time in Rege lab.

During the course of my dissertation work I had the great honor of working and studying alongside Dr. Huang- Chiao Huang, Dr. Sutapa Barua, Dr. David Taylor, Dr. James Ramos, Dr. Jordan Yaron, Dr. Bo Wang, Dr. Kevin Timms, Dr. Hongguang Lu, Dr. James Faust, Dr. Jia Zheng, Dr. Caroline Addington, Patti Senechal Willis, Xiao Wang, Lalitha Venkataraman,

Shubhangi Nagar, Rohini Vidyashankar, Vimala Bharadwaj, Sri Krishna, Matthew Christensen, Karthik Pushpavanam Subramanium, Russell Urie, Rajesh Niti, Kristen Lee, Brian Johnson, Brian Thompson and Brianne Petritis. I also gained immeasurable insight from working with Dr. Thrimoorthy Potta, Dr. Bhavani Miryala, Dr. Sudhakar Godeshala, Dr. Sheba Goklany, Dr. Fengyu Su, Dr. Liqiang Zhang, Dr. Xiangxing Kong, Dr. Roger Johnson, Dr. David Capco, Dr. Vikram Kodibagkar, Sandhya Gangaraju, Juan Vela and the rest of the CBDA, Rege Lab and BME PhD family. I consider each of these talented scientists and engineers not only colleagues and mentors, but also good friends.

I could not have succeeded without valuable technical help and training from Dr. Honor Glenn, Dr. Debra Baluch and Dr. Tong Fu who have extensively helped me with confocal microscopy set up and experimentation and flow cytometry for my experiments.

I would also like to thank Fred Pena, Al Thompson and Donley Hurd who were always very responsive to technical and IT related issues. I would like to acknowledge Tom Colella, Sara Avery and Roy Erickson for their help in successful completion of my critical experiments. My work would not have been possible without immense help from Philip Schulz and Stephanie Williams from Sierks Lab.

I would like to acknowledge Dr. Marco Santello, Dr. Stephen Helms Tillery, SBHSE and GPSA for providing me with financial assistance towards conference presentations and PhD completion. I am fortunate to have met and lived alongside members of Mesa Sai Center. Their weekly spiritual and humanitarian volunteer activities kept me grounded, humble and always positive. I would like to thank my roommates Arvind Thirumalai, Advait Sakhalkar, Prasanth Lade and Hemanth Kumar for making my stay outside of lab very enjoyable. Big thanks to Ujjwala Aunty, Jaya Aunty, Sunitha Aunty, Vidya Aunty, Mrs. Godeshala and others for their help with delicious food and concern throughout my graduate stay.

In my almost 6 years at Arizona State University I have had many amazing professors and instructors, and I would like to give special acknowledgement to Dr. Jeffrey Wilson, Dr. Douglas Montgomery, Dr. Robby Roberson, Dr. Doug Chandler, Dr. Jing Li and David Lowry. Lastly, I want to thank my family for their support and encouragement.

TABLE OF CONTENTS

Page

CHAPTER Page

CHAPTER Page

LIST OF TABLES

LIST OF FIGURES

Figure Page

Figure Page

Figure Page

Figure Page

CHAPTER 1: INTRODUCTION

AMINOGLYCOSIDE-DERIVED POLYMERIC MATERIALS FOR BIOMEDICAL APPLICATIONS

Aminoglycosides are anti-bacterial therapeutic agents composed of amino-modified glycosides or any organic molecule that contains aminosugar substructures. These aminoglycosides inhibit the gram-negative bacterium by broadly inhibiting their protein synthesis [1]. Aminoglycosides such as streptomycin, neomycin, irreversibly bind to the bacterial ribosomal RNA and cause improper translation. Alternately, other aminoglycosides such as amikacin bind to the 30S sub-unit of the bacterial ribosomes and inhibit their proper functioning by blocking active translation [2-6]. Aminoglycosides have multiple easily conjugable hydrophilic functional groups such amino and hydroxyl groups. These groups can be actively linked together to generate small to medium chain polymers (molecular weight 3-5 kDa) and other crosslinked polymeric hydrogels [5]. These polymers are not only biocompatible and hydrophilic, but also contain amino and hydroxyls for further conjugation or desired cargo delivery [5]. In the studies presented in this dissertation, crosslinked aminoglycoside hydrogels have been used for generating high-throughput 3D tumor microenvironment models (3DTMs), high-throughput models of tumor dormancy, relapse and micrometastases etc. These high-throughput models of tumor dormancy and relapse have been used for rational drug discovery and development. Also presented are the studies on utilizing the aminoglycoside hydrogels in form of microbeads and macroporous gels as novel chromatographic resins for plasmid DNA binding and recovery and micellar delivery of anticancer drug mitoxantrone towards TRAIL sensitization.

1.1. HIGH-THROUGHPUT 3D CANCER CELL CULTURE PLATFORMS

High-throughput cell culture platforms are extremely useful in resource intensive processes of drug discovery, development and validation. These platforms provide rapid and cost-effective alternatives to conventional animal testing methodologies for drug discovery [7-8]. Often, these platforms are used for drug discovery and validation prior to small and large animal testing [9-11]. These platforms allow for initial confirmation and validation of the drug/biologic activity, thereby

reducing the risk associated with its future. These platforms are currently being used to discover novel drugs against diseases such as cancer [7, 12-13], Alzheimer's [14], cystic fibrosis [15] etc. Unlike 2D cancer cell culture platforms, 3D cancer spheroid cell models capture multiple complexities such as extensive cell-cell contacts, cell-ECM contacts (tumor-stoma interactions), zones of differential cell proliferation, zones of hypoxia, nutrient gradients, necrosis, different gene and protein expression profiles that closely represent the tumor in-vivo [16-17]. As cells are surrounded by either other cells or ECM in the in-vivo environment, flat 2D cell culture surfaces do not adequately take into account those interactions. Thus, these 2D cell culture platforms can often result in misleading and non-predictive data for in-vivo responses [18-19].

It is however important that the 3D cancer cell culture models closely mimic the disease or tissue in-vivo. Extensive research work continues to develop robust 3D cell culture models that closely mimic the tumor in-vivo. Conventionally, 3D cell cultures have been generated on non-adhesive gels such as agarose, PEG gels, hanging drop cultures, low adhesion-corning plates etc [13, 20-21]. Low substrate adhesivity prompts the cells to attach to one another generating a 3D spheroidal mass. Techniques such as hanging drop cultures pose certain challenges in high-throughput culture due to the low volume of liquid that can be used for such cultures. They also require special low evaporation platforms to avoid significant loss of media [13, 20]. 3D spheroids have also been generated using spinner flasks and suspension techniques. A significant limitation of suspension cultures is the generation of spheroids with different sizes that require further filtration and separation to isolate the right size. [22].

Other gels such as Matrigel, collagen gel, laminin or fibronectin-coated gels have also been used to generate 3D cancer cell culture platforms [23]. Unlike the previously described non-adhesive gels, these gels present surfaces rich in adhesive ligands that closely mimic the in-vivo microenvironment. However, these specialized gels also require advanced temperature control strategies in order for proper gelation. Pickl et al. [24] showed that human epidermal growth factor receptor (HER2) overexpressing cancer cells show considerable differences towards trastuzumab in 2D versus the 3D cell culture platforms. 2D cell culture surfaces largely induce HER2 and HER3 heterodimers whereas 3D culture largely generates homodimers. Presence of homodimers

also shows enhanced response to trastuzumab. Birgersdotter et al. [19] showed large global gene expression differences between solid tumors and immortal cell lines used to study them and showed that inclusion of stromal cells into the co-culture significantly improved the outcome.

We used the aminoglycoside hydrogels ('Amikagels') as novel substrates for high-throughput cell culture. Crosslinking units of adhesive aminoglycoside amikacin and non-adhesive PEGDE resulted in the novel hydrogel ('Amikagel'). By varying the mole ratios of the two monomers (Amikacin and PEGDE), different hydrogels could be prepared with varied chemo-mechanical properties. Unlike other contemporary hydrogels for 3D cell-culture like agarose or Matrigel that instantly gel upon temperature modulation, amikagel preparation and gelation was tunable by temperature variation. Amikagels with high mechanical stiffness and low adhesivity generated hydrogels that were non-adhesive and conducive for 3D spheroid formation. We generated multiple singular as well as co-culture spheroids of bladder, prostate, breast and pancreatic cancer cell types using the amikagels. This dissertation will delve in-depth into the physico-chemical and mechanical properties of amikagels and their influence on spheroid formation and its phenotype.

1.2. TUMOR DORMANCY AND RELAPSE

Primary treatments after a cancer diagnosis include chemotherapy, radiotherapy, biologic therapy, surgery or a combination of the above [25]. Often, these treatments cause reduction in the primary tumor size and the cancer is said to be in treatment-induced remission once it is not detectable by conventional imaging techniques. However, a number of times, cancer relapses from remission, causing tumor metastases in the primary or distant secondary sites leading to patient death [26-27]. In fact, 90% of cancer deaths are due to metastases to distant sites such as bone, liver and lungs etc [28]. Deaths due to breast and prostate cancer metastases account for majority of deaths in patients with those diseases [29]. It is now widely believed that cancer cells undergo prolonged periods of dormancy before relapse. In this dormant state, these cancer cells exhibit low cell proliferation profiles, low metabolic consumption and are highly resistant to conventional chemotherapeutics that exclusively target the actively dividing phenotype (Figure

1.2) [30]. Increasing evidence points towards a definitive phase of prolonged G0/G1 arrest ('cellular dormancy') of micrometastatic nodules rather than balanced proliferation to support prolonged viability before relapse [27]. Upon relapse, these cancer cells give rise to highly aggressive forms of tumor metastases, often causing death as a result. Research has shown that cancer cells from primary tumor shed and migrate to the distant secondary sites (bone, liver and lung) even before the detection of the primary tumor [26, 30]. Dormancy at distant disseminated sites has been shown to be induced by the local microenvironment, which is foreign to the invading cancer cells [31]. These populations of non-dividing G0/G1 arrested cancer cells that evade traditional chemotherapy regimens indicate poor prognosis for the patient [32]. Ablation of these cancer cell systems in their dormant state can not only completely eliminate the disease, but also reduce the risk of tumor relapse. There is a need to develop high-throughput in-vitro systems (HTS) that can capture the tumor dormancy in a 96 well plate format [33-34]. These high-throughput systems (HTS) could allow the rapid discovery, development and validation of dormancy-specific drugs, their combinations and novel formulations towards drug delivery etc (**Fig. 1-1**) [13].

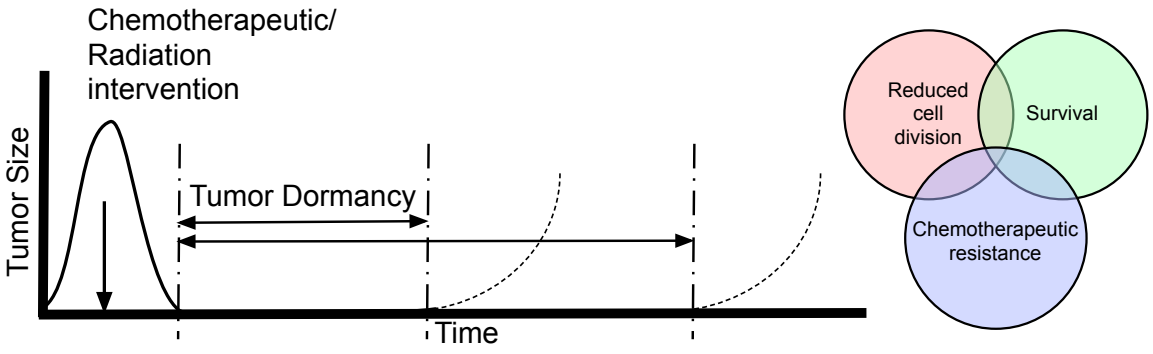

Figure 1-1. Tumor dormancy and relapse timeline. Tumor dormancy is the phase between the cancer remission to relapse characterized by cancer cells with low rates of cell division and high chemotherapeutic resistance.

Wenzel et al. [35] developed an 384 well agarose gel (1.5% wt/vol) based breast cancer T47D multicellular tumor spheroid culture in high-throughput. The T47D multicellular tumor spheroid consisted of regions of active growth towards the exterior and internal low-growth regions with low cell division rates. While the exterior regions were susceptible to paclitaxel and

cisplatin, cells in the inner regions with intermediate oxygen supply were resistant to those drugs. Utilizing the high-throughput system, the authors identified compounds that not only ablate the actively dividing cells, but also the dormant cancer cells. Authors identified respiratory inhibitors as compounds that work to ablate the dormant regions in the MCTS. While respiratory inhibitors can effectively ablate the dormant tumors, it is important to note that these could also indiscriminately kill the normal dividing cells, making delivery of these drugs specifically to target cells equally important. In addition, agarose substrate might not be suitable for large-scale platforms without sophisticated temperature control technologies. We developed a novel aminoglycoside based hydrogel that is highly temperature controllable and induced spheroid formation with high viability and complete dormancy. In our comparative studies, Amikagel fared better than agarose gel in inducing complete tumor dormancy in bladder cancer cells. In fact, bladder cancer cells were almost completely arrested in the G0/G1 phase of cell cycle on Amikagels. These results are of significance since very few methods have been developed for generating high-throughput 3D models of total tumor cell dormancy; most methods using 3D models have demonstrated only ~70% cells in the G0/G1 phase of the cell cycle for cancer cells at best [36].

Previous research has closely linked upregulation of p38, p27 and p16 proteins with the induction of tumor dormancy and cell cycle arrest in the G0/G1 phase [37-39]. Ghiso et al. [40] reported that the ratio of ERK/MAPK and p38 proteins regulate the entry or exit of cells from tumor dormancy in many cell types. Higher p38 protein was associated with dormant state of cells in-vivo whereas higher ERK/MAPK was associated with proliferation. Further, Ranganathan et al.[37] showed that p38 induced dormancy, initiated by microenvironmental changes (loss of integrin adhesion to fibronectin rich surfaces [41]) induced PERK activation that reduced translation and phosphorylated eukaryotic translation initiator factor 2α (eIF2α), arresting cells in the G0/G1 state. Some cell types can also induce dormancy independent of p38, by directly upregulating several CDK inhibitors such as p21, p27 and p16 [42]. In fact, p38 protein has also been shown to modulate several downstream CDK inhibitors such as p21, p27 and p16 that work to induce cell cycle arrest and dormancy [43-44]. Barkan et al. [42] showed that dormant breast cancer D2.0R

tumors have high expression of p27 (~77% of cell nuclei) and lower amounts (~50%) of p16 CDK inhibitors. These dormant D2.0R breast cancer cells when injected into mice invaded distant metastatic sites and remained as single quiescent cells for prolonged periods of time before metastases. Near complete total dormancy achieved on Amikagel platform allows its usage as a clinically relevant model for high-throughput drug discovery. Not only can we study the induction and maintenance of tumor dormancy on this platform, but also study the incidences of relapse from the dormant phenotype.

Our cellular model of tumor dormancy involves transitional cell carcinoma T24 bladder cancer and UMUC3 bladder cancer cell lines. Bladder cancer is one of the leading urothelial cancers, the 7th leading cause of new cancers each year in USA and is the 4th leading cause of cancer deaths [45-46]. Most of the bladder cancer deaths are associated with the metastases of the cancer cells to the lymph nodes, lungs, liver and bone areas [46]. Previous research has shown that T24 cells undergo cell-cycle G0/G1 arrest upon cell-cell contact mediated by $p27^{Kip1}$ expression and subsequent CDK inhibition [39, 47]. We hypothesized that a 3D cell culture platform that effectively induces robust cell-cell adhesions would likely induce dormancy in these cancer cells. Upon doing so, a high-throughput model platform to accurately study the dormancy phase of cancer cells can be established. Such a high-throughput model of cellular dormancy will allow for rational drug discovery, development, validation and delivery. Not only can the model of cellular dormancy be established, a subsequent high-throughput model of relapse from tumor dormancy can also be established. Our research centered on developing amikagel hydrogel formulations that can rapidly induce dormancy behavior and relapse in the cancer cells.

Previous works have also shown significant heterogeneity in the T24 cell line and its metastatic potential [48]. While some reports describe T24 cell line as non-tumorigenic due to poor growth rate and poor tumor formation in mice, several reports state the cell line as highly metastatic [48-50]. Makridakis et al. [51] reported that injection of T24 cells into mice resulted in tumor formation only in 33% of the mice. Gildea et al. [47] isolated the T24 metastatic cell fractions from the heterogeneous T24 cell population and showed significant differences in HRAS expression, beta-catenin levels in the metastatic T24M cells. It is now believed that the T24 cell line consists

of a heterogeneous mix of cells with different phenotypes within the same population. While decades worth of research has progressed into isolating and understanding the metastatic version of the bladder cancer cell line and strategies to ablate them, almost no research has been performed in trying to understand and ablate the dormancy in these cancer cell lines. We use these bladder cancer cells as a model to understand tumor dormancy in general. In our work, we have worked to understand and ablate the dormant bladder cancer 3D tumor microenvironments (3DTMs) by targeting the cellular adaptations in tumor dormancy.

Relapse and reawakening from tumor dormancy is almost always associated with significant mortality [52]. Relapse from tumor dormancy has been shown to be associated with changes in the extracellular environment around the dormant tumor [38]. Barkan et al.[42] showed a switch from dormant to relapse behavior in breast cancer cells via fibronectin – β-integrin mediated signaling. Addition of fibronectin to growth factor reduced gels resulted in significant proliferation and migration of dormant D2.0R breast cancer cells [42]. In bladder cancer, changes in extracellular matrix have been associated with metastasis and migration of the cancer cells [53]. Incidentally, the cells that tend to migrate and metastasize are the ones with lower expression of beta-catenin levels, higher MMP expressing cells etc [47]. Aberrant expression of N-cadherin has also been associated with poor prognosis of bladder cancer [54]. N-cadherin protein expression along with E-cadherin modulation is a hallmark of epithelial to mesenchymal transition (EMT) event and has been linked to poor prognosis for the bladder cancer patient [55]. However, reduction or complete absence of N-cadherin has been associated with increased migration, metastases in multiple cancer cell types including bladder cancer. Reduction of N-cadherin or complete absence of N-cadherin has been connected to extremely poor prognosis for bladder cancer patients [55-57]. In a study of bladder cancer patient samples by Jager et al. [58], N-cadherin reduction and absence was identified to be an extremely poorer prognostic indicator than expression of N-cadherin (which was also a significant prognostic indicator of invasive cancer disease).

We hypothesized that transferring the dormant T24 3DTMs from non-adhesive and mechanically stiff Amikagel formulations to a more adhesive, mechanically pliant Amikagel formulations could result in relapse and migration of metastatic populations of the cells. We

hypothesized that cells with differential expression of N-cadherin could be isolated from within the population of T24 cells by modulating the chemo-mechanics and adhesivity of the substrate matrix. In order to do so we varied the ratio of the input monomers amikacin and PEGDE to generate different formulations of Amikagel with varying adhesivities and studied the relapse of the cancer cells from tumor dormancy. Our goal for this work has been to develop a novel high-throughput platform that not only captures complete tumor dormancy, but also relapse and further metastatic cell migration and micrometastases formation for rapid drug discovery, validation, delivery and development (**Fig. 1-2**).

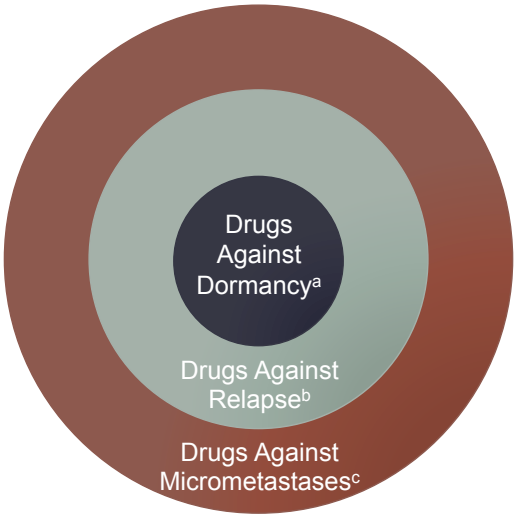

Figure 1-2. T24-3DTM Amikagels as a proposed drug screening platform against multiple cancer phenotypes. T24 3D-DTM Amikagel system as high-throughput drug screening platform against tumor specific phenotypes of a) total dormancy, b) relapse from dormancy and c) cell escape and micrometastases captured within a 96 well plate.

1.3. TARGETING CELLULAR ADAPTATIONS IN TUMOR DORMANCY AND RELAPSE

Dormant cells utilize a number of pathways to adapt to their dormant state. Targeting these adaptations could allow us to selectively ablate the dormant cancer cells, sparing the other non-dividing healthy cells. Ranganathan et al. [37] revealed significant ER stress response in the dormant human epidermoid-carcinoma cell line HEp3 cells. In their proteomic analysis, several key ER stress markers such as BiP/GRP78, XBP-1, HSP47 and PERK were activated in dormant cancer cells. Ranganathan et al. [37] associated the upregulation of ER stress markers as an adaptation of the dormant state. The authors suggested that dormant cells might be chronically

under ER stress and utilize the adaptations to survive. In our studies, we found that the total protein content per cell in the dormant state was slightly but significantly upregulated, indicating strategies to target the ER and the protein production pathway could be beneficial. We focused on ways to induce and accelerate the ER stress in the dormant cells as a strategy to ablate them. Our strategy has been to induce and overwhelm the dormant cancer cell with chronic ER stress.

Endoplasmic Reticulum (ER) is an organelle that is responsible for ensuring proper folding of the nascent peptides into 3D protein structures [59]. Ribosomes associated with the endoplasmic reticulum deposit nascent linear peptides into the ER after mRNA translation [60]. In the ER, the nascent peptides are properly folded into 3D structures via the help of multiple chaperones such as calcium dependent chaperones calnexin and calreticulin and other assistive proteins etc [61-62]. Any disturbance in the chaperone assisted folding of the nascent peptides or otherwise results in protein misfolding and accumulation. Accumulation of misfolded or unfolded proteins results in activation of cellular adaptation cascade known as unfolded protein response (**Fig. 1-3**) [63]. The cascade activates multiple pathways focused on initially trying to restore balance to the ER and relieve the ER stress [64]. In an event of chronic ER stress, the pathway focuses on inducing apoptotic cell death in the stressed cell [65-66].

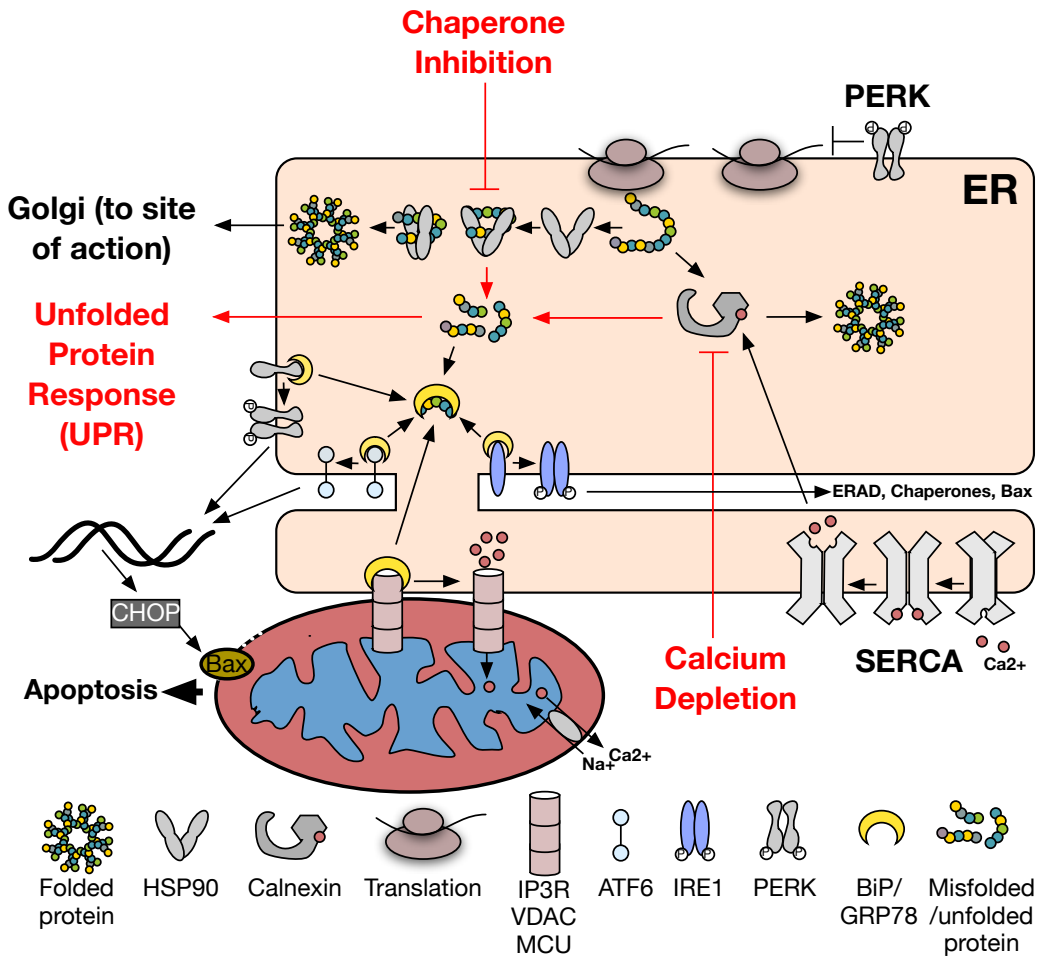

Figure 1-3. ER stress adaptation pathways during protein unfolding or misfolding. Cellular adaptation under protein misfolding or ER stress results in a cascade of cell signalling events collectively referred to as unfolded protein response (UPR). HSP90, Calnexin – Chaperones required for proper folding of nascent proteins, IP3R-VDAC-MCU – Pores that direct calcium entry from ER to mitochondrial matrix, SERCA – Scarcoplasmic/Endoplasmic Reticulum $Ca2^{+}$-ATPase calcium channel for maintaining ER calcium levels, ATF6 – Activating Transcription factor 6, Ire1 – Ionositol requiring enzyme 1, PERK – protein kinase RNA-like endoplasmic reticulum kinase, BiP – Binding Immunoglobulin protein

Accumulation of misfolded/unfolded proteins sequesters the adaptor protein BiP/GRP78 that causes the activation of significant number of downstream effectors [67-68]. Under normal conditions, binding of BiP/GRP78 adaptor protein to a number of downstream effectors such as ATF6, IRE1, PERK and IP3R keeps them under check. But sequestration of the adaptor by the misfolded proteins activates the cascade. In a well-elucidated pathway (**Fig. 1-3**), accumulation of misfolded proteins in ER causes the activation of two main pathways, the Ire1/XBP-1 and ATF6-

dependent pathway and PERK/eIF-2alpha phosphorylation-dependent pathway [69-70]. Dimerization of Ire1 causes autophosphorylation and intronic splicing of XBP-1 mRNA and spliced XBP-1 protein production which causes transcriptional activation of multiple chaperone proteins to repair the misfolded/unfolded proteins [70]. Phosphorylation of PERK via oligomerization tends to reduce the ribosomal translation in order to reduce the load of nascent proteins being deposited into the ER [71]. PERK and ATF6 also cause transcriptional activation of multiple pro-apoptotic factors such as CHOP [65]. Spliced XBP-1 protein also causes transcriptional activation of lipid synthesis, foldases and ERAD (ER associated protein degradation), which ubiquitinylates the misfolded/unfolded proteins for their removal via proteasome [72]. The aim of these responses is to remove misfolded/unfolded proteins from the ER and relive the ER stress.

If the cellular adaptation pathways are unable to relieve the ER stress, the cell enters a phase towards apoptotic death under chronic ER stress. Under chronic ER stress, the pro-apoptotic proteins CHOP and Bax, Bak are produced which puncture the outer mitochondrial membrane. CHOP is a multifunctional transcriptional activator that is closely linked with chronic ER stress associated apoptosis. CHOP is responsible for transcriptional activation of multiple pro-apoptotic proteins such as Bax and Bak, which work to puncture the outer mitochondrial membrane. Further, the intra-ER and cytoplasmic calcium is pumped into mitochondrial matrix via specialized IP3R-VDAC-MCU set of channels during prolonged ER stress (**Fig. 1.4**). Pumping of calcium ions into the mitochondrial matrix results in erosion of the mitochondrial potential difference between the matrix and the outer mitochondrial membrane space resulting in mitochondrial swelling, and eventual lysis [66, 73-76]. Mitochondrial depolarization releases pro-apoptotic proteins cytochrome c and SMAC/DIABLO into the cytoplasm [77]. Cytochrome c stimulates the formation of multi-protein apoptosome complex along with pro-caspase 9. Apoptosome complex causes self-catalytic event and activation of caspase 9 [78]. Activated caspase 9 cleaves and activates multiple other pro-caspases such as pro-caspase 3,6 and 7 resulting in apoptosis [75-76]. The mitochondrial depolarization and lysis represent a "point of no return" in the apoptosis-signaling cascade. In addition, permeabilization of single mitochondria

results in release of reactive oxygen species into the cytoplasm that act to depolarize more mitochondria, thus amplifying the effect and accelerating apoptosis [79].

Our approach has been to identify novel drug combinations that not only sensitize the dormant cancer cells to apoptotic death, but also accelerate the process towards apoptotic death. By identifying strategies that work to accelerate the cell death, we were able to speed up the dormant cancer cell death process. Relapse from tumor dormancy is often associated with changes in the local microenvironment. Barkan et al. [42] showed that the relapse and metastases of the dormant cancer cells could be avoided by targeting the cytoskeleton of the relapsed cells. Barkan et al. targeted phosphorylation of myosin light chain by myosin light chain kinase that is required for actin stress fiber formation and subsequent cell migration during the relapse. Our strategies have focused on targeting the cellular mechanisms that allow relapsed cells to bind and interact with the substrate during cell migration and relapse. In this dissertation, using the high-throughput dormancy relapse platform, we explored and identified strategies that work to inhibit or accelerate the relapse from dormant tumors.

1.4. Cross-Linked Aminoglycoside Polymers For Nucleic Acid Biotechnology

Aminoglycoside based polymers have also been used to deliver important therapeutic cargoes into the mammalian cells. Potta and Zhen et al.[80] hypothesized that the cationic charge of aminoglycosides at physiological pH and their natural affinity towards nucleic acids could be exploited to bind and deliver anionic plasmid DNA if aminoglycosides could be assembled into polymeric structures. Delivery of plasmid DNA encoding therapeutic proteins to cells that lack them could benefit patients with deadly diseases such as cancer, cystic fibrosis and AIDS. Potta and Zhen et al.[80] developed a library of 56 aminoglycoside-based polymers by crosslinking 7 different aminoglycosides (neomycin sulfate, kanamycin sulfate, streptomycin sulfate, apramycin sulfate, paromomycin sulfate, sisomicin sulfate and amikacin hydrate) with 8 different cross-linkers (1,4-cyclohexanedimethanol diglycidyl ether (CDDE), neopentylglycol diglycidyl ether (NPGDE), 1,4-butanediol diglycidyl ether (BGDE), ethyleneglycol diglycidyl ether (EGDE), poly (ethyleneglycol) diglycidyl ether (PEGDE), poly(propyleneglycol) diglycidyl ether (PPGDE),

resorcinol diglycidyl ether (RDE) and glycerol diglycidyl ether (GDE)). pGL3 plasmid coding for luciferase protein was delivered to the cells to quantify the transfection efficacy of the polymers. Nanoscale aminoglycoside polymer-pGL3 polyplexes were delivered to PC3 and 22Rv1 human prostate cancer cells, MiaPaCa2 human pancreatic cancer cells and MB49 bladder cancer cells. Aminoglycoside polymers prepared using apramycin, paromomycin and sisomicin crosslinked with RDE and GDE respectively were identified as lead polymers that generated highest transfection efficacy. Almost all the lead polymers showed higher transfection efficacy compared to pEI at the best N/P ratio. Potta and Zhen et al. also showed robust transfection efficacy of the lead aminoglycoside-based polymers in presence of fetal bovine serum, indicating their stability in binding and delivering plasmid cargo to the cells in high serum concentrations (transfection efficacy dropped under 2 fold).

In order to understand the quantitative structure-property relationship of the polymer and its transgene efficacy, authors employed support vector machine (SVM) based algorithms to build both classification (SVM) and regression models (SVR). A total of 139 molecular descriptors were employed to accurately capture the quantitative information of the aminoglycoside-based polymers. Output variable of transfection efficacy was regressed against 139 input molecular descriptor variables to identify key independent variables that impact transfection efficacy (log10 (RLU/mg)). The training model had a squared Pearsons' correlation coefficient (r^2) of 0.78 and a coefficient of determination (R^2) of 0.78. Cross-validated model generated using part of training set which used other remaining data as validation set gave r^2 and R^2 values of 0.65 each, indicating the robust predictive power. Five descriptors, PEOE_VSA_PPOS, logP (o/w), RECON_SIEPMax, BCUT_PEOE_3, and RECON_PIPMax were seen to significantly explain the transfection efficacy of the aminoglycoside-based polymers and were used to generate the QSAR model. These descriptors describe the 2D electrostatic map (total polar surface area), molecular hydrophobicity, electrostatic potential, partial molecular charges and electron density at van der Waals surface of the molecule respectively. QSAR model indicated that balance between hydrophobic and hydrophilic moieties, basicity of the amine groups largely influence the transfection efficacy of the aminoglycoside-based polymers.

Miryala et al.[81] reported further improvement in the transfection efficacy of the lead polymers via quaternization. Miryala and her co-authors conjugated glycidyl trimethyl ammonium chloride groups to the amino groups in the aminoglycoside polymers. These GTMAC groups provided the lead polymers with a permanent positive charge due to the quaternary ammonium groups. These quaternary ammonium modified lead polymers were better transfection agents compared to their parental polymers. Miryala et al.[81] reported that their lead polymers performed 2-4 times better than the comparison lipofectamine 3000. Miryala et al. [82] also developed lipid-conjugated aminoglycoside polymers to prepare nanoparticles for transgene delivery. Alkanoyl conjugations were achieved by reacting alkanoyl chloride to the aminoglycoside polymers resulting in lipopolymers. In most cases transgene delivery using lipopolymers was found to be better than the polymers alone. Long chain stearoyl (C_{18}) groups conjugated to lead polymers (neomycin-glycerol diglycidyl ether (NG) and apramycin-glycerol diglycigylether (AG)) were noted to generate higher transgene expression compared to hexanoyl (C6) and myristoyl (C14) groups. QSAR cheminformatic SVR-based model indicated that high number of amines on polymers, hydrophobic chain length, smaller lipid-polymer conjugation ratios collectively contribute to enhance the transgene delivery efficacy of the lipopolymers.

In our work [83], we exploited the binding affinity of aminoglycosides to nucleic acids for plasmid DNA ('pDNA') binding and desorption in a chromatographic setting. We developed a novel aminoglycoside ('Amikacin') based hydrogel microbeads/microresins ('Amikabeads') to adsorb and desorb pDNA for its potential usage as chromatographic resins. Conversion of freely soluble aminoglycosides into hydrogel microbeads via crosslinking allowed their usage as chromatographic resins. These aminoglycoside microbeads were prepared using emulsion based polymerization (**Fig. 1-4**). No other conventional pDNA chromatographic resins utilize the natural affinity of aminoglycosides towards pDNA chromatography [84]. Presence of abundant conjugable groups such as hydroxyls and amines will also allow for conjugation of multiple other pDNA specific groups on the surface of amikagel microbeads towards its use in one-step pDNA isolation from bacterial broths.

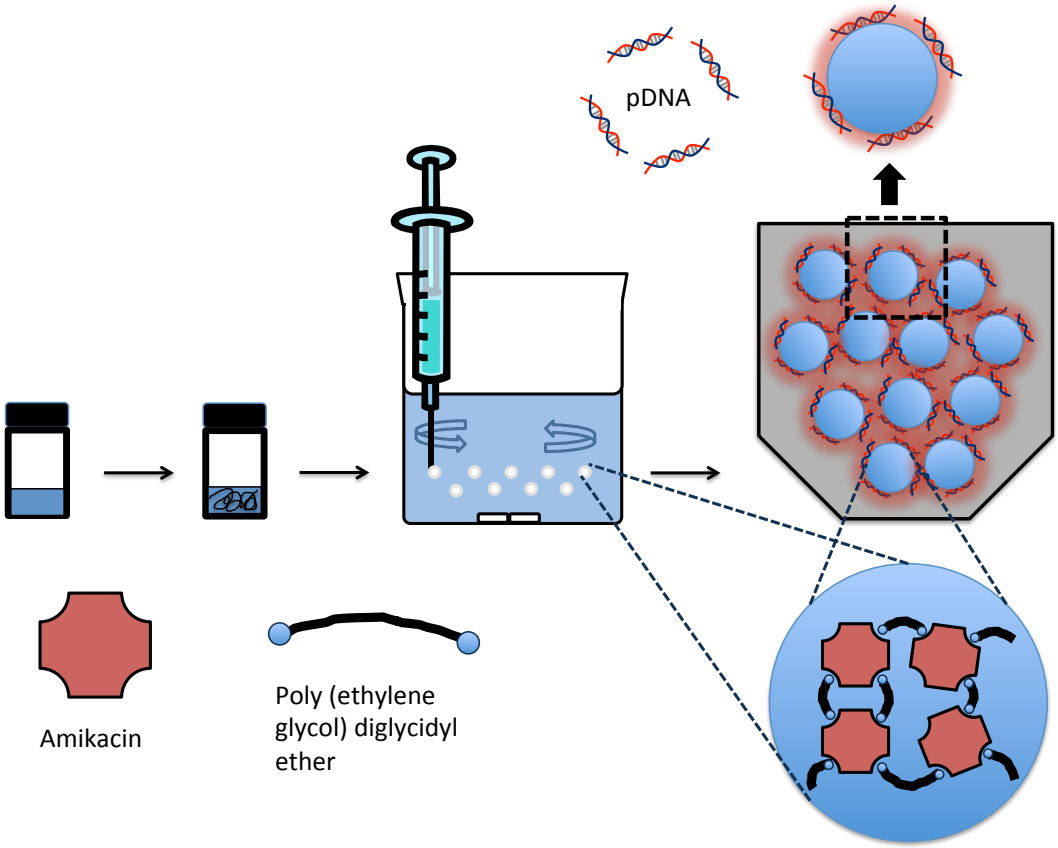

Figure 1-4. Formulation of Amikagels as chromatographic resins. Novel aminoglycoside based microbeads ('Amikabeads') were prepared using the emulsion-polymerization method.

Binding of plasmid DNA was significantly improved by converting the primary amines to quaternary ammonium groups via GTMAC conjugation, thus giving them a permanent positive charge. Conversion of the amine groups of Amikabeads to quaternary ammonium groups caused significantly higher plasmid DNA binding to the resins at pH 8.5, 25^{O}C and 10 mM Tris-Cl buffer similar to that observed by Miryala et al [81]. The binding capacity of the quaternized Amikabeads was comparable to the commercially existing alternatives such as gigaporous rigid ceramic HyperD-Q polymerized hydrogel resins [84]. This dissertation describes the development of suitable buffer systems to elute maximal plasmid DNA from the parental and quaternized amikagel based chromatographic resins. In the end, we show that the novel Amikabeads can also be used to extract mammalian cell DNA from whole cell systems for applications into on-site PCR etc.

1.5. THESIS CONTRIBUTIONS

This dissertation describes multiple inventions regarding design and development of aminoglycoside based hydrogels for applications in high-throughput cell culture models of tumor dormancy, relapse (for drug discovery and development) and novel chromatographic resins for plasmid DNA biotechnology:

1. The first demonstration and development of amikacin aminoglycoside based hydrogel with tunable chemo-mechanical properties of mechanical stiffness and adhesivity.
2. Aminoglycoside based hydrogels for high-throughput 3D cell culture platforms of prostate, bladder, breast and pancreatic cancer cell types.
3. High-throughput in-vitro platform of tumor dormancy, relapse and micrometastases in a 96 well plate format
4. Identification of chronic ER stress as a novel pathway to induce apoptosis in dormant bladder cancer tumors.
5. Acceleration of chronic ER stress induced apoptosis by exogenous delivery of calcium to the cell cytoplasm.
6. Identification of material strategies for rapid isolation and separation of metastatic cell fractions from a heterogeneous cancer cell population.
7. Design and development of novel aminoglycoside based microbeads and macroporous gels for pDNA binding and recovery.

In addition, this dissertation also describes generation of novel acrylic devices for high-throughput generation of user desired polymeric scaffolds and micellar mitoxantrone drug delivery of TRAIL sensitizer to sensitize multiple cancer cell lines to TRAIL mediated cell death:

1. Micellar delivery of anticancer drug mitoxantrone towards TRAIL sensitization of bladder, prostate and breast cancer cell lines in-vitro.

2. Design and development of high-throughput acrylic based devices for rapid and high-throughput generation of user desired macroporous and non-macroporous polymeric scaffolds.

CHAPTER 2: AMINOGLYCOSIDE-DERIVED HYDROGEL ('AMIKAGEL') AS A NOVEL SUBSTRATE FOR HIGH-THROUGHPUT GENERATION OF 3D TUMOR MICROENVIRONMENTS (3DTMS)

2.1. INTRODUCTION

Two dimensional (2D) monolayer cultures are ubiquitous in cell-based molecular investigations. However, 2D cultures often fail to capture the complexity inherent in three dimensional tissues [85]. Significant disadvantages of these systems include inability to achieve in vivo-like extensive cell-cell adhesions [86], considerable differences in cellular morphologies [87], minimal nutrient and metabolite gradients [34], differences in gene expression profiles [88] and absence of cell-ECM interactions [89] and absence of vascularization etc. In order to circumvent these problems, three dimensional (3D) cellular models [21] have been proposed and developed in diverse fields of developmental/embryonic biology [90], cancer biology [91], drug discovery [92], and regenerative medicine [93]. Of these, developments of multicellular three-dimensional tumor spheroids that closely mimic the native tumor microenvironmental intricacies are of critical importance. These three dimensional tumor microenvironment (3DTM) models can capture the cellular and metabolic profiles of tumors, and demonstrate defined regions of outer proliferating cells, intermediate quiescent cells and innermost necrosis, generated due to limitations in nutrient, oxygen and metabolic transport. In particular, 3DTMs generated by co-culturing epithelial cancer cells with their stromal/stellate counterparts can provide insights into tumor-stroma interactions, and cell-ECM interactions, in addition to shedding light on their roles in carcinogenesis and metastasis [94]. High throughput generation of 3DTMs can lead to fundamental advancements in tumor biology and facilitate realistic drug screening in the context of tumor complexity, reduced drug and metabolite transport, drug and radiation resistance, and induced hypoxia due to the three dimensional architecture.

The ability to chemically or biologically engineer the substrates supporting the 3DTMs can provide exquisite control over important spheroid properties such as metastasis [95], growth and proliferation [96], angiogenic ability [97-98] etc. These properties if captured in-vitro, can serve as

important models to study the disease. Liang et al. [95] showed that fine tuning the matrix stiffness of PEG-collagen gel can dictate metastatic properties into 3D liver tumor spheroids. Also, synthetic hydrogels have been created with growth factors attached to mimic native tissues to probe cell-ECM interactions during tumor growth, metastasis and resistance [96].

Generation of 3D cell spheroids can be facilitated by methods such as hanging drop cultures, rotary suspension cultures, and culture on non adherent substrates (agarose) and Matrigel® [20, 99-102]. In principle, the hanging drop technique allows high throughput generation of spheroids under gravity via cell-cell adhesion, but is tedious and can accommodate only small amount of media, thereby requiring frequent refreshing of the media. This system can also lead to poor yields. Conventional suspension cultures generated using spinner flasks for spheroid growth often result in a heterogenous population of spheroids, making the isolation of spheroids with desired sizes difficult. Existing gels including agarose and Matrigel can undergo undesired gelling during experimentation, making their use without temperature controlled robotic liquid handling systems quite stressful during high-throughput assays. In addition, Matrigel is expensive compared to other alternatives, needs maintenance of cold temperatures whilst transferring and has batch-to-batch variations, thus reducing the flexibility of operating protocols. Low adherent cell culture plates provide a non-adhesive surface that cannot be tuned to provide differential mechanical input to the 3DTM if desired by the user. In addition, some of these substrates also lack optical transparency leading to considerable challenges in live bioimaging in a confocal microscopy experimental setting.

This chapter describes the discovery and detailed characterization of a new, highly versatile, optically transparent aminoglycoside antibiotic-based polymeric hydrogel material (Amikagel), whose chemo-mechanical properties could be heavily engineered. Important properties such as hydrogel mechanical stiffness, hydrogel adhesivity, gelation kinetics etc were easily controlled by temperature modulation and by varying the input monomer mole ratios. Amikagel thus formed, supported formation and maintenance of high-throughput cultures of three-dimensional tumor microenvironments (3DTMs) across multiple cancer cell lines of breast, bladder and pancreatic cancer.

2.2. MATERIALS AND METHODS

Materials

Amikacin hydrate (AH) (referred to as amikacin henceforth), docetaxel, wortmannin, chloroquine, propidium iodide, ribonuclease-A, poly (ethyleneglycol) diglycidyl ether (PEGDE), sodium orthovanadate and sodium fluoride were purchased from Sigma-Aldrich (St. Louis, MO), and used without further purification. Bortezomib was obtained from Selleck Chem (Houston, TX). Mitoxantrone was obtained from Ontario Chemicals (Guelph, ON). Thapsigargin and ROCK inhibitor Y-27632 dihydrochloride were obtained from Santa Cruz Biotech (Dallas, TX). Calcein AM/ethidium homodimer Live/Dead stain®, AlexaFluor 568-Phalloidin (actin-binding), 4', 6-diamidino-2-phenylindole (DAPI) and Collagenase Type-2 were purchased from Life Technologies, (Carlsbad, CA). T24 and UMUC3 human bladder cancer cells were obtained from Professor Christina Voekel-Johnson at Medical University of South Carolina, Charleston, SC as part of an existing collaboration. These cell lines were verified for their authenticity through Bio-Synthesis Inc (Lewisville, TX). PC3-eGFP prostate cancer cells were obtained as a gift from Anne Cress' lab and Experimental Mouse Shared Service (EMSS)/ Cancer Center Support Grant (CCSG), University of Arizona Cancer Center. MTT and XTT cell proliferation kit, prostate stromal cells (WPMY-1) and PC3 prostate carcinoma cells were purchased from American Type Culture Collection (ATCC) (Manassas, VA) [103]. Bj5ta human foreskin fibroblasts were obtained from Center for Biosignatures Discovery Automation (CBDA), Biodesign Institute, ASU as part of an existing collaboration. NIH3T3 murine fibroblasts were obtained from Professor David Capco, School of Life Sciences, Arizona State University, Tempe, AZ as part of an existing collaboration. Cell culture media – RPMI media, DMEM with L-glutamine, Pen-Strep solution: 10000-units/mL penicillin and 10000-µg/mL streptomycin in 0.85% NaCl were purchased from Hyclone (Logan, UT). Premium heat inactivated fetal bovine serum (FBS) was purchased from Atlanta Biologicals (Flowery Branch, GA). Cell culture-treated 24 and 96 well plates were purchased from Corning Life Sciences (Corning, NY). Growth Factor reduced (Basement membrane) Matrigel matrix was obtained from Corning (Bedford, MA) and molecular biology grade agarose was obtained from Fisher Scientific (Pittsburgh, PA). Nanopure water was used in all preparations.

Amikagel synthesis

Ring-opening polymerization between amine groups of amikacin hydrate and epoxide groups of poly (ethylene glycol) diglycidyl ether (PEGDE) resulted in the formation of a novel hydrogel henceforth called 'Amikagel'. Different stoichiometric ratios of amikacin and the cross-linker PEGDE were dissolved in Nanopure® water, mixed and incubated at 40°C for 7.5 h, in order to obtain Amikagels AM1, AM2, and AM3 of different compositions (Table 1). The final concentration of amikacin was 10 wt% in all gels. All experiments were carried out in triplicate unless otherwise mentioned.

Optical transparency measurements

40 µL of amikagel pregel solution was added to wells of a 96 well plate. After gelation of the gel as described above, an absorbance sweep was performed from the wavelength 400 nm to 700 nm and was compared to a well with no gel as control. Any absorption peaks measured were considered as reduction in transparency of the hydrogel.

Rheological Measurements

Rheological measurements were carried out at 25°C with an AR-G2 rheometer (TA Instruments) using parallel-plate configuration in the oscillatory mode. Amikagel samples of different mole ratios were prepared in a high-throughput device to yield gel discs of diameter 8 mm and 3 mm thickness. 8 mm was chosen to match the dimension of the upper parallel plate. These Amikagel discs were loaded between the plates till the samples were in contact with the upper and lower plates (normal force applied 1N). Once in contact, a time sweep of 180 seconds was performed at an angular frequency of 0.1 rad/sec was conducted at a fixed strain of 0.1%. Storage (G') and loss (G") moduli were experimentally determined as a function of applied frequency and absolute shear modulus (|G*|) was estimated. The storage modulus (G') gives information about material elastic properties and its mechanical stiffness, while loss modulus (G") provides information about

the viscous/liquid properties of the material. Absolute shear modulus representing the stiffness of the hydrogel was calculated as $|G^*| = (G'^2 + G''^2)^{0.5}$.

High throughput device design

A novel acrylic device was designed to rapidly generate Amikagel discs of desired dimensions in high-throughput for the rheological studies. In any experiment on a parallel plate AR-G2 rheometer, it is recommended that the diameter of the sample gel disc match the diameter of upper parallel plate. As the gelation of the hydrogel takes a considerable time on the device, it was prepared in an external high-throughput device and the rheological properties of the Amikagel disc were then measured. A novel design for the high-throughput device was conceived and created on the AutoCAD software. These designs were then produced on 0.17 inch thick acrylic sheet using a CO_2 laser cutter (Universal laser systems) at ~100% power and 5% speed. The designs were tested and modified to achieve high satisfaction for easy high-throughput generation of hydrogel discs.

FT-IR Spectroscopy of Amikagels

Extent of Chemical cross-linking developed between the epoxide and amine groups upon Amikagel gelation was studied using FT-IR.Amikagel FT-IR measurements were made with Perkin-Elmer FT-IR system (Spectrum GX). In a typical example, 0.2 gm of Amikacin Hydrate was allowed to react with 0.45 ml of PEGDE, incubated 7.5 h at 40°C for gel formation. After incubation, the sample was immediately freeze dried and pressed into pellet with potassium bromide for infra-red spectroscopy measurements. Amikagel sample before gelation was used as control in the experiment.

Swelling studies

Different Amikagels were prepared as stated above. Amikagel discs of diameter ~ 10mm and thickness ~ 1mm were cut, placed on a glass slide and immersed into Nanopure® water (ca. 40 ml, 37^{o}C, 48 hours). After removal of excess water, the samples were weighed to determine the

wet weight (W_{wet}). The discs were then freeze dried and weighed again to determine (W_{dry}). Amikagel

The degree of swelling (DS) was calculated as follows:

$$DS = \frac{\left(W_{wet} - W_{dry}\right)}{W_{dry}}$$

Scanning electron microscopy of fractured Amikagels

The inner network morphology of cross-linked Amikagel was studied using FE-SEM (Field Emission Scanning Electron Microscopy). Amikagels were prepared as described in section 2.4, frozen, fractured and mounted onto an aluminum stud. The samples were lyophilized, and the freeze-dried sample was fractured and sputter-coated with gold for 240 s (E1030 Ion sputter). The interior of the Amikagel sample was visualized using a Field Emission Scanning Electron Microscope (FE-SEM; PHILIPS FEI XL-30 SEM) at 25kV. The thickness of the sample was 3 mm in these experiments.

Scanning electron microscopy of wet Amikagel surface

Constituent components of Amikagel were reacted as described in section 2.4 and hydrated with Nanopure® water at 37°C for 12 hours. The water in hydrated Amikagels was exchanged with acetone by incubating specimens for 15 minutes each in a graded acetone series. The gels were subsequently dried through the critical point of CO2 and sputter coated with Pt-Au using the instruments Balzer CPD 020 and a Technics sputter coater respectively. Images were scanned with a JOEL JSM scanning electron microscope operating at 15 keV housed in the W.M. Keck Bioimaging facility at Arizona State University.

Generation of 3D Tumor Microenvironment models (3DTMs)

Cell culture

3DTMs were generated using single cell lines or co-cultures of cancer cells with stromal cells on AM3 (Table 1). Different cancer cell lines including, T24 and UMUC-3 bladder cancer, PC3 and

PC3-eGFP prostate cancer and MDA-MB-231 breast cancer were employed in the generation of 3DTMs. Stromal cells including NIH3T3 murine fibroblasts, BJ-5ta human foreskin fibroblasts, WPMY-1 human prostate stromal cells were also used. T24, MDA-MB-231, WPMY-1 and Bj-5ta cells were propagated in DMEM supplemented with 10% (v/v) fetal bovine serum and 1% (v/v) penicillin and streptomycin (Pen-Strep solution: 10000 units/mL penicillin and 10000 µg/mL streptomycin in 0.85% NaCl). For NIH3T3 cell propagation, 1% (v/v) sodium pyruvate was added and fetal bovine serum was replaced with calf serum in the media. For all the remaining cell lines, RPMI media supplemented with 10% (v/v) fetal bovine serum and 1% (v/v) penicillin and streptomycin was used.

Generation of 3D-DTMs using Amikagels

1 ml of amikagel AM1, AM2 and AM3 pre-gel solutions were filtered through a 0.20 µm filter and 40 µL of the filtrate was added to each well of a 96 well plate. The plates were sealed with paraffin tape (Parafilm, Menasha, WI) and incubated in an oven maintained at 40^{o}C for 7.5 hours. After gelation, the surfaces of Amikagels were washed with 150 µL of Nanopure® water for 12 hours, in order to remove traces of unreacted monomers. All 3D-DTM experiments were set up by liquid overlay culture [104] of cells on top of Amikagel surface in a total volume of 150 mL media /well; either 100,000 cancer cells alone (single culture) or 50,000 stromal cells followed by 50,000 cancer cells (co-culture) were incubated, unless indicated otherwise in specific cases. After 48 hours of incubation, 50% of the media in the wells was replaced with fresh media i.e. DMEM/RPMI + 10% (v/v) FBS + 1% (v/v) Pen-Strep at regular intervals of 48 hours. Care was taken to withdraw and add the media slowly so as to not perturb 3D-DTM formation. Fresh media was added every 48 hours following cell plating. For 3D-DTM generation on 24 well plates, 400 µL of pre-gel volume was used instead of 40µl. Different co-culture 3D-DTM systems are represented as fibroblast/stromal cells-epithelial cells (e.g. NIH3T3-T24, WPMY-1-T24) to accurately indicate the sequence of their addition. In most cases, 3D-DTMs were formed 5-7 days following culture on Amikagels.

Scanning electron microscopy (SEM) of 3D-DTMs

Unless otherwise stated, all materials were purchased from Electron Microscopy Sciences (EMS; Hatfield, PA) and used when fresh. 3D-DTMs, approximately ~1 mm in diameter, were manually manipulated with a fire-polished glass Pasteur pipet and washed three times using phosphate-buffered saline (PBS) in wells of a 96-well plate. 3D-DTMs were cytologically preserved with 0.1 M cacodylate buffer made fresh with 2% glutaraldehyde and 1% formaldehyde at room temperature for 1 hour. Specimens were washed 5 times with 0.1 M cacodylate buffer, and subsequently post-fixed in 1% OsO_4 for 2 hours at room temperature in the dark. After extensive washes in nanopure deionized (DI) water, the samples were dehydrated through a graded ethanol series, and dried through the critical point of CO_2 using Blazer CPD 020. Spheroids were immobilized on aluminum stubs and sputter coated with Pt-Au using a Technics sputter coater. Images were collected according to the conditions described in section above.

Actin staining

Unless otherwise stated, all reagents used for immunocytochemistry were purchased from Sigma Aldrich (St. Louis, MO). Different 3D-DTMs were fixed in 4% formaldehyde in 1X PBS for 12 hours before their transfer to 30% sucrose solution (w/v) for another 12 hours. Fixed spheroids were collected in Tissue Tek and flash frozen in liquid nitrogen. Following this, 3D-DTMs were cut into thin sections of ~40 µm thickness using a cryotome maintained at -14^{o}C. The cut sections were placed on a positively charged glass slide and dried at 37^{o}C to facilitate the attachment of the cryosection to the charged slide. Once dried, the 3D-DTM sections were thawed in 100 mM PBS with 2% formaldehyde (v/v) added to it. Cells were permeabilized with an intracellular buffer (ICB) (ICB contained the following ingredients: 100 mM KCl, 5 mM $MgCl_2$, and 20 mM HEPES (pH 6.8)) with 2% formaldehyde and 0.1% Triton X-100 for 10 minutes at room temperature in the dark. Cells were washed 3 times for 15 minutes per wash in ICB containing 1% bovine serum albumin (ICB-BSA) with gentle agitation. Fluorophore-conjugated actin-binding drug, Alexa Fluor 568 Phalloidin was used in this study to label filamentous actin. Phalloidin was diluted from the stock at a 1:200 µL dilution in antibody dilution buffer (ICB modified to contain 0.01% Tween-20

and 1% non-fat dry milk) and allowed to incubate on the sections over night in a humidified chamber protected from light at room temperature. The sections were washed 3 x 15 minutes with ICB-BSA the following morning, and the nuclear probe 4', 6-diamidino-2-phenylindole (DAPI) was challenged at 1:100 dilution in ICB for 15 minutes at room temperature. The sections were subsequently mounted in Vectashield (Vector Labs) and the cover slips were sealed at the edges with optically clear nail polish. All images were collected on a Leica SP5 laser scanning confocal microscope housed in the WM Keck Bioimaging Facility at ASU. The images shown represent maximum projection overlays with the z-axis set to scan at intervals of 0.4 µm. Images were adjusted linearly for contrast and brightness.

Hematoxylin & Eosin (H&E) staining of 3D-DTMs

Spheroidal 3D-DTMs, approximately 1 mm in the longest dimension, were collected by manual manipulation of a fire-polished glass pipette and subjected to several washes with PBS. The specimens were subsequently fixed overnight in freshly prepared Bouin's fluid (75% saturated solution of picric acid, 5% glacial acetic acid in neutral-buffered formalin (pH 7.0) at 4°C with gentle agitation. Fixed specimens were dehydrated through graded ethanol series and embedded in Paraplast+. Serial 10 µm thick sections were collected on glass slides and incubated at 42°C overnight. Paraffin was removed with histology-grade toluene, and the slides were rehydrated through an ethanol series in Coplin jars, and washed for 5 minutes in Barnstead Nanopure filtered water (resistance of 18.2 MΩ). Basophilic elements (e.g. nuclei) of the cells were stained using Mayer's hematoxylin for 15 minutes at room temperature followed by 20 minutes in running tap water. The samples were counterstained with eosin for 5 minutes and incubated through increasing graded ethanol series. Slides were briefly transitioned from ethanol to toluene and incubated in 100% toluene for 2 minutes. Drops (approximately 15 µL) of Permount served to mount glass cover slips permanently. The slides were dried in a chemical hood overnight and imaged with a Nikon inverted microscope fitted with an Olympus DP26 color camera housed in the W.M. Keck Bioimaging Facility at ASU.

Cell cycle analyses

Following five days of incubation on AM3, 3D-DTMs of T24 cells with NIH3T3 murine fibroblast cells were harvested for cell cycle analysis. Four or five individual 3D-DTMs of T24 cells alone or UMUC3 cells alone were harvested on the 7th day after seeding on Amikagels, collected in an eppendorf tube. 50 µL of 5 mg/ml collagenase was added to 3D-DTMs prepared using fibroblast helper cells for 30 minutes at 37°C in order to facilitate their disassembly by gentle pipetting. Single cell 3D-DTMs were disassembled using manual pipetting. Disassembled 3D-DTM cells were then centrifuged at 200 r.c.f. in order to collect the cell pellet. The pellet was resuspended in a solution of 1% v/v 1X Triton-X, 5% (v/v) fetal bovine serum (FBS), 50 µg/mL propidium iodide, and 0.006-0.01 units/mL ribonuclease A. After incubation for 30 minutes on ice, cells were analyzed for their cell cycle profiles using flow cytometry; the propidum iodide (PI) signal was detected using an excitation at 535 nm and emission at 617 nm. Voltages of the FL2-A, SSC and FSC channels were adjusted in order to obtain best representative peaks for alignment of 2n (diploidy – G0/G1) peak to 200 intensity units during flow cytometry. FL2A (FL2-Area) provides the information regarding the pulse area of the emitted fluorescence signal (total cell fluorescence) whereas SSC and FSC provide the information regarding the forward scatter and the side scatter light from the sample. FSC is a measure of diffracted light from the sample proportional to cell surface area or size and SSC is proportional to cell granularity or internal complexity.

Investigation of Chemotherapeutic Drug Efficacy on 3D-DTM Viability

Different concentrations (12.5, 25, 50 and 100 µM) of the anticancer drugs docetaxel, (10-40 µM) mitoxantrone, or (250-500 µM) thioTEPA were added to 3D-DTMs formed after 5-7 days of initial cell seeding on Amikagel. Drugs were added to 3D-DTMs of T24 cells co-cultured with NIH3T3 murine fibroblasts on day 5, but added to 3D-DTMs of T24 cells alone on day 7 due to the different times required for their formation. After 96 hours of drug exposure, T24 3D-DTMs were disassembled using manual pipetting. Co-culture 3D-DTMs were disassembled using 50 µl of 5 mg/ml collagenase for 20 minutes and cell viability was assessed by Live/Dead® staining followed

by flow cytometry. 3D-DTM viability was also measured using MTT/XTT assay as described previously [105].

Statistical Analyses

Averages have been expressed as mean ± SD. Two-tailed t-test with 95% CI was used analyze and compare the percent cell death data of individual drugs. One-way ANOVA has been used to study the differences between the effectiveness of multiple drugs and their combinations. Tukey's multiple comparisons test was used during multiple pairwise comparisons whereas Dunnett's multiple comparisons test was used while comparing multiple means to a single one (control). $p<0.05$ indicated significance in the analyses. All analyses were performed using the Prism GraphPad software. All experiments have been performed at least n=2 independent experiments with three replicates each unless specified.

2.3. RESULTS AND DISCUSSION

Amikagel formation and characterization

Reaction of amines, present in the aminoglycoside amikacin, with epoxides in the PEGDE cross-linker resulted in the formation of a new hydrogel, 'Amikagel' (**Fig. 2-1 (i)**) that underwent a sol-gel transition upon incubation at 40^{o}C (**Fig. 2-1 (ii), A-B**). Of particular interest was the presence of an aliphatic primary amine in amikacin which can be cross-linked rapidly. In addition, the presence of multiple sugar groups in Amikacin along with the cross-linker poly (ethylene glycol) (PEG) was hypothesized to yield biocompatible hydrogels. The epoxide groups of PEGDE upon reaction with amines of amikacin formed covalent bonds among adjacent aminoglycoside molecules, thus generating a cross-linked hydrogel network that underwent a sol-gel transition at 40^{o}C (**Fig. 2-1 (ii), A-B**). Three chemo-mechanically different Amikagels (AM1, AM2 and AM3) were prepared by varying the mole ratios of the monomers; amikacin and PEGDE. **Fig. 2-1** shows the synthesis procedure, and **Table 2-1** shows different hydrogel compositions, AM1, AM2, and AM3, generated.

Table 2-1. Stoichiometric amounts of Amikacin Hydrate (AH) and Poly (ethylene glycol) diglycidyl ether (PEGDE) used in preparation of different Amikagels.

Amikagel Composition	
Amikagel	**Mole Ratio (AH: PEGDE)**
AM1	**1:1.5**
AM2	**1:2**
AM3	**1:3**

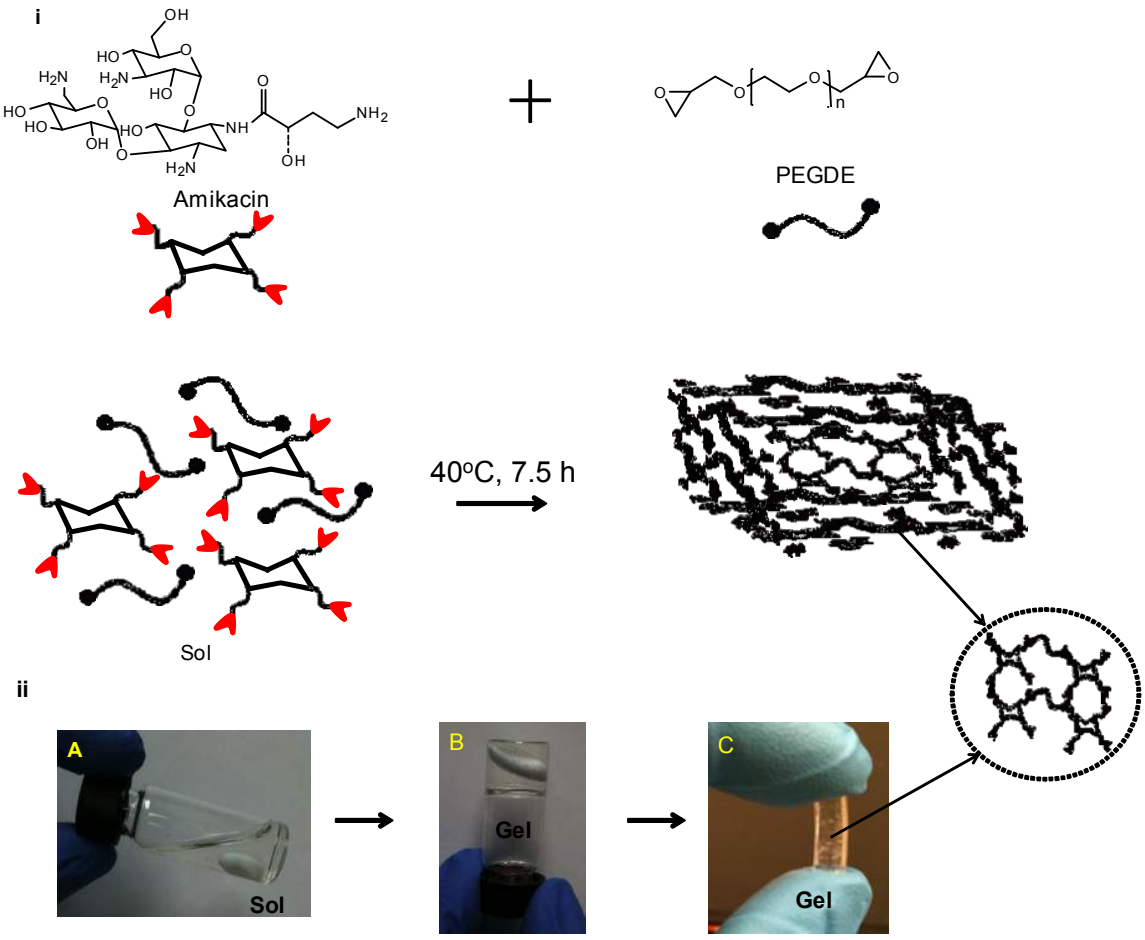

Figure 2-1. Schematic of Amikagel formation. (i) Amikacin hydrate and poly (ethylene glycol) diglycidyl ether (PEGDE) were reacted in nanopure water at room temperature. **(ii).** Characteristic **(A)** sol to **(B)** gel transition of Amikagel at 40° C after 7.5 h of incubation. **(C)** Amikagel held between fingers.

Fig. 2-2 shows the time required for formation of Amikagels AM1, AM2 and AM3 as a function of temperature. The time required for gelation at a given temperature, decreases as the amount of PEGDE increases (i.e. AM 3 ~ AM 2 < AM 1). In addition, as the gelation temperature was increased, the time required for gelation reduced indicating a temperature controllable Amikagel formation process. At the highest temperature tested of 75^{o}C, complete gelation was achieved within 20 minutes for all the three gels. As the temperature increases, the rate of reaction between the epoxide groups of PEGDE and amine groups of amikacin moieties are likely to react rapidly leading to faster gelation. Similarly, higher amount of the crosslinker will allow for faster crosslinking between the PEGDE and the amikacin groups leading to faster gelation.

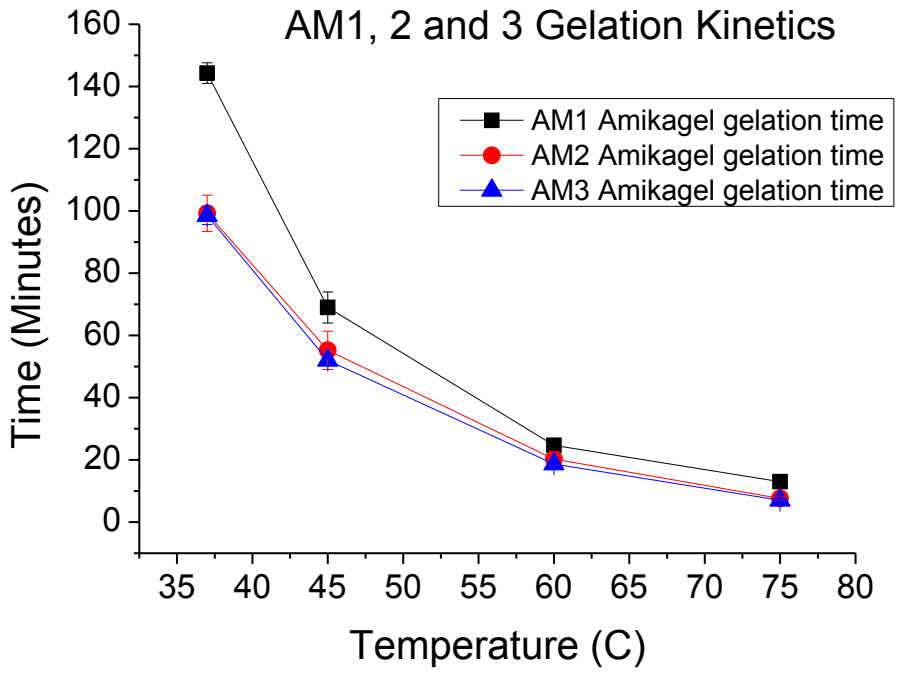

Figure 2-2. Temperature dependent kinetics of Amikagel gelation. At higher temperatures (60°C and 75°C) there was no significant difference recorded for the time required for gelation between AM1, 2 and 3 Amikagels. At 37°C, AM2 and AM3 amikagels were found to gel before AM1 gel (p-value < 0.01).

FT-IR spectra of Amikagel AM3 was recorded immediately after mixing the monomers (t=0) and after completion of cross-linking (t=7.5 hours) of the monomers at 40°C (**Fig. 2-3**). Epoxide specific stretch peaks were seen in the range of 860-950 cm^{-1} in the spectra at t=0, measured immediately after mixing the monomers. However, the epoxide peaks largely disappeared in the Amikagel hydrogel (t=7.5h), indicating the consumption of epoxide groups during hydrogel formation. In addition, a large number of secondary amines formed due to the ring-opening reaction between amines and epoxides, were seen at t=7.5h (secondary amine specific stretch peaks at 2873 cm^{-1}). The hydrogel also showed a broad absorption band from 3024-3756 cm^{-1}, indicating presence of a large number of hydroxyl groups (3552 cm^{-1}) and primary amines NH_2 (3336 cm^{-1}). A strong twin peak at 1351 cm^{-1} confirmed the presence of ether links in the hydrogel, while the band at 1103 cm^{-1} was indicative of the glycosidic linkage (C-O-C) present in amikacin. Carbonyl group stretching is indicated by the peak at 1656 cm^{-1} and the absorption band indicative of the $-CH_2-CH_2-O-$ moiety of PEG was seen around 2956 cm^{-1}.

Taken together, FT-IR studies show consumption of epoxides and generation of secondary amines during hydrogel formation, thus confirming the formation of cross-linked network between amikacin and PEGDE.

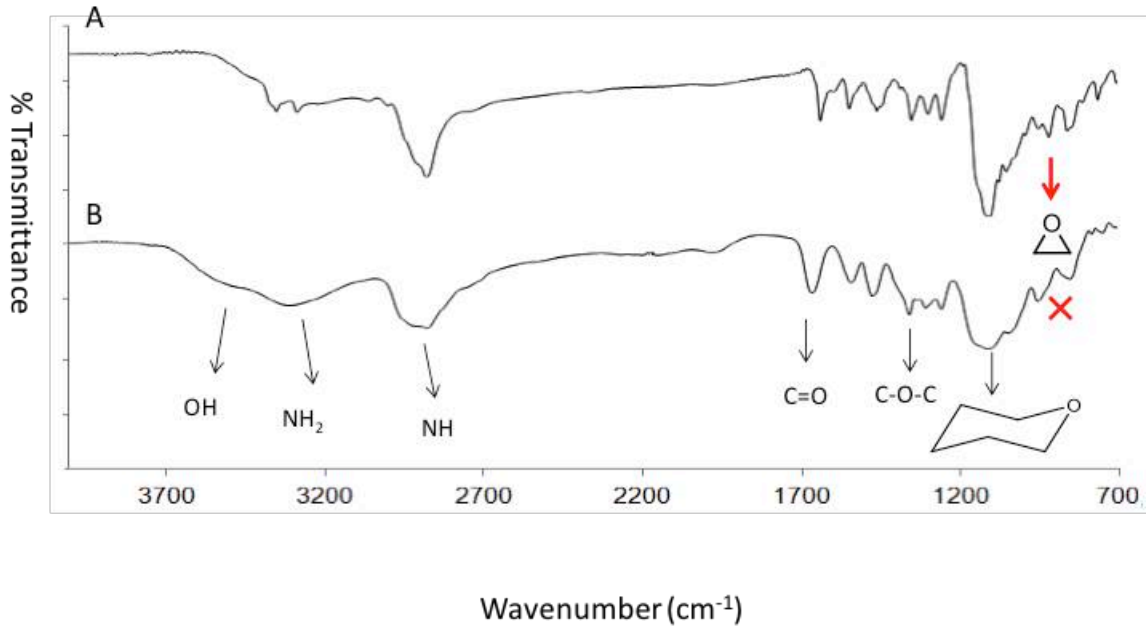

Figure 2-3. FT-IR spectrum of freeze-dried Amikagel (AM3). FT-IR spectrum at **(A)** initial (t=0) and **(B)** after (t=7.5 hr) incubation at 40° C temperature.

Optical transparency to visible light (wavelengths – 400-700 nm) of Amikagel AM3 was investigated to identify the wavelengths of light that may not be used in for bio-imaging studies on the gel. The absorbance profiles of amikagels show these hydrogels were as optically transparent as empty plastic well of 2D tissue culture 96 well plate (**Fig. 2-4**). Absorbance peaks of both amikacin and PEGDE lie majorly in UV regions of 250-400 nm, with minimal absorbance in the visible light region, making the gel optically transparent for bio-imaging applications such as confocal microscopy, fluorescence imaging, live cell imaging etc [106-107].

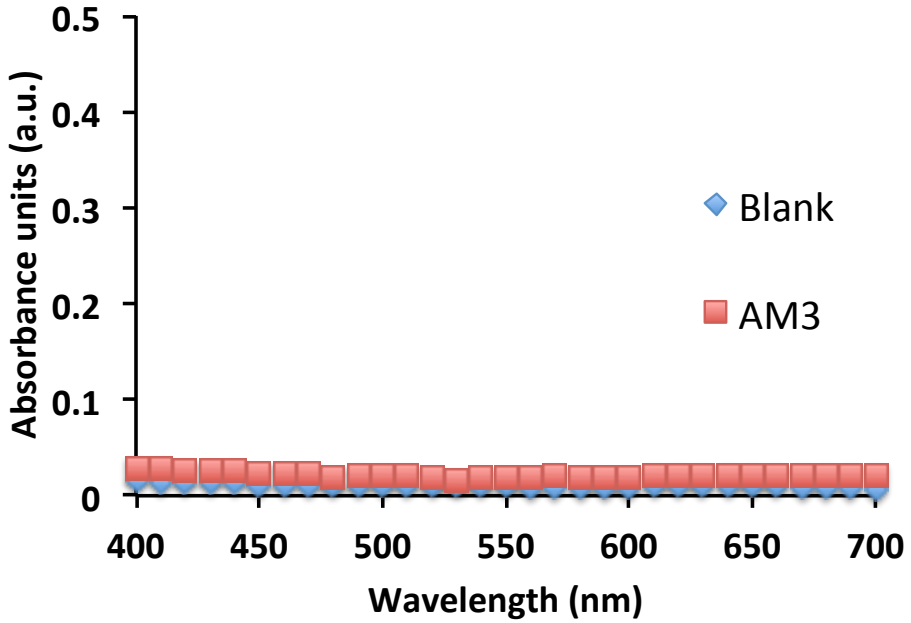

Figure 2-4. Absorbance of AM3 Amikagel. AM3 Amikagel showed minimal absorbance in the visible light region indicating its easy use in multiple fluorescent bioimaging applications.

Amikagel Material Properties

Amikagels AM1, AM2 and AM3 were characterized for complex modulus (rheological characterization), swelling ratios, hydrophilicity, inner crosslinking, surface morphology and adhesivity to elucidate different properties of the novel material.

High Throughput Device for Amikagel Generation For Parallel Plate Rheological Measurements

The storage modulus (*G'*) and loss modulus *(G")* of chemically cross-linked Amikagels were determined using oscillatory rheology experiments at room temperature using the parallel plate AR-G2 rheometer. In order to create circular gel discs in high-throughput that match the dimension of upper parallel plate (8 mm) (recommended), a novel high-throughput device was designed. Traditional techniques using cylindrical wells castings, test tubes or syringes etc to generate the discs largely suffer from non-reproducibility and are not high-throughput.

We developed three generations of acrylic devices that housed gaps within them for gelation. The first and second generation devices did not generate easy recoverable gel discs (**Fig. 2-5A**). For example, the second-generation device contained cavities could be filled up with pre-gel solution, leading to in-situ gelation (**Fig. 2-5B**). Although the gelation was satisfactory, the recovery of columns from the device proved tricky. Second-generation acrylic design was plagued with issues of less recovery of fully formed Amikagel discs. Learning from the previous two generations, we designed the third generation of acrylic geometry (**Fig. 2-5 C-F**), which showed very high success in high throughput Amikagel generation.

Third generation acrylic designs consisted of two mirror pieces with semi-circular teeth (diameter - 0.8 cm) that could be linked to each other to generate one unit (**Fig. 2-5 C-F**). Both cylindrical pieces were wrapped with a layer of paraffin film for easy assembly and disassembly. One of the flat sides of the device was covered with paraffin film to prevent any leakage. The cylindrical gap created by assembling the unit was filled with Amikagel pre-gel solution for gelation. After gelation, the recovery of gels was found to be very easy. One of the greatest strengths of this device was the incorporation of the central break-line that can dissociate the pieces of the device after the gel is formed very easily. Usage of parafilm also ensured minimal adhesion of the gel with the film. The gels tended to stay unbroken during their recovery and were directly used for rheological studies. This third generation acrylic design was found to be far superior compared to other two previous generations in its ease of use and the reproducibility for Amikagel production. The entire method was tested by at least two/three independent operators across more than 50 independent experiments (n>50).

Additional design insets were created to increase the throughput of the device (**Fig. 2-5 E-F**). As shown in (**Fig. 2-5 E-F**), multiple additional insets were developed to add to the existing device. The insets have semi-circular teeth on both sides and can be joined in between the two end pieces of the existing device. These insets were greatly able to increase the throughput of the device.

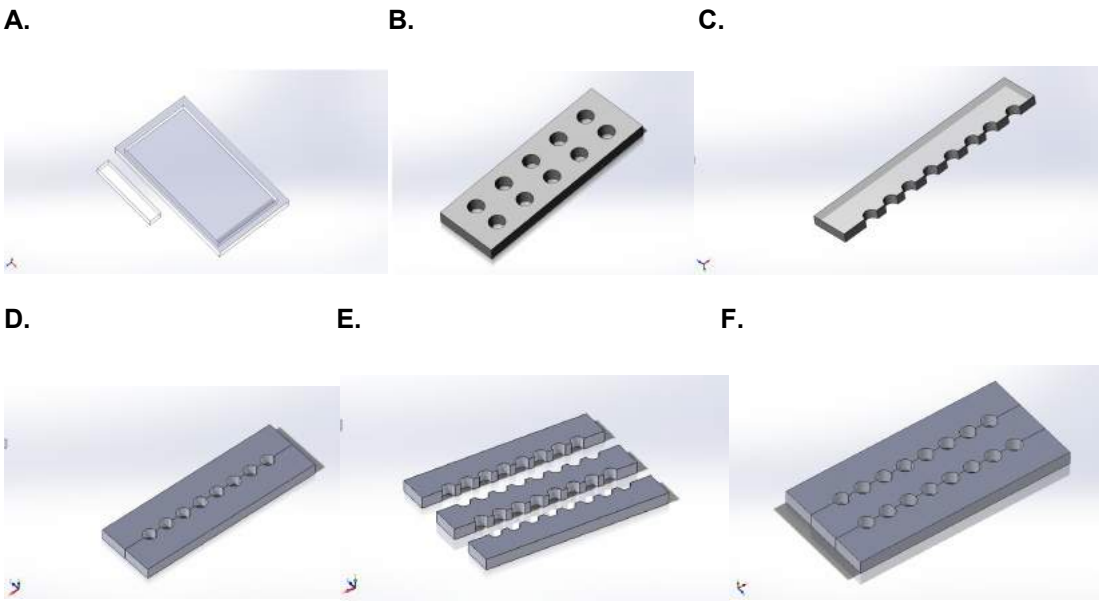

Figure 2-5. **High throughput device for Amikagel generation. (A)** First **(B)** Second **(C-D)** Third generation acrylic designs for high-throughput Amikagel generation. Third generation of the acrylic was found to be the ideal for the gel recovery after gelation. Mirror pieces of acrylic geometries with semicircular teeth were combined to form a central circular gap to allow for pre-gel to gel formation. **(E-F)** Insets to increase the throughput of the device are shown. These insets have semi-circular teeth on both sides and attach to the end pieces to increase the throughput/device.

Rheological Analysis Of Amikagels

|G*| values of Amikagels (AM1, AM2 and AM3) depended on the mole ratio of Amikacin: PEGDE added to form the hydrogel. Amikagels AM1, AM2 and AM3 possessed material stiffness *(|G*|)* of 17 kPa, 84 kPa, and 135 kPa when dehydrated, and 36 kPa, 140 kPa and 215 kPa, when fully hydrated (**Fig. 2-6**). In all cases, the absolute shear modulus was noted to significantly increase after complete hydration of the gels ($p<0.05$, two-sided student's t-test). It is likely that the water forms additional bonds within the crosslinked hydrogel structure, thus introducing new nodes to store elastic energy. This could lead to increase in the absolute shear modulus of the gel after hydration.

Amikagels showed higher values of *G′* (storage modulus) compared to *G″* (loss modulus) and exhibited a loss angle (δ) ~ 1, indicating that Amikagels are predominantly elastic ($\delta \sim 0^{o}$)

and not viscous (δ ~ 90^{o}) in nature. As the amount of PEGDE relative to Amikacin increased, the absolute shear modulus *(|G*|)* of the gels increased (AM3>AM2>AM1). Higher amounts of PEGDE likely resulted in higher cross-linked gels, increase in degree of cross-linking, which, in turn, caused the increase in their mechanical stiffness due to increase in the nodes available for storage of elastic energy.

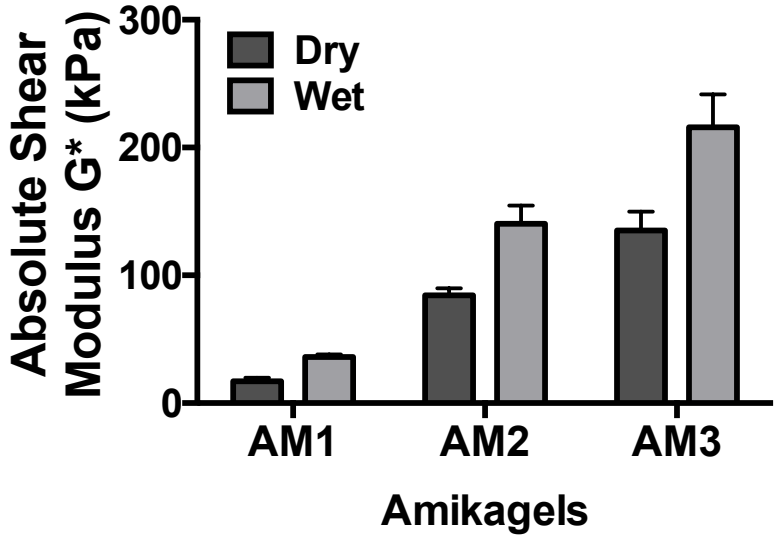

Fig. 2-6. Absolute shear modulus measurement of wet and dry Amikagels. |G*| absolute shear modulus (material mechanical stiffness) of AM1, AM2 and AM3 amikagels before (dry) and after (wet) hydration respectively.

Other Structural Properties Of Amikagels

Macroscopic surface morphology and microscopic inner cross-linked networks of Amikagels were studied using Field Emission Scanning Electron Microscopy (FE-SEM). As expected, the PEGDE content and degree of cross-linking had a significant impact on both surface and interior morphology of Amikagels. The folding on the hydrogel surface, as shown in **Fig. 2-7A**, increased with increase in the degree of cross-linking. AM1 Amikagel had a predominantly smooth surface, which increasingly turned into grooves and ridges as the PEGDE content increased. Internally, as the PEGDE content and degree of cross-linking increased, the pore sizes of the fractured Amikagels decreased (**Fig. 2-7B**) (AM3>AM2>AM1). Increase in degree of cross-linking between adjacent aminoglycoside molecules could have directly led to the reduced pore sizes and a stiffer hydrogel.

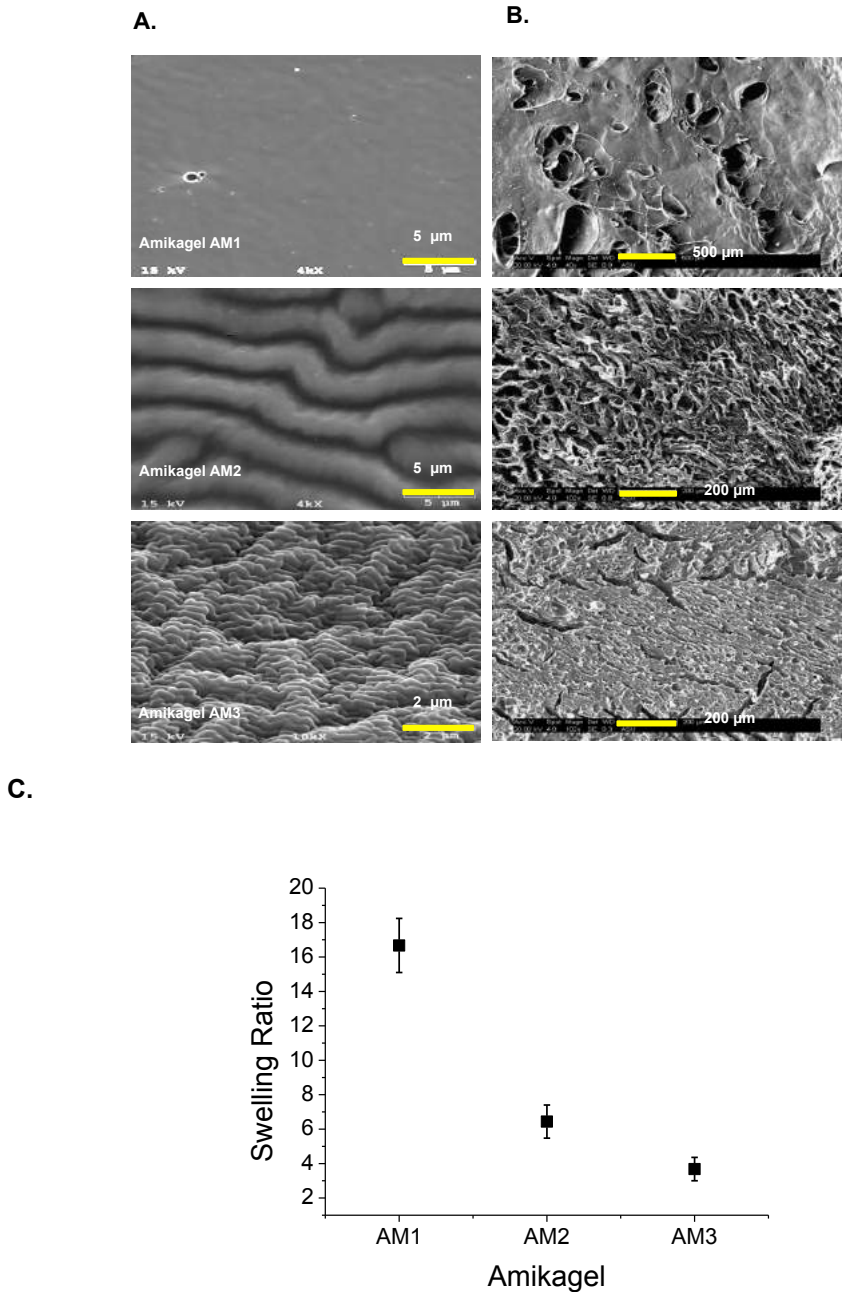

Figure 2-7: Characterization of Amikagels using electron microscopy and swelling studies. Scanning Electron Microscopy (SEM) images of **(A)** different Amikagel surfaces, and **(B)** fractured Amikagels. **(C)** Swelling ratios of Amikagels after 48 h incubation at room temperature in Nanopure water. Lower crosslinking ratios led to higher swelling of the Amikagels, likely due to porous crosslinks, which could absorb water to swell up.

Amikagels **1**, **2** and **3** exhibited swelling ratios of 16.7, 6.4, and 3.7, respectively (**Fig. 2-7C**) which is similar to other PEG crosslinked hydrogels [108]. Swelling ratios depended on the degree of cross-linking in the hydrogel network; as the degree of cross-linking increased, the swelling ratios decreased. It is likely that as the degree of cross-linking increases, gel strength increases due to the extensive crosslinks and rigidity of the network, which, in turn, prevents the gel from swelling. Increased porosity of AM1 hydrogel could have aided in increased water absorption and retention after hydration, thus increasing its swelling ratio.

Next, we carried out contact angle measurements on dehydrated Amikagels in order to investigate the hydrophilicity and wettability of the surface. Contact angles (θ) of Amikagels AM**1**, AM**2** and AM**3** were found to be 52.2 ± 1.1^{o}, 54.4 ± 2.9^{o} and 48.01 ± 4.0^{o} respectively, indicating an overall hydrophilic gel surface. Contact angle (θ) of less than 90^{o} is considered a hydrophilic surface whereas beyond 90^{o} constitutes a hydrophobic one [109]. Hydrophilicity of the surface did not change with respect to the amount of PEGDE crosslinker used. As amines, hydroxyls and the glycol units together contribute to the hydrophilicity, lowering the amount of one of them could be compensated by another.

Presence of poly(ethylene glycol) as a cross-linker imparted Amikagels with hydrophilicity, biocompatibility and was hypothesized to provide a non-adherent surface too. Polyethylene glycol rich surfaces are known to be non-adhesive [110]. The surface adhesivity of Amikagels were observed by introducing bladder cancer and prostate stromal cells on to the surface. Upon introduction of cells to AM3 Amikagel surface, cells attained a rounded morphology and self-assembled into 3D spheroidal tumor microenvironments (3DTMs), indicative of minimal attachment to the surface. Cell spreading was noticed on AM1 and 2 amikagels (**Fig. 2-8 A and B**). Increased PEG content along with higher mechanical stiffness in AM3 hydrogels could be attributed to the non-adhesivity of AM3's surface. Cell spreading on AM1 and AM2 hydrogels could be attributed to their higher number of unreacted surface primary amines along with lower PEG content (**Fig. 2-8 A and B**). Non-attachment of cells to AM3 surface was hypothesized to promote and generate self-assembled cellular masses that could capture tumor micro-environmental intricacies useful in multiple biological studies.

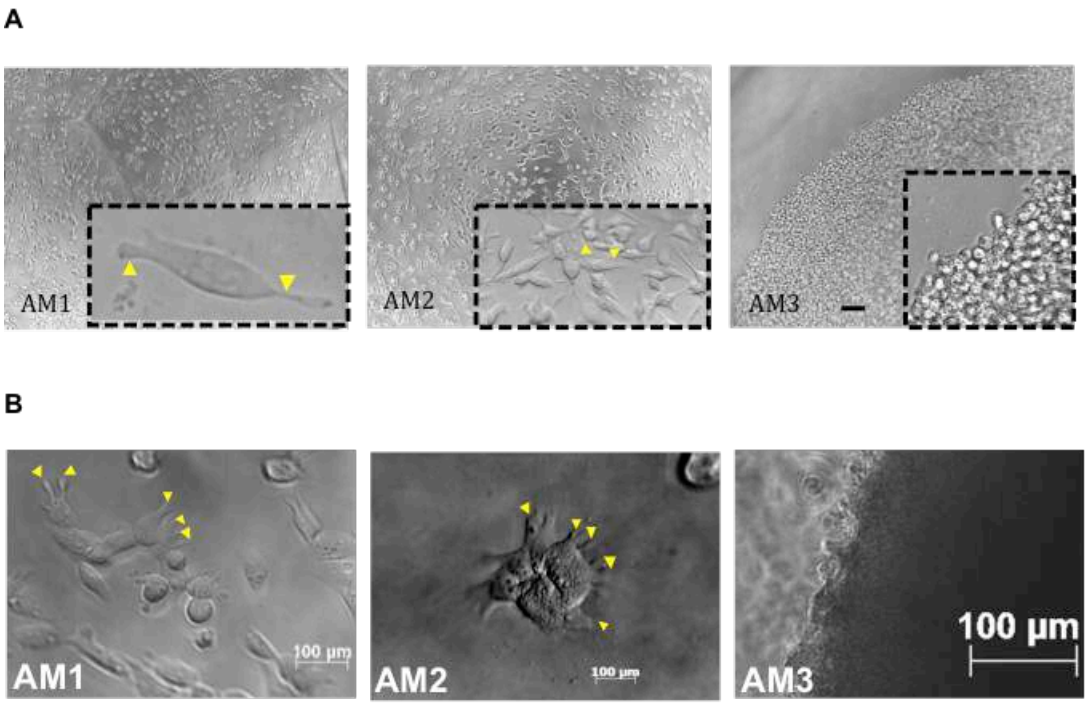

Figure. 2-8. Adhesion of mammalian cells on chemo-mechanically tuned Amikagels. (A) T24 bladder cancer cells and **(B)** WPMY-1 prostate stromal fibroblasts were cultured on Amikagels of different compositions with varied surface adhesive properties. Notice the elongated cellular appendages on AM1 and AM2 Amikagels that seem absent on cells cultured on AM3 Amikagel imaged after 24 hours of culture. Scale Bar: 100 µm.

Formation of Three-Dimensional Tumor Microenvironments (3DTMs) on Amikagels

Prostate, bladder, breast, or pancreatic cancer cells, when cultured either alone or together with stromal / stellate / fibroblast cells on AM3 resulted in the formation of a single spheroidal 3DTM in every well (**Fig. 2-9 A-C**), likely facilitated by the high mechanical stiffness and non-adhesivity of the hydrogel.

A.

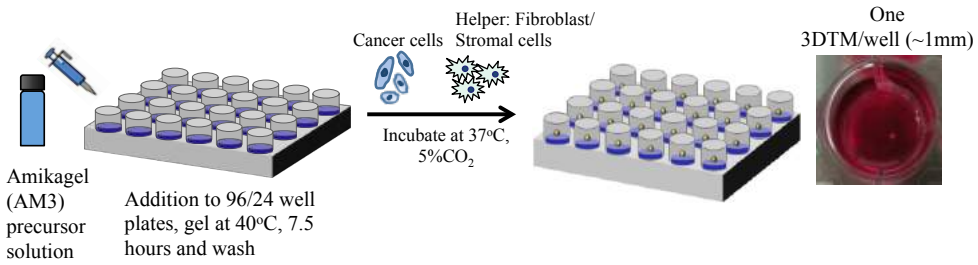

B.

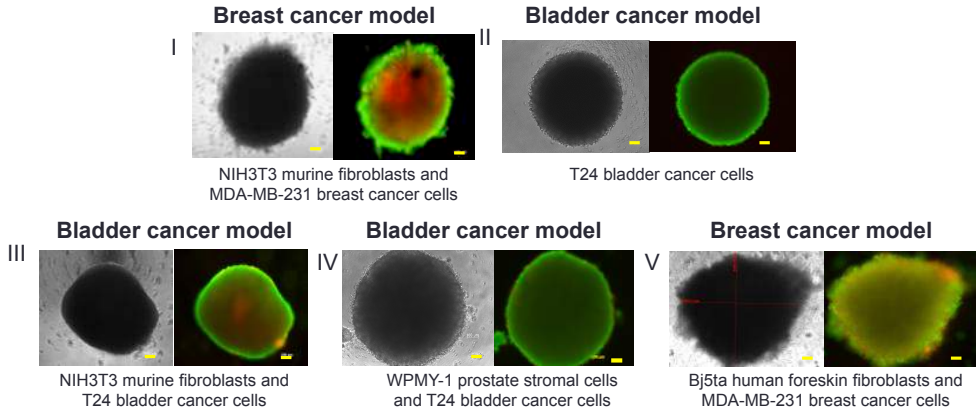

C.

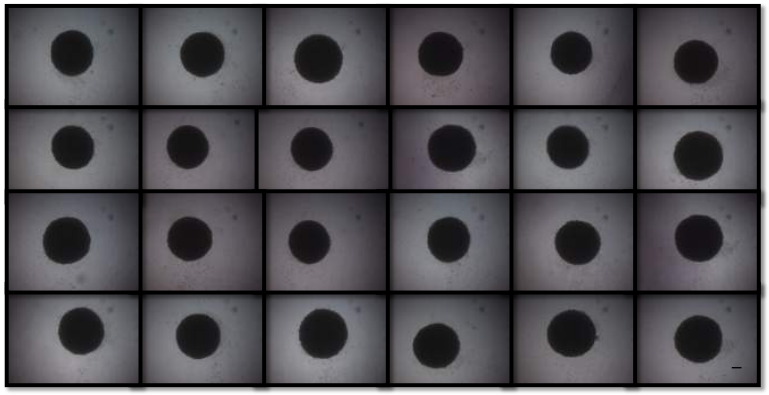

Figure 2-9. High-throughput generation of 3D tumor microenvironments on Amikagel. (A) High-throughput generation of 3D tumor microenvironments (3DTMs) on AM3 Amikagel; the 3DTM (0.8-1mm diameter) can be visualized using the naked eye. **(B)** Phase-contrast and fluorescence (Live-Dead®) images of breast, and bladder cancer 3DTMs. Scale bar = 100 µm. **(C)** Representative phase-contrast image of high-throughput generation of T24 3DTMs in 24 wells coated with AM3. Formation of 'one well-one 3DTM', with near-uniform sized 3DTMs, can be seen after 7 days of initial seeding. Scale bar = 100 µm.

Live/dead® staining of the 3DTMs generated using NIH3T3 murine fibroblasts / Bj5ta human foreskin fibroblasts indicated an outer green (viable) 'ring' with an inner red (dead / dying) core, indicating a metabolically active and viable outer shell of cells, along with a stressed inner core of cells (**Fig. 2-9B i, iii and v**). Co-cultures of cancer cells with helper fibroblast cells often resulted in a live outer shell (intracellular calcein fluorescence) with a stressed core (red staining due to ethidium homodimer binding the extracellular DNA), likely due to hypoxia and necrosis in the core of the 3DTMs (**Fig. 2-9B i, iii and v**). Big size of the 3DTMs (<400 μm diameter) with dense ECM production due to presence of fibroblast cells could lead to difficulties in nutrient and metabolite entry and gas exchange resulting in a necrotic phenotype in the center of the spheroids [7, 111]. However, 3DTMs generated using T24 cells/WPMY-1 cells alone did not show prominent red-staining in the core, indicating differential biochemical consequences depending on the cells employed (**Fig. 2-9B ii and iv**). Single cell 3DTMs generated using T24 bladder cancer cells also did not show any signs of stressed interior (**Fig. 2-9B ii**) absence of NIH3T3 fibroblasts and dense accompanying ECM. The size of 3DTMs was modulated by seeding different cell densities on AM3; the longest dimension of the 3DTMs could be tailored from ~300 μm to ~1200 μm with increasing cell density (**Fig. 2-10**).

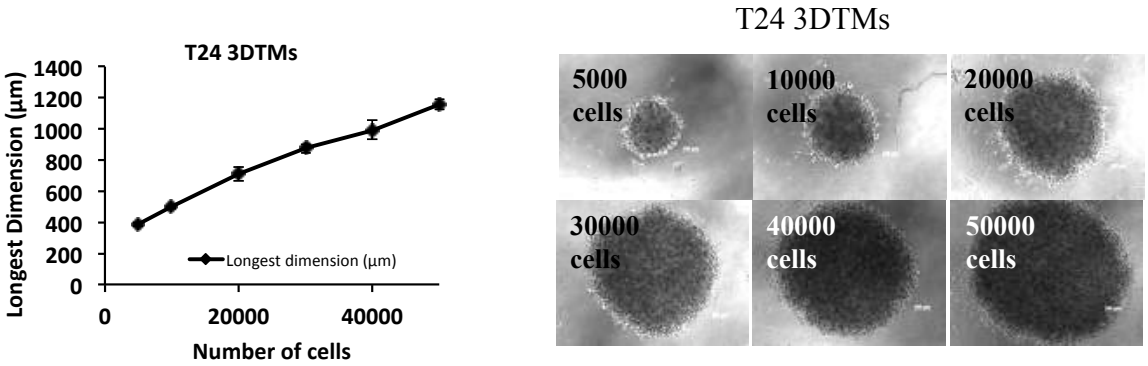

Figure 2-10. 3D-DTM characterization. Control of 3DTM size by using different cell seeding densities per well in a 96-well plate coated with AM3. Scale bar = 100 μm.

Co-culture of PC3-EGFP (PC3 human prostate cancer cells constitutively expressing GFP) along with red-fluorescent quantum dot loaded NIH3T3 fibroblasts indicated that both, cancer cells and stromal cells were present throughout the 3DTM after proper mixing (**Fig. 2-11**).

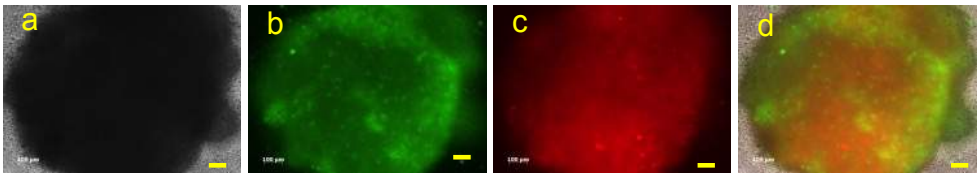

Figure 2-11. Distribution of cells in a co-culture system. Quantum Dot (QD)-loaded NIH3T3 fibroblasts and PC3-EGFP (EGFP expressing prostate cancer cells) co-culture 3DTM on AM3. **(A)** Phase contrast image, **(B)** GFP emission of PC3-EGFP prostate cancer cells, **(C)** dsRED emission from QD-loaded fibroblastss (**D**) Overlay. Scale =100 µm.

The simplicity and fidelity of the Amikagel platform are significant advantages over other more complicated methods including suspension cultures using microcarrier beads in rotating wall bioreactors [112] or shaker systems [22] which typically result in the formation of heterogeneous spheroid populations.

Effect of Amikagel chemo-mechanical properties on 3DTM formation

Mechanical strength, non-adhesivity and surface functionalization can have significant impact on the formation and fate of in vitro tumor models [113]. As shown **Fig. 2-9B**, T24 cells and NIH3T3-T24 co-culture systems formed single 3DTMs when cultured on Amikagel AM3. Of the three Amikagels, AM3 possesses the highest mechanical stiffness and lowest cell adhesivity (**Table 2-1**) due to the highest degree of cross-linking. Kinetics of 3DTM formation on Amikagels was studied by imaging cells at regular intervals following seeding. T24 bladder cancer cells first formed a freely floating cell sheet, approximately 1-2 cells thick, within the first two days of culture on AM3 Amikagel. The cell sheet subsequently folded upon itself resulting in the formation of a single 3DTM in an individual well (**Fig. 2-12 and 2-13**). It is likely that the shape of the meniscus affects the shape of 3DTM formation leading to differences in the final 3DTM shape. Mechanical stiffness of the hydrogel and the shape of the hydrogel groove have been shown to influence the spheroid shape [113-114].

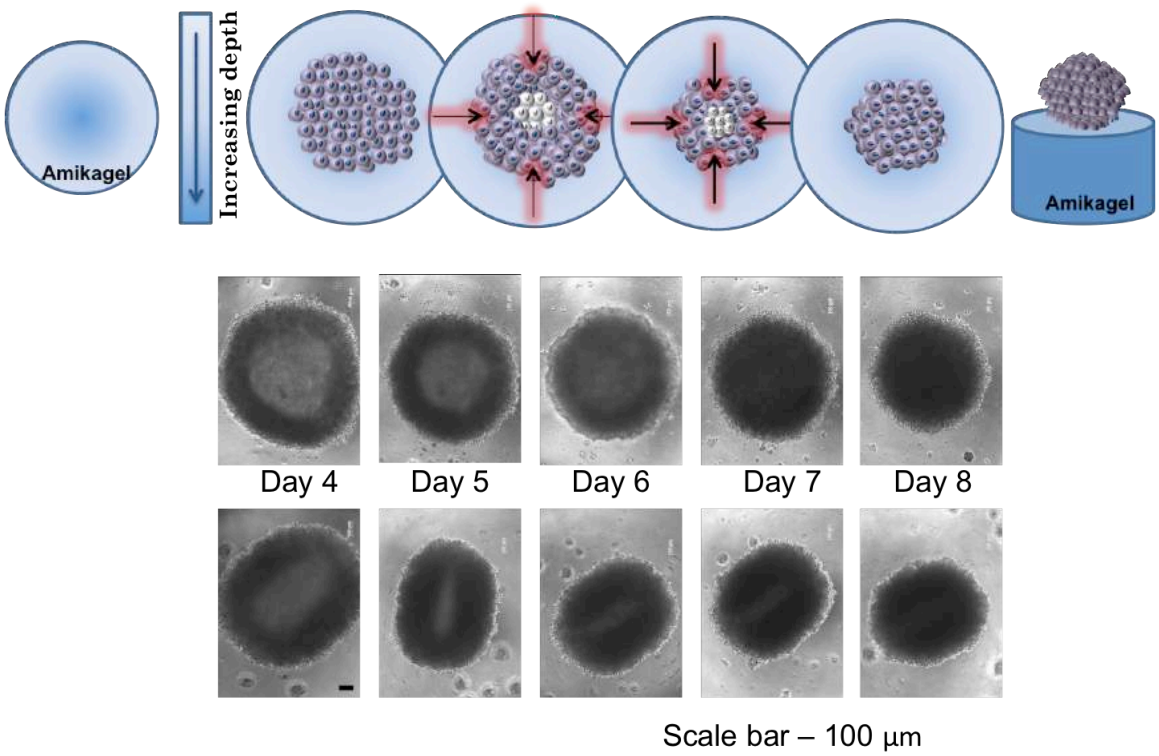

Figure 2-12. Kinetics of formation of T24 3DTMs on AM3 Amikagel. T24 cells formed a cell-sheet, which slowly folded upon itself to give rise to a condensed 3DTM.

Stromal cells significantly enhanced the kinetics of 3DTM formation; for example, the NIH3T3 murine fibroblast cells -T24 co-culture system formed 3DTMs in 3 days while T24 cells formed 3DTMs over 7 days in absence of stromal cells (**Fig. 2-13**). It is likely that stromal cell-epithelial cell interactions, in presence of the non-adhesive AM3 Amikagel, facilitate faster formation of 3DTMs compared to T24 cells by themselves. The lower mechanical strengths and higher cellular adhesivities of AM1 Amikagels (**Fig. 2-13**) resulted in the formation of multiple smaller 3DTMs in contrast to 3DTM formation on AM3 Amikagels under conditions of equal cell seeding densities (**Fig. 2-13**). T24 cells assembled into micro-colonies (~100 μm diameter) on day 4-5 (**Fig. 2-13**). Addition of NIH3T3-cells to the mixture also formed small micro-clusters, which were noted to merge on day 4 (**Fig. 2-13l**). Gildea et al. found that metastatic fraction of T24 cells formed small microcolonies on soft agar gels and hypothesized a role of paracrine signaling inducing the microcolony formation [47]. It is likely that a similar mechanism could be

involved in the microcolonies observed in the AM1 gel where the metastatic fraction of cell population induces the formation of the microcolonies on the AM1 gel.

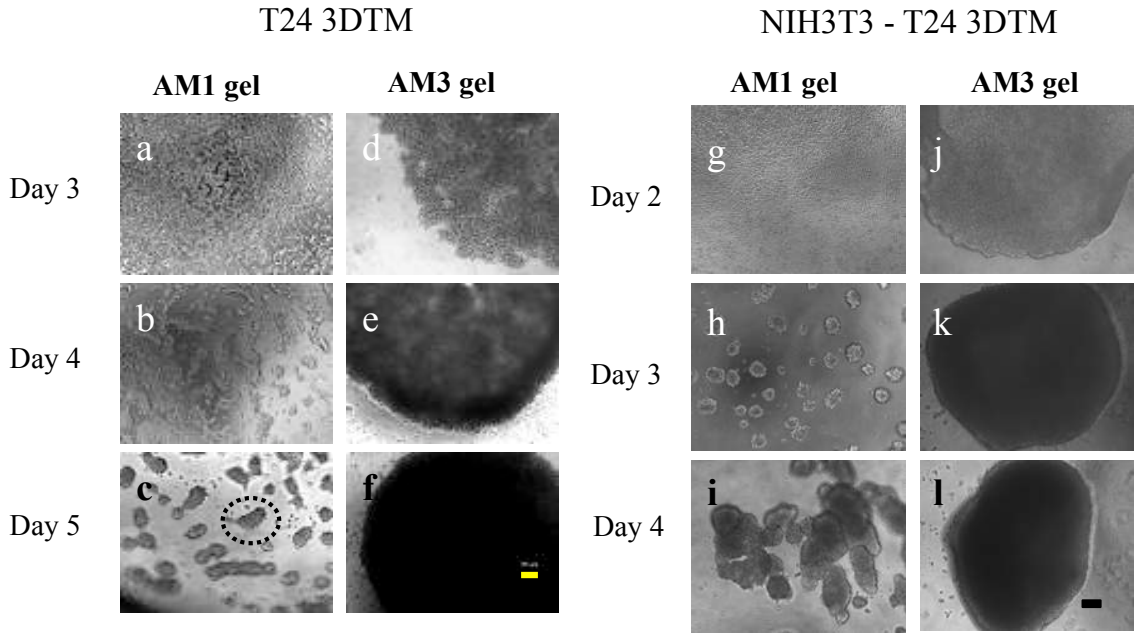

Figure 2-13. Effect of Amikagel chemo-mechanical properties on T24 and NIH3T3-T24 co-culture 3DTM formation. Scale bar = 100 µm. On AM1 Amikagel, T24 cells (**A-C**) and NIH3T3-T24 cells (**G-I**) formed micro-clusters (Average longest dimension: 112 ± 34 µm) whereas larger 3DTMs can be seen on AM3 Amikagel in both cases. Micro-clusters of NIH3T3-T24 cells were noted to merge on day 4, unlike T24 cells alone.

Cell Cycle Profile of 3DTMs

Arrest of cells in the G0/G1 phase of the cell cycle is a key characteristic feature of tumor dormancy [32], and is responsible for resistance to chemotherapeutics that are typically effective against rapidly dividing cells. Cell cycle analyses indicated the formation of viable fully dormant 3D T24 bladder cancer microenvironments (called '3D-DTMs' hereafter) on AM3; ~95% of the cell population was arrested in the G0/G1 phase of the cell cycle (**Table 2-2 and Fig. 2-14 A-B**).

Table 2-2. Cell cycle analysis of 2D cell cultures vs. 3D-DTMs (3D dormant tumor microenvironments) for different bladder cancer cell lines as individual and co-cultures.

Cell line	Cell cycle phase	2D culture	3D-DTMs
T24 bladder 3D-DTMs	M1 (G1/G0)	54 ± 2 %	95 ± 3 % (**)
	M2 (S)	17 ± 2 %	2 ± 1 %
	M3 (G2/M)	28 ± 3 %	3 ± 2 %
UMUC3 bladder 3D-DTMs	M1 (G1/G0)	57 ± 1 %	68 ± 4 % (**)
	M2 (S)	15 ± 1 %	2 ± 1 %
	M3 (G2/M)	19 ± 1 %	10 ± 3 %
NIH3T3-T24 Co-culture 3D-DTMs	M1 (G1/G0)	--	82 ± 2 %
	M2 (S)	--	11 ± 4 %
	M3 (G2/M)	--	4 ± 1 %

** Indicates $p<0.0001$ for cell population in the G0/G1 phase of the cell cycle for T24 and UMUC3 3D-DTMs compared to their corresponding 2D cultures, respectively. Statistical significance determined using Student's t-test of at least n=3 independent experiments.

This is in stark contrast to the cell cycle profile of 2D culture of T24 cells in which ~54% cells were in the G0/G1 phase of the cell cycle (**Table 2-2 and Fig. 2-14 A-B**). T24 cells transitional cell carcinoma of bladder origin [48]. Transitional cells line the outer epithelium of the bladder and serve as the outermost layer of cells that are directly in contact with the urine [115]. Being epithelial in origin, the healthy non-cancerous transitional cells are terminally differentiated, epithelial in origin and express E-cadherin as a intercellular marker [116-117]. The switch of these outer bladder epithelial cells into bladder transitional cancer cell phenotype is very often associated switch and transition from epithelial to mesenchymal phenotype (EMT). Specifically, EMT of bladder is associated with downregulation of epithelial marker E-cadherin and upregulation of mesenchymal marker N-cadherin [54-55, 58, 118]. N-cadherin is a widely accepted intercellular marker that represents the EMT, metastases from primary cancer site and is usually constitutes poor prognosis for the patient [58]. T24 cells are known to be E-cadherin null with high

expression of N-cadherin cell surface marker [54, 118]. However, they have been shown to be very heterogenous in their metastatic ability [48, 50]. Multiple researchers have shown T24 cells to contain heterogenous population of metastatic and non-metastatic cell fractions [47-48]. T24 cells are known to be contact inhibited [39], and aggregation of cells within the 3DTM likely mimics this. Previous research has shown presence of p27 CDK inhibitor in the T24 cells, that reduces it tumorigenicity in mice [39]. Separately, dense surface expression of N-cadherin has been directly linked to increase in hypophosphorylated pRb levels leading to accumulation of p27 CDK inhibitor via lower ubiquitination and cell cycle arrest in G1 phase in confluent cultures of CHO cells. It is likely that a very similar mechanism of cell cycle arrest is active in N-cadherin rich T24 cells [119]. Capturing tumor dormancy in high-throughput is very significant as it can allow for large scale rational drug discovery, delivery and further development.

UMUC3 human bladder cancer cells also demonstrated the formation of 3D-DTMs that were arrested in the G0/G1 phase, although the extent was not as high as in T24 cells (**Table 2-2 and Fig. 2-14 C-D**). Co-culture of NIH3T3 and T24 cells formed 3DTMs with a majority of the cell population arrested in G0/G1 and S phases of the cell cycle indicating dormancy (**Table 2-2**). A modest amount of cell apoptosis was seen in the case of UMUC3 cells, which is likely possible since high mechanical stress and non adhesivity of the substrate promote have been shown to lead to cell cycle arrest [42] and death in some cases [113]. Consistent with cell cycle arrest, T24 3D-DTMs also demonstrated significantly reduced media (nutrient) consumption compared to actively dividing T24 cells, further indicating their dormant nature (**Fig. 2-14E**).

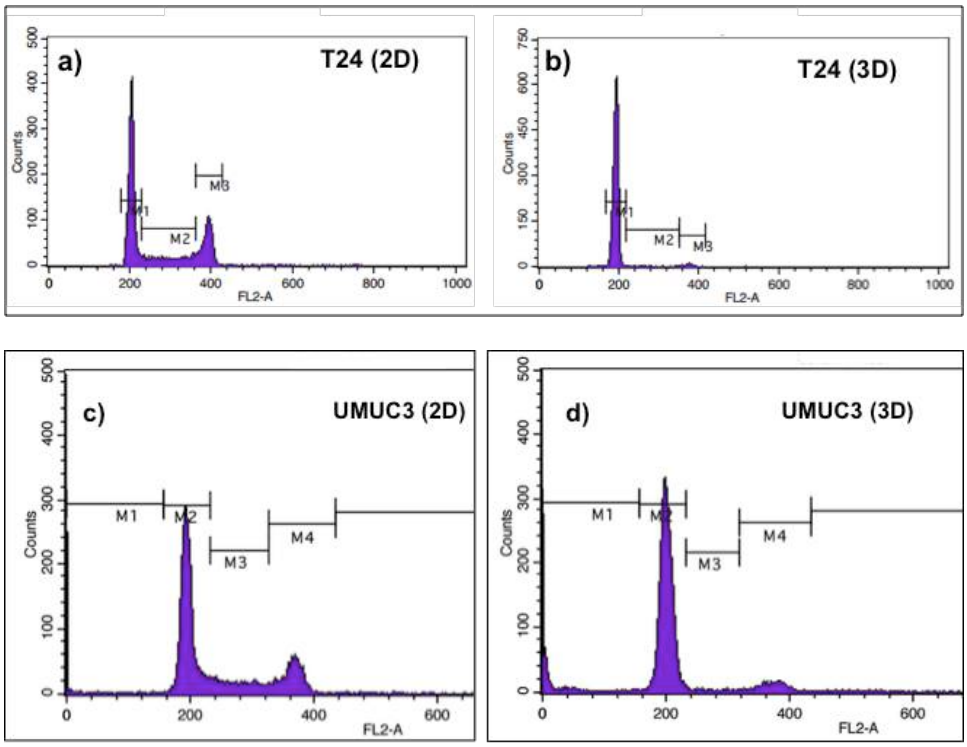

E. Reduced metabolite consumption of T24 3D-DTMs compared to actively dividing T24 cells.

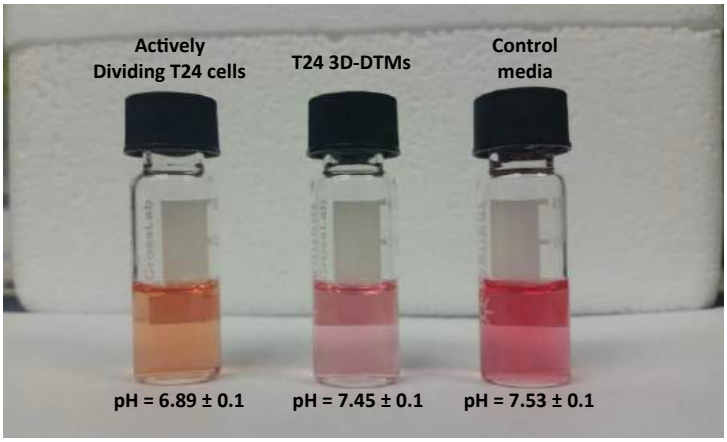

Figure 2-14. Cell cycle distribution - Cell cycle analysis of (**A**) 2D culture vs. **(B)** 3D-DTM for T24 human bladder cancer cells and **(C)** 2D culture vs. **(D)** 3D-DTM for UMUC3 human bladder cancer cells. ** indicates $p<0.0001$ for cell population in the G0/G1 phase of the cell cycle for T24 and UMUC3 3D-DTMs compared to their corresponding 2D cultures, respectively. (n=3, independent experiments). Statistical significance determined using Student's t-test. (**E**) Reduced metabolic (media) consumption was observed in case of T24 3D-DTMs compared to that in case of actively proliferating 2D culture. Cell culture media on the 3D-DTMs did not significantly change color or pH after 48 hours of cell seeding.

The propensity for 3D-DTM formation on agarose and Matrigel® was investigated since these substrates are commonly used in 3D cell culture. The mechanical properties of 1% and 10% agarose gels were comparable to those of AM1 and AM3, respectively (**Fig. 2-15A**).

A.

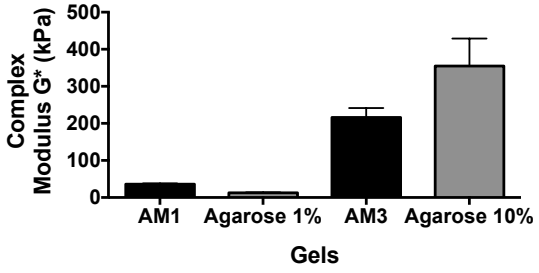

B.

3DTM formation	AGAROSE GEL	AMIKAGEL
AM1/1%	Yes	No
AM3/10%	No	Yes

C. 1% agarose gels 10% agarose gels

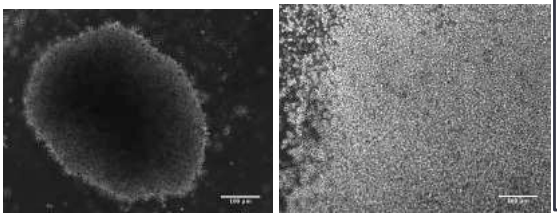

D.

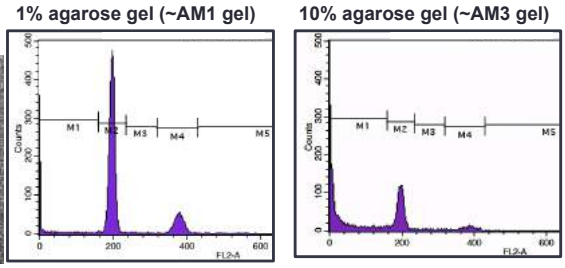

Cell cycle	1% AGAROSE GEL	10% AGAROSE GEL
Pre G0/G1 phase (M1)	9.7 ± 0.5	70.8 ± 0.2
G0/G1 phase (M2)	74 ± 0.2	24.4 ± 0.5
G2/M phase (M4)	14.8 ± 0.2	3.7 ± 0.3

Figure 2-15. **T24 cells on Agarose (comparison with Amikagels).** (**A**) Absolute shear modulus of 1% and 10% agarose gel was determined to be similar to that of AM1 and AM3 gels respectively. (**B**) T24 spheroid formation was seen to occur only on AM3 and 1% agarose gels. (**C**) Phase contrast image of T24 cells on 1% and 10% agarose gels respectively after 7 days of culture. Scale = 100 µm (**D**) Cell cycle distribution of T24 cells on agarose gels (1% and 10% gels) after 7 days of culture. AM3 was better in inducing complete dormancy in T24 cells compared to 10% agarose.

Extensive cell death was seen on 10% agarose gels which demonstrate high mechanical stiffness, while a single spheroid was seen on 1% agarose gels whose mechanical stiffness was similar to that of AM1 Amikagels (**Fig. 2-15 B-C**). However, in contrast to the extensive (~95%) arrest of T24 cells in the G0/G1 phase of the cell cycle on AM3, only ~70% T24 cells were seen

in the G0/G1 phase on 1% agarose gels (**Fig. 2-15 D**). Other 3D culture methods have shown ~70% cells in the G0/G1 phase of the cell cycle, which is not representative of complete arrest [36]. T24 cells cultured on formed multiple clusters with invasive protrusions on Matrigel®, and induced a change in media color which was indicative of active growth and proliferation (**Fig. 2-16**) and not arrest. Increasing evidence points towards a definitive phase of quiescence (prolonged G0/G1 arrest) rather than balanced proliferation to support prolonged viability before relapse [27]. To our knowledge, the Amikagel platform is the first of its kind that results in a single, near-total dormant 3D-DTMs in vitro.

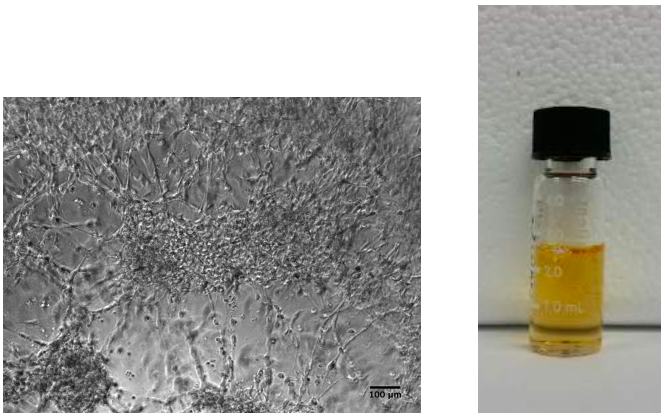

Figure 2-16. T24 cells on Matrigel (comparison with Amikagels). 25,000 T24 cells on Matrigel after 7 days of seeding were seen attached to the surface. Scale = 100 µm. Cell culture media after 48 hours of 25,000 T24 cell culture on Matrigel was seen to be yellowish indicating active consumption and metabolism unlike T24 3D-DTMs.

Morphological and Biochemical Characterization of 3D-DTMs. Scanning electron microscopy (SEM) of fibroblast-cancer cell co-culture 3D-DTMs showed a compact 3D-DTM which contained fibrous structures, which are formed likely due to deposition of extracellular matrix (ECM) by the fibroblasts (**Fig. 2-17 A-B**) [120-121].

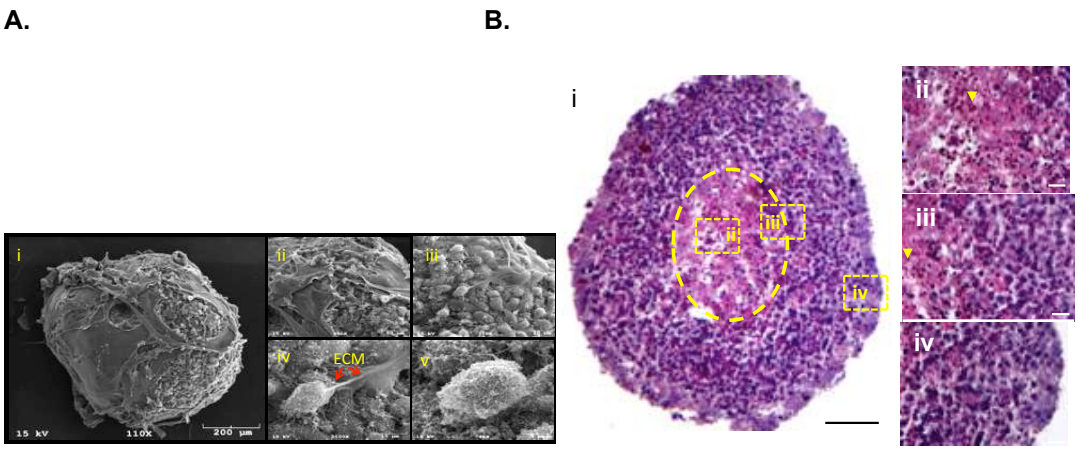

Figure 2-17. NIH3T3-T24 3D-DTM characterization - SEM and H&E staining **(A)** Scanning Electron Microscopy (SEM) images of **(i-v)** NIH3T3-T24 co-culture 3D-DTMs. Images **ii-v** show NIH3T3-T24 3D-DTM at higher magnifications, with most cells showing a rounded morphology. NIH3T3-T24 3D-DTMs were covered with fibrous material indicative of extracellular matrix (ECM) formation (red arrows). **(B)** Hematoxylin and Eosin (H&E) staining of 3DTMs: NIH3T3-T24 3D-DTM. Scale = 100 µm and insets (**i**- central necrotic core, **ii**-middle densely packed cells and **iii**-outer loosely packed cells) Scale = 20 µm. Yellow pointers indicate condensed nuclei indicative of pyknosis.

In contrast, 3D-DTMs of T24 cells alone did not show presence of significant amounts of fibrous structures (**Fig. 2-18 A(i-iii)**). The ability to generate ECM in 3D cell systems is important since cancer cell-stromal cell interactions are known to play a critical role in the local tumor microenvironment [122].

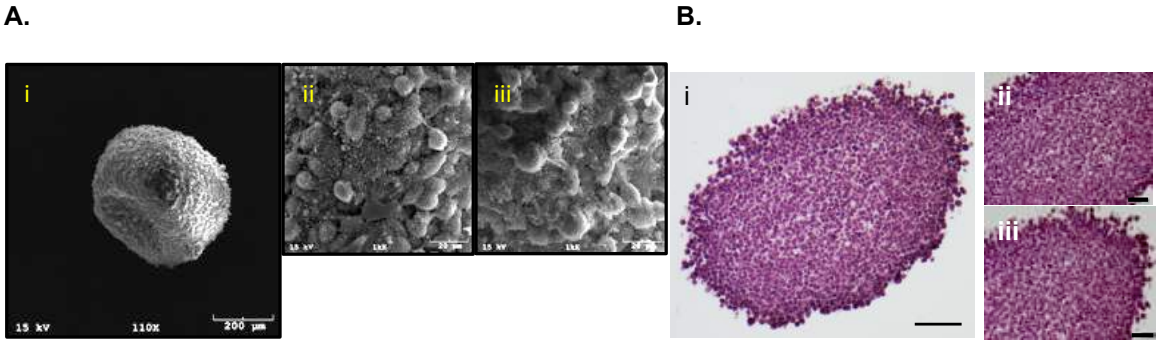

Figure 2-18. T24 3D-DTM characterization - SEM and H&E staining **(A)** Scanning Electron Microscopy (SEM) images of **(i-iii)** T24 3D-DTMs. Images **ii, iii and iv** show rounded cell morphology of T24 3D-DTM. **(B)** Hematoxylin and Eosin (H&E) staining of T24 3D-DTM, indicated minimal to no necrotic areas unlike NIH3T3-T24 3D-DTMs. Scale bar = (i) 100 µm and (ii and iii) 50 µm.

Hematoxylin and eosin (H&E) staining of NIH3T3-T24 3D-DTMs indicated the presence of three distinct regions: loosely packed cells in the periphery, densely packed cells in the middle,

and a necrotic region in the middle that showed prominent nuclear blebbing and absence of distinct cellular boundaries (**Fig. 2-14B, i-iv**). Presence of a necrotic core due to hypoxia and nutrient deprivation is common in tumors, and has been reported in spheroids greater than 400-500 μm in diameter [7]. Presence of a necrotic core in NIH3T3-T24 3D-DTM could also be a result of the dense ECM formed (**Fig. 2-17 A-B (i-iv)**) [123]. Unlike NIH3T3-T24 3D-DTMs, T24 3D-DTMs by themselves did not demonstrate significant ECM like fibres and a distinct necrotic core region (**Fig. 2-18A-B (i-iii)**). It is likely that lower ECM deposition in T24 3D-DTMs is responsible for easier access of nutrients throughout the spheroid. H&E staining results also were consistent with Live/Dead® staining of 3D-DTMs which indicated that the outer cell layers were actively proliferating while inner cell layers were metabolically inactive / stressed in co-culture 3D-DTMs (**Fig. 2-9B**); however, T24 3D-DTMs without fibroblasts did not show predominant dead regions in the core. (**Fig. 2-9B**). Actin staining of 40 μm thick T24 3D-DTM cryosections (**Fig. 2-19**) indicated that F-actin (red stain) localized along the intracellular cortical regions. Unlike 2D cell cultures, where cellular F-actin stress fibers support strong cell-substratum interactions [124], localization of F-actin filaments in the cellular cortex in T24 3D-DTMs indicate increased cell-cell interactions, rather than cell-substratum interactions, leading to cell cycle arrest.

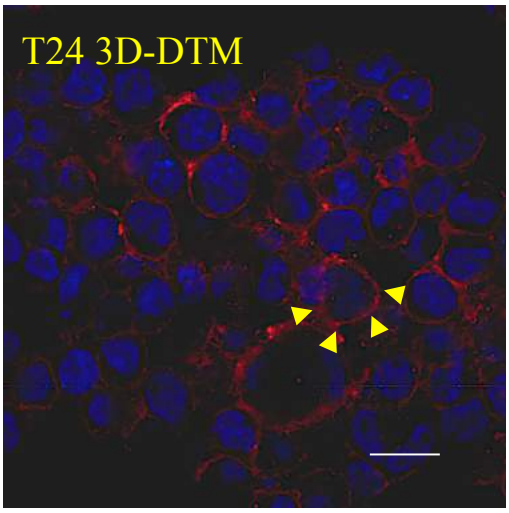

Figure 2-19. Actin staining of T24 3D-DTMs - Actin staining on sections of T24 3D-DTM. Red: Phalloidin-Alexa 548 stained actin, Blue: DAPI. Scale = 20 μm. Note: The distribution of actin is cortical in T24 3D-DTMs.

We also tested the presence of cell-cell intercellular contacts in T24 3D-DTMs using EDTA calcium chelation and removal. Integrins and cadherins require calcium for their effective functioning and calcium removal from media would cause these integrins and cadherins to fail, leading to instant cell dissociation. Upon addition of 4 mM EDTA for 12 hours, we noticed a complete disassembly of the 3D-DTM, without any significant loss to the cell viability (**Fig. 2-20 A-C**). T24 cells are known to be E-cadherin null, positive for N-cadherin and are known to contain β1 integrins. Our results using EDTA based calcium removal indicate that there are cell-cell interactions present (likely cadherin and integrin based) in T24 3D-DTMs and cortical presence of actin likely supports those interactions (**Fig. 2-20**).

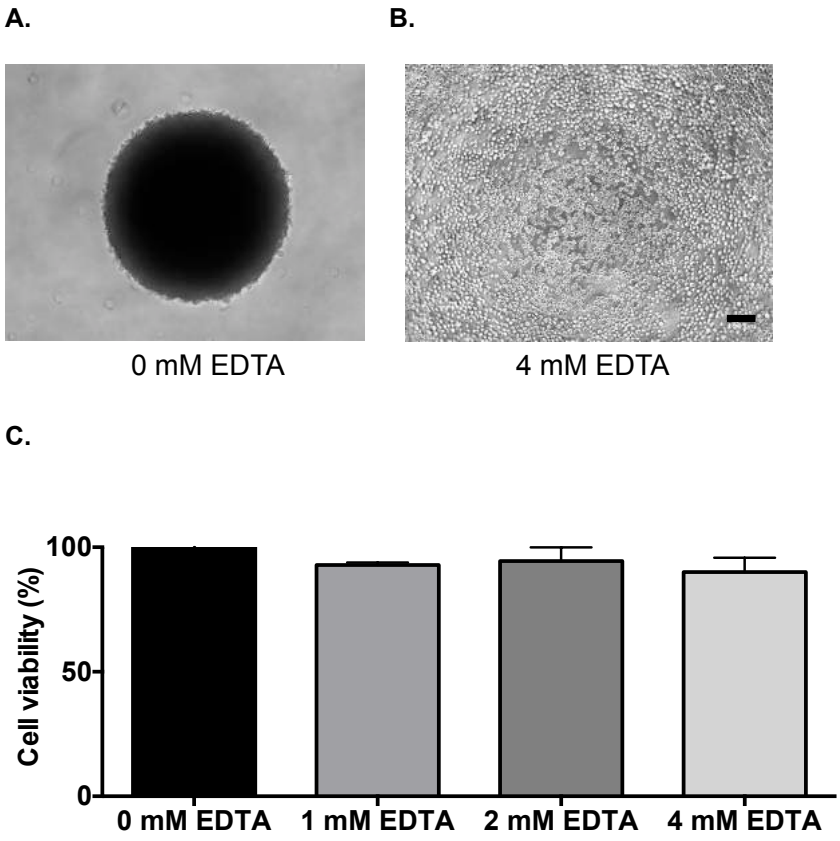

Figure 2-20. EDTA treatment of T24 3D-DTMs – Treatment with **(A)** 0 mM (representative image) and **(B)** 4 mM EDTA (representative image) for 12 hours followed by slight shaking. Removal of calcium by EDTA completely disassociated the T24 3D-DTM but did not change its viability to a large extent **(C)**. Scale = 100 μm.

Chemoresistance of 3D-DTMs

T24 and NIH3T3-T24 co-culture 3D-DTMs were treated with different doses of the DNA-damaging drug mitoxantrone [125] or microtubule-stabilizing drug docetaxel in order to investigate their response to conventional anticancer therapeutics [25]. NIH3T3-T24 3D-DTMs were resistant for up to 80 μM mitoxantrone even after 96 h of treatment (**Fig. 2-21 A-C**).

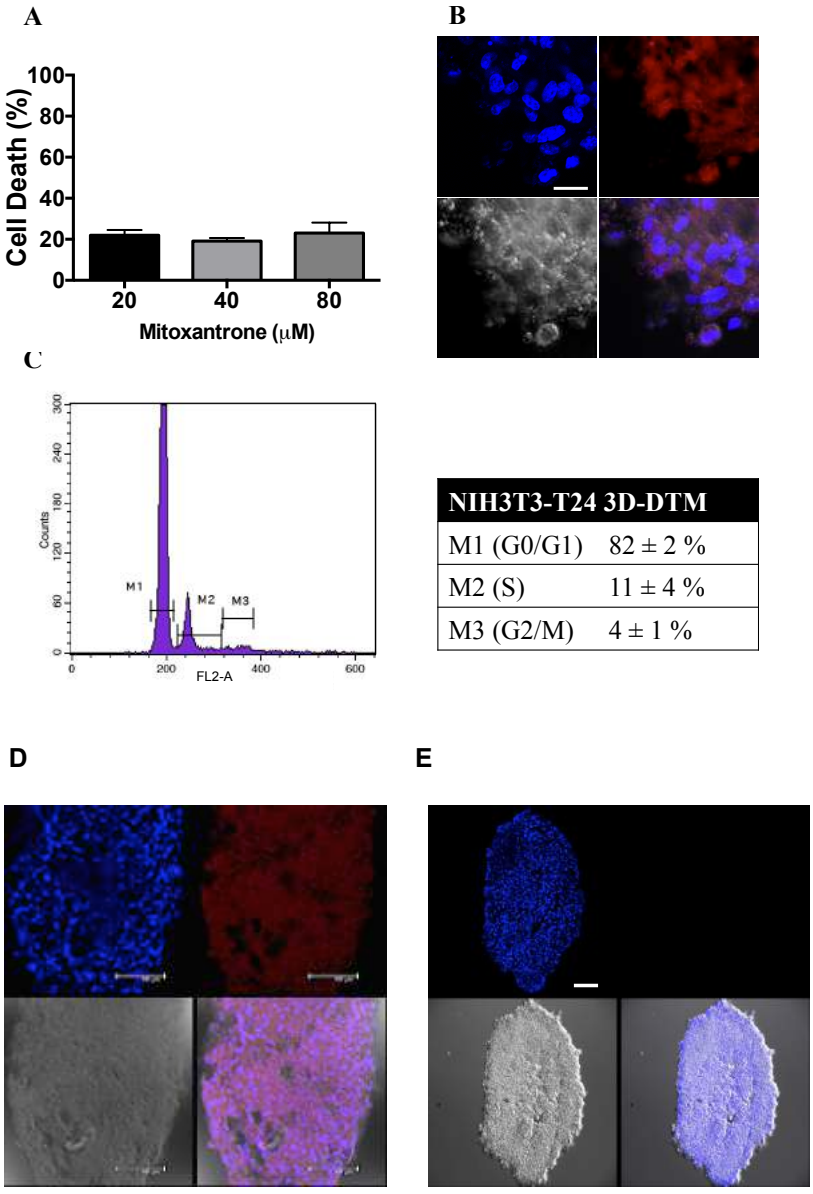

NIH3T3-T24 3D-DTM	
M1 (G0/G1)	82 ± 2 %
M2 (S)	11 ± 4 %
M3 (G2/M)	4 ± 1 %

Figure 2-21. Mitoxantrone delivery to NIH3T3-T24 3D-DTMs: **3D-DTM drug resistance. (A-C)** Chemotherapeutic treatment of NIH3T3-T24 3D-DTMs using mitoxantrone. **(A)** Cell viability (%; determined using the MTT assay) after exposure of NIH3T3-T24 3D-DTM to the drug for 96 hours. 3D-DTMs were treated with collagenase (50 µl of 5 mg/ml) prior to MTT assay to allow for disassembly. **(B)** Visualization of mitoxantrone (40 µM; false red colour; excitation: 637 nm; emission: 670 nm) penetration into NIH3T3-T24 3D-DTM after 24 hours of drug administration. All 3D-DTM sections were counterstained with DAPI (false blue colour; excitation: 350 nm, emission: 470 nm) in order to visualize cell nuclei. Scale = 20 µm. **(C)** Representative image of cell cycle distribution of NIH3T3-T24 3D-DTMs cultured on AM3 for 5 days. Most cells were arrested in G0/G1 and S phase of the cell cycle, indicating probable dormancy. Table showing the percent distribution of cells of NIH3T3-T24 3D-DTM in different phases of the cell cycle. **(D)**. Visualization of mitoxantrone (40 µM; false red colour; excitation: 637 nm; emission: 670 nm) penetration into NIH3T3-T24 3D-DTM after 24 hours indicates extensive penetration of the drug into the 3D-DTM. Scale =100 µm **(E)**. Blank control, i.e. NIH3T3-T24 3D-DTMs not treated with mitoxantrone;

absence of far-red fluorescence after 24 hours is due to lack of presence of the drug. Scale =100 µm.

This is in striking contrast to the LC_{50} (dose of drug which induces loss in 50% cells) of mitoxantrone (9 µM) in 2D cultures of T24 cells [125]. We verified that lack of cell death was not due to poor drug penetration into the 3D-DTM; fluorescence micrscopy indicated mitoxantrone localization throughout the NIH3T3-T24 3DTM in 24 hours (**Fig. 2-21D**), which was not seen in the control (**Fig. 2-21E**). T24 3D-DTMs were also resistant to mitoxantrone and docetaxel (**Fig. 2-22 and 2-23**); treatments as high as 100 µM docetaxel induced only 10% cell death in T24 3D-DTMs, even though LC_{50} values for 2D proliferating cultures were substantially lower (**Fig. 2-24**).

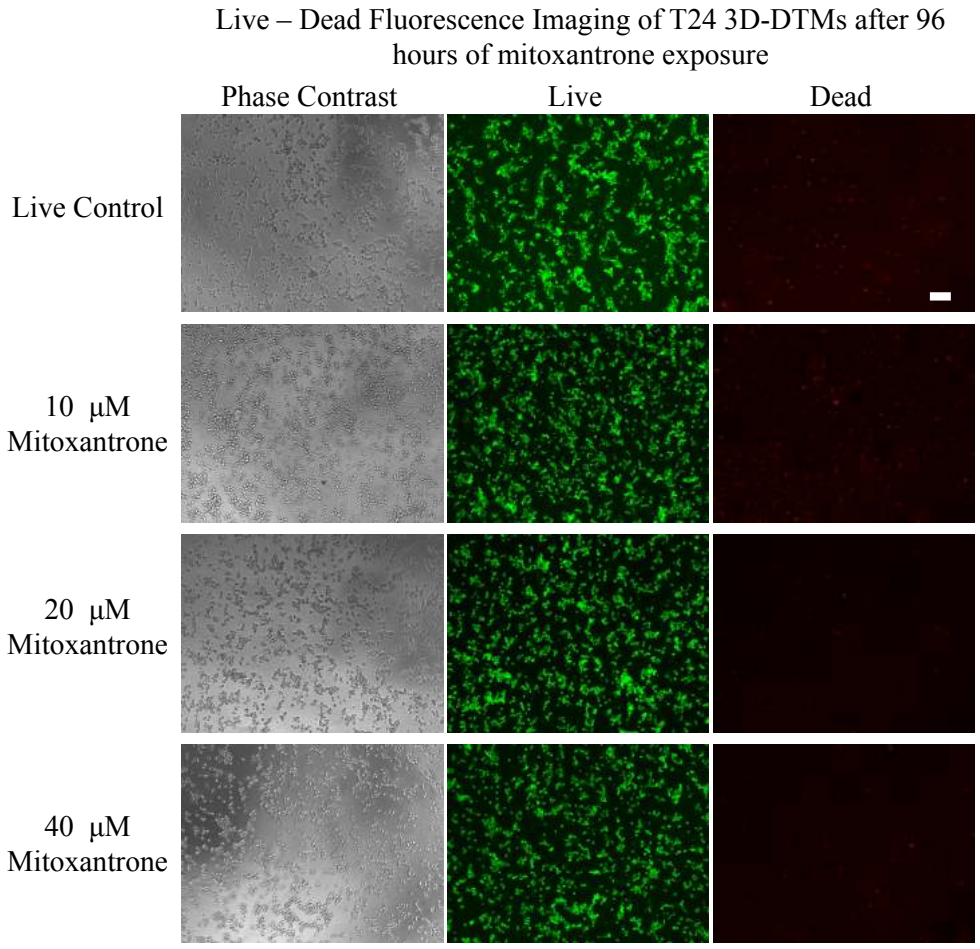

Figure 2-22. Treatment of T24 3D-DTMs with mitoxantrone (A). Live/dead® staining of disassembled T24 3D-DTMs after 96 hours of exposure with different doses of mitoxantrone**.** Increasing the concentration of mitoxantrone did not have significant impact on the cell viability of T24 cells in the 3D-DTMs. Scale = 100 µm.

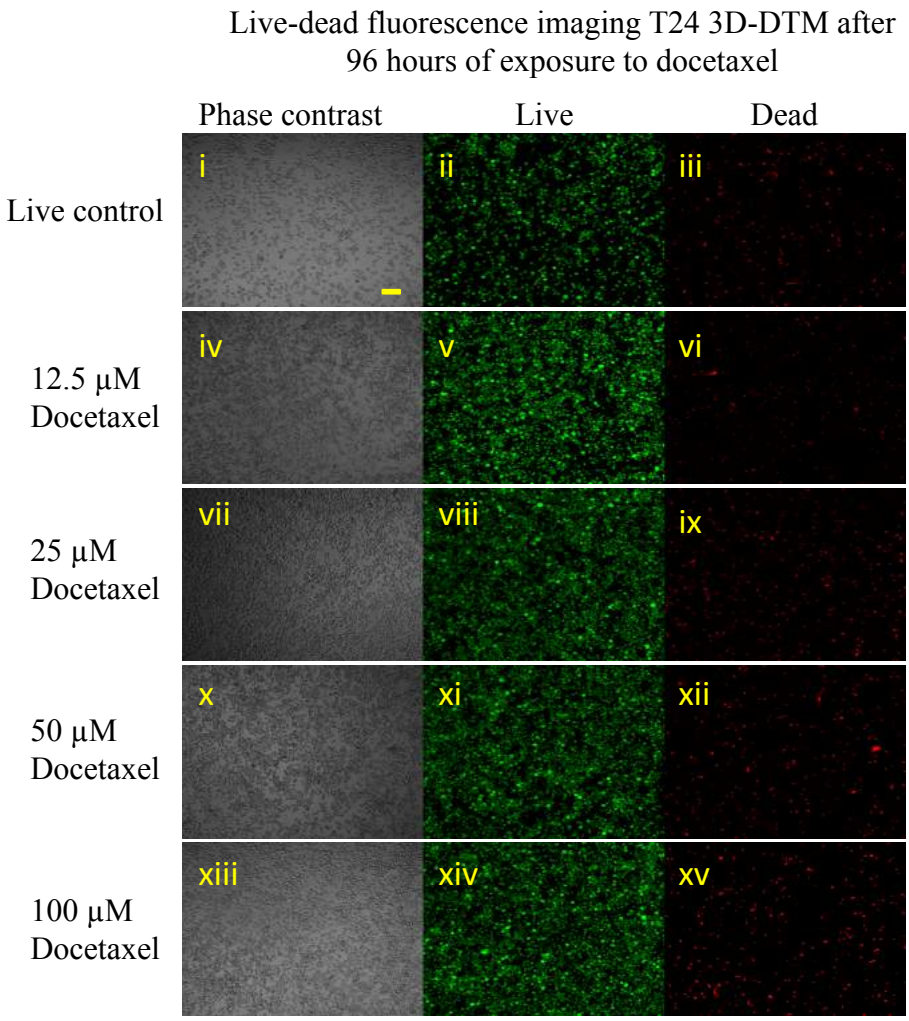

Figure 2-23. Treatment of T24 3D-DTMs with docetaxel. Live/dead® staining of disassembled T24 3D-DTMs after 96 hours of exposure to different doses of docetaxel. Increasing the concentration of docetaxel did not have any impact on the cell viability of T24 cells in the 3D-DTMs. Scale = 100 µm.

This low sensitivity to conventional anti-proliferative chemotherapeutic drugs is a key hallmark of cancer dormancy. Due to the arrest of these cancer cells in the non-mitotic phases of cell division, the effect of docetaxel and other conventional drugs is likely minimal. Docetaxel, prevent cell mitosis and division by stabilizing the microtubules. Docetaxel treated microtubules are unable to depolymerize and hence do not

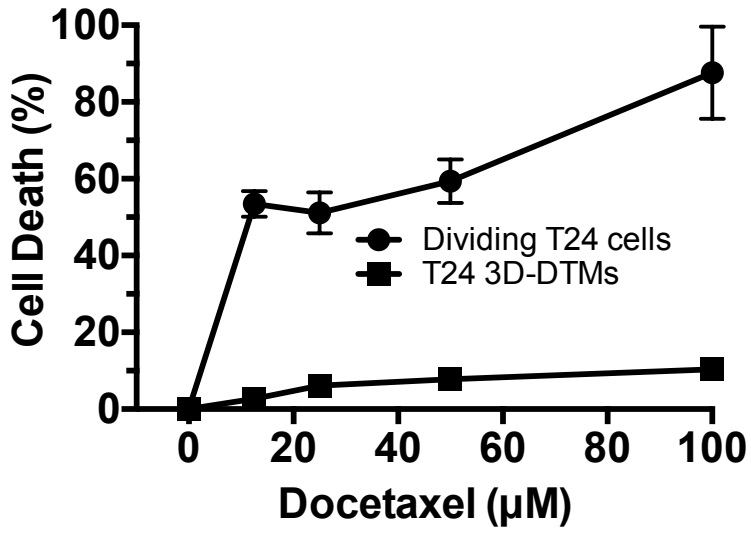

Figure 2-24. **Docetaxel dose response on T24 3D-DTMs**. Comparison of cell death (%) following treatment of 2D proliferating (circles) and 3D dormant (3D-DTMs) T24 cells with docetaxel for 96 hours. LC_{50} for 2D culture was ~10 μM, while T24 3D-DTMs showed very high resistance to docetaxel.

Arrest of cells in the G0/G1 phase and negligible presence of cells in the dividing G2/M phase contribute significantly to the observed chemotherapeutic resistance in 3D-DTMs (**Table 2-2**). Taken together, 3D-DTMs formed on Amikagels demonstrate key hallmarks of tumor cell dormancy including arrest in the G0/G1 phase of the cell cycle and high resistance to anti-proliferative chemotherapeutics. Thus, the Amikagel platform is an attractive technology for fundamental studies as well as identification of drugs against dormancy.

2.4. CONCLUSION

Novel aminoglycoside hydrogel (Amikagel) was prepared by crosslinking amikacin with crosslinker polyethylene glycol diglycidyl ether. Physico-chemical properties of Amikagel such as cell-substrate adhesivity, mechanical stiffness, pore size and gelation kinetics were tunable based on the mole ratios of the monomers used. Increasing the ratio of PEGDE to amikacin reduced the adhesivity of the substrate and increased its mechanical stiffness. At a ratio of 1:3, the Amikagel was found most suitable to generate a high-throughput spheroidal cell culture platform. Multiple cancer cells of prostate, pancreas, breast and bladder cancer were seen to form spheroidal

3DTMs with or without the help of additional helper fibroblast or stellate or stromal cells. T24 bladder cancer cells generated dormant 3DTMs, were completely arrested in G0/G1 phase of cell cycle, were highly viable and were produced in high-throughput on Amikagels with high-fidelity. NIH3T3-T24 co-culture 3D-DTM generated on Amikagels were seen to produce abundant fibrous like structures likely ECM with necrotic core due to limitations in nutrient transfer and metabolite transfer. Due to their dormant phenotype, the 3D-DTMs generated on Amikagels were seen to be very resistant to conventional anticancer drugs such as mitoxantrone and docetaxel. Our platform provides a novel chemo-mechanically tunable hydrogel platform that can capture important cancer phenotypes of tumor dormancy and drug resistance allowing for further rational drug discovery approaches.

CHAPTER 3: ACCELERATION OF ER STRESS INDUCED DORMANT CANCER CELL DEATH BY EXOGENOUS CALCIUM SUPPLEMENTATION

3.1. INTRODUCTION

Interventions including surgery, chemotherapy and radiotherapy constitute standard treatment options for patients with primary cancer [126]. However, a significant proportion of patients experience cancer metastasis to distant secondary disease sites such as bone, liver and lymph nodes [127-129]. Cancer metastasis represents the single largest contributor of patient mortality and it still remains technically incurable [130].

Studies have shown that cancer cells can disseminate from primary tumor to secondary sites such as bone even before its detection and treatment [30]. Often in these cases of metastasis, tumor cells initially undergo prolonged periods of dormancy, which are followed by relapse [30]. Increasing evidence points towards a definitive phase of prolonged G0/G1 arrest ('cellular dormancy') of micrometastatic nodules rather than balanced proliferation to support prolonged viability before relapse [27]. Upon relapse, these cancer cells give rise to highly aggressive forms of tumor metastases, often causing death as a result. Dormancy at distant disseminated sites has been shown to be induced by the local microenvironment, which is foreign to the invading cancer cells [31]. These populations of non-dividing G0/G1 arrested cancer cells evade traditional chemotherapy regimens that rely on actively dividing cells for their activity and thus indicate poor prognosis for the patient [32].

Tumor resistance to drugs severely limits the success of modern chemotherapy in eliminating cancer diseases [131]. Sensitive cancer cells are eliminated following exposure to chemotherapeutic drugs, while resistant and dormant cells survive the treatment. Ultimately, these dormant and resistant cells repopulate, causing a relapse of the disease at the primary location, as well as at distant metastatic sites. Dormant cells can exist either as minimal residual disease in which, cells are present at the site of primary tumor after surgical resection, or as distant disseminated cells in metastatic sites such as bone, liver and lymph nodes [52]. At a

molecular level, proteins p38, p27 and p21 have all been implicated in inducing dormancy and cell cycle arrest in cancer cells. In studies by Ranganathan et al. [37] Higher p38 protein was associated with dormant state of cells in-vivo whereas higher ERK/MAPK was associated with proliferation. Further, Ranganathan et al. [37] showed that p38 induced dormancy, initiated by microenvironmental changes (loss of integrin adhesion to fibronectin rich surfaces [41]) induced PERK activation that reduced translation and phosphorylated eukaryotic translation initiator factor 2α (eIF2α), arresting cells in the G0/G1 state. Some cell types can also induce dormancy independent of p38, by directly upregulating several CDK inhibitors such as p21, p27 and p16 [42]. In fact, p38 protein has also been shown to modulate several downstream CDK inhibitors such as p21, p27 and p16 that work to induce cell cycle arrest and dormancy [43-44].

Ablation of these cancer cell systems in their dormant state can not only eliminate the disease, but also reduce the risk of tumor relapse. We have previously developed novel high-throughput amikagel platform that induced total bladder cancer 3D viable spheroid formation and complete tumor dormancy (almost 95% of the cells were arrested in G0/G1 phase of the cell cycle). Bladder cancer 3D-DTMs also showed very high resistance to conventional chemotherapeutics such as microtubule stabilizing docetaxel and DNA intercalating drug mitoxantrone.

This chapter describes the bioengineered high-throughput approaches to develop an in-vitro completely dormant drug discovery platform. Utilizing the amikagel based high-throughput dormant platform, we discovered novel drugs and drug combinations that work to ablate the dormant cancer phenotype. Bioengineered high-throughput, in vitro systems of tumor dormancy and relapse can allow for large-scale rational screening of lead drugs and their combinations, thus aiding cancer drug discovery and delivery [12]. Taken together, we describe a versatile high-throughput, in vitro platform for phenotype-specific drug screening, and for investigating fundamental biochemical and cellular phenomena in tumor dormancy and relapse.

3.2. MATERIALS AND METHODS

Materials

Amikacin hydrate (AH) (referred to as amikacin henceforth), docetaxel, wortmannin, chloroquine, propidium iodide, ribonuclease-A, poly (ethyleneglycol) diglycidyl ether (PEGDE), sodium orthovanadate and sodium fluoride were purchased from Sigma-Aldrich (St. Louis, MO), and used without further purification. Bortezomib was obtained from Selleck Chem (Houston, TX). Thapsigargin and ROCK inhibitor Y-27632 dihydrochloride were obtained from Santa Cruz Biotech (Dallas, TX). Caclimycin ionophore was obtained from RPI Corp (Mount Prospect, IL). 16:0 PC (DPPC) 1,2-dipalmitoyl-sn-glycero-3-phosphocholine was obtained from Avanti Lipids (Alabaster, Alabama) to prepare the liposomes. Calcium chloride dihydrate was obtained EMD millipore (Billerica, MA). Calcein AM/ethidium homodimer Live/Dead stain®, JC-1 Dye—Mitochondrial Membrane Potential Probe were purchased from Life Technologies, (Carlsbad, CA). T24 human bladder cancer cells were obtained from Professor Christina Voekel-Johnson at Medical University of South Carolina, Charleston, SC as part of an existing collaboration. These cell lines were verified for their authenticity through Bio-Synthesis Inc (Lewisville, TX). MTT and XTT cell proliferation kit were purchased from American Type Culture Collection (ATCC) (Manassas, VA) [103]. Cell culture media – RPMI media, DMEM with L-glutamine, Pen-Strep solution: 10000-units/mL penicillin and 10000-µg/mL streptomycin in 0.85% NaCl were purchased from Hyclone (Logan, UT). Premium heat inactivated fetal bovine serum (FBS) was purchased from Atlanta Biologicals (Flowery Branch, GA). Cell culture-treated 24 and 96 well plates were purchased from Corning Life Sciences (Corning, NY). RIPA buffer, Halt protease inhibitor cocktail (100X), Super Signal West Femto Maximum sensitivity substrate, and Fluo-4 Direct™ Calcium Assay kit were obtained from ThermoScientific (Waltham, MA). Tris, glycine, SDS, Blotting-Grade Blocker, 2X Laemmli Sample Buffer, Mini Precast PROTEAN gels and precision plus protein standards (Dual color) were obtained from BioRad (Hercules, CA). Growth Factor reduced (Basement membrane) Matrigel matrix was obtained from Corning (Bedford, MA) and molecular biology grade agarose was obtained from Fisher Scientific (Pittsburgh, PA). Amersham Hybond P

0.45 PVDF membrane was purchased from GE healthcare (Buckinghamshire, UK). CHOP D46F1 Rabbit mAb primary antibody, β-actin Rabbit Ab primary antibody and anti-rabbit IgG HRP-linked secondary antibodies were obtained from Cell Signaling (Boston, MA). Nanopure water was used in all preparations.

Amikagel synthesis

Ring-opening polymerization between amine groups of amikacin hydrate and epoxide groups of poly (ethylene glycol) diglycidyl ether (PEGDE) resulted in the formation of a novel hydrogel henceforth called 'Amikagel'. Different stoichiometric ratios of amikacin and the cross-linker PEGDE were dissolved in Nanopure® water, mixed and incubated at 40°C for 7.5 h, in order to obtain Amikagels AM1, AM2, and AM3 of different compositions (**Table 1)**. The final concentration of amikacin was 10 wt% in all gels. All experiments were carried out in triplicate unless otherwise mentioned.

Preparation of calcium liposomes

16:0 PC (DPPC) 1,2-dipalmitoyl-sn-glycero-3-phosphocholine was dissolved in chloroform at a concentration of 20 mg/mL. 1 mL of the lipid solution in chloroform was dried under a constant stream of filtered air. The lipid crust was desiccated for 24 hours under vacuum to remove all traces of chloroform. The lipid crust was hydrated in 1 mL of sterile filtered 200 mM calcium chloride solution. The mixture was vortexed for 30 seconds followed by heating at 55^{o}C for 60 minutes with vortexing every 15 minutes. Next, the liposomes were sonication for 45 minutes in a bath sonicator at a temperature of 55^{o}C. The loading percent was increased inside the vesicles using repeated freeze thaw method. Lipid –calcium chloride solution was heated to 55^{o}C (above the transition temperature of the DPPC) for one minute and rapidly cooled to -60^{o}C. 10 cycles of repeated freeze thaw were performed. The unencapsulated calcium was removed via ion exchange using Amberlite IR-120+, H^{+} form activated by incubating the resin in 1M HCl for 24 hours prior to the exchange. After the exchange, the solvent around liposomes was brought to 10 mM HEPES buffer, pH 7.4, adjusted using 10M NaOH. Encapsulated calcium content was

determined using the atomic absorption spectroscopy at the range of 1-5 ug/mL (detection range of the instrument). Size and the zeta potential of the liposomes were measured using Malvern Zetasizer Nano (Malvern Instruments, MA). Calcium liposomes were always freshly prepared before use.

Generation of 3D Dormant Bladder Tumor Microenvironment model (3DTMs)

Cell culture

T24 bladder cancer cells were propagated in DMEM supplemented with 10% (v/v) fetal bovine serum and 1% (v/v) penicillin and streptomycin (Pen-Strep solution: 10000 units/mL penicillin and 10000 µg/mL streptomycin in 0.85% NaCl). For NIH3T3 cell propagation, 1% (v/v) sodium pyruvate was added and fetal bovine serum was replaced with calf serum in the media. For all the remaining cell lines, RPMI media supplemented with 10% (v/v) fetal bovine serum and 1% (v/v) penicillin and streptomycin was used.

Generation of 3D-DTMs using Amikagels

1 ml of amikagel AM1, AM2 and AM3 pre-gel solutions were filtered through a 0.20 µm filter and 40 µL of the filtrate was added to each well of a 96 well plate. The plates were sealed with paraffin tape (Parafilm, Menasha, WI) and incubated in an oven maintained at 40^{o}C for 7.5 hours. After gelation, the surfaces of Amikagels were washed with 150 µL of Nanopure® water for 12 hours, in order to remove traces of unreacted monomers. All 3D-DTM experiments were set up by liquid overlay culture [104] of cells on top of Amikagel AM3 surface in a total volume of 150 mL media /well; 100,000 cancer cells alone (single culture) were incubated, unless indicated otherwise in specific cases. After 48 hours of incubation, 50% of the media in the wells was replaced with fresh media i.e. DMEM/RPMI + 10% (v/v) FBS + 1% (v/v) Pen-Strep at regular intervals of 48 hours. Care was taken to withdraw and add the media slowly so as to not perturb 3D-DTM formations. Fresh media was added every 48 hours following cell plating. For 3D-DTM generation on 24 well plates, 400 µL of pre-gel volume was used instead of 40µl. 3D-DTMs were

formed 5-7 days following culture on AM3 Amikagels and were studied for drug treatments after 7 days.

Quantification of total cell protein content and mitochondrial activity of 3D-DTMs and 2D cells

100,000 T24 cells seeded on AM3 Amikagels were disassembled via manual pipetting followed by trypsinization. Cells plated on 2D cell culture plates were disassembled via trypsinization. Trypsin was deactivated using serum containing media after cellular disassembly from 3D-DTMs, pelleted by centrifugation at 800 rpm for 10 minutes and washed thoroughly in 1X PBS before lysis to avoid any contamination from the serum proteins. The washed cells were counted and lysed using 5X promega cell lysis buffer diluted to 1X lysis buffer concentration in 1xPBS. 100,000 cells from 3D-DTMs were collected after 7 days of seeding on AM3 Amikagels. The total protein content in the cells was measured by BCA assay. BSA standards were used to generate a standard curve of absorbance vs. protein concentration. The total protein content was expressed as a ratio to the total cell number.

100,000 disassembled cells (by manual pipetting) collected from 3D-DTMs on AM3 Amikagels and actively dividing 2D cultures were incubated with 1:2 ratio (v/v) of Activated XTT regent: cell culture media for 3.5 hours as per vendor's protocol. After 3.5 hours, the absorbance of the orange color indicative of mitochondrial activity was measured at 475 nm and background was measured at 660 nm. The mitochondrial activity of the 2D and 3D-DTM cell sample were measured and expressed in absorbance units.

Investigation of Chemotherapeutic Drug Efficacy on 3D-DTM Viability

Bortezomib, thapsigargin and wortmannin drugs were added at different concentrations (0.5, 1, 5, 10 and 20 μM) to T24 3D-DTMs after 7 days of seeding on AM3 Amikagel. After 96 hours of exposure, the 3D-DTMs were disassembled by manual pipetting followed by XTT assay to estimate cell viability. Cell death (%) was estimated from the cell viability data and used for

analyses. Cell viability was also assessed by Live/Dead® staining. For combination studies, drug concentrations inducing ~10% death were chosen.

For single agent calcimycin ionophore studies, calcium concentration of 1.8 and 5 mM was used with ionophore of different concentrations (0.1, 0.5, 1, 5 and 10 μM) for 24 hours followed by XTT assay to estimate remaining cell viability. Calcium liposomes were also added at a concentration of 175, 350 and 700 μM to the dormant cells to 24 hours followed by XTT assay. In all cases, concentrations of drugs that induced ~10% cell death as single agents were used for combination studies.

0.5-μM calcimycin was treated together with either 1.8-mM calcium (present in cell culture media) or 5 mM calcium (additional 3.2 mM calcium chloride added to media). These concentrations were chosen since they induced ~10% single agent cell death in 24 hours (Fig. 3G). Higher concentrations of calcimycin (5 μM and 10 μM) with or without calcium induced significantly higher cell death in 24 hours, and were therefore not used (Fig. 3G).

Fluorescence microscopy and Flow Cytometry of 3D-DTMs

Mitochondrial membrane potential detection

Mitochondrial membrane potential after treatment with bortezomib, thapsigargin, calcimycin and calcium was identified using JC-1 dye. 100,000 T24 cells seeded on AM3 gels for a week were treated with bortezomib (0.5 μM) and thapsigargin (0.5 μM), calcimycin (5 μM), calcium (5 mM) and their respective combinations for 24 and 48 hours. They were resuspended in DMEM media supplemented with 100X dilution of the JC-1 dye and distributed into 24 well plates for fluorescence measurements. After incubation for one hour at 37^{o}C, the cells were imaged using the biotek plate at an excitation of 485 nm and emission of 528 nm (green) and 590 nm (red). Green fluorescence indicated presence of mitochondrial depolarization whereas red emission indicated intact mitochondria.

Intracellular Calcium Imaging

T24 3D-DTMs grown on AM3 were treated with calcimycin (0.5 and 5 μM) with calcium (5 mM) and calcium liposomes (175 μM) for 3 hours. Following 3 hours, the 3D-DTMs were disassembled using rapid pipetting and cells were collected by centrifugation. The cells were washed with 1X PBS and resuspended in 50 μL cell culture media + 50 μL Fluo-4-AM dye solution (prepared as per vendor's recommendation). After incubation for 60 minutes, the cells were imaged at excitation: 494 nm, emission: 516 nm. Green color fluorescence was used as an indicator of intracellular calcium concentration. Intracellular calcium fluorescence was quantified using imageJ.

Western Blotting

100,000 cells seeded on AM3 were treated with bortezomib (0.5 μM) and Thapsigargin (0.5 μM), Calcimycin (5 μM), Calcium (5 mM) and their respective combinations for 24 hours, following which the cells were collected, washed with ice-cold 1X PBS, and lysed in 500 μL of RIPA buffer (25mM Tris.HCl pH 7.6, 150mM NaCl, 1% NP-40, 1% sodium deoxycholate, 0.1% SDS) supplemented with sodium orthovanadate (1 mM), sodium fluoride (1 mM), and 100 μL of 100X Halt protease inhibitor cocktail at 4^{o}C. The lysates were then sonicated thrice for 10-15 seconds on ice and collected by centrifugation (16,000 rpm, 20 minutes, 4^{o}C). Supernatants containing the whole cell protein were stored at -20^{o}C for subsequent use.

BCA assay was used to quantify the total protein content of the cell lysates. Equivalent quantities of whole cell proteins (4 μg) were combined with 2x Laemmli buffer containing 5% β-mercaptoethanol, and were heat denatured for 5 minutes at 95^{o}C. Equal amounts of protein (4 μg) were then loaded into to the wells of pre-cast gels and run for 35 minutes at 200 V in running buffer (25 mM Tris, 190 nM glycine, and 0.1% SDS, pH = 8.3). The proteins were transferred to a methanol-activated Hybond PVDF membrane for 30 minutes at 20 V in the transfer buffer (25 mM Tris, 190 mM glycine, and 20% methanol, pH = 8.3). The Hybond PVDF membrane was rinsed with 1X PBST and blocked with 3% blocking buffer 3x for 5 minutes each. The membrane was then incubated with the primary antibody for 12 hours at 4^{o}C (1:1000 CHOP D46F1 Rabbit mAb

primary antibody) and (1:5000 β-actin Rabbit Ab primary antibody). After three washes with 3% blocking buffer, the membrane was incubated in the secondary antibody (Anti-rabbit IgG HRP-linked Antibody) at 1:2000 dilution in the dark for 2.5 hours at 25^{o}C. Following three washes with 1X PBST, the membrane was developed using Super Signal West Femto Maximum sensitivity substrate and viewed under chemiluminescence.

Areas of the proteins actin and CHOP on the nitrocellulose membranes were measured using image-J software. The CHOP proteins from treatment samples were then normalized to their actin content and expressed, which was further expressed as a percentage of the live control.

Statistical Analyses

Averages have been expressed as mean ± SD. The effectiveness of the drug combinations were quantified using the combination index (CI) by Chou-Talalay method. Two-tailed t-test with 95% CI was used analyze and compare the percent cell death data of individual drugs. One-way ANOVA has been used to study the differences between the effectiveness of multiple drugs and their combinations. Tukey's multiple comparisons test was used during multiple pairwise comparisons whereas Dunnett's multiple comparisons test was used while comparing multiple means to a single one (control). $p<0.05$ indicated significance in the analyses. All analyses were performed using the Prism GraphPad software. All experiments have been performed at least n=2 independent experiments with three replicates each unless specified.

3.3. RESULTS AND DISCUSSION

Dormant cells show high mitochondrial activity and total per cell protein content

Drugs against dormant tumors are an unmet biomedical need, which is borne by the poor efficacy of conventional chemotherapeutics against this phenotype. Several treatments are effective at addressing primary cancer disease, but relapse from prolonged states of dormancy after remission presents a significant challenge for improving patient outcomes. It is now widely believed that some cancer cells undergo a period of dormancy and escape chemotherapy due to

their differential phenotype [27]. Ablation of cancer cells in their dormant state, either as part of primary chemotherapy or as maintenance treatment, can likely lead to an increase in progression-free survival. Capture of these dormant phenotypes on a high-throughput in vitro platform can facilitate discovery and development of novel drugs targeted to the dormant tumor phenotype.

We focused our attention to mechanisms other than DNA and microtubule damage, which are default approaches for anticancer therapeutics [132-133]. G0/G1 phase of cell cycle is largely associated with RNA synthesis via transcription and protein production via translation. Cellular arrest in the G0/G1 phase of cell cycle has been associated with increased protein content in cells [134]. T24 3D-DTMs showed marginally higher per cell protein content compared to the 2D actively dividing cells (approximately 1.3 fold higher) (**Fig. 3-1A**). The 3D-DTMs showed a per cell protein content of approximately 0.30 ± 0.10 ng/cell whereas 2D actively dividing cells showed a total per cell protein content of 0.22 ± 0.09 ng/cell. Previous work has found the total cell protein content to be in a similar range of approximately 0.3-0.5 ng/cell [135]. The increase in total protein content in 3D-DTMs is also consistent with previous results showing arrest in G0/G1 phase leads to higher per cell protein content [134].

The dormant 3D-DTMs also showed a mildly lower mitochondrial activity compared to the actively dividing 2D cells (**Fig. 3-1B**). Both T24 and actively dividing 2D T24 cancer cells showed approximately similar absorbance values after exposure to XTT assay for 3.5 hours. T24 3D-DTMs showed a mild reduction in the mitochondrial activity (0.85 fold) compared to the actively dividing 2D T24 cells. It is likely that the spheroidal shape of the 3D-DTM could limit oxygen diffusion into the core of the 3D-DTM leading to reduced mitochondrial activity [94]. However, we did not see any signs of necrosis in the T24 3D-DTM core after H&E staining (**Fig. 2-18**). These results indicate that targeting mitochondria and protein production pathway could lead to development of novel therapeutics that targets the dormant tumors. While T24 3D-DTMs show very high resistance to conventional chemotherapeutics such as docetaxel and mitoxantrone due to its non-dividing status, it is likely that these drugs could sensitize T24 3D-DTMs to cell death (**Fig. 2-23 and 2-24**).

A.

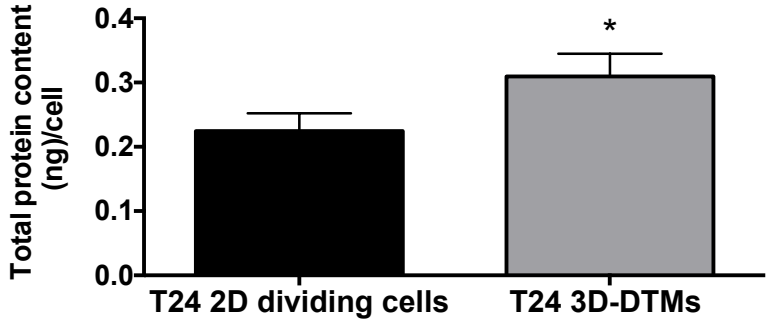

B.

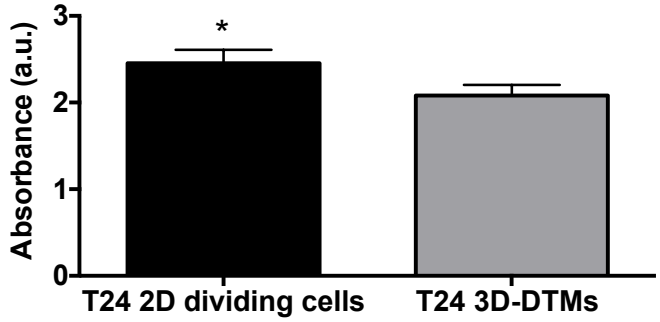

Figure 3-1. Total protein content and mitochondrial activity in dormant cancer cells vs. actively dividing cells. **(A)** Total protein content in T24 3D-DTMs is higher than that in actively dividing cells on a per-cell basis. (n=3, $p<0.05$, 1.3 fold higher, Student's t-test). **(B)** Mitochondrial activity measured using XTT assay showed higher activity in 2D cells compared to T24 3D-DTMs. (n=3, $p<0.05$, 1.3 fold higher, Student's t-test). The numbers of cells were equal in both the groups tested.

Ablation of 3D-DTMs by targeting the Cellular Protein Production Machinery and Mitochondria

We found that protein production in T24 3D-DTMs was modestly, but significantly, higher than in 2D cells (**Fig. 3-1 A**). We hypothesized that small molecules can be used to inhibit key molecular targets in the active protein production machinery, leading to induction of chronic ER stress and subsequent ablation of dormant cancer cells (**Fig. 3-2 A-B**). It has been previously shown that microenvironment induced p38-mediated tumor dormancy leads to upregulation of ER stress and promotes an unfolded protein response (UPR), which confers a pro-survival mechanism in dormant cells [37]. Proteomic analysis of p38-mediated dormant HEp3 squamous carcinoma cells showed an upregulation of UPR (ER stress chaperone BiP and PERK) resulting in resistance to

doxorubicin [67]. Although ER stress is a pro-survival adaptive mechanism adopted by cancer cells, chronic ER stress eventually leads to cell death.

Thapsigargin, an ER-specific calcium channel blocker, is known to reduce calcium concentration in the ER lumen, causing malfunctioning of calcium-dependent ER chaperones [136], and concomitant elevation in the cytoplasmic and mitochondrial concentration of calcium. Improperly functioning calcium dependent chaperones such as calnexin and calreticulin, cause production of misfolded or unfolded proteins. Thapsigargin has also been implicated to induce ER stress by inhibiting autophagic autophagosome-lysosome fusion [137].

A.

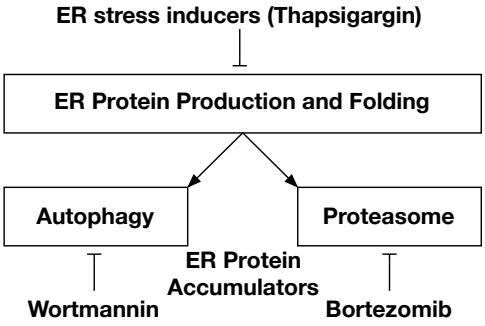

B.

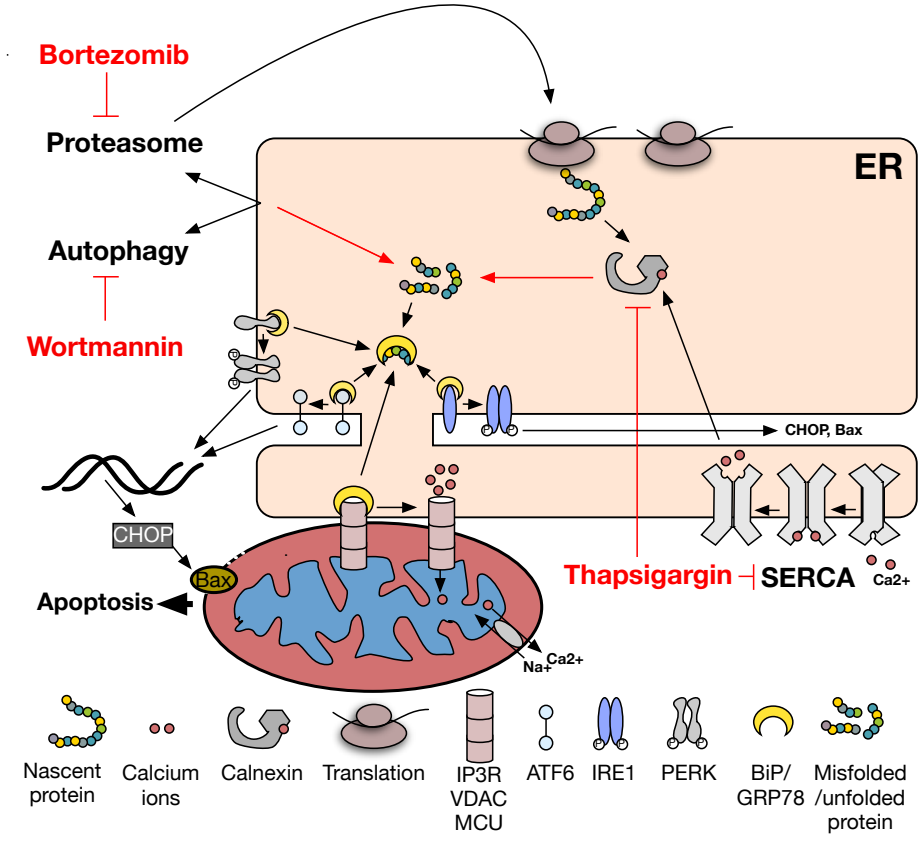

Figure 3-2 Hypothesis driven rational drug discovery against tumor dormancy. (A) Mechanism-based combination treatment in which ER stress inducers (SERCA inhibitor thapsigargin or T) that cause protein misfolding are treated in concert with autophagy or proteasome inhibitors wortmannin (W) or bortezomib (B), respectively. **(B)** Chronic ER stress due to accumulation of misfolded proteins in the ER leads to activation of multiple pro-apoptotic proteins leading to mitochondrial depolarization.

Thapsigargin treatment (15 μM) resulted in a loss of viability in ~50% T24 3D-DTMs after 96 hours of treatment (**Fig. 3-3 A**). This is a significantly improved response compared to docetaxel, or mitoxantrone. Under chronic ER stress, cells can utilize protein degradation pathways including proteasome degradation and / or autophagy to remove misfolded / unfolded proteins [63, 138] promoting cell survival. We therefore hypothesized that a combination of ER stress inducers and proteasome / autophagy inhibitors would demonstrate synergistic activity for the ablation of 3D-DTMs (**Fig. 3-2 A**). Bortezomib is a highly selective, reversible inhibitor of 26S proteasome. The boron atom of the bortezomib drug binds to the catalytic site of the 26S proteasome with high affinity and selectivity, thereby inhibiting it. Under this inhibition, the proteasome cannot perform its regular functions of degrading ubiquitinylated proteins, and peptides. The proteasome also cannot degrade ubiquitinylated misfolded or unfolded proteins and therefore acts to amplify the ER stress under inhibition by bortezomib [63, 139-141]. Bortezomib is FDA approved for treatment of relapsed multiple myeloma and mantle cell lymphoma [142-144]. Due to its reversible nature, resistance against bortezomib has been documented leading to the development of second-generation proteasome inhibitor drugs such as carfilzomib, ONX 0912 and NPI-0052 that bind proteasome irreversibly [145-146]. Wortmannin is a potent, selective and reversible PI3 kinase inhibitor that inhibits organelle sequestration in autophagy [147]. Prevention of organelle sequestration leads to malfunctioning and inhibition of autophagic processes. Under ER stress, cell uses autophagy to sequester and degrade misfolded proteins in the ER, which fails to occur under wortmannin mediated PI3-kinase inhibition [148].

Single-agent toxicity of 0.5 μM wortmannin (W) (autophagy inhibitor) and bortezomib (B) (proteasome inhibitor) were minimal (<10% cell death; **Fig. 3-3 B**). Similar results were observed with 0.5-μM thapsigargin (T) that induced death in only 5% 3D-DTM cells at this low dose of the drug. The LC_{50} value of single-agent bortezomib (2-μM) was significantly lower than that of thapsigargin (15 μM) indicating high dependence of dormant cancer cells on functional proteasome activity for survival (**Fig. 3-3 A**). It is likely that these 3D-DTMs recycle folded proteins generated in the ER under the dormant status to survive. Hence, bortezomib inhibition

effectively sensitizes these cancer cells compared to the other drugs used. All three drugs (B, T and W) showed dose dependent toxicity (**Fig. 3-3 A**).

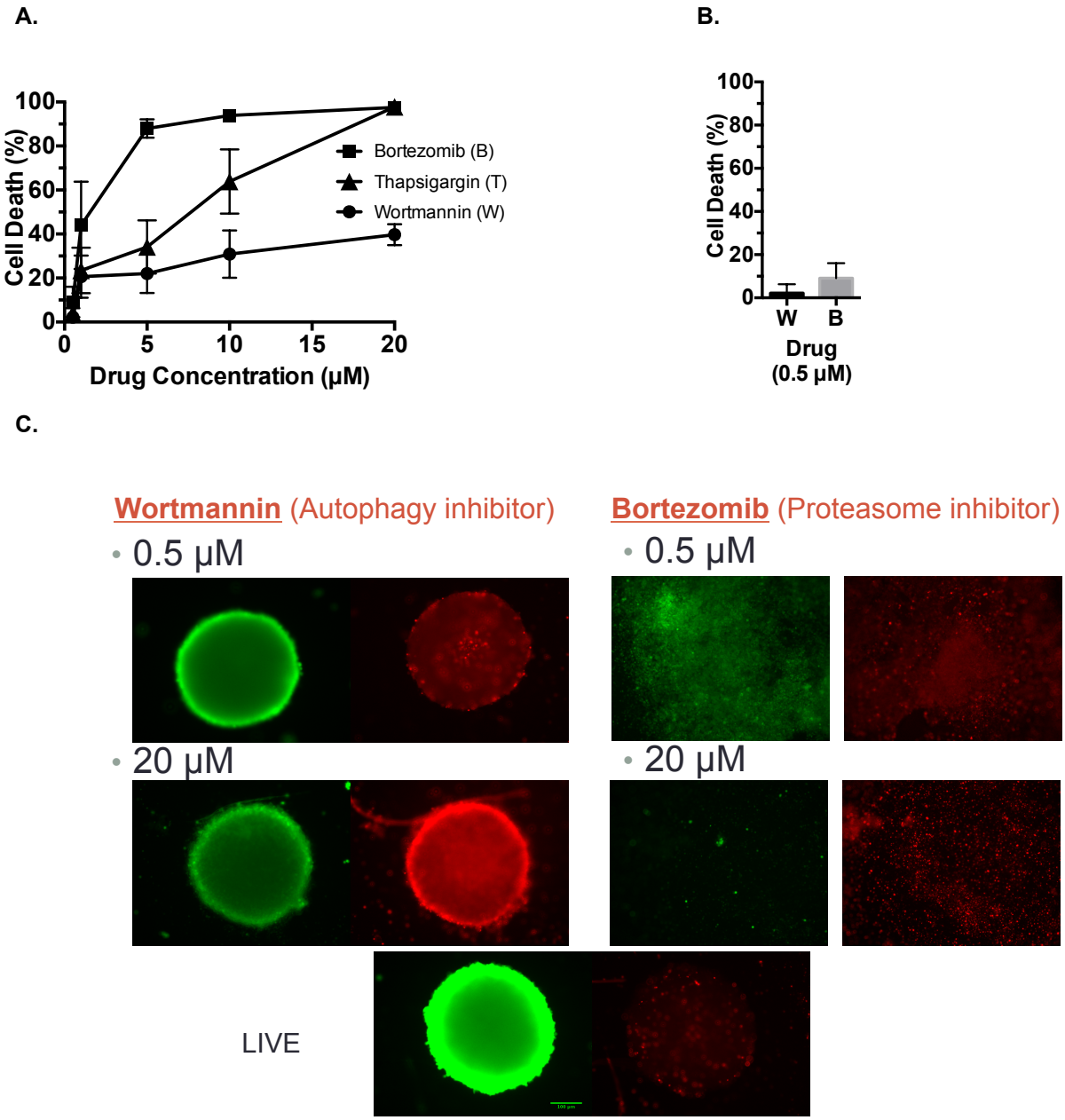

Figure 3-3. ER stress induces death in dormant cancer cells. (A) Cell viability following treatment of T24 3D-DTMs with single-agent thapsigargin (T), bortezomib (B) or wortmannin (W). **(B)** Treatment of T24 3D-DTMs with 0.5 μM B or W resulted in death of <10% cells in either case. **(C)** T24 3D-DTMs were treated with autophagy inhibitor wortmannin and proteasome inhibitor bortezomib (0.5-20 μM) as shown after treating with Live-Dead® stain (Calcein AM-EthD-1). Bortezomib was very effective in inducing cell death on the dormant T24 3D-DTMs. Spheroid morphology was completely lost during the wash steps during the treatments with bortezomib. Scale = 100 μm in all cases. Live-Dead staining revealed similar results to that of XTT data.

Single agent drug concentrations inducing under 10% cell death in 96 hours were chosen for the combination studies. Proteasome inhibitor and autophagy inhibitor drugs bortezomib (B), and wortmannin (W) induced ~10% death as single agents at a concentration of 0.5 μM and were chosen in the combination studies with different concentrations of thapsigargin (0.5 – 20 μM) (**Fig. 3-3 A-B**). Combination of 0.5 μM W and 0.5 μM T did not result in increase in cell death even at higher doses of thapsigargin (**Fig. 3-4 A and C**). A combination of 0.5 μM B + 0.5 μM T however, resulted in near-total ablation of 3D-DTM in 96 hours (**Fig. 3-4 B and C**). The combination index (CI) for the B+T treatment was 0.1 ± 0.03 (Chou-Talalay method), which indicates very strong synergy between the two drugs for ablation of the dormant cancer cell phenotype. These results indicate the heavy dependence of T24 3D-DTMs on functional proteasome activity for their survival. Treatment with low concentrations of thapsigargin caused a depletion of calcium ions in the ER, which affects the activity of several calcium-dependent ER chaperones. This, in turn causes generation and accumulation of misfolded proteins leading to ER stress and unfolded protein response [66, 149]. Inhibition of the proteasome degradation machinery using bortezomib likely causes an accumulation of unfolded proteins leading to induction of chronic ER stress) which ultimately induces death of dormant cells. The relatively low concentrations of the individual drugs required for complete ablation of dormant tumor cells is promising since this can help minimize side-effects in eventual treatments [150].

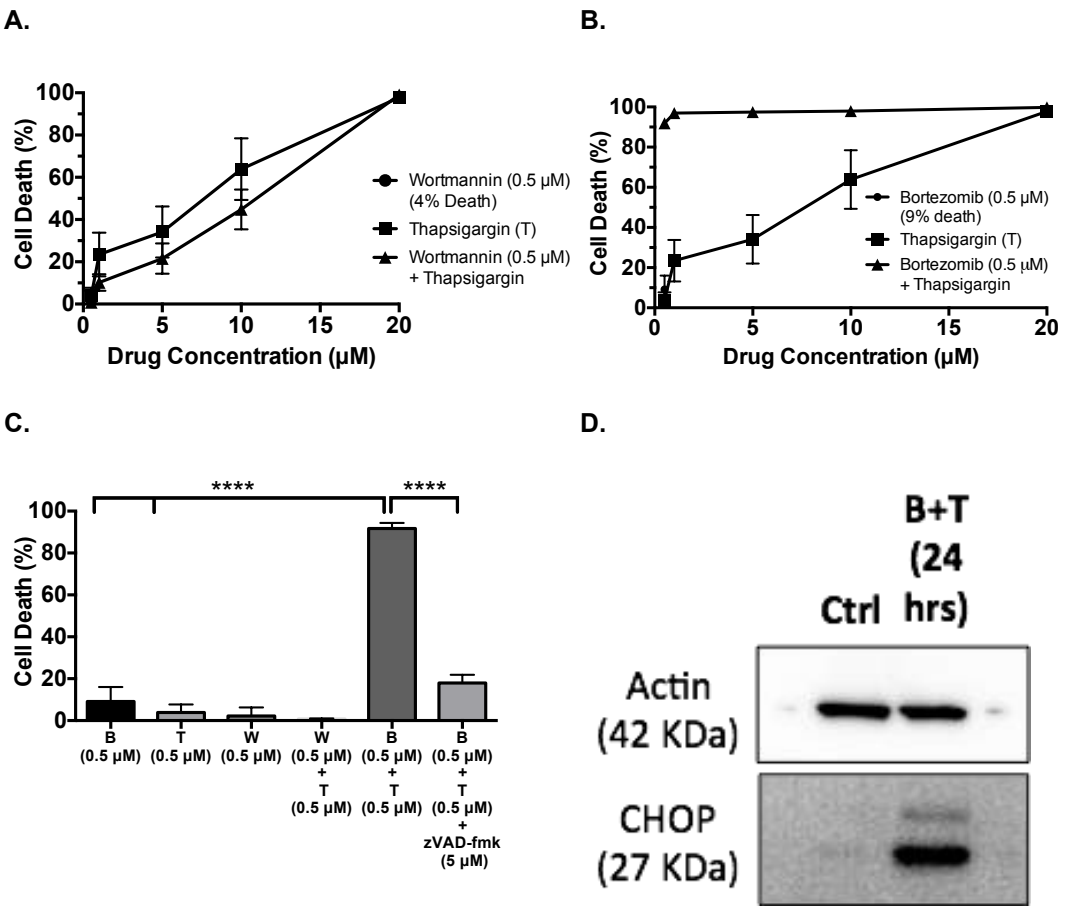

Figure 3-4. Chronic ER stress induces death in dormant cancer cells. (A) Wortmannin (0.5 μM) with thapsigargin did not induce significant synergistic cell death in T24 3D-DTMs. **(B)** Bortezomib (0.5 μM) with thapsigargin induced significant synergistic cell death in T24 3D-DTMs. **(C)** Combination of thapsigargin with bortezomib induces synergistic increase in cell death in 3D-DTMs (96 hours) leading to near-total ablation of the dormant phenotype. A combination index (CI_{B+T}) = 0.1 ± 0.025 indicates strong synergy between the two drugs. Reversal of cell death upon pan-caspase inhibition using the inhibitor zVAD-fmk indicated that the combination of T and B induced caspase-mediated apoptosis in 3D-DTMs. W+T did not induce synergistic cell death.

Chronic ER stress is known to induce cell death via mitochondrial depolarization [151], which acts as a significant amplifier of cell death during the stress [74]. In addition, mitochondrial depolarization acts as a point of no return for cellular apoptosis [152]. While mitochondria could be targeted directly using mitochondrial respiratory inhibitors, our results indicated that mitochondrial activity is relatively lower in the T24 3D-DTMs compared to 2D T24 cells, while the total protein content is higher (**Fig. 3-1 A-B**). Previous results have shown that mitochondrial respiratory inhibitors can sensitize dormant cancer cells to death in the core of multicellular spheroids [35].

Chronic ER stress due to accumulation of misfolded proteins in ER causes the activation of two main pathways, the Ire1/XBP-1, ATF6-dependent pathway and PERK/eIF-2alpha phosphorylation-dependent pathway which activate chaperone and pro-apoptotic protein production (**Fig. 3-2 B**) [74, 151]. Cell death is achieved by upregulation of pro-apoptotic transcription factor such as CHOP, Bak and Bax that puncture the mitochondrial outer membrane. We observed an overexpression of the pro-apoptotic protein CHOP following treatment of 3D-DTMs with bortezomib and thapsigargin, which was an indication of ER stress induced in these cells by the drugs (**Fig. 3-4 D**) [65]. We also observed that treatment with a pan-caspase inhibitor, z-VAD-fmk, significantly rescued 3D-DTMs from B+T treatment (**Fig. 3-4 C**), which is consistent with findings that indicate involvement of caspases 3, 9, and 12 in ER stress mediated apoptosis [153]. Mitochondrial depolarization results in generation of apoptosome that causes activation and autocatalytic self-cleavage of multiple pro-caspase 9 units. Activated caspase-9 further cleaves and activates caspase-3 initiating the caspase cascade [154]. Mature caspases actively cleave the aspartate units of critical proteins that are involved in structural stability, DNA repair leading to regulated cell death [155].

Nanoparticle and ionophore-mediated delivery of calcium accelerated dormant cancer cell death under chronic ER stress

Ablation of 3D-DTMs following treatment with bortezomib and thapsigargin occurs over a period of 96 hours; kinetics studies revealed minimal losses in viability (< 2% death) at 24 hours following treatment (**Fig. 3-5 A**). We therefore sought to develop strategies for accelerating death of dormant tumor cells. Strategies that can accelerate therapeutic outcomes could save cost and time to achieve a therapeutic outcome.

Upon induction of chronic ER stress, the transcription factor CHOP expression induces expression of Bax and Bak, which puncture the outer mitochondrial membrane [65]. Concomitantly, efflux of calcium ions from the ER and cytoplasm into the inner mitochondrial matrix via the IP3R-VDAC-MCU channels elevates the calcium concentration in the matrix. Elevation of calcium concentration in the matrix results in mitochondrial depolarization leading to influx other counter

ions and water [73]. These events result in mitochondrial swelling and rupture leading to cell death [74]. We therefore hypothesized that raising the concentration of calcium ions in the cytoplasm following exogenous delivery of the cation will accelerate cell death under chronic ER stress conditions induced by B+T. Exogenous delivery of calcium will increase the total pool of calcium available in the cell for depolarization of mitochondria leading to hastening of mitochondrial depolarization and eventual death.

Nanoparticle calcium delivery

Calcium influx into cells is very tightly regulated in order to prevent sudden necrotic death; minimal amounts of extracellular calcium can enter epithelial cells via passive diffusion due to the presence of TRP vanilloid family of ion channels that regulate entry [156]. Indeed, significantly elevated concentrations of extracellular calcium in cell culture media (up to 40 mM) had minimal impact on viability of 3D-DTMs even after 96 hours of treatment (**Fig. 3-5 B**).

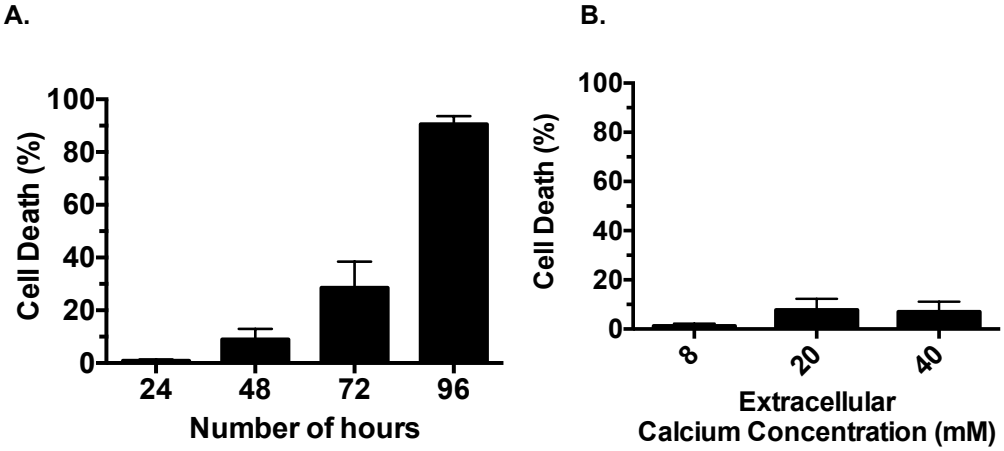

Figure 3-5. Cell death after B+T and calcium in cell culture media. (A) Combination of 0.5 μM Bortezomib (B) and 0.5-μM thapsigargin (T) induced less than 2% death in 24 hours and induced complete cell death only in 96 hours. **(B)** Dormant cancer cell death after treatment with different concentrations of extracellular calcium chloride for 96 hours is shown. Less than 10% cell death was observed even with treatment of about 40 mM extracellular calcium chloride. (Cell culture media has extracellular calcium of 1.8 mM).

In addition to regulating entry, intracellular calcium spikes are immediately buffered by ER and mitochondria [157]. However, in presence of thapsigargin-induced stress, the ER

demonstrates significantly reduced ability to buffer intracellular calcium levels [136]. We therefore hypothesized that delivery of calcium using nanoparticles or ionophores (e.g. calcimycin) will increase the intracellular levels of the cation in 3D-DTMs, increase the load on mitochondria and accelerate cell death. Nanoparticle/Ionophore mediated elevation in intracellular calcium concentration coupled with calcium entry via store-operated calcium entry (SOCE) STIM1-Orai1 channels under thapsigargin induced ER calcium stress could cause further elevation in cytoplasmic calcium levels and accelerate cell death [158].

Dipalmitoylphosphatidylcholine (DPPC) liposomes (average hydrodynamic diameter: 115 nm and zeta potential value: +25 mV) were loaded with 12 ± 5 mM calcium chloride (n=3 independent experiments) and delivered to T24 3D-DTMs (**Fig. 3-6 A-B**). Dipalmitoylphosphatidylcholine (DPPC) lipids have a transition temperature of approximately 41^{o}C, which provide stability to the liposome at room temperature [159]. In addition, the permanently positive quaternary ammonium group on dipalmitoylphosphatidylcholine (DPPC) lipids can effectively resist leakage of loaded positively cargo from these liposomes to the outside. DPPC liposomes have also been shown to be stable in presence of serum[160]. In our studies, these liposomes were stable for at least 48 hours in presence of serum, which is sufficient for intracellular delivery of calcium (**Fig. 3-6 C**). We studied the release of calcium from DPPC liposomes in presence of 150 mM salt (1X PBS) and 10% fetal bovine serum. As shown in **Fig. 3-7**, the release of calcium occurred within the first 6 hours from liposomes, followed by almost no release. It is likely that the release of calcium will be accelerated in presence of cells. In-vivo liposomal calcium formulations will likely use a more serum stable liposomes prepared with distearoylphosphatidylcholine DSPC lipid and other pegylated co-lipids. Liposomes prepared with DSPC lipid have a transition temperature of 55^{o}C that is more stable than DPPC due to two additional carbons in the hydrophobic chain [161].

A.

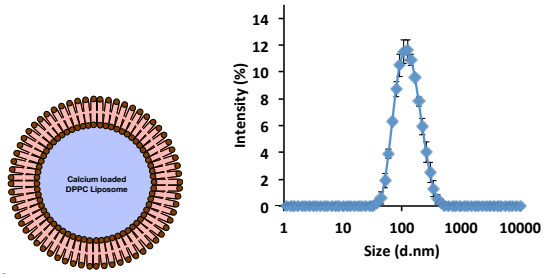

Size (dia)	115 ± 2 nm
Zeta potential	26 ± 5 mV
PDI	0.197
Loading capacity	12 ± 5 mM in 20 mg/ml lipid

B.

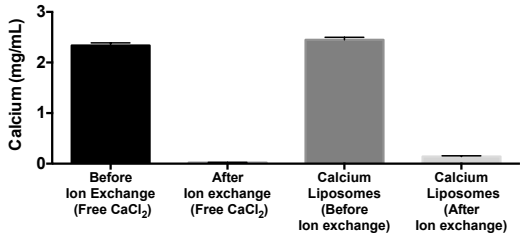

C.

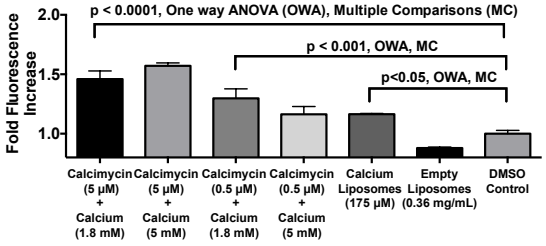

D.

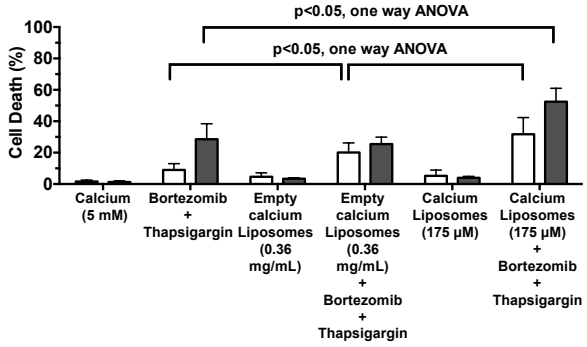

E.

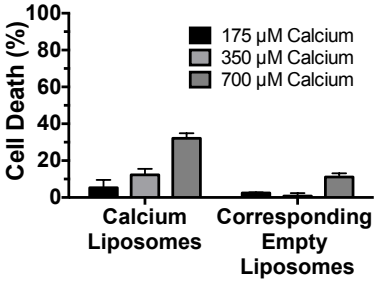

Figure 3-6. Acceleration of chronic ER stress induced death after exogenous delivery of calcium via liposomes. (A) DPPC calcium loaded liposomes were generated using multiple-freeze thaw method. The size (diameter) and zeta potential were measured approximately at 115 nm and 26 mV. **(B)** Free unencapsulated calcium was removed from the liposome system using H^+ activated ion exchange system. The ion exchange system was noted to remove ~99% of the free calcium as measured using the $CaCl_2.2H_2O$ control (atomic absorption spectroscopy). Calcium loaded in liposomes (approximately 12 ± 5 mM). **(C)** Intracellular calcium fluorescence in T24 3D-DTMs was measured using Fluo-4 dye after 3 hours of calcium delivery using calcimycin or calcium liposomes. Fold increase over DMSO control is indicated (baseline calcium concentration – 1.8 mM in the media) (N=2) **(D)** Calcium-loaded liposomes (175 µM) accelerated T24 3D-DTM death in combination with bortezomib (0.5 µM) and thapsigargin (0.5 µM) at 48 h (open bars) and 72 h (shaded bars). Empty DPPC liposomes were also seen to cause a slight increase in cell death but significantly lesser than the combination of B, T and calcium liposomes. (* - p<0.05, ** - p<0.01, *** - p<0.001, **** - p<0.0001) **(E)** Single agent calcium loaded DPPC liposomes and empty liposomes showed dose dependent toxicity after 24 hours exposure. 175 µM concentration of calcium in liposomes was chosen to study the acceleration as it induced ~10% single agent cell death in 24 hours.

Liposomal delivery of calcium to the cytoplasm induced a significant acceleration in 3D-DTM cell death at a concentration of 175 μM (**Fig. 3-6 D**). Treatment with calcium liposomes alone induced death in ~10% of the 3D-DTM cell population (24 and 48 hours) (**Fig. 3-6 D-E**). A concentration dependent cell death was observed in the T24 3D-DTMs after treatment with calcium liposomes. We observed ~37% cell death in 48 hours upon using calcium liposomes together with B+T, which increased to ~52% at 72 hours. In both these cases, 3D-DTM cell death was significantly higher than when cells were treated with B+T in absence of liposomal calcium (**Fig. 3-6 D**). Increasing calcium loading in liposomes can be employed to further enhance cell death at earlier times.

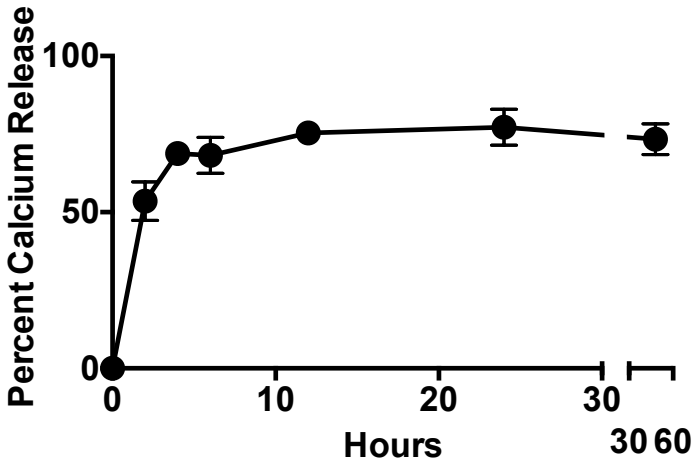

Figure 3-7. Release of calcium from DPPC liposomes in presence of 150 mM salt (1X PBS) and 10% FBS. DPPC calcium loaded liposomes showed a controlled release profile of calcium during dialysis.

Delivery of these drugs in liposomes is an attractive strategy since liposomes can be specifically targeted to cancer cells using targeting ligands. In addition, co-formulation of calcium with drugs that induce, amplify and accelerate ER stress (e.g. B+T) mediated death is also possible. While bortezomib is already FDA approved for multiple myeloma [162], the pro-drug form of thapsigargin is in clinical trials against multiple tumor types etc. [163], indicating the translational potential of these findings. Formulating chemotherapeutic treatment strategies that can synergize, accelerate and reduce treatment times while maintaining efficacy could diminish the side effects of toxic anti-cancer drugs and reduce costs in the future. To our knowledge, this is the first report

that employs delivery of exogenous calcium in order to accelerate ER stress induced cancer cell death. The Amikagel platform can facilitate rapid discovery of such novel drug combinations for tumor dormancy and help accelerate their translation to the clinic.

Ionophore mediated calcium delivery

Calcium ionophore calcimycin shows high affinity to divalent cations such as calcium and magnesium and traffics them into the cell via the lipid bilayer [164]. Single agent calcimycin ionophore treatment with 1.8 mM and 5 mM calcium induced a concentration dependent cell death. The cell death was significantly higher after the treatment with higher concentration of calcimycin (**Fig. 3-8 A**). Higher concentration of calcium with calcimycin likely causes rapid delivery of calcium into the cytoplasm of the cell leading to necrotic death.

Treatment with the ionophore calcimycin together with calcium (calcimycin-calcium) also resulted in an acceleration of cell death induced by ER stress. Individual combinations of calcimycin (0.5 μM)-calcium (5 mM or 1.8mM) or bortezomib-thapsigargin (0.5 μM each) did not induce significant loss in 3D-DTM viability (10-15% cell death at 24 and 48 hours) (**Fig. 3-8 B**). In contrast, their combination caused significantly increased death (~60% in 48 hours) (**Fig. 3-8 B**), indicating acceleration of cell death when low concentration of calcimycin (0.5 μM)-calcium (5 mM or 1.8 mM) was treated with B+T (0.5 μM each) (**Fig. 3-8 B and C (i)**). While B+T induced ~90% death over 96 hours, calcimycin-calcium induced the same extent of death within 48 hours (**Fig. 3-8 B**). The enhancement in cell death induced by calcium delivery was sustained for 96 hours (**Fig. 3-8 B**). This acceleration was reversible following pan-caspase inhibition, indicating the role of caspase-induced apoptosis in accelerated 3D-DTM death at lower concentrations of calcimycin-calcium (**Fig. 3-8 C (ii)**). Pan-caspase inhibition did not rescue dormant cells from death under higher concentrations of calcimycin-calcium treated along with B+T, indicating that caspase-medicated apoptosis was likely not involved; cell death likely occurs due to necrosis following rapid ion influx at these higher concentrations (**Fig. 3-9**).

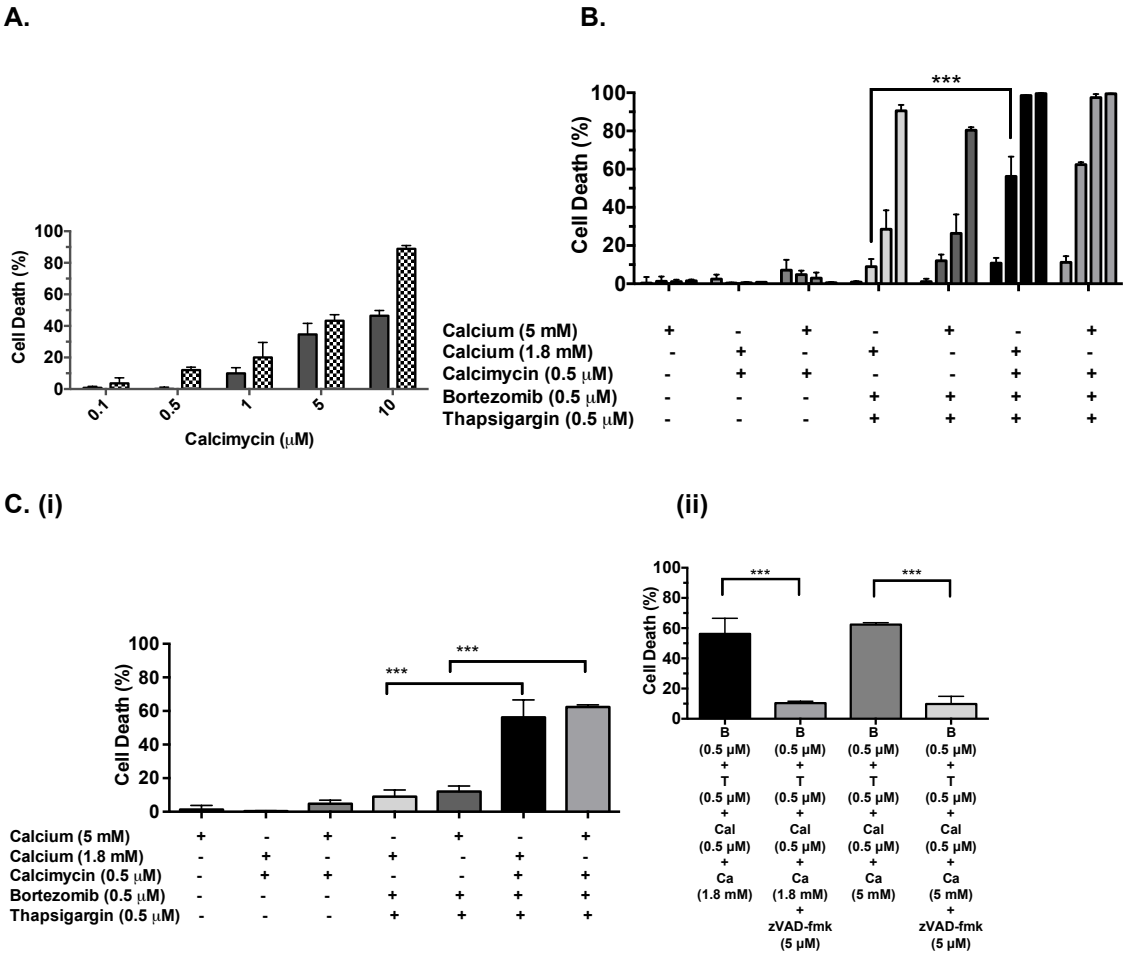

Figure 3-8. Acceleration of chronic ER stress induced death after exogenous delivery of calcium via ionophore. (A) Viability of T24 3D-DTMs treated with of different concentrations of calcimycin- calcium (1.8 mM or 5 mM). Use of 5 mM calcium concentration resulted in modest increase in T24 3D-DTM cell death. Supplementation of 5 mM calcium (checkered bars) with calcimycin increased the cell death compared to that seen with 1.8 mM calcium (solid bars). **(B)** T24 3D-DTMs were treated with bortezomib (0.5 μM), thapsigargin (0.5 μM), calcimycin (0.5 μM) or calcium (1.8 mM and 5 mM) and their combinations for 24, 48, 72 or 96 hours (sequence of bars). While bortezomib and thapsigargin induced approximately 10% death in 48 hours, their combination with calcium and calcimycin (0.5 μM) induced significantly higher death ($p<0.001$) (~65%). **(C) (I).** Viability of T24 3D-DTMs following treatment with bortezomib (0.5 μM), thapsigargin (0.5 μM), calcimycin (cal; 0.5 μM) or calcium (Ca; 1.8 mM and 5 mM) and their combinations (48 h). **(ii).** 3D-DTM death induced by calcimycin, calcium, bortezomib and thapsigargin (48 h) was reversed upon addition of the pan-caspase inhibitor (5 μM zVAD-fmk) indicating an apoptotic cell death acceleration. (One-Way ANOVA, multiple comparisons) (* - $p<0.05$, ** - $p<0.01$, *** - $p<0.001$, **** - $p<0.0001$).

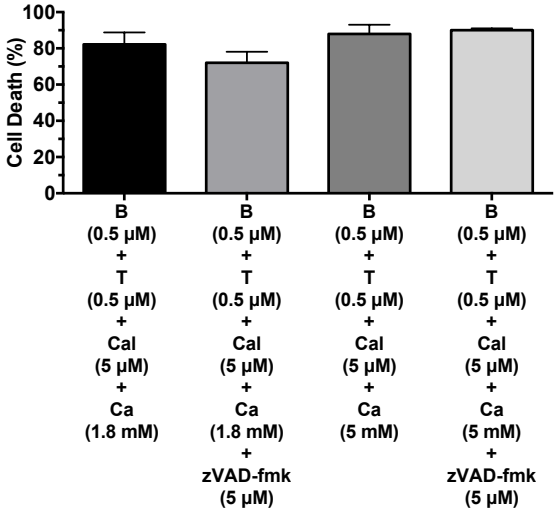

Figure 3-9. Pancaspase is ineffective in reversing cell death after high concentration of calcimycin. Pancaspase inhibition did not rescue cells from death after treatment with high concentration of calcimycin (5 µM) combined with bortezomib (0.5 µM), thapsigargin (0.5 µM) and calcium (1.8 mM or 5 mM), indicating a predominant necrotic death at higher concentrations of calcimycin (48 hour time point).

Increased mitochondrial depolarization drives the acceleration of dormant apoptotic cancer cell death under ER stress inducers - calcium supplementation

We next investigated mitochondrial depolarization, CHOP expression and intracellular calcium fluorescence in order to gain a mechanistic understanding into calcium-induced acceleration of 3D-DTM death. Intracellular calcium fluorescence was significantly higher than the DMSO control at 3h following delivery of the cation using calcimycin and calcium liposomes (**Fig. 3-10, 3-6C**), confirming that an increase in calcium levels precedes the enhancement of 3D-DTM cell death seen at 48 h. In the absence of B+T-induced ER stress, calcimycin (0.5 µM) with calcium (5 mM or 1.8 mM) did not induce CHOP expression that correlated with minimal cell death seen under these conditions. However, significantly higher CHOP expression was noted when calcimycin-calcium was added along with B+T, indicating the role of CHOP in the acceleration of apoptosis (**Fig. 3-11 A**). CHOP expression was high following calcium delivery with calcimycin in presence of B+T irrespective of the concentration of calcium delivered (1.8 mM or 5 mM) (**Fig. 3-11 A**). A modest level of mitochondrial depolarization was observed following treatment with B+T (0.5 µM

each) alone. However, combination of B+T with calcimycin (0.5 μM)-calcium (5 mM or 1.8 mM) (**Fig. 3-11 B**) caused significantly higher mitochondrial depolarization than B+T alone (**Fig. 3-11 B**). Treatment with single agent calcium liposomes caused significantly higher mitochondrial depolarization compared to corresponding empty liposomes. Combination of B, T and calcium liposomes also caused significantly higher mitochondrial depolarization compared to B+T alone (**Fig. 3-12**). Treatment with calcium alone neither induced CHOP expression nor mitochondrial depolarization compared to the live control, which is consistent with its minimal intracellular transport and the concomitant negligible loss in cell viability (**Fig. 3-8 A-B**). Our results indicate that chronic ER stress induced by bortezomib and thapsigargin, in concert with calcium delivery, can enhance mitochondrial depolarization and CHOP expression, which ultimately results in the observed enhancement of 3D-DTM cell death.

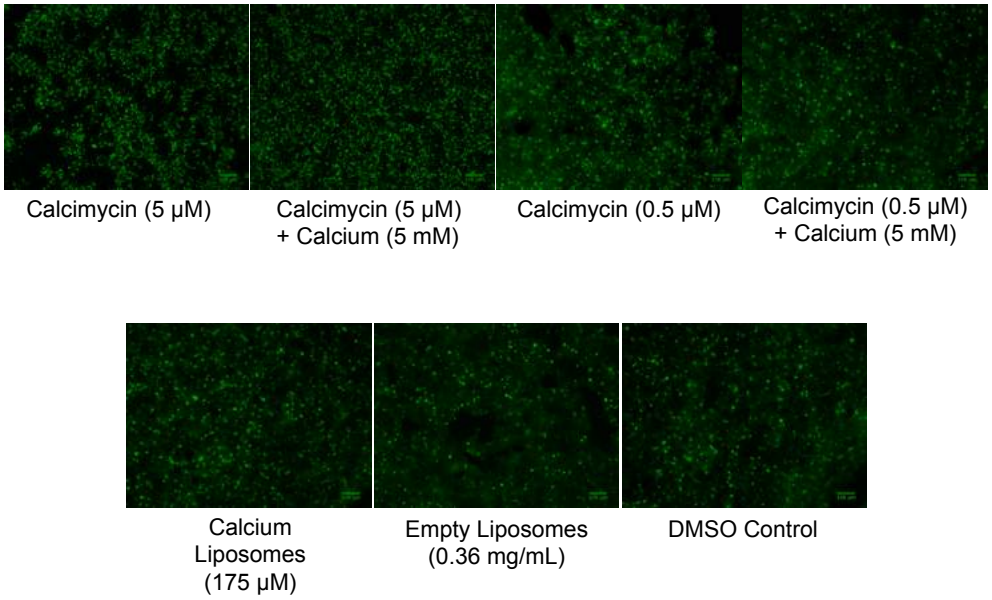

Figure 3-10. Intracellular calcium fluorescence in T24 3D-DTMs following delivery using calcimycin or calcium liposomes. Intracellular calcium concentration was imaged by administering Fluo-4-AM dye after 3 hours of exposure to various treatment modalities. Calcium fluorescence was imaged at ex: 494 nm and em: 516 nm (green fluorescence). Scale bar = 100 μm. Representative figure from N=2.

A.

CHOP /Actin	0.04	0.13	0.03	4.27	2.27	8.49	10.26	
Standard Deviation	0.02	0.05	0.01	1.78	0.68	2.67	4.49	

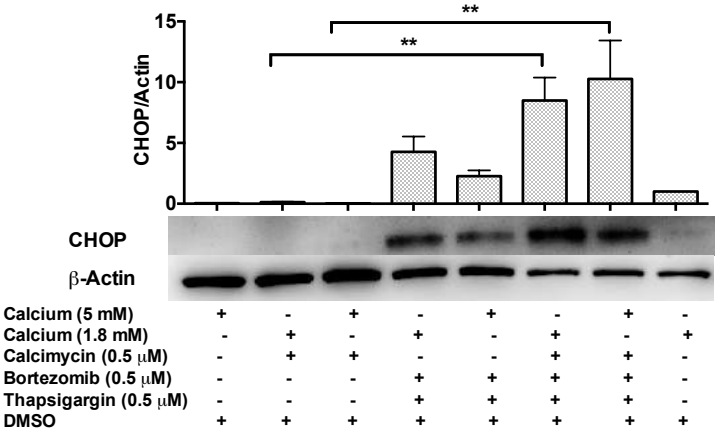

B.

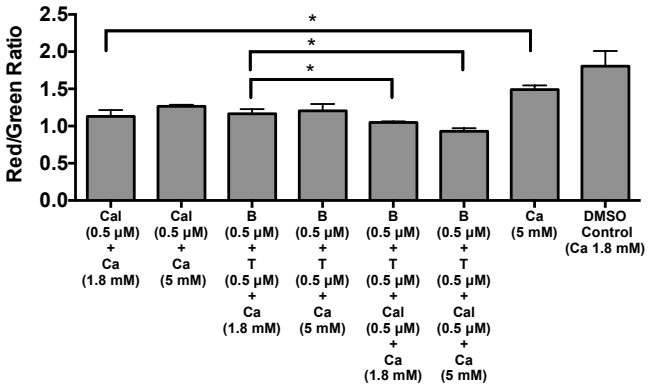

Figure 3-11. Mechanistic understanding of dormant cell death acceleration. Bortezomib + thapsigargin treatment induced significant expression of CHOP (24 h) which is indicative of ER stress. Calcimycin-calcium treatments did not induce significant upregulation of the CHOP protein. **(C)** Mitochondrial depolarization activity measured using JC-1 dye after treatment with bortezomib (0.5 μM), thapsigargin (0.5 μM), calcimycin (0.5 μM)-calcium (1.8 mM or 5 mM) and their combinations for 48 hours. Fluorescence units were measured using Biotek plate reader and the ratio of the green and red emissions were calculated. Combination treatments of B, T and calcimycin with and without additional calcium induced significantly higher mitochondrial depolarization compared to B-T alone (*$p<0.05$, One way ANOVA).

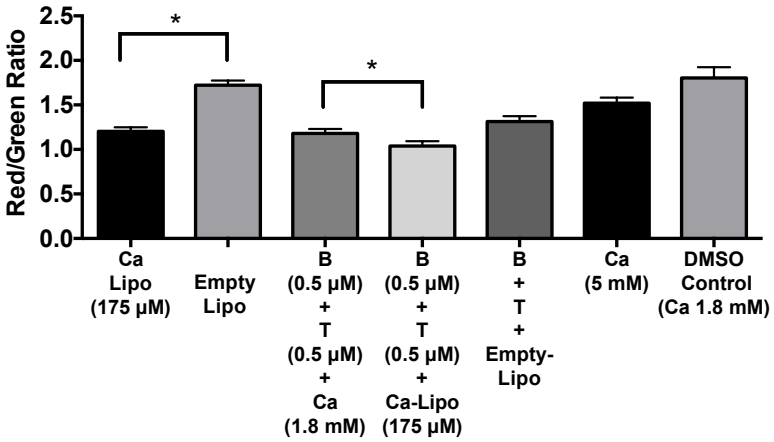

Figure 3-12. Mitochondrial depolarization after B, T and calcium liposome delivery. Mitochondrial depolarization activity measured using JC-1 dye after treatment with bortezomib (0.5 µM), thapsigargin (0.5 µM), calcium liposomes (175 µM) and the corresponding empty liposomes and their combinations for 48 hours. Fluorescence units were measured using Biotek plate reader and the ratio of the green and red emissions were calculated. Combination treatments of B, T with calcium liposomes induced significantly higher mitochondrial depolarization compared to B-T alone. Calcium liposomes also induced significantly higher mitochondrial depolarization compared to empty liposomes. (N=2)
In all cases the significance relates to the following: * - $p<0.05$, ** - $p<0.01$, *** - $p<0.001$, **** - $p<0.0001$, One way ANOVA.

Proposed mechanism of acceleration of ER stress mediated apoptotic cell death

Under stress using thapsigargin, the calcium entry into the endoplasmic reticulum is blocked due to SERCA inhibition. Depleted calcium in the ER causes multiple calcium dependent chaperones to malfunction leading to the production of misfolded/unfolded proteins and cause ER stress. ER stress kickstarts multiple downstream pathways that work to repair the cell and remove the ER stress, collectively known as unfolded protein response (UPR effect). This pathway works by activating transcription and translation of multiple chaperones to repair the unfolded proteins. In addition, translation of new proteins is slowed down in order to reduce the load of protein production on the ER. Under chronic ER stress, multifunctional transcriptional regulator CHOP protein is produced which transcriptionally activates the production of multiple pro-apoptotic proteins such as Bax and Bak. Bax and Bak work to puncture the outer mitochondrial membrane leading to mitochondrial depolarization and apoptosis. Simultaneously, calcium from the ER and cytoplasm is pumped into the mitochondrial matrix, reducing and removing the potential

difference between the inner and the outer membrane, leading to mitochondrial swelling and rupture. This two-way mode of cell death, works to depolarize the mitochondria and achieve cellular apoptosis in these dormant cells. Under thapsigargin mediated blockade of ER, exogenous calcium delivered to the cell cytoplasm cannot be buffered by the ER, leaving all of it for mitochondrial depolarization under chronic ER stress (**Fig. 3-13**).

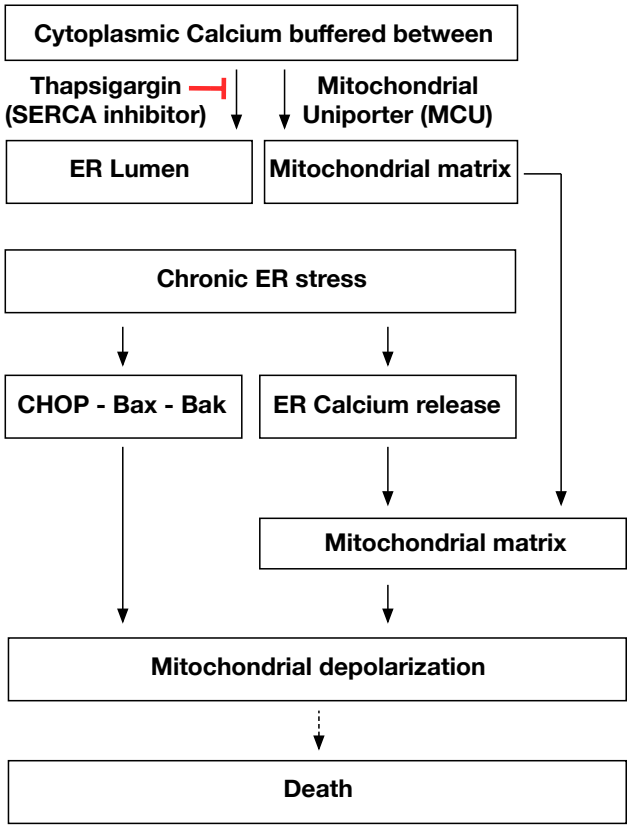

Figure 3-13. Proposed pathway of ER stress induced apoptosis and acceleration of cell death after intracellular calcium supplementation. Increase of cytoplasmic calcium in presence of thapsigargin is likely to buffer only with mitochondria (as calcium entry into ER is blocked) accelerating its depolarization and eventual cell death under chronic ER stress.

3.4. CONCLUSIONS

These 3D dormant tumor microenvironments were susceptible to drugs that were able to induce chronic ER stress. Increase in intracellular calcium levels (e.g. mediated by nanoparticle delivery) further accelerated death of 3D-DTMs induced by drugs that induce ER stress. The use of liposomal delivery of calcium in concert with ER stress inducers is a novel approach for ablating

the dormant tumor phenotype. Taken together, the Amikagel platform facilitates high-throughput formation of 3DTMs for applications in drug screening and investigations in fundamental tumor biology. This high-fidelity platform can be employed for identifying drugs that can reverse and / or ablate the dormant phenotype, as well as obviate cell escape from dormant tumors, leading to novel discoveries for the clinical management of cancer diseases.

CHAPTER 4: MODULATION OF AMIKAGEL CHEMO-MECHANICAL PROPERTIES LEADS TO RELAPSE FROM TUMOR DORMANCY

4.1. INTRODUCTION

Tumor dormancy is a widely accepted phenomena that is believed to occur in patients after primary course of treatment. Dormancy state can confer strong drug resistance in cancer cells against therapeutic regimens that are focused exclusively on eliminating actively dividing cells. Once the drug regimen is removed or completed, these dormant cancer cells are waiting ticking bombs, ready to relapse upon cue. Relapse from tumor dormancy often occurs after an indefinite period of time. After relapse, the cancer manifests as metastases in primary or distant locations that often result in patient mortality. Mortality due to metastases accounts for the highest percentage of deaths associated with the cancer disease. In fact, 90% of cancer deaths are due to metastases to distant sites such as bone, liver, lungs etc [28]. Deaths due to breast and prostate cancer metastases account for majority of deaths in patients with those diseases [29]. Relapse from tumor dormancy has been shown to be associated with changes in the extracellular environment around the dormant tumor [38]. Changes such as angiogenic bursts [165-166], adhesive microenvironments [38], TGF-β production [167] have been linked to initiation of relapse from tumor dormancy.

In bladder cancer, changes in extracellular matrix have been associated with metastasis and migration of the cancer cells [53]. The cancer cells that tend to migrate and metastasize are the ones with lower expression of beta-catenin levels, higher MMP expressing cells etc [47]. Breakdown of ECM by MMP production allows the metastatic cancer cells to migrate and invade into the blood stream and other secondary organs such as lymph nodes. Aberrant expression of N-cadherin has been associated with poor prognosis of bladder cancer [54]. N-cadherin protein expression along with E-cadherin down-regulation is a hallmark of epithelial to mesenchymal transition (EMT) event and has been linked to poor prognosis for the bladder cancer patients [55]. However, reduction or complete absence of N-cadherin has been associated with increased migration, metastases in multiple cancer cell types including bladder cancer and even poorer

prognosis for the patient [55-57]. In a study of bladder cancer patient samples by Jager et al. [58], N-cadherin reduction and absence was identified to be an extremely poorer prognostic indicator than expression of N-cadherin (which was also a significant prognostic indicator of invasive cancer disease).

We hypothesized that transferring the dormant T24 3DTMs from non-adhesive and mechanically stiff Amikagel formulations to a more adhesive, mechanically pliant Amikagel formulations could result in relapse and migration of metastatic populations of the cells. We hypothesized that cells with differential expression of N-cadherin could be isolated from within the population of T24 cells by modulating the chemo-mechanics and adhesivity of the substrate matrix and their propensity to relapse and migrate. In order to do so we varied the ratio of the input monomers amikacin and PEGDE to generate different formulations of Amikagel with varying adhesivities and studied the relapse of the cancer cells from tumor dormancy. Our goal for this work has been to develop a novel high-throughput platform that not only captures complete tumor dormancy, but also relapse and further metastatic cell migration and micrometastases formation for rapid drug discovery, validation, delivery and development. This chapter describes our work to induce relapse from dormancy in bladder cancer by chemo-mechanical modulation of Amikagels.

4.2. MATERIALS AND METHODS

Materials

Amikacin hydrate (AH) (referred to as amikacin henceforth), docetaxel, propidium iodide, ribonuclease-A, poly (ethyleneglycol) diglycidyl ether (PEGDE), were purchased from Sigma-Aldrich (St. Louis, MO), and used without further purification. ROCK inhibitor Y-27632 dihydrochloride was obtained from Santa Cruz Biotech (Dallas, TX). T24 human bladder cancer cells were obtained from Professor Christina Voekel-Johnson at Medical University of South Carolina, Charleston, SC as part of an existing collaboration. These cell lines were verified for their authenticity through Bio-Synthesis Inc (Lewisville, TX). Cell culture media – RPMI media, DMEM with L-glutamine, trypsin, and Pen-Strep solution: 10000 units/mL penicillin and 10000 µg/mL streptomycin in 0.85% NaCl were purchased from Hyclone (Logan, UT). Premium heat

inactivated fetal bovine serum (FBS) was purchased from Atlanta Biologicals (Flowery Branch, GA). Cell culture-treated 24 and 96 well plates were purchased from Corning Life Sciences (Corning, NY). Nanopure water was used in all preparations.

Amikagel synthesis

Ring-opening polymerization between amine groups of amikacin hydrate and epoxide groups of poly (ethylene glycol) diglycidyl ether (PEGDE) resulted in the formation of a novel hydrogel henceforth called 'Amikagel'. Different stoichiometric ratios of amikacin and the cross-linker PEGDE were dissolved in Nanopure® water, mixed and incubated at 40°C for 7.5 h, in order to obtain Amikagels AM1, AM2, and AM3 of different compositions (Table 1). The final concentration of amikacin was 10 wt% in all gels. All experiments were carried out in triplicate unless otherwise mentioned.

Adhesivity of Amikagels

Adhesivity of Amikagels was qualitatively estimated by comparing the adhesivity of T24 cells to the 2D cell culture plates vs. Amikagels after wash assay. 10,000 T24 cells were added to AM1, AM3 and 2D cell culture plates. After 3 hours of incubation at 37^{o}C, 95% humidity, 5% CO_2 the media was removed and cells were washed thrice with 1X PBS under minor agitation. The remaining cells were trypsinized and collected. Cells were counted and the adhesivity was qualitatively expressed as a percentage of number of cells attached to the 2D cell culture plates versus amikagels.

Generation of 3D-DTMs using Amikagels

1 ml of amikagel AM1, AM2 and AM3 pre-gel solutions were filtered through a 0.20 µm filter and 40 µL of the filtrate was added to each well of a 96 well plate. The plates were sealed with paraffin tape (Parafilm, Menasha, WI) and incubated in an oven maintained at 40^{o}C for 7.5 hours. After gelation, the surfaces of Amikagels were washed with 150 µL of Nanopure® water for 12 hours, in order to remove traces of unreacted monomers. All 3D-DTM experiments were set up

by liquid overlay culture [104] of cells on top of Amikagel surface in a total volume of 150 mL media /well; either 100,000 cancer cells alone (single culture) or 50,000 stromal cells followed by 50,000 cancer cells (co-culture) were incubated, unless indicated otherwise in specific cases. After 48 hours of incubation, 50% of the media in the wells was replaced with fresh media i.e. DMEM/RPMI + 10% (v/v) FBS + 1% (v/v) Pen-Strep at regular intervals of 48 hours. Care was taken to withdraw and add the media slowly so as to not perturb 3D-DTM formation. Fresh media was added every 48 hours following cell plating. For 3D-DTM generation on 24 well plates, 400 µL of pre-gel volume was used instead of 40µl. Different co-culture 3D-DTM systems are represented as fibroblast/stromal cells-epithelial cells (e.g. NIH3T3-T24, WPMY-1-T24) to accurately indicate the sequence of their addition. In most cases, 3D-DTMs were formed 5-7 days following culture on Amikagels.

Impact of Amikagel Chemo-Mechanical Properties on Resistance and Dormancy of T24 3D-DTMs.

T24 3D-DTMs were first formed on AM3, and transferred to AM1s on the seventh day following initial cell seeding, in order to investigate the role of chemo-mechanical properties of Amikagels on 3D-DTM fate, dormancy and escape from dormancy. Upon transfer, 3D-DTMs were monitored for cell spreading and motility on the gel for an additional 7 days. After 7 days, cell cycle analysis was carried out on the all 3D-DTMs as described in the previous sections.

Long-term experiments were also carried out where 3D-DTMs were continuously monitored for 15 days after their transfer from AM3 gel to AM1 gel. In order to study the effect of drug treatment, T24 3D-DTMs were first treated with 0-100 µM docetaxel for 96 hours after 7 days of initial seeding of cells on AM3 gel. After 96 hours of this drug treatment, the 3D-DTMs were transferred to AM1 gel to study how different chemo-mechanical properties influenced escape from dormancy. Similar studies were also performed using ROCK inhibitor Y-27632 (20 µM).

10,000 Individual T24 cells were plated on AM1 gel with 0 and 100 µM docetaxel for 24 hours to study the filopodial extensions formed on AM1 gel.

N-cadherin expression on Relapsed and Dormant after relapse cells on AM1

After 15 days of transfer of T24 3D-DTM to AM1, the relapsed cells and the remnant mother 3D-DTM were collected and expanded on fresh 2D cell culture plates. After 48 hours of expansion, 600,000 cells of the two cell populations were collected for N-cadherin surface expression studies. Briefly, the cells were detached from the surface using 20 mM EDTA in ice-cold 1X PBS. After 30 minutes of rocking at 4^{o}C, the cells were collected and blocked with wash buffer (1X PBS containing 2% FBS) for 30 minutes at 4^{o}C. Wash buffer and block buffer were composed of 1X PBS containing 2% FBS. After 30 minutes of washing, the cells were incubated with primary antibody at a concentration of 20 µg/mL in 1X PBS containing 2% FBS at 4^{o}C for 1 hour under gentle rocking. The cells were collected by centrifugation and washed three times, five minutes each in ice-cold wash buffer. The anti-mouse secondary antibody conjugated with Alexa-488 was added to the cells at a dilution of 1:200 for 30 minutes in 1X PBS containing 2% FBS at 4^{o}C followed by three washes. Flow cytometry was performed as described before. N-cadherin expression on cell populations was expressed as mean fluorescent peak.

Dormancy after relapse

Plasticity of relapsed cancer cells was measured by replating them on AM3 after relapse. Cell cycle profile was measured to understand whether the relapsed cells can undergo dormancy upon returning to the mechanically stiff, non-adhesive environment. 100,000 relapsed cells were plated as an overlay culture on AM3 gel. After 7 days of culture, the cell cycle distribution of the cells was estimated via procedure described in the previous chapter.

Statistical Analyses

Averages have been expressed as mean ± SD. The effectiveness of the drug combinations were quantified using the combination index (CI) by Chou-Talalay method. Two-tailed t-test with 95% CI was used analyze and compare the percent cell death data of individual drugs. One-way ANOVA has been used to study the differences between the effectiveness of multiple drugs and their combinations. Tukey's multiple comparisons test was used during multiple pairwise

comparisons whereas Dunnett's multiple comparisons test was used while comparing multiple means to a single one (control). $p<0.05$ indicated significance in the analyses. All analyses were performed using the Prism GraphPad software. All experiments have been performed at least n=2 independent experiments with three replicates each unless specified.

4.3. RESULTS AND DISCUSSION

Cellular escape from tumor dormancy and formation of micrometastasis-like nodules

Escape from dormancy is characterized by return to a more aggressive and proliferating tumor phenotype either at the primary site or at distant metastatic sites, often resulting in patient mortality [32]. Escape of cancer cells from quiescence / dormancy can be facilitated by changes in the microenvironment. Barkan et al. [42] showed that dormancy of quiescent D2.0R breast cancer cells could be reversed by supplementing fibronectin as the extracellular matrix. Fibronectin supplementation induced β1 integrin mediated signaling, which, in turn, led to cell proliferation. Changes in ECM mechanical properties are known to play a significant role in the metastasis of bladder transitional cell carcinoma [168].

We therefore asked if modulation of Amikagel chemo-mechanical properties could induce escape of 3D-DTMs from dormancy. T24 3D-DTMs, generated on mechanically stiff and non-adhesive AM3, were transferred to more adhesive but mechanically weaker AM1, in order to model changes in the tumor microenvironment. T24 cells escaped from the 'mother 3D-DTM' within just 24 hours following transfer to AM1 (**Fig. 4-1A-B**).

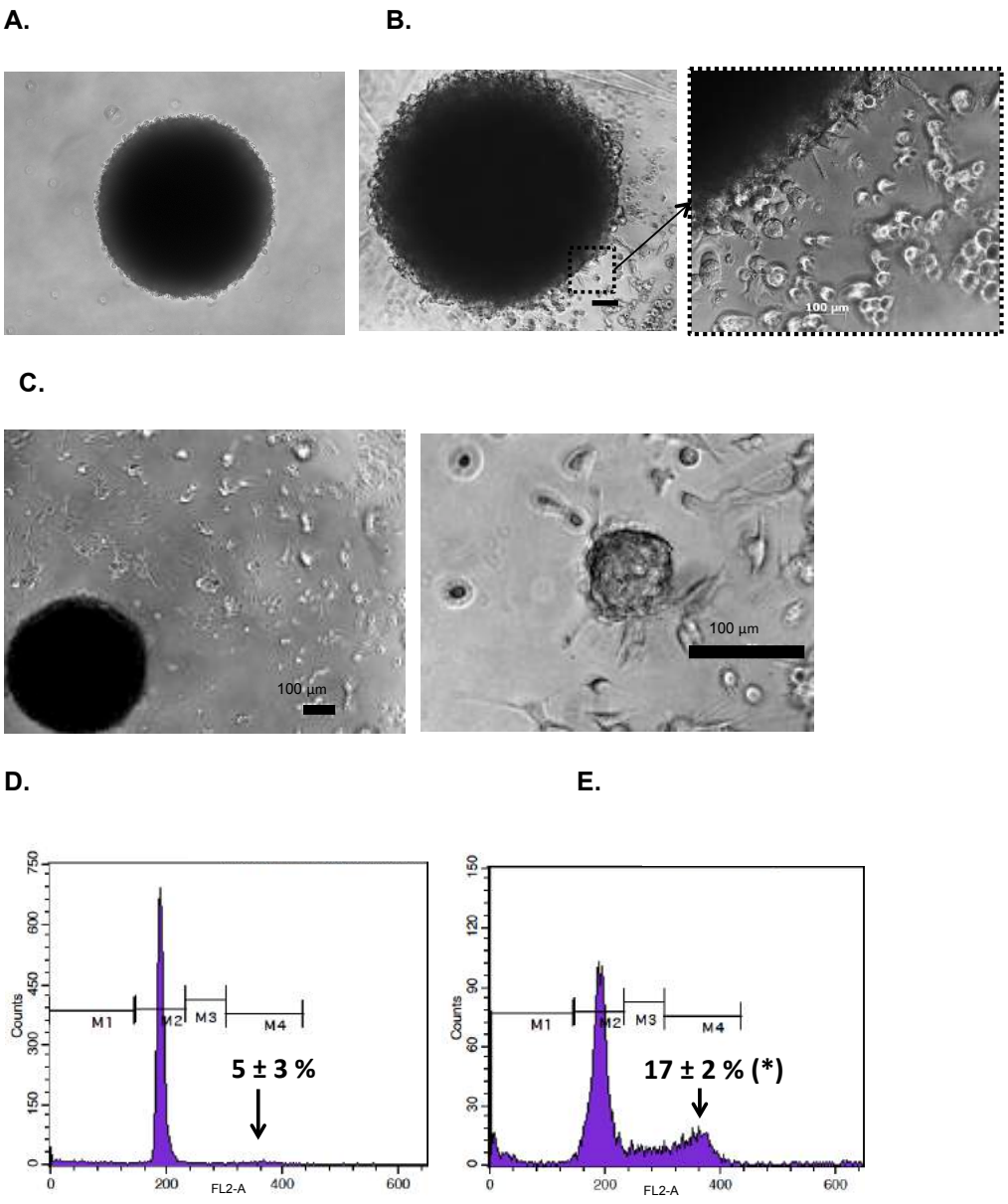

Figure 4-1. Chemo-mechanical engineering of Amikagels induces relapse from dormancy. T24 3D-DTMs were transferred from AM3 to AM1 Amikagels and visualized for changes in morphology. Phase contrast image of the transferred 3DTM at **(A)** Day 0, **(B)**. Day 1, and **(C)** Day 15 after transfer. Following transfer of dormant T24 3DTMs from AM3, cell shedding on AM1 resulted in the formation of microcolonies, 70-100 µm diameter, within 15 days **(C)**. Representative images are shown. Scale bar = 100 µm in all cases. **(D)** Cell cycle distribution indicated that the 'mother' T24 3DTM remained in near-complete arrest in the G0/G1 phase (~90% cells in G0/G1 phase). However, cells that escape the dormant mother 3D-DTM, spread on AM1 and form microcolonies showed a more proliferative profile (17% cells in the G2/M phase compared to 5% G2/M cells in the mother spheroid). * indicates p-value = 0.004 (Student's t-test) for the G2/M populations of escaped cells compared to the dormant mother 3DTM, indicating an actively proliferating population in the shed cells.

However, no cell escape was observed when 3D-DTMs generated on AM3 were transferred onto freshly prepared AM3 instead of AM1, (**Fig. 4-2**), indicating that the different chemo-mechanical microenvironment played a key role in escape of cells. At 15 days following transfer, it was clear that not all cells had left the mother 3D-DTM placed on AM1.

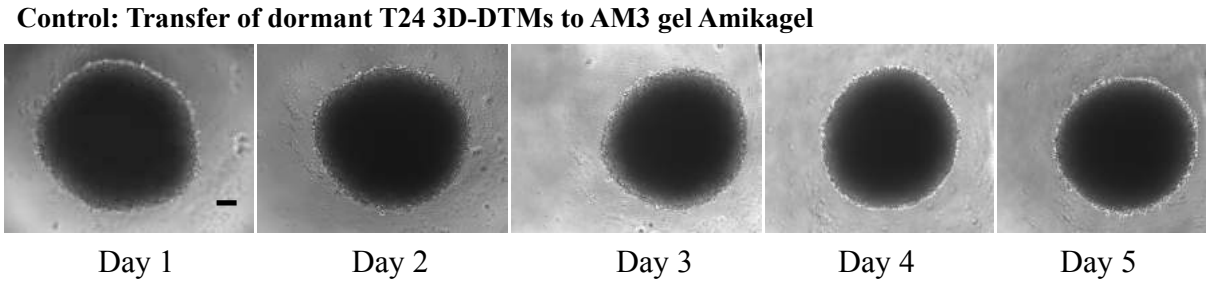

Figure 4-2. Transfer of T24 3D-DTM to AM3 gel did not cause any relapse. T24 3D-DTMs generated on an AM3 did not show any signs of cell spreading and escape when transferred from the 'forming' AM3 to a newly made AM3. Scale =100 μm.

Interestingly, cells that escaped formed micrometastasis-like nodules, 70-100 μm in diameter, on AM1 at significant distances away from the mother 3D-DTM (**Fig. 4-1C**). Cell cycle studies, seven days following transfer, indicated that the 'mother 3D-DTM' continued to remain dormant (**Fig. 4-1D**), while the shed cells (**Fig. 4-1E**) demonstrated increased number of proliferating cells (**Fig. 4-1D-E**). These results clearly show that chemo-mechanical changes in the vicinity of the dormant bladder cancer cells can result in immediate relapse from tumor dormancy, metastases and microcolony formation.

Chemo-mechanical engineering of Amikagels isolates the aggressive and metastatic cell types of the population

We studied the N-cadherin expression on the expanded populations of the mother 3D-DTM and the relapsed cells and found significant differences between them (**Fig. 4-3A**). N-cadherin expression was almost 50% lower in the relapsed cells compared to the cells that remained dormant after relapse (Mother 3D-DTM) (**Fig. 4-3B-C**). Changes in media color was further indicative of active metabolism and proliferation in case of shed cells on AM1, indicating a reversal of these cells from a dormant to proliferative phenotype compared to the mother 3D-DTM (**Fig. 4-3C**).

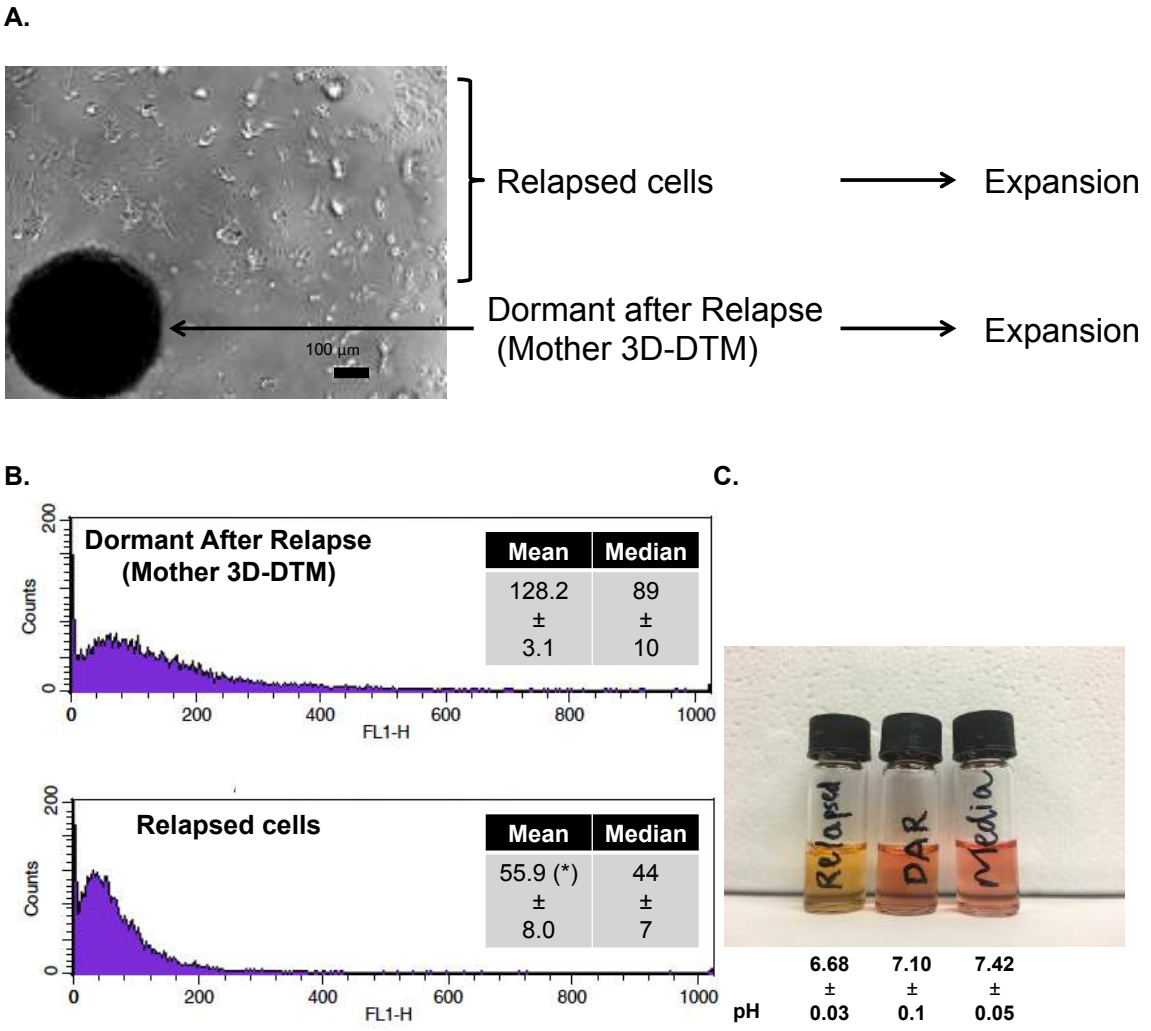

Figure 4-3. Relapsed cells have significantly lower expression of N-cadherin on their surface (A) Relapsed and mother 3D-DTM were collected and expanded after 15 days of transfer. **(B)** Relapsed cells were observed to have lower N-cadherin levels (significantly lower fluorescence) compared to cells that remained dormant after relapse (Mother 3D-DTM). **(C)** Relapsed cells were also observed to actively consume media compared to the expanded mother 3D-DTM cells. * indicates p-value <0.05 (n=2, Student's t-test)

T24 cell line is known to be heterogeneous with a mix of metastatic and non-metastatic cell fractions [47, 51]. Low N-cadherin has been associated with significantly poor prognosis and accelerated death in bladder cancer [58]. Modulating Amikagel's adhesivity allowed for selective migration, isolation and easy recovery of N-cadherin poor population of T24 cells. Highly adhesive substrates such as 2D tissue culture plate caused total invasion and substrate integration of the 3D-DTM, making the recovery difficult. Amikagel's adhesivity was found to be ~40-50% lower than 2D tissue culture plate and hence made it easier only for metastatic cells to

escape (**Fig. 4-4A**). The non-metastatic cells remained together with the mother 3D-DTM allowing for very easy recovery. Transfer of T24-3D-DTM to cell culture treated plate caused mass migration of cells in a cell sheet format, which was very difficult to recover without trypsinization (**Fig. 4-4B**).

A.

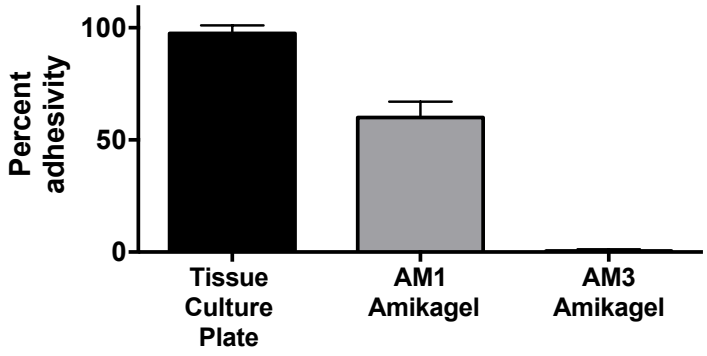

B.

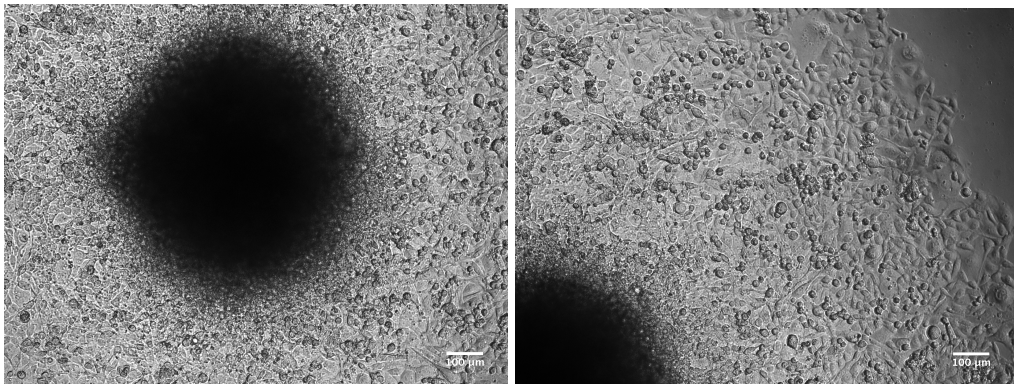

Figure 4-4 Cell migration pattern on 96 well plate tissue culture plastic was significantly different than Amikagel. (A) Qualitative measurement of amikagel adhesivity compared to 2D tissue culture plastic indicated ~40% lower adhesivity **(B)** Transfer of T24 3D-DTM to tissue culture plastic resulted in mass cell migration as cell sheets unlike AM1 which induced selective cell relapse (representative day 5 image). Scale =100 µm

After expansion of the two populations of relapsed cells and the mother 3D-DTM, we also studied their potential to generate 3D-DTM. We observed that both the cell fractions still generate 3D-DTMs with different proportions of cells in the G2/M phase. Relapsed cells had slight but significantly more number of cells in the G2/M phase of the cell cycle on the plate compared to the cells from mother 3D-DTM (**Fig. 4-5**). Easy formation of 3D-DTMs from cells collected after

first round of selection and separation will allow for further iterations of cell separation and purification.

A. **B.**

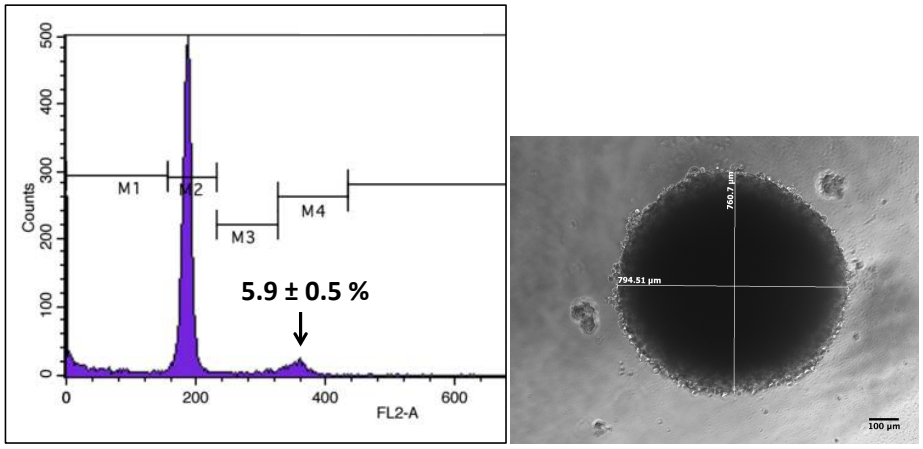

C. **D.**

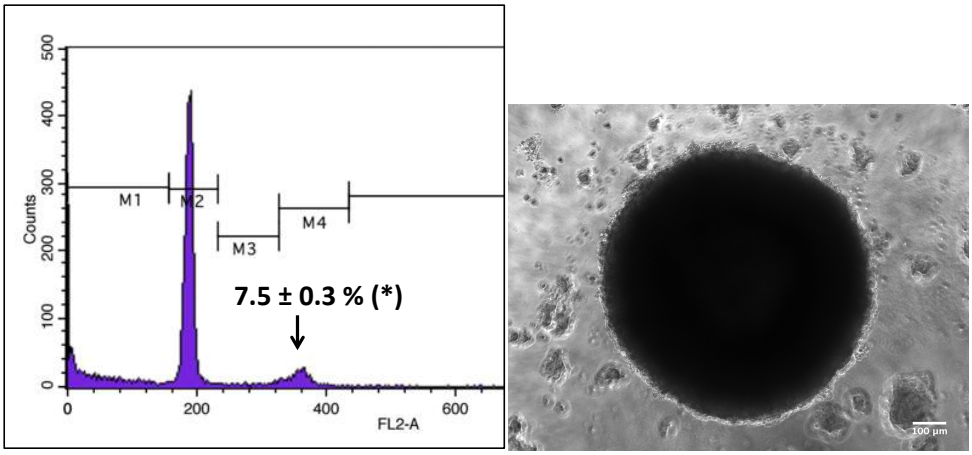

Figure 4-5 Expanded relapsed and mother 3D-DTM cell populations resulted in dormant formation for further enrichment
(A-B) Expanded cell populations from dormant mother 3D-DTMs resulted in dormant spheroids with G0/G1 arrested cell profile. **(C-D)** Expanded cell populations from relapsed cells also resulted in 3D-DTMs with slight difference in the G0/G1 arrested cell profile. 3D-DTMs generated from relapsed cells had significantly higher number of cells in the G2/M phase of cell cycle compared to the 3D-DTMs generated from dormant cells. Scale =100 µm

Here, taking a cue from bladder cancer escape and metastasis following ECM mechanical changes [169], we show that chemo-mechanical modulation of Amikagel can engender relapse of certain cancer cells from dormancy. The relapsed cells demonstrated a proliferative

phenotype, with lower N-cadherin levels and a some of these formed micrometastasis-like colonies on the gel. Gildea et al. showed that the tumorigenic variant of T24 cells formed microcolonies on soft agar and they suggested a paracrine signaling pathway of communication between these cells activated upon mutual contact [47]. These cells also had higher expression of HRAS, lower expression of β-catenin that led to focal adhesion disassembly and invasion. T24 cells are known to be mesenchymal-like, E-cadherin null and contain heterogeneous N-cadherin expression [118], which makes our selective, heterogeneous cell escape and subsequent microcolony formation results unique and very interesting. By modulating the adhesivity of the substrate, Amikagel could induce the migration of only the most metastatic, N-cadherin poor cells, allowing for easy separation and recovery unlike 2D tissue culture plastic.

Further evidence of heterogeneity was evident in Makridakis et al.'s work [51] of generating in-vivo tumors after injecting T24 cells subcutaneously into the flanks of fifteen adult male SCID mice. Of these, only five mice bore tumorigenic outgrowths of T24 cells (~33%). Modulation of Amikagel chemo-mechanical properties likely facilitated the separation of this heterogeneous population into N-cadherin rich dormant and N-cadherin poor relapsed and micrometastases-like colony forming cells. While N-cadherin is a significant prognostic factor in bladder cancer progression, reduction of N-cadherin was found to be associated with enhanced patient mortality rates in multiple cancer including bladder and hepatocellular carcinoma [55, 58, 170]. Selective and easy substrate assisted isolation and recovery of N-cadherin poor metastatic cells significantly improves the clinical relevance of Amikagels in bladder cancer and other metastatic cancers. Chemo-mechanical biomaterial strategies could allow for engineering substrate adhesivities to directly isolate the most metastatic cell types, rather than doing so repeatedly in the mice [171]. For example, a previous research by Nicholson et al.[171] demonstrated a lengthy procedure of isolation and enrichment of highly metastatic fraction of T24 cells by sequential injection into mice over 30-40 weeks. T24 cells were injected into six-week– old NCr nu/nu mice and were allowed to form metastases. The first generation metastatic cells were collected and reintroduced into mice to further enrich the metastatic population and so on. Three generations of enrichment took almost 30-40 weeks. Our engineered adhesivity strategy of metastatic cancer cell isolation can

drastically cut down the time required to do so. We believe our strategy provides a completely synthetic, antibody free method to isolate metastatic fraction of heterogeneous cell populations. Contemporary technologies for metastatic cell isolation utilize antibody or serum coated surfaces that selectively bind the metastatic cells, antibody based flow sorting, differential rolling of metastatic versus non-metastatic cells for specific cell isolation etc [172-175]. Our engineered adhesivity Amikagel substrate can provide a better modality for metastatic cell isolation due to its high chemo-mechanical tunability, ease of preparation, no antibody requirement and easy recoverability of the separated cancer cells.

Taken together, modulating chemo-mechanical properties of Amikagels resulted in 3D models of (1) tumor dormancy, (2) cellular escape from dormancy, (3) formation of micrometastasis-like nodules, and (4) selective isolation of highly metastatic cell fractions using a single completely synthetic platform.

Drugs against relapse and micrometastases formation

Maintaining cancer cells in a dormant state has been investigated as a strategy for avoiding tumor metastasis [176], although eventual relapse from dormancy remains a major concern in this approach. The Amikagel platform can facilitate an investigation into drugs that can inhibit relapse / escape from dormancy. Docetaxel treatment (12.5 μM-100 μM) significantly reduced cellular escape from the mother 3D-DTM (**Fig. 4-6 A-C**), likely due to its ability to inhibit cell migration. Li et al. [177] previously reported that docetaxel reduced the expression of phospho-AKT and phospho-FAK by approximately ~41% and ~34% respectively compared to untreated T24 cells; both AKT and FAK are involved in regulating bladder cancer cell migration [177]. In addition, docetaxel has also been shown to effectively inhibit cdc42, which promotes formation of actin-rich filopodia and their extension prior to cell migration in other cancer cell lines [178-179]. Filopodial extensions were not observed on cells shed on AM1 after T24 3D-DTMs docetaxel treatment (**Fig. 4-6 B-C, Black arrows**). Culture of individual T24 cells on AM1 gel after being treated with docetaxel also showed reduced generation of filopodial extensions (**Fig. 4-7, Black arrows**).

A.

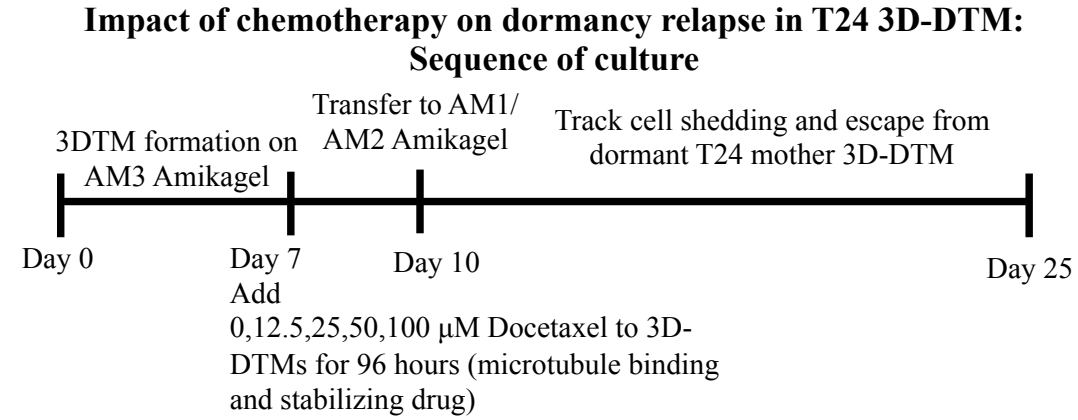

B. **C.**

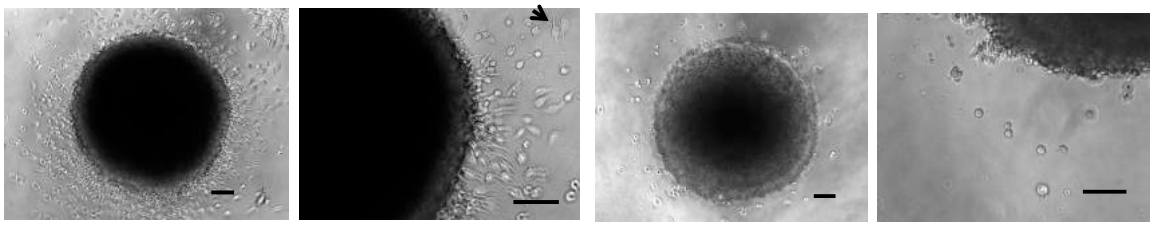

D. **E.**

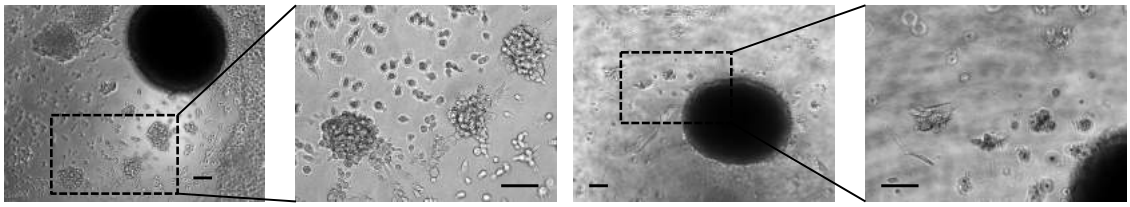

Figure 4-6. Effect of chemotherapeutic drug (docetaxel) treatment on escape from dormancy of T24 bladder cancer 3D-DTMs. (A). Experimental sequence. **(B).** Representative image of dormant T24 3D-DTM grown on AM3 and transferred to AM1; this 3DTM was not treated with docetaxel. Image taken after 48 hours of transfer of dormant T24 3D-DTM to AM1 gel showed significant cell escape from the dormant mother 3D-DTM. **(C).** Representative image of dormant T24 3D-DTM formed and subsequently treated with 100 µM docetaxel on AM3. The pre-treated 3D-DTM was then transferred to AM1. Image taken after 48 hours of transfer of the docetaxel pre-treated dormant T24 3D-DTM to AM1 gel. As seen in the picture, significantly lesser number of cells escaped the mother spheroid after pre-treatment with docetaxel. Microcolony formation in case of **(D)** untreated and **(E)** 100 µM docetaxel pre-treated T24 3D-DTMs after 15 days of transfer to AM1. Docetaxel pre-treatment significantly reduced cell escape and microcolony formation. Scale bar = 100 µm in all cases.

Formation of micrometastasis-like nodules was also drastically reduced following docetaxel-treatment, while untreated 3D-DTMs continued to demonstrate formation of these microcolonies (**Fig. 4-6 D-E**). T24-3D-DTMs treated with docetaxel remained viable and showed a dormant cell cycle profile following treatment, indicating that reduction of cell escape from dormancy is not due to cell death.

A.

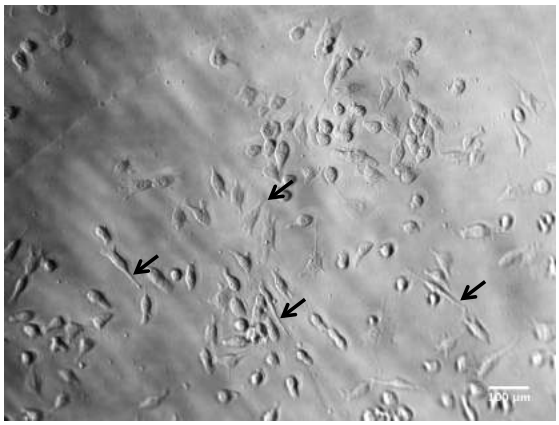

B.

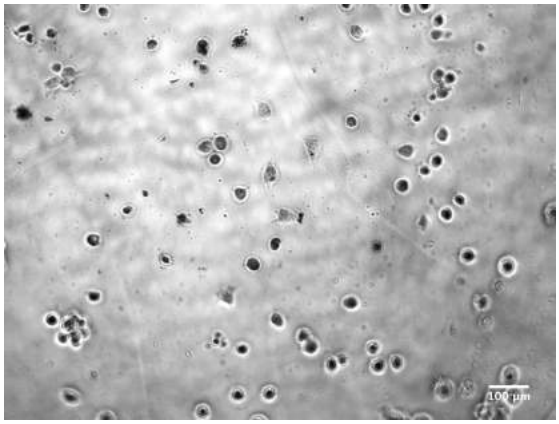

Figure 4-7. Effect of chemotherapeutic docetaxel treatment on filipodial generation in T24 cells. (A). Untreated T24 cells showed significant filopodial formation **(B)** and docetaxel treatment prevented the formation of filopodia resulting in decrease of total filopodial expression. 100 μM docetaxel treated cells on AM1 gel are shown. Scale =100 μm

Cell cycle distribution of docetaxel-treated mother 3D-DTM (**Fig. 4-8**) showed a modest increase of cells in the sub-G0/G1 phase of the cell cycle. This indicates a slight increase in the

number of cells undergoing apoptosis, which is consistent with previous cell viability results observed with docetaxel. No significant differences were observed in cells in the G2/M phase of the cell cycle between the untreated 3D-DTM and docetaxel-treated 3D-DTM (**Fig. Fig. 4-8**). However, the escape of some cells from the mother 3D-DTM after docetaxel treatment and insignificant changes in the viability of the 3DTM are indicative of the challenges in restricting tumors to a dormant state when microenvironment conditions eventually change (e.g. change in adhesivity and / or mechanical properties as in case of transfer from AM3 to AM1).

A.

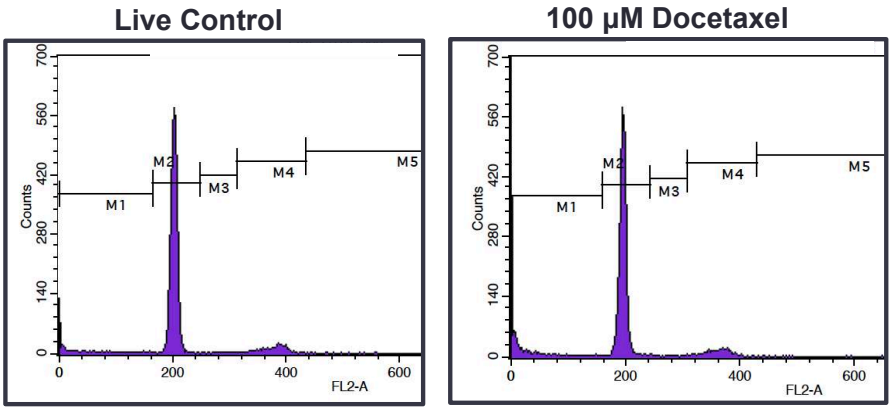

B.

Percent cells	Live T24 3D-DTMs	50 µM Docetaxel Treated T24 3D-DTMs	100 µM Docetaxel Treated T24 3D-DTMs
Pre G0/G1 Phase	12 ± 7.6	22.6 ± 0.55	28.9 ± 5
G2/M Phase	6 ± 1.27	6 ± 0.07	6.24 ± 0.55

Figure 4-8. Cell cycle analysis of T24 3D-DTMs after 96 hours with docetaxel on AM3. (**A**) Cell cycle distribution of T24 3D-DTMs after treatment without and with 100 µM docetaxel for 96 hours (M1 – Pre G0/G1 phase, M2 – G0/G1 phase, M3 – S phase, M4 – G2/M phase, M5 – Multiploid cells). (**B**) Distribution of cells in pre-G0/G1 and G2/M phases after treatment with 0 µM, 50 µM and 100 µM docetaxel for 96 hours.

The Amikagel platform can also lead to the identification of drugs that promote cellular escape from dormancy. Liu. S et al. reported that ROCK inhibitor (Y-27632) could prevent

invasive MCF-7 cell metastases to bone [180]. However, ROCK inhibition was also shown to activate dormant MCF-7 cells into invasion [181]. Treatment of the mother 3D-DTM with the ROCK inhibitor Y-27632 resulted in an increase in the relapse of cells from dormancy upon transfer to AM1 (**Fig. 4-9**), which is consistent with results reported in Yang et al. [181].

A.

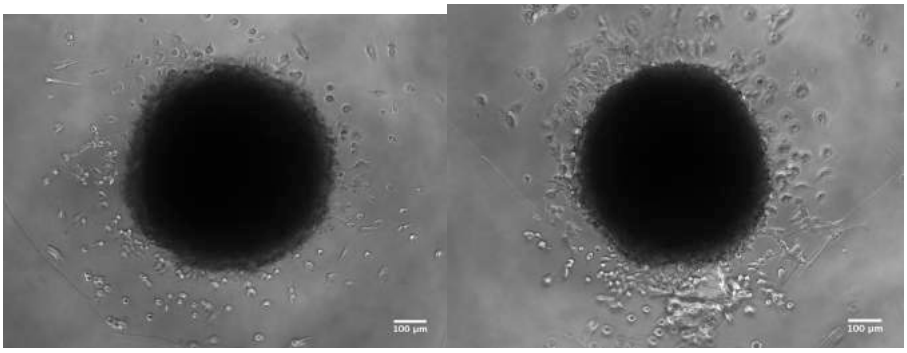

B.

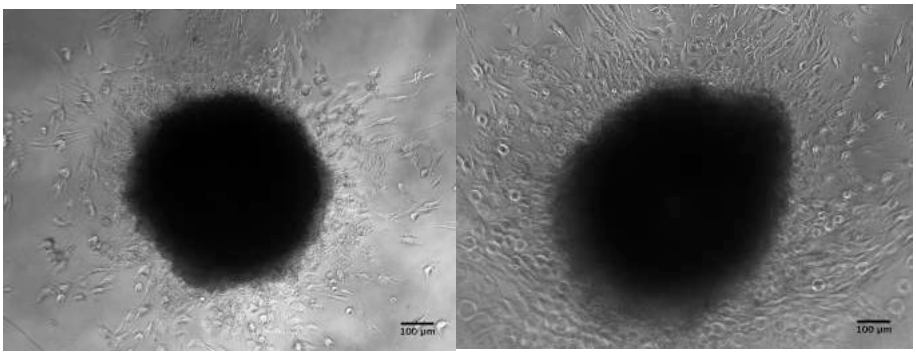

C.

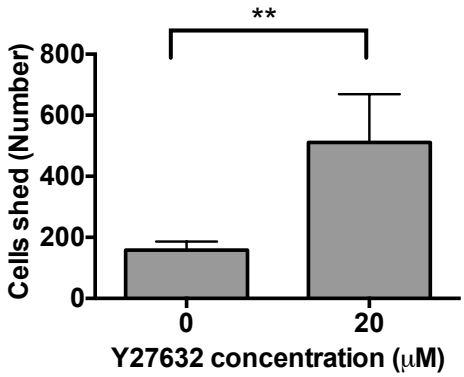

Figure 4-9. ROCK inhibition using Y27632 caused increase in the number of cells that shed from the mother T24 3D-DTM after transfer to AM1 gel. (**A**) Representative images of cells shedding after 3 days of transfer to AM1 gels (No Y27632 treatment). (**B**) Representative images of cells shedding after 3 days of transfer to AM1 gels (20 μM Y27632 treatment). Scale = 100 μm in all cases. (**C**) Treatment with Y27632 showed a significant increase in cell shedding from mother T24 3D-DTM. (p=0.013)

Pre-treatment with the ROCK inhibitor did not change the cell cycle profile of T24 3D-DTMs on AM3 (**Fig. 4-10**). It however, significantly increased the number of cells leaving the

spheroid on AM1 (**Fig. 4-9 A-C**). Use of a conventional anti-proliferative chemotherapeutic (docetaxel) was able to significantly reduce but not completely eliminate escape of cells from dormancy. In contrast, use of a ROCK inhibitor further enhanced relapse from dormancy. ROCK inhibition has been implicated in activating actin depolymerization on the rear end and activating Rac1 leading to the observed increase in migration [182]. We did not observe any changes in the N-cadherin expression after treatment with ROCK inhibitor, which rules out downregulation of N-cadherin expression after ROCK treatment.

A.

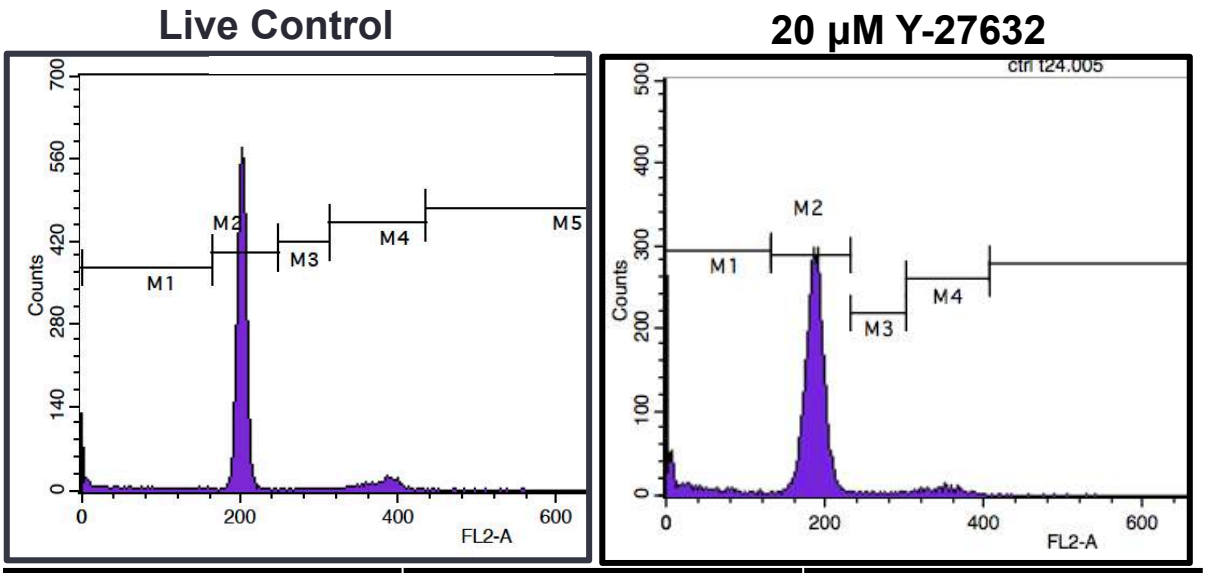

B. Cell cycle phase	Untreated 3D-DTMs	20 µM Y-27632 Treated 3D-DTMs
Pre G0/G1 Phase	12 ± 7.6	23 ± 0.5
G2/M Phase	6 ± 1.27	3.8 ± 0.5

Figure 4-10. Cell cycle analysis of T24 3D-DTMs after 96 hours with ROCK inhibitor Y-27632 on AM3. (**A**) Cell cycle distribution of T24 3D-DTMs after treatment without and with 20 µM Y-27632 for 96 hours (M1 – Pre G0/G1 phase, M2 – G0/G1 phase, M3 – S phase, M4 – G2/M phase, M5 – Multiploid cells). (**B**) Distribution of cells in pre-G0/G1 and G2/M phases after treatment with 0 µM and 20 µM Y-27632 for 96 hours.

Utilizing our high-throughput relapse platform, we showed that common chemotherapeutic docetaxel which could not ablate the dormant cell, worked towards actively

inhibiting the relapse and ROCK inhibitor that has been shown to inhibit cell migration, actually promoted cell escape. Taken together, our results demonstrated the simplicity of the Amikagel platform for studying relapse. We put forth a unique regimen of drugs that are very effective in complete accelerated ablation of dormant cancer cells and significantly inhibit tumor relapse and escape. We believe our hydrogel platform sets the stage for multiple high-throughput studies for the discovery of new drugs that can reduce cancer dormancy, relapse and micrometastasis in future.

4.4. CONCLUSION

Modeling microenvironment changes by changing the chemo-mechanical properties of Amikagels resulted in escape of cancer cells from the dormant 'mother 3DTM'. Shed cells formed micrometastasis-like nodules 70-100 μm in diameter at significant distances from the mother 3DTM, indicating that micro-environment changes can promote reversal of the dormant phenotype, which is consistent with clinical observations. Relapsed cells had significantly lower expression of N-cadherin than cells from mother 3D-DTMs. Engineered Amikagel adhesivity strategies allowed easy isolation of metastatic cancer cell fractions from heterogeneous cancer cell population. Docetaxel pre-treatment reduced while Y-27632 (ROCK inhibitor) enhanced cells shed from the mother 3DTM. Taken together, the Amikagel platform facilitates high-throughput formation of 3DTMs for applications in drug screening and investigations in fundamental tumor biology. This high-fidelity platform can be employed for identifying drugs that can reverse and / or ablate the dormant phenotype, as well as obviate cell escape from dormant tumors, leading to novel discoveries for the clinical management of cancer diseases.

CHAPTER 5: AMINOGLYCOSIDE ANTIBIOTIC-DERIVED ANION-EXCHANGE MICROBEADS FOR PLASMID DNA BINDING AND IN SITU DNA CAPTURE

5.1. INTRODUCTION

Plasmid DNA (pDNA) is being investigated in several applications in biotechnology and medicine, including gene therapy against cancer, AIDS [183-185] and cystic fibrosis[186], DNA based gene vaccinations [187] and in vitro transfections for cellular manipulation[188]. Plasmid DNA molecules are extra-chromosomal pieces of double-stranded DNA[189] which confer selective advantages including antibiotic resistance in bacteria, and can be transferred to other species via horizontal gene transfer [190-191]. In cancer gene therapy, therapeutic plasmids, which code for functional tumor suppressor proteins, are delivered to cancer cells [80]. DNA-based gene vaccinations involve either direct intramuscular / intradermal injection of naked pDNA or lipid-coated delivery of the same to the target tissues [192-193].

Plasmids are usually grown in rapidly dividing Escherichia coli, and can be obtained by employing different downstream purification steps [194]. Anion-exchange chromatography [195], affinity-based chromatography [196], hydrophobic interaction chromatography [197], and size-exclusion and perfusion chromatography [198] have been explored for purification of pDNA. Affinity-based chromatography methods utilize specific interactions between pDNA and surface-immobilized affinity ligands for selective binding [199]. Pseudo-affinity and affinity ligands including arginine and histidine [200], zinc fingers [201], LacI-LacZ moieties [202] and triple helix forming nucleotide sequences [203] have been explored in affinity-based DNA purification approaches. Hydrophobic interaction chromatography (HIC) has also been investigated as a purification step due to differences in hydrophobicities of RNA, proteins, genomic DNA, lipopolysaccharides and pDNA [204-205].

Anion-exchange chromatography is widely used for pDNA chromatography, and relies on electrostatic interactions between the negatively charged backbone of pDNA and positively charged microbeads (resin) [195]. For example, Q Sepharose Fast Flow resins consist of 6% crosslinked solid agarose beads that are approximately ~90 μm in diameter. These resins,

functionalized with quaternary amines, have been used for pDNA binding and purification (~1.3 mg/mL pDNA binding capacity) [84, 206]. In addition, super-porous / macroporous flow-through beads (e.g. POROS 50) combine high surface areas with high capacities for plasmid DNA binding and purification (~10 mg/mL pDNA binding capacity) [84].

We have previously investigated aminoglycosides and aminoglycoside-derived materials for DNA binding and delivery [5, 80, 207]. Here, in this chapter we discuss the synthesis, characterization and evaluation of novel anion-exchange microbeads (Amikabeads) derived from an aminoglycoside antibiotic, amikacin, with an eye towards applications in DNA biotechnology. Microbeads displaying quaternary amine functionalities ('Amikabeads-Q') demonstrated significantly higher pDNA binding compared to parental amikacin-derived microbeads with primary / secondary amine moieties ('Amikabeads-P'). While high salt concentrations were effective in desorbing pDNA from Amikabeads-P, recovery of pDNA from Amikabeads-Q was greatly improved when hydrophobic modifiers (isopropanol) were included in the elution buffer. Finally, Amikabeads were also employed for mammalian cell lysis and concomitant in situ DNA sequestration directly from these cells.

5.2. MATERIALS AND METHODS

Materials

Amikacin hydrate and poly(ethylene glycol) diglycidyl ether (PEGDE) were purchased from Sigma-Aldrich Inc. (St. Louis, MO). Silicone oil and mineral oil were purchased from Acros Organics (Pittsburgh, PA, USA). The surfactant Span-80 was purchased from TCI America (Portland, Oregon). Nanopure water was used for all preparations unless otherwise stated. BD Precision Glide 27G1 ¼ needles and 5 mL syringes were purchased from Becton, Dickinson and Company (Franklin Lakes, NJ). Calcein AM / ethidium homodimer-I Live/Dead stain® was purchased from Life Technologies, (Carlsbad, CA). PC3 human prostate carcinoma cells were purchased from American Type Culture Collection (ATCC; Manassas, VA). Cell culture media - RPMI, Pen-Strep solution: 10000 units/mL penicillin and 10000 µg/mL streptomycin in 0.85% NaCl solution were purchased from Hyclone (Logan, UT). Qiagen Giga kit and Maxi kit (pDNA extraction kits) were purchased from Qiagen Inc. (Alameda, CA).

Preparation of Parental Amikagel microbeads (Amikabeads-P)

Amikabeads-P (P: parental) were generated using the emulsion polymerization method [208]. Amikacin hydrate (100 mg, 0.17 mmoles) was dissolved in 1 ml nanopure water followed by addition of poly(ethylene glycol) diglycidyl ether (PEGDE) in a mole ratio of 1:2 to generate a uniform mixture. The mixture was stirred at 100 rpm and pre-gelled for 4 minutes at 70^{o}C. After 4 minutes, the solution was collected in a syringe and dispensed slowly into a solution of mineral oil and 1% (w/v) Span-80 through 27 G1$^{1/4}$ BD-Precision Guide needle. The mineral oil-surfactant solution was maintained at 65^{o}C throughout the process. Approximately ~500 µL of the pre-gel solution was dispensed into the heated oil phase within 25 minutes under constant stirring of 260 rpm. The beads were allowed to gel for 10 minutes after their addition followed by extensive washing and size measurements

The beads were collected by centrifugation for 10 minutes at 5500 rpm. Oil was washed off the surface of the beads by using a solution of ~1% (v/v) Tween 20 detergent. Following detergent washes, the beads were finally washed multiple times with nanopure water. The particle diameters of Amikabeads-P were measured using phase-contrast microscopy; fifty beads were chosen randomly from each batch and their diameters were recorded. The averaged bead diameter of these samples was used as an indicator of size in subsequent analyses.

Formation of Amikabeads-Q by Quaternization of Amikabeads-P Microbeads

Amines and hydroxyls present in Amikabeads-P were quaternized using glycidyl trimethyl ammonium chloride in an aqueous solution. Excess glycidyl trimethyl ammonium chloride (GTMAC) was mixed with Amikabeads at 200 rpm in nanopure water for 24 hours at 70^{o}C followed by extensive washing [209]. Quaternization was qualitatively confirmed using the ninhydrin assay [80], as well as a fluorescein binding assay [210]. Briefly, commercially available ninhydrin reagent (200 µL) was added to 1 mg of Amikabeads P and Q and incubated at 99^{o}C for 10 minutes, and the color change was visually observed and recorded. For fluorescein binding studies, Amikabeads P and Q were incubated with 1% (v/v) NaOH solution in nanopure water for

20 minutes. Fluorescein sodium (200 µL of 50 mg/mL), in 1% (v/v) NaOH solution (pH > 12) made in nanopure water, was added to both bead samples. The beads were mixed with the fluorescein solution for 10 minutes, and then separated by centrifugation at 5000 rpm for 5 minutes. The beads were extensively washed with 1 mL solution of 1% (v/v) NaOH in nanopure water. The retention of fluorescein dye was visually observed and used as a qualitative indicator of quaternization.

Determination of swelling ratio of Amikabeads

Twenty wet Amikabeads were randomly chosen, and their diameters were measured using phase-contrast microscopy as described before. The volumes of each of these respective beads were calculated based on these diameters. The volumes of the swollen wet beads were denoted as V_{wet}. After this measurement, Amikabeads were allowed to dry at 65^{o}C for 24 hours. Once dry, the diameters of the same beads were measured again, and their volume, V_{dry}, was calculated. The swelling ratio or SR of the beads was calculated as following:

SR = Swollen gel volume/Dry gel volume (v/v)

Determination of Amikabead Amine Content

Amikabeads-P and -Q (1 mg) were freeze-dried and collected as a powder following which, 1 ml nanopure water was added to them. The ninhydrin assay reagent (100 µL) was added to 100 µL of 1 mg/mL Amikabead dispersion. The resulting solution was boiled at 99^{o}C for 10 minutes. The absorbance of the final colored solution was measured at 570 nm. The amine content was determined by comparing the absorbance of the sample solution to a calibration curve generated using glycine standards.

Total surface area and porosity estimation using BET method

Surface area and porosity of Amikabeads were measured via BET nitrogen sorption technique. The water in Amikabeads was gradually exchanged with acetone by suspending the beads in graded acetone series. Once the Amikabeads were soaked in 100% acetone, they were dried

under vacuum before proceeding with the BET analysis. Dry Amikabeads were weighed into analytical glassware and subjected to 35^{o}C temperature for 11 hours under constant purging with ultra high purity (UHP) nitrogen on a FlowPrep 060 Degasser. Once degassed, the sample was connected to the Micromeritics Tristar II 3020 sample port in order to carry out the experiment under vacuum in presence of liquid nitrogen. The porosity and total surface area per mg of Amikabeads were calculated.

Scanning Electron Microscopy of Amikabeads

The surface morphology of Amikabeads was visualized using Field Emission Scanning Electron Microscopy (FE-SEM; Philips FEI XL-30 SEM) at 25kV. Amikabeads were placed on double-sided carbon adhesive tape attached on the aluminum stub, and were sputter-coated with Au-Pt for 120 seconds using E1030 ion sputter. Approximately 8 nm thick Au-Pt coating was deposited on the beads on double carbon adhesive tape. SEM was performed at a voltage of 3 kV.

pDNA binding to Amikabeads

Amikabeads-P (~2 mg) were incubated with 15,000-200,000 ng of pDNA (pGL4.5) in 10 mM Tris-Cl buffer, pH 8.5 (buffer I), for 24 hours at room temperature (25^{o}C) in order to allow pDNA binding to the beads. All Amikabeads were washed with buffer I for 6 hours prior to addition of any pDNA. NanoDrop Spectrophotometer was used to measure the pDNA content in the supernatant after incubation with the beads. The amount of pDNA adsorbed onto the beads was calculated by mass balance. An adsorption isotherm was generated by calculating the amount of pDNA adsorbed on the beads at corresponding equilibrium pDNA concentrations in the supernatant. The isotherm data were fitted to a Langmuir isotherm, in order to determine the maximum binding capacity (Q_{max}) and the binding constant (K) for the Amikabeads. The Langmuir adsorption isotherm equation is shown below:

$$Q_e = \frac{(Q_{max} * K * C_e)}{1 + (K * C_e)}$$

where,

Q_e = The amount of pDNA bound to the Amikabeads at equilibrium (µg/mg)

C_e = Concentration of pDNA in the solution at equilibrium (mg/L)

K = Langmuir adsorption constant. (L/mg)

Q_{max} = Maximum amount of pDNA bound to Amikabeads (µg/mg)

The Langmuir equation was linearized, and $1/Q_e$ vs. $1/C_e$ were plotted in order to calculate Q_{max} from the slope of the curve and the adsorption constant (K) from the intercept.

The effect of increasing salt concentration on the adsorption of pDNA on Amikabeads was also studied; 10 mM Tris-Cl was supplemented with 290 mM NaCl (buffer II), 690 mM NaCl (buffer III), and 990 mM NaCl (buffer IV), and used to allow pDNA to bind to the microbeads. The linear form of the Langmuir adsorption isotherm was used to determine parameters under these high-salt conditions as described below:

$$x = K_e * C_e;$$

where:

x = The amount of pDNA bound to 1 mg of Amikabeads (µg/mg)

K_e = Partition coefficient of pDNA between solution and the adsorbent (Amikabeads) (L/mg**)**

C_e = Equilibrium concentration of pDNA in the solution (mg/L)

In case of Amikabeads-Q, 15,000-400,000 ng of pDNA were added to ~1 mg of the quaternized beads for 24 hours in 200 µL buffer I in order to allow for binding at 25^{o}C. After 24 hours, the static batch binding capacity of the quaternized beads was studied by determining the amount of pDNA adsorbed on to the beads, using procedures similar to those described above. The pH was maintained at 8.5 in all cases.

Visualization of pDNA bound to Amikabeads-P and Q

Amikabeads-P and Q (1 mg) were incubated with 40,000 ng and 200,000 ng of pDNA in 200 µL of buffer I for 24 hours at 25^{o}C respectively. pDNA-Amikabead aggregates were imaged at 10X

magnification using a Zeiss light microscope to measure their size. The average size of aggregates was estimated by measuring their longest length in micrometers.

Fluorescence confocal microscopy was carried out in order to visualize pDNA on the Amikabeads. After incubation of pDNA with Amikabeads for 24 hours at 25^{o}C, 10 μM ethidium homodimer-1 was added to both, Amikabeads-P and Q for 20 minutes. Ethidium homodimer-I is a high-affinity nucleic acid stain that demonstrates high fluorescence upon binding to DNA, while its fluorescence is quenched in aqueous media [211]. After 20 minutes, the beads were separated by centrifugation, and 200 μL of Fluoro-gel with Tris-Cl buffer (Electron Microscopy Sciences, Hatfield, PA) was added to them. The beads were mounted on a glass slide and sealed with nail polish. Ethidium homodimer-I fluorescence was observed using excitation at 514 nm, and the emission was recorded at 628 nm. The control Amikabead samples were prepared in the exact same manner, except that no pDNA was added. Adsorption of pDNA on Amikabeads was determined using Leica SP5 confocal microscopy using a 20X objective.

Desorption of bound pDNA from Amikabeads P and Q

Amikabeads-P (2 mg) were loaded with 15000-100,000 ng of pDNA in buffer I at 25^{o}C, in order to ensure loading in the linear as well as non-linear portion of the adsorption isotherm. The pDNA-loaded Amikabeads-P were first washed with 200 μL of buffer I for 30 minutes before adding the salt solution for desorption. The amount of pDNA desorbed during the wash step was also determined. The amount of pDNA desorbed following addition of salt solutions was determined using absorbance measurements (Nanodrop) after 24 hours of exposure to 1 mL Tris-Cl buffer with 1 M salt (0.99 M NaCl and 10 mM Tris-Cl, pH 8.5) and 1 mL Tris-Cl buffer with 1.3 M salt (50 mM Tris-Cl and 1.25 M NaCl, pH 8.5) with 15% isopropanol at 25^{o}C. The desorption buffers were refreshed after every 24 hours for Amikabeads-P until there was no further pDNA desorption from the beads.

Amikabeads-Q (1 mg) were loaded with approximately 250,000 ng of pDNA in buffer I at 25^{o}C; a lower amount of Amikabeads-Q was used in the desorption experiments due to the higher binding capacities of these materials. pDNA-loaded Amikabeads-Q were first washed with

200 µL of buffer I for 30 minutes before adding the salt solution for desorption. The amounts of pDNA desorbed were determined using absorbance measurements (Nanodrop) after 12 hours of exposure to different desorption buffers at 25^{o}C. These included, 1 mL Tris-Cl buffer with 1 M salt (0.99 M NaCl and 10 mM Tris-Cl, pH 8.5), Tris-Cl buffer with 1.3 M salt (50 mM Tris-Cl and 1.25 M NaCl, pH 8.5), Tris-Cl buffer with 1.3 M salt (50 mM Tris-Cl and 1.25 M NaCl, pH 8.5) supplemented with 15% isopropanol, and Tris-Cl buffer with 1.3 M salt (50 mM Tris-Cl and 1.25 M NaCl, pH 8.5) supplemented with 30% isopropanol. The desorption was also carried out at 50^{o}C using Tris-Cl buffer with 1.3 M salt (50 mM Tris-Cl and 1.25 M NaCl, pH 8.5) supplemented with 15% and 30% isopropanol respectively. The desorption buffers were refreshed after every 12 hours for Amikabeads Q until there was no further pDNA desorption from the beads.

The volume of Amikabead slurry was determined in order to compare pDNA binding efficacies of Amikabeads-P and Q microbeads with those of commercially available pDNA binding resins. It was determined that ~1 mg of Amikabead-Q slurry had a volume of 50 µL whereas 2 mg of Amikabead-P amounted to ~75 µL slurry volume as prepared. The static binding capacities of Amikabeads-P and Q resins were extrapolated to 1 mL of slurry volume, and their binding capacities were compared to commercially available resins. These analyses were carried out in order to enable a back-of-the-envelope comparison of Amikabeads with existing materials.

Agarose gel electrophoresis of the desorbed pDNA

Agarose gel electrophoresis (AGE) analysis was carried out in order to investigate the integrity of the pDNA desorbed from Amikabeads. Briefly, 1 µL pDNA (~200 ng/µL) desorbed from the beads was mixed with 10 µL gel loading dye (IBI 6X gel loading dye), loaded on 1% agarose gel, and run under a potential of 150 V for 30 minutes using 1X TAE buffer (Tris base, acetic acid and EDTA buffer). Qualitative differences between the pDNA stock used for loading on Amikabeads, and pDNA desorbed from Amikabeads P and Q were visualized under ultraviolet light.

Cell viability of PC3 prostate cancer cells after exposure to Amikabeads-P and -Q

Parental (P) and quaternized (Q) Amikabeads (100-500 µg) were added to 10,000 PC3 prostate cancer cells grown in RPMI cell culture media in 96 well plates for 24 hours, in order to first determine their effect on cell viability. After 24 hours, the viability of the PC3 cells was estimated using a colorimetric MTT assay in which, 10 µL of MTT reagent was added to the cells for 3 hours followed by detergent-mediated cell lysis. The absorbance of solubilized formazan crystals was measured at 570 nm and the background absorbance was measured at 670 nm. The resultant absorbance was used as a measure to estimate the cell viability of the PC3 prostate cancer cells.

Viability of PC3 prostate cancer cells following treatment with Amikabeads P and Q was also determined using the Live-Dead assay. 1 µM calcein AM and 2 µM ethidium homodimer-I in RPMI media were added to the PC3 prostate cancer cells for 20 minutes. After 20 minutes, the green fluorescence of calcein was observed using excitation: 485 ± 10 nm and emission: 530 ± 12.5 nm filter, and red fluorescence of nucleic acid bound ethidium bromide was observed using excitation: 530 ± 12.5 nm and emission: 645 ± 20 nm filter.

In situ Sequestration of DNA from Cancer Cells using Amikabeads

Amikabeads-P were used to induce cell lysis of PC3 human prostate cancer cells in order to facilitate extraction of cellular DNA. Amikabeads-P (100-500 µg) were added to 10,000 PC3 cells following seeding for 24 hours on a 96 well plate. After 24 hours of incubation, 2 µM ethidium homodimer-I was added to the cells exposed to the beads as described above. Captured genomic DNA, bound on Amikabeads-P was visualized using fluorescence microscopy using ethidium homodimer-1.

5.3. RESULTS AND DISCUSSION

Generation of Microbeads (Amikabeads) derived from an Aminoglycoside Antibiotic

Aminoglycoside antibiotics including neomycin, streptomycin, kanamycin, apramycin and paromomycin are known to prevent growth of gram-negative bacteria by inhibiting protein synthesis [212]. The mode of action of aminoglycoside antibiotics involves binding and stabilizing 16s rRNA and complexing with 30S subunit of ribosome. This, in turn, inhibits protein synthesis

and causes bactericidal activity [213]. Aminoglycosides possess biocompatible sugar groups as well as multiple amines in the same molecule. Their natural affinity towards nucleic acids, makes them excellent candidates for generating diverse materials in nucleic acid biotechnology [5, 80, 214]. Here, we report the generation of amikacin antibiotic-derived microbeads, 'Amikabeads', as anion-exchange resins for potential use in pDNA purification as well as in situ capture of DNA from mammalian cells [215].

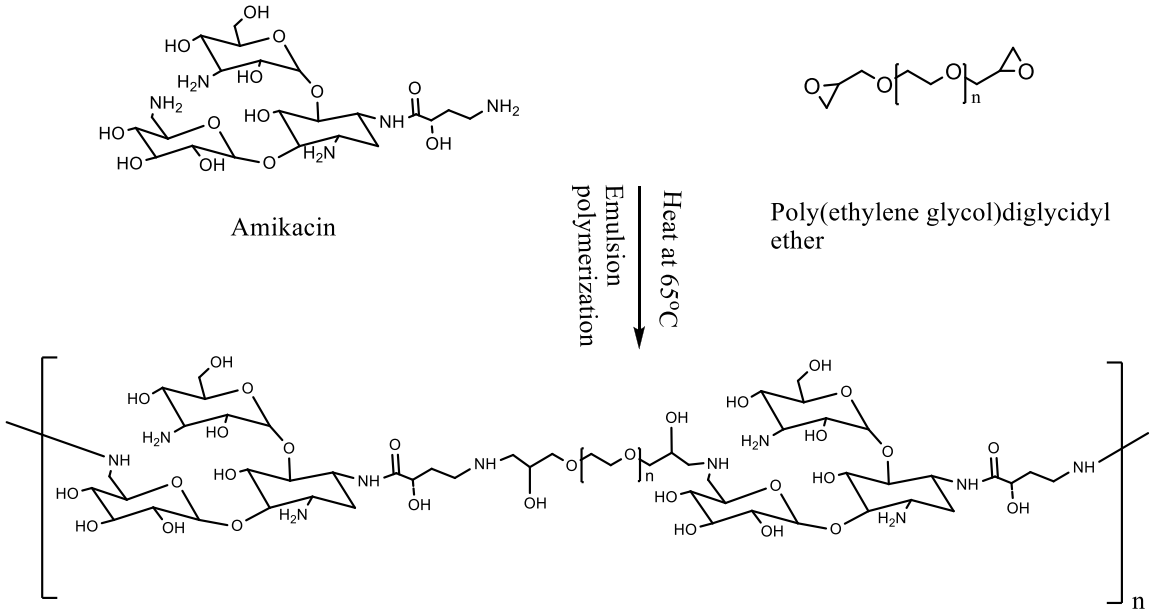

Figure 5-1. Amikagel as micro-resins for pDNA binding. Schematic of the reaction between amikacin hydrate and poly(ethylene glycol) diglycidyl ether (PEGDE), resulting in the formation of Amikagel (hydrogel).

Reaction between amines present in amikacin with the epoxide groups in PEGDE resulted in the formation of a crosslinked hydrogel ('Amikagel') as shown in **Figure 5-1**. It was hypothesized that multiple amines in Amikagel, particularly in the form of microbeads, can be exploited for nucleic acid (pDNA) biotechnology. Parental Amikabeads-P were generated using an emulsion polymerization method (**Figure 5-2 A-B**); a crosslinking ratio of 1:2 amikacin to PEGDE was used.

A.

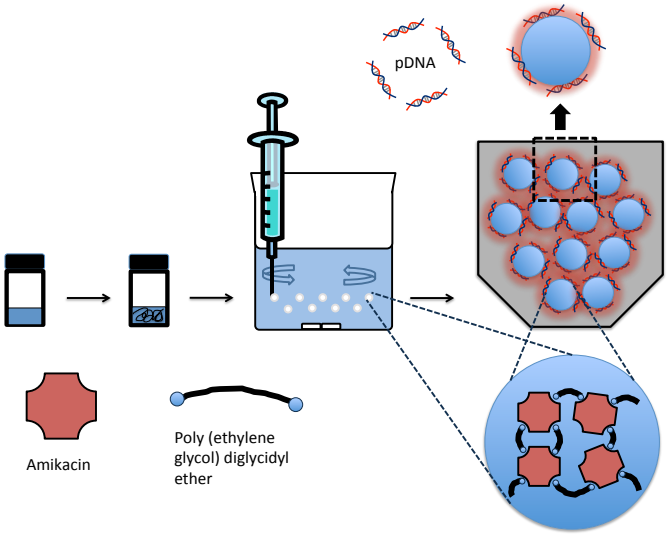

B.

C.

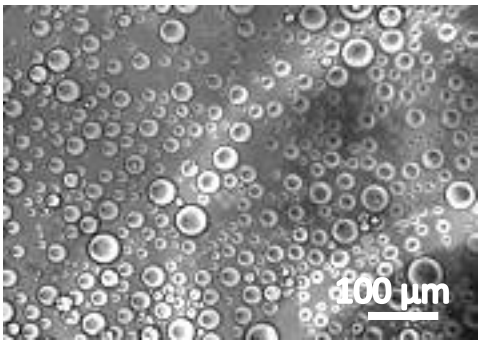

D.

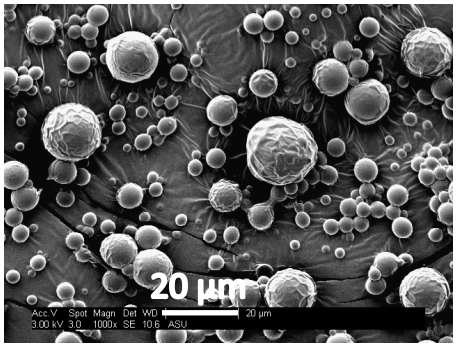

Figure 5-2. Schematic of Amikabead-P synthesis. (A-B) Amikabeads were prepared by pre-gelling the Amikagel solution for 4 minutes at 70°C. The pre-gelled Amikagel solution was added to mineral oil bath supplemented with 1% Span 80 surfactant and maintained at 65°C. **(C)** Phase-contrast image of Amikabeads-P generated after emulsion polymerization of Amikacin-PEGDE in mineral oil-1% Span 80 solution. Scale bar: 100 µm. **(D)** Scanning electron microscopy (SEM) image of Amikabeads indicates spherical particles with an average diameter of ~9 ± 4 µm (calculated over 50 beads).

The amikacin-PEGDE mixture formed a solid hydrogel within ~8 minutes when stirred at 100 rpm at 70^{o}C. Hence, a pre-gelling time of 4 minutes was chosen, following which, the pre-gelled Amikagel solution was introduced into the heated mineral oil phase (65^{o}C, constant stirring at 260 rpm) (**Figure 5-2**). In all cases, mineral oil was supplemented with 1% Span-80 surfactant (w/v) in order to stabilize the water-in-oil microemulsion. Microbeads synthesized in absence of Span-80 were irregular, non-spherical, and appeared aggregated (**Figure 5-3**).

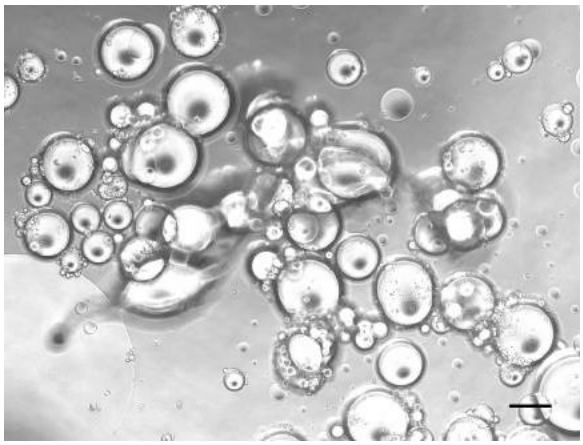

Figure 5-3. **Optical image of Amikabeads-P prepared with silicone oil**. Amikabeads prepared in silicone oil in absence of stabilizing surfactant were irregularly shaped. Scale bar = 100 µm

Amikabeads-P formed in mineral oil were separated from the oil phase by centrifugation at 5000g for 10 minutes following which, the microbeads were extensively washed with nanopure water supplemented with 1% (v/v) Tween 20. Addition of Tween 20 allowed the removal of remaining Span-80 and mineral oil. Tween and Span surfactants are often mixed together in order to generate surfactants of desired Hydrophilic : Lipophilic Balance (HLB) values (Note: An HLB value of more than 10 is necessary in order to ensure surfactant solubility in water). Given the insolubility of Span-80 in water (HLB value of 4.3), Tween-20 (HLB value of 16.3) was added to solubilize and remove any remaining Span-80 and mineral oil [216]. The steps used to generate Amikabeads-P are shown in **Figure 5-2 A-B**.

Characterization of Amikabeads

Shape and Particle Size of Amikabeads

Amikabeads-P generated using the above emulsion system had spherical morphologies and demonstrated minimal aggregation (**Figure 5-2C, Figure 5-3**), although in eventual chromatographic applications, Amikabeads will be tightly packed together as the solid phase. Amikabeads-P were sputter-coated with 8 nm thick coating of Au-Pt in order to visualize them using scanning electron microscopy (SEM). As shown in **Figure 5-2D**, Amikagel-P microbeads had a predominantly spherical shape with smooth as well as rough surface morphology, which is similar to other hydrogel microbeads described previously [217]. The average diameter of Amikabeads-P was ~ 9 ± 4 mm (**Figure 5-2D**), and was dependent on the number of times the mixture of mineral oil and span 80 was used in serial batches. Upon repeated usage of mineral oil and span 80, the diameters of Amikabeads demonstrated a modest increase ($p<0.01$, one-way ANOVA) (**Figure 5-4A**).

A. **B.**

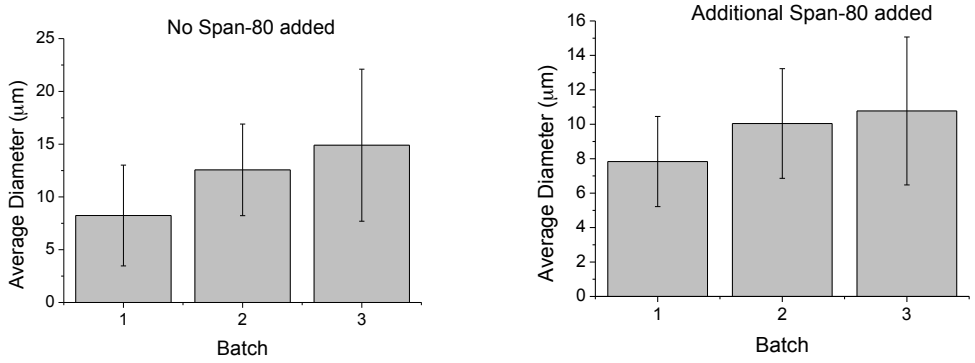

	No Span-80 added	Span-80 added
p–value of One-way ANOVA	0.00162	0.174

Figure 5-4. Amikabeads diameter after emulsion polymerization method of preparation. Average Amikabead-P diameter ± one standard deviation (in microns) of three consecutive batches (**A**) in absence and (**B**) in presence of Span-80. The p-values for the one-way ANOVA test are also shown for n=5 independent experiments.

We hypothesized that introduction of additional fresh Span-80 after every batch of Amikabead synthesis could limit the batch-to-batch variation in the bead size. This supplementation would account for any losses in Span-80 by thermal degradation during the preparation of each batch. As seen in **Figure 5-4B**, the diameter of Amikabeads-P did not change significantly with addition of 400 mg of fresh Span-80 after each batch of preparation. An observed p-value of 0.174 indicated that it is not possible to reject the null hypothesis that particle diameters in all three consecutive batches are the same in **Figure 5-4B** (p-value threshold of 0.05 for statistical significance). Thus, addition of Span-80 indeed reduced the batch-to-batch variation in particle diameter / size. Following this observation, we were able to mix different batches in order to obtain high amounts of Amikabeads-P for subsequent investigations.

Amikabeads-P demonstrated a swelling ratio of approximately 1.74 ± 0.2 (or 174%). This behavior is similar to commercially available anion-exchange resins, which demonstrate swelling ratios of up to 200% [218]. For example, quaternary ammonium group-containing polystyrene-divinylbenzene (PS-DVB) beads, used as strong anion exchange resins, demonstrated a swelling ratio of 1.7, which is very similar to that of Amikabeads [219].

Amine content of Amikabeads

The presence of accessible amine moieties is critical for the use of Amikabeads in anion-exchange applications. Furthermore, presence of reactive amines allows for subsequent conjugation chemistries if required. The reaction of ninhydrin reagent with reactive (primary and secondary amines) results in colorimetric changes; a bluish-purple color can be observed upon reaction with primary amines [220]. Reaction of a 0.5 mm model Amikabead with 100 µL of ninhydrin reagent at 70^{o}C for ten minutes resulted in the formation of intense bluish-purple color throughout the bead (**Figure 5-5**). The amine content of lyophilized Amikabeads-P was estimated to be 1.8 ± 0.3 µmoles of amine per milligram of Amikabeads.

A. **B.**

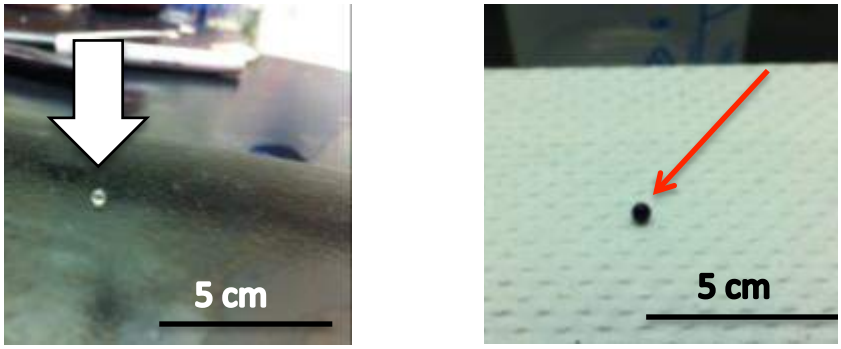

Figure 5-5. **Amikabeads-P ninhydrin assay**. **(A)** Optical image of 0.5 mm model Amikabead-P indicated by an arrow. **(B)** Reaction with the ninhydrin assay reagent resulted in blue-purple color throughout the Amikabead (red arrow), indicating presence of reactive primary amines.

pDNA Binding to Amikabeads-P

The binding of pDNA to Amikabeads-P was determined using batch adsorption assays, in order to determine the potential use of these microbeads as anion-exchange resins. The pGL4.5 luciferase pDNA was used as a model plasmid in all batch binding experiments. The pGL4.5 plasmid codes for luciferase reporter protein, which is commonly used for analyzing the transfection efficacy of various non-viral vectors [221]. A Langmuir adsorption isotherm was used to fit the experimental data and obtain parameters including the maximum binding capacity (Q_{max}) and equilibrium binding constant (K). **Table 5-1A** shows the different parameters generated by fitting the experimental adsorption isotherm data to a Langmuir isotherm; the Langmuir adsorption equation was converted to its linear form in order to determine the Q_{max} value.

Table 5-1. Langmuir adsorption isotherm parameters of plasmid DNA binding to Amikabeads at 25°C

A. Adsorption of plasmid DNA to Amikabeads-P in presence of 10 mM Tris-Cl buffer (pH 8.5) (Buffer I)

ID	Average bead size (µm)	Q_{max} (µg/mg)	K (L/mg)	R-square
1	10 ± 3	56.0	0.01	0.97
2	11 ± 5	46.4	0.02	0.88
3	12 ± 4	31.5	0.05	0.96

B. Adsorption of plasmid DNA to Amikabeads-P in presence of 300 mM Tris-Cl -NaCl buffer (pH 8.5) (Buffer II) and 600 mM Tris-Cl -NaCl buffer (pH 8.5) (Buffer III)

ID	Average bead size (µm)	Salt concentration	K (L/mg)	R-square
Buffer II				
1	12 ± 4	300 mM	13.0	0.63
2	10 ± 3	300 mM	13.2	0.71
3	10 ± 4	300 mM	17.8	0.79
Buffer III				
4	12 ± 6	600 mM	13.8	0.31
5	11 ± 5	600 mM	18.3	0.27
6	10 ± 5	600 mM	21.7	0.49

The average (n=3) maximum adsorption capacity (Q_{max}) calculated by fitting the adsorption isotherm of the Amikagel-P microbeads was approximately 44.5 µg pDNA/mg of Amikabeads-P with an equilibrium constant K of 0.04-0.06 L/mg at an equilibrium pDNA concentration (solution phase) of 300-400 mg/L. Further increasing the concentration of pDNA in the solution phase did not result in any increase in the amount of DNA adsorbed on Amikabeads-P, indicating saturation **(Figure 5-6A, diamonds)**.

A.

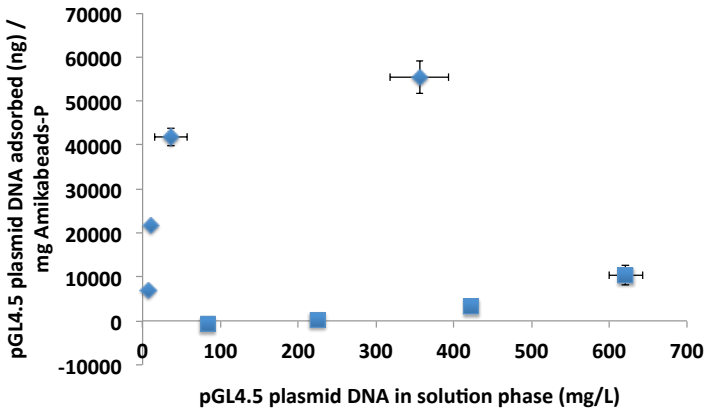

B.

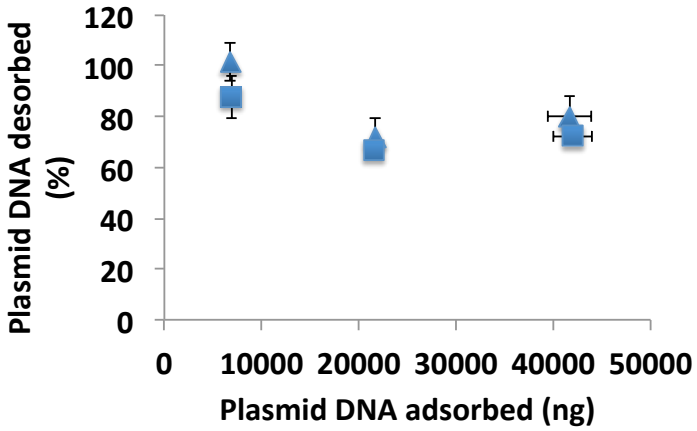

Figure 5-6 Plasmid DNA adsorption and desorption from Amikabeads-P. (A) Isotherm of pGL4.5 plasmid DNA adsorption on Amikabeads-P of diameter 11 ± 4 µm in presence of (Buffer I) 10 mM, Tris.HCl buffer, pH 8.5, at 25°C for 24 hours (diamonds). Maximal adsorption (Q_{max}) = 44.5 µg of plasmid DNA / mg of Amikabeads-P (n=3) (diamonds). Effect of (Buffer II) 0.3 M salt on plasmid DNA adsorption on Amikabeads of average diameter 12 ± 4 µm (squares). Reduced pDNA binding can be observed, indicating that electrostatic interactions drive adsorption.

(B) Desorption of plasmid DNA from Amikabeads-P (1 mg) using Tris-Cl buffer with 1 M salt (0.99 M NaCl, 10 mM Tris-Cl, pH 8.5) after 24 hours (diamonds), and Tris-Cl buffer with 1.3 M salt (1.25 M NaCl, 50 mM Tris-Cl, pH 8.5) supplemented with 15% isopropanol (squares) at 25°C.

pDNA binding to Amikabeads-P was significantly reduced in presence of 0.3 M (buffer II) and 0.6 M salt (buffer III) (**Table 5-1B**). As expected, higher salt concentrations screen electrostatic charges and obviate interactions between negatively charged DNA molecules and the positively charged Amikabeads-P. The saturation amount of pDNA on Amikabeads-P was not calculated under these elevated salt concentrations, since the adsorption isotherm was found to

be in the linear range, even for very high pDNA concentrations in the solution phase (**Figure 5-6A; squares**).

Recovery of pDNA from Amikagels-P bound under low salt conditions (i.e. 10 mM Tris-Cl, pH 8.5) was investigated using Tris-Cl buffer with 1 M salt (0.99 M NaCl and 10 mM Tris-Cl, pH 8.5) and Tris-Cl buffer with an organic modifier (50 mM Tris-Cl and 1.25 M NaCl, with 15% isopropanol, pH 8.5). Approximately 70-100% of originally adsorbed pDNA was desorbed when a salt concentration of 1M was used. No enhancement in desorption was observed when a buffer with higher salt concentration and isopropanol was used (**Figure 5-6B**), indicating that hydrophobic modifiers did not help recovery from Amikabeads-P. Higher percentages of desorption was observed when lesser amounts of pDNA were adsorbed onto the beads, indicating marginal losses in recovery at higher loadings (**Figure 5-6B**).

Quaternization of Amikagel-P beads enhances pDNA binding

Amikacin has 4 primary amines, one secondary amine and 8 hydroxyl groups. It was hypothesized that quaternization of amine groups can help increase the content of positive charges in the microbeads. This in turn, was anticipated to result in enhanced pDNA binding efficacy. The amines on the microbeads were therefore modified to quaternary amines using glycidyl trimethyl ammonium chloride (GTMAC); at neutral or acidic pH, only the amines of the amikacin react with the epoxide group of GTMAC as an addition reaction [209] (**Figure 5-7A**).

A. Amikagel Microbead Quaternization

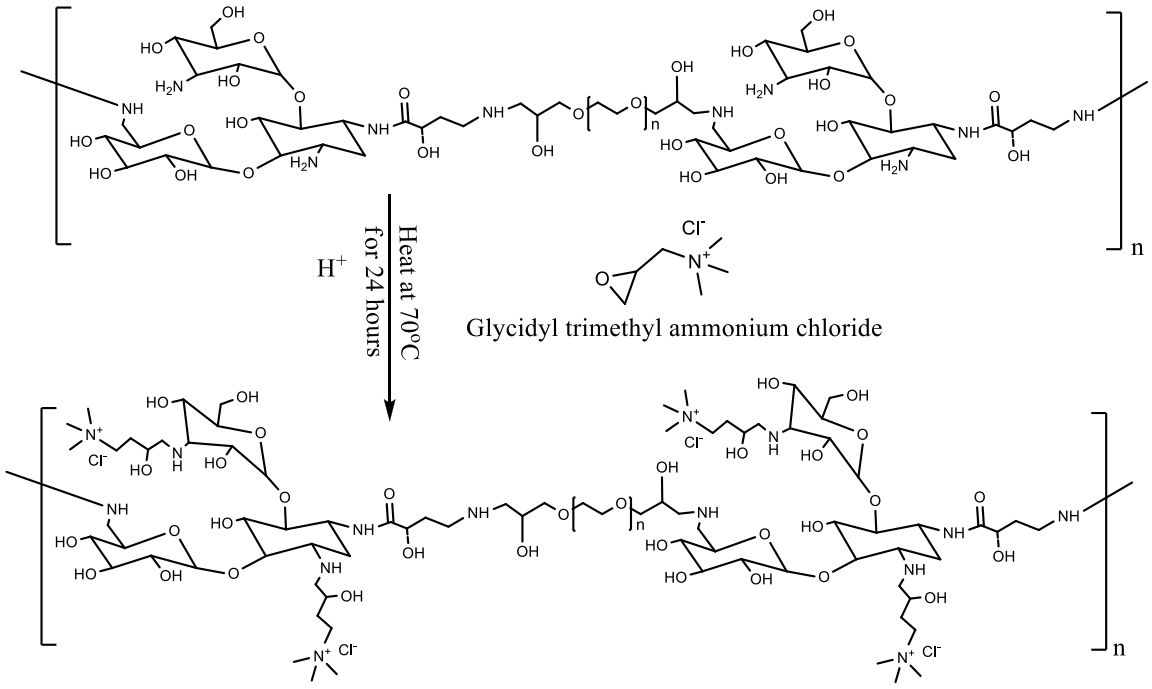

B.

C.

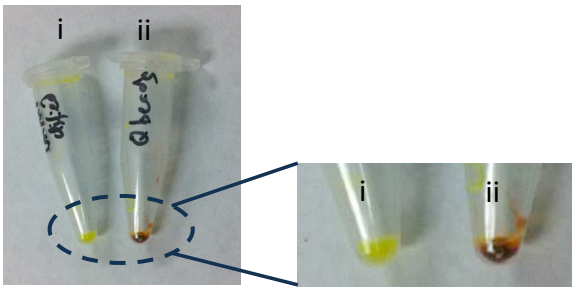

Figure 5-7. Conversion of Amikabeads-P to Amikabeads-Q. (A) Amikabeads-P were reacted with excess glycidyl trimethyl ammonium chloride (GTMAC) at 70°C for 24 hours in order to generate quaternized Amikabeads-Q. **(B)** Ninhydrin test on ~1 mg unmodified Amikabeads-P (left) and quaternized Amikabeads-Q (right) are shown. Formation of blue-purple color indicates presence of reactive (primary) amines. **(C)** Fluorescein binding assay after incubating (i) Amikabeads-P and (ii) Amikabeads-Q with 200 µL of 50 mg/mL of fluorescein sodium in 1% (v/v) NaOH solution (pH>12) in nanopure water for 10 minutes, followed by extensive washing. Formation of intense red color in the pellet indicates increased retention of by Amikabeads-Q, and thus, presence of quaternary amine groups. Lesser retention of fluorescein was observed in the case of the parental Amikabeads-P.

Formation of quaternary amines on Amikabeads was verified using both, the ninhydrin assay as well as the fluorescein-binding assay. Ninhydrin reagent reacts with primary amines resulting in the formation of a blue-purple colored product. However, as expected, quaternized

Amikabeads-Q did not demonstrate a blue color unlike unmodified Amikabeads-P (**Figure 5-7B**). The fluorescein-binding assay was also able ascertain quaternization in Amikabeads-Q; in presence of 1% (v/v) NaOH (pH > 12), the primary amines present on amikacin are no longer positively charged, whereas the quaternary amines on the quaternized beads retain the permanent positive charge. Hence, the negatively charged fluorescein can interact with and bind the quaternary ammonium moieties in Amikabeads-Q, but not the primary amines in Amikabeads-P (**Figure 5-7C**). Adsorption experiments indicated that Amikabeads-Q demonstrated significantly higher ($p<0.001$) pDNA loading capacities than Amikabeads-P (**Figure 5-8 A-B)**.

A.

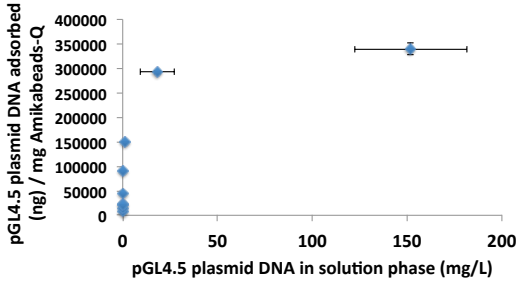

B.

Batch of Amikabeads-Q	Average Diameter (µm) ± 1 S.D (Standard Deviation)	Q_{max} DNA Binding Capacity (µg pDNA bound/mg of beads)
n=1	12 ± 6	333.3
n=2	15 ± 7	277
n=3	10 ± 6	296

C.

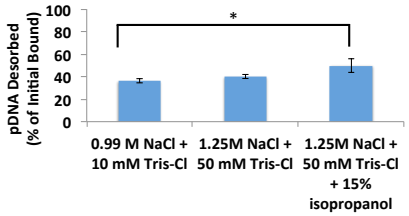

D.

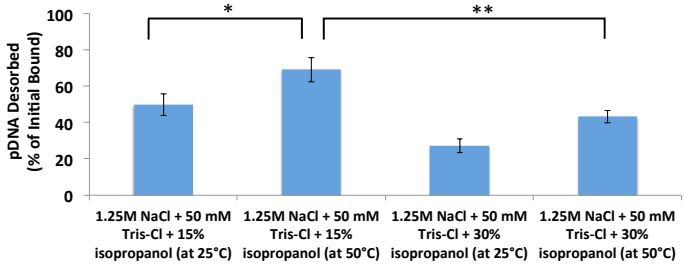

Figure 5-8. Plasmid DNA adsorption and desorption from Amikabeads-Q. (A) Adsorption isotherm of pGL4.5 plasmid DNA on quaternized Amikabeads-Q (Average diameter: 12 ± 6 µm) in (Buffer I) 10 mM, Tris.HCl buffer, pH 8.5, at 25°C following equilibration for 24 hours. Quaternization of Amikabeads greatly enhanced the plasmid DNA binding capacity compared to Amikabeads-Q ($p<0.001$). **(B)** Q_{max} calculated for three independent adsorption experiments in 10 mM, Tris.HCl buffer, pH 8.5, at 25°C. Average Q_{max} calculated for Amikabeads-Q was ~ 300 µg of plasmid DNA / mg of Amikabeads-Q. **(C)** The percentage of bound pDNA desorbed with Tris-Cl buffer with 1 M salt (0.99 M NaCl, 10 mM Tris-Cl, pH 8.5), Tris-Cl buffer with 1.3 M salt (1.25 M NaCl, 50 mM Tris-Cl, pH 8.5) and Tris-Cl buffer with 1.3 M salt (1.25 M NaCl, 50 mM Tris-Cl, pH 8.5) supplemented with 15% isopropanol is shown. Significantly higher desorption of pDNA was observed when isopropanol was used in the eluent ($p<0.05$*, Students' t-test). **(D)** Desorption of pDNA from Amikabeads-Q at elevated temperature (50°C) and higher percentage of isopropanol (30%). Increasing the temperature from 25°C to 50°C significantly improved the amount of pDNA desorbed ($p<0.05$*, Students' t-test) while increasing the percentage isopropanol in the buffer from 15% to 30% had the opposite effect ($p<0.001$**, Students' t-test).

Average Q_{max} values, determined after n=3 independent experiments, were approximately 300 µg pDNA/mg of Amikabeads-Q at an equilibrium pDNA concentration of 150-200 mg/L. This pDNA loading was approximately 30% of the weight of the Amikabeads-Q and is almost 7-fold higher than that on Amikabeads-P. It is likely that the primary amines on Amikabeads-P are only partially protonated at the pH employed in the pDNA binding studies (pH=8.5), while the quaternary amines in Amikabeads-Q have a permanent positive charge[222]. This difference in positive charge content could partly be responsible for higher pDNA binding to Amikabeads-Q compared to Amikabeads-P.

In a recent study by Koga et al. [223], methyl groups on a tetramethylammonium ion were found to promote hydrophilicity at a range of 0-0.08 mole fraction of the solute. Coulombic interactions between the permanent positive charge on Amikabeads-Q and the strongly anionic moieties on pDNA likely overcome the hydration of the hydrophilic quaternary amine groups on the microbeads, and result in strong pDNA-Amikabead-Q binding. Following the primary Coulombic binding, it is possible that multiple methyl groups on Amikabeads-Q participate in collective additional secondary (e.g. hydrophobic) interactions, resulting in enhanced binding to pDNA. However, the hydrophobic character / interactions is likely to be relatively modest in comparison to the high hydrophilic / cationic character imparted by quaternized amines.

Amikabeads-Q demonstrated a slightly higher average diameter than Amikabeads-P (10.8 µm for Amikabeads-P and 13.9 µm for Amikabeads-Q; **Figure 5-9**).

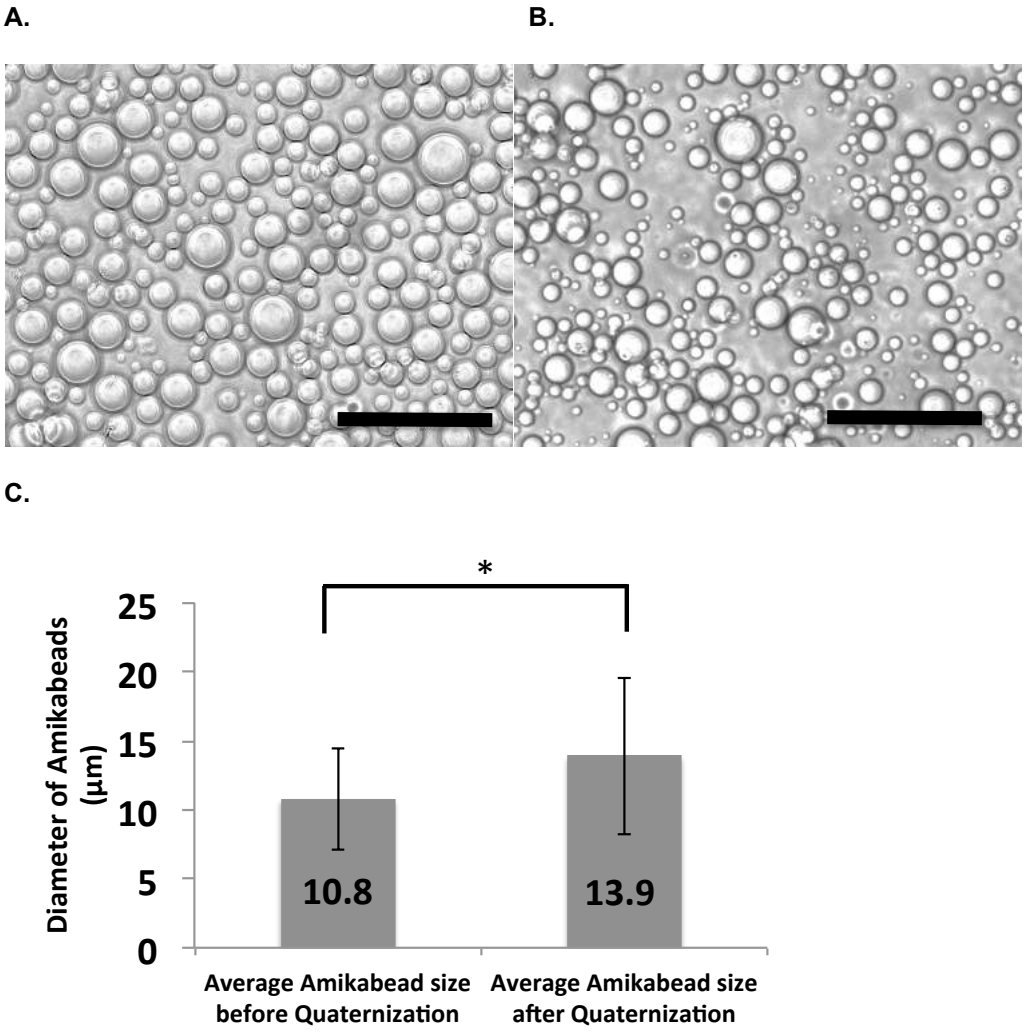

Figure 5-9. Representative images of Amikabeads before and after quaternization. Amikabeads ~11 ± 4 µm in diameter **(A)** before and **(B)** after quaternization using glycidyl trimethyl ammonium chloride (GTMAC) are shown. Scale bar = 100 µm. **(C)** Graphical representation of diameter of Amikabeads-P and -Q. Quaternization did not change the spherical shape, but modestly increased the average diameter of Amikabeads by ~1.3 fold (* indicates $p<0.005$).

This increase in average diameter of Amikabeads-Q could be due to repulsion between the quaternized charges. However, this is likely to have a minimal contribution to the observed increase in pDNA binding capacity of Amikabeads-Q since the increase in surface area over Amikabeads-P is not significant (~1.66-fold increase in Amikabead-Q surface area over Amikabead-P surface area).

Static binding capacities of commercially available resins typically range from 1 to 10 mg of pDNA/mL of resin slurry. Gigaporous rigid ceramic HyperD-Q polymerized hydrogel resins containing quaternary amine moieties and quaternized polyethyleneimine-containing porous resins (POROS HQ resins) possess among the highest static binding capacities at ~10 mg of pDNA/mL of resin slurry [84]. Static pDNA binding capacities of Amikabeads-Q and Amikabeads-P were estimated to be ~6 mg of pDNA/mL of resin slurry and ~1.2 mg of pDNA/mL of resin slurry, respectively, which are comparable to that of several commercially available resins.

Desorption of pDNA from Amikabeads-Q

Up to 40% of bound pDNA was desorbed from Amikabeads-Q when eluted with Tris-Cl buffer containing 1M salt (0.99 M NaCl and 10 mM Tris-Cl, pH 8.5) at 25^{o}C (**Figure 5-8C**). This relative desorption was significantly less in percentage than that from Amikabeads-P. Thus, while Amikabeads-Q were able to bind higher quantities of pDNA, complete recovery of the beads was not possible using 1 M salt as the elution buffer. It is known that addition of small organic molecules to desorption buffers reduces the polarity of the solution, which can facilitate desorption of molecules from resins [224-225]. Improved recovery was seen when Tris-Cl buffer containing 15% isopropanol (1.25 M NaCl and 50 mM Tris-Cl, pH 8.5) was employed for pDNA desorption at 25^{o}C (**Figure 5-8C**). However, use of 1.25M NaCl did not enhance desorption of pDNA from Amikabeads-Q in absence of isopropanol (**Figure 5-8C**), indicating that the hydrophobic modifier was important for pDNA recovery from Amikabeads-Q. It is important to note that use of 15% (v/v) isopropanol did not enhance pDNA desorption from Amikabeads-P (**Figure 5-6B**) indicating that secondary hydrophobic interactions did not play a role in pDNA binding to the parental microbeads.

We observed that while use of 15% isopropanol (v/v) in the elution buffer signficantly enhanced desorption of pDNA from Amikabeads-Q, use of 30% isopropanol resulted in lower pDNA desorption from the microbeads **(Figure 5-8D)**. Our results are consistent with previous observations in the literature. For example, Chang et al. [226] reported higher pDNA desorption from a substrate modified with tetraethyl quaternary ammonium groups in presence of ~20%

isopropanol (v/v), when compared to ~40% isopropanol (v/v). Tseng et al. [225, 227] suggested the existence of a threshold volume percentage up to which, presence of an alcohol in the liquid phase can help overcome hydrophobic interactions while not greatly influencing the solution dielectric constant. This, in turn, allows for increased desorption of an adsorbed molecule from the surface, as seen in case of pDNA desorption from Amikabeads-Q when 15% isopropanol was used in the desorption buffer. Once this threshold is crossed, increased alcohol content in the desorption buffer results in an increase in the dielectric constant of the liquid phase. This, in turn, can strengthen the magnitude of electrostatic interactions between a biomolecule and the adsorbent material. This is likely the cause for lower pDNA desroption from Amikabeads-Q when 30% isopropanol was employed in the liquid phase desorption buffer.

Finally, pDNA desorption was significantly increased when the temperature was raised from 25^{o}C to 50^{o}C ($p<0.001$) **(Figure 5-8D)** in presence of 15% isopropanol; a recovery of ~ 70 ± 6% of initially adsorbed pDNA was obtained at 50^{o}C. Higher temperatures are known to facilitate increased desorption of pDNA from chromatographic columns [228], and our results are along expected lines. The quality of the recovered pDNA from the unmodified Amikabeads-P and the quaternized Amikabeads-Q was determined by running it on a 1% agarose gel. As shown in **Figure 5-10**, the desorbed pDNA recovered by the addition of salt was of the same integrity as that of the pDNA that was loaded on the resin, indicating that Amikabeads did not induce any visible or gross damage to pDNA.

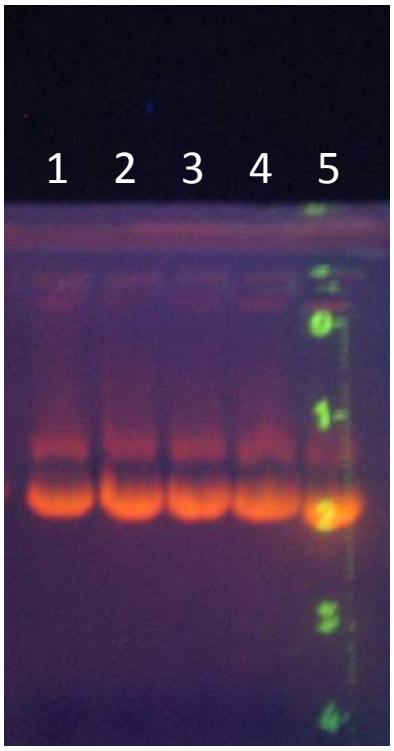

Figure 5-10. Agarose gel electrophoresis of desorbed and recovered pDNA. Agarose gel electrophoresis (AGE; 1% agarose gel) of desorbed plasmid DNA recovered from unmodified parental (P) and quaternized (Q) Amikabeads. Vertical Lanes 1 and 2 – Plasmid DNA desorbed from quaternized Amikabeads-Q (n=2). Lanes 3 and 4 - Plasmid DNA desorbed from unmodified Amikabeads-P (n=2). Lane 5 – Stock solution of plasmid DNA used in the binding studies. No visible differences can be seen between the desorbed pDNA and the stock pDNA, indicating that gross integrity of pDNA is maintained upon binding and desorption from Amikabeads P and Q.

Visualization of Amikabeads before and after pDNA Binding

Confocal fluorescence microscopy was employed in order to visualize the localization of pDNA on the Amikabeads upon binding. As shown in **Figure 5-11**, pDNA was predominantly found to adsorb on the surface of both, Amikabeads-P and -Q.

A.

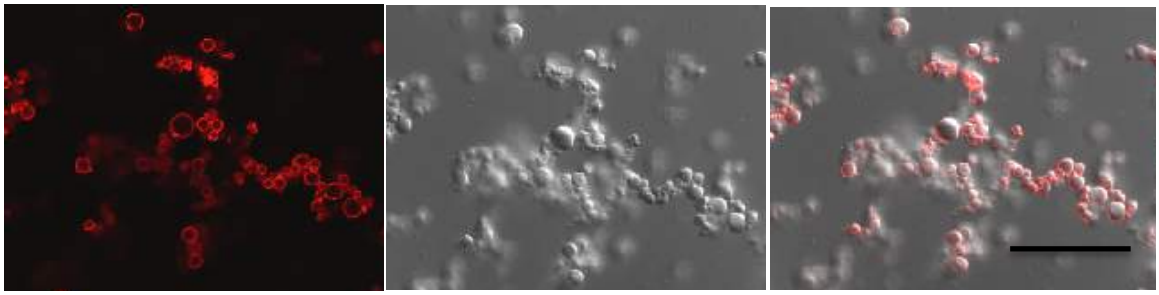

B.

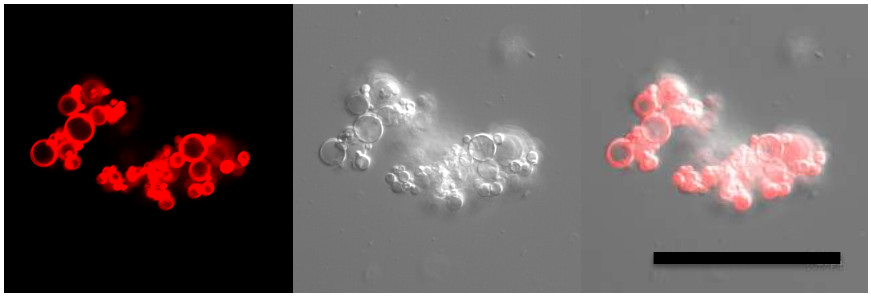

C.

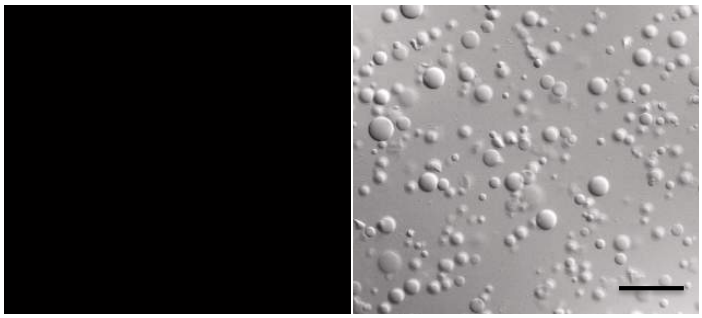

Figure 5-11. Confocal microscopy of pDNA loading on Amikabeads. Confocal microscopy of pDNA loading on **(A)** Amikabeads-P (average diameter: ~9 ± 4 μm) and **(B)** Amikabeads-Q (average diameter: ~14 ± 6 μm) is shown. Amikabeads-P and Q (1 mg each) were incubated with 40,000 ng and 200,000 ng of pDNA respectively, in 10 mM Tris-Cl buffer, pH 8.5 at 25^{o}C for 24 hours. Following washes, the beads were stained with 2 μM ethidium homodimer-1 for 20 minutes prior to imaging. Fluorescence of ethidium homodimer-1 was visualized using an excitation of 528 nm and emission of 617 nm (red color). Plasmid DNA adsorbed on the surface of both, Amikabeads-P and Q, with minimal penetration into the beads. Amikabead clusters were observed after addition of plasmid DNA, possibly due to the bridging. **(c)** Amikabeads not treated with pDNA did not demonstrate ethidium homodimer-1 fluorescence and clustering. A representative image of Amikabeads-Q is shown. Scale bar = 100 μm in all cases.

BET analysis indicated that Amikabeads-P possessed a surface area of approximately 2.0 m^2/g and a pore size of 4.0 nm. This pore size is consistent with that of several existing ion-

exchange resins, but indicates challenges that may be associated with pDNA transport and penetration into the beads, given the larger size (70-100 nm) of super-coiled pDNA [229]. These results can explain the observation that pDNA binding is primarily observed on the surface of Amikabeads.

Amikabeads-P and -Q were found to aggregate following binding of pDNA on their surfaces, likely due to bridging of the biomacromolecule and the beads (**Figure 5-11 A-C**). It is important to note that pDNA loading was in the non-linear part of the adsorption isotherm in both cases. Neither Amikabeads-P nor Amikabeads-Q were found to aggregate in absence of pDNA loading (**Figures 5-2, 5-9,** and **5-12 A-B**). The average aggregate size of pDNA with Amikabeads-Q was significantly higher than that of Amikabeads-P ($p<0.001$, Students' t-test; **Figure 5-12 C-E**). It is likely that the higher cationic content on Amikabeads-Q allows the formation of bigger aggregates upon pDNA binding, compared to those seen in case of Amikabeads-P.

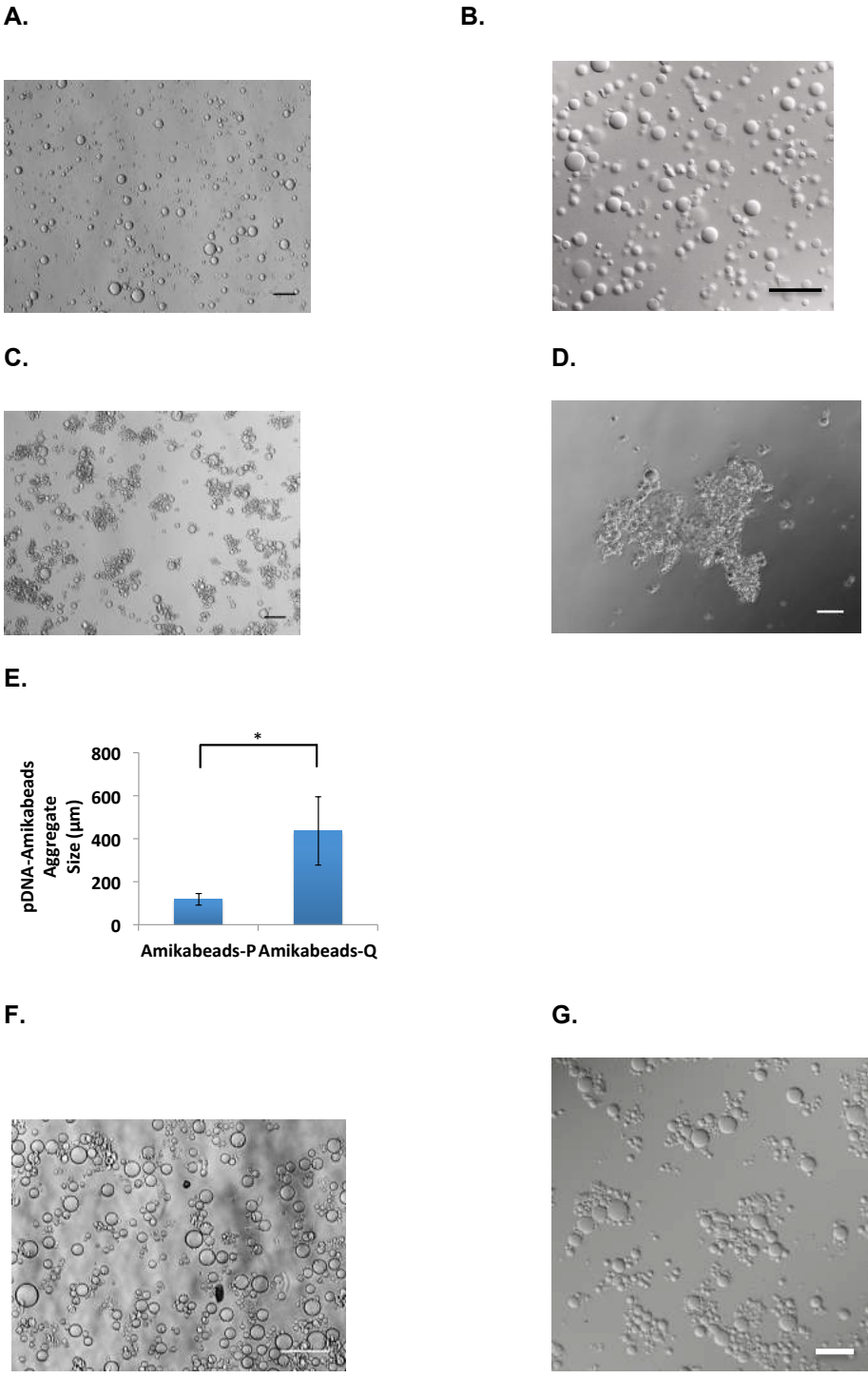

Figure 5-12. Optical image of (A,C) Amikabeads-P and (B,D) Amikabeads-Q before and after loading with **(C)** 40,000 ng and **(D)** 280,000 ng of pDNA/mg of beads respectively. **(E)** Comparison of average aggregate sizes of Amikabeads P and Q after loading with pDNA. pDNA-Amikabeads-Q aggregates were significantly bigger than pDNA-Amikabeads-P aggregates (*$p<0.001$, Students' t-test). Optical images of **(F)** Amikabeads-P and **(G)** Amikabeads-Q after desorption with Tris-Cl buffer with 1 M salt (10 mM Tris-Cl, 990 mM NaCl, pH 8.5) and Tris-Cl buffer with 1.3 M salt (50 mM Tris-Cl, 1.25 M NaCl, pH 8.5) respectively. Scale bar = 100 µm.

Desorption of pDNA from both, Amikabeads-P and -Q, resulted in a decrease in aggregate size (**Figure 5-12 F-G**), likey due to reduction in bridging between the biomacromolecule and the microbeads. Larger aggregate sizes were seen in case of Amikabeads-Q compared to Amikabeads-P following desorption of pDNA. This is likely due to differences in the initial amounts of pDNA present on the microbeads, as well as in the amounts of pDNA desorbed in both cases. As described before, lower relative amounts of pDNA were desorbed from Amikabeads-Q compared to that from Amikabeads-P (~40% of initially adsorbed pDNA for Amikabeads-Q vs. ~75% of initially adsorbed pDNA for Amikabeads-P using 1 M salt). It is also possible that desorption is more challenging from Amikabeads-Q given the larger size of the aggregate first formed upon pDNA adsorption on these microbeads comapred to pDNA-Amikabead-P aggregates. This, in turn, can contribute to the higher aggregate sizes observed for Amikabeads-Q compared to those for Amikabeads-P seen after pDNA desorption (**Figure 5-12 F-G**).

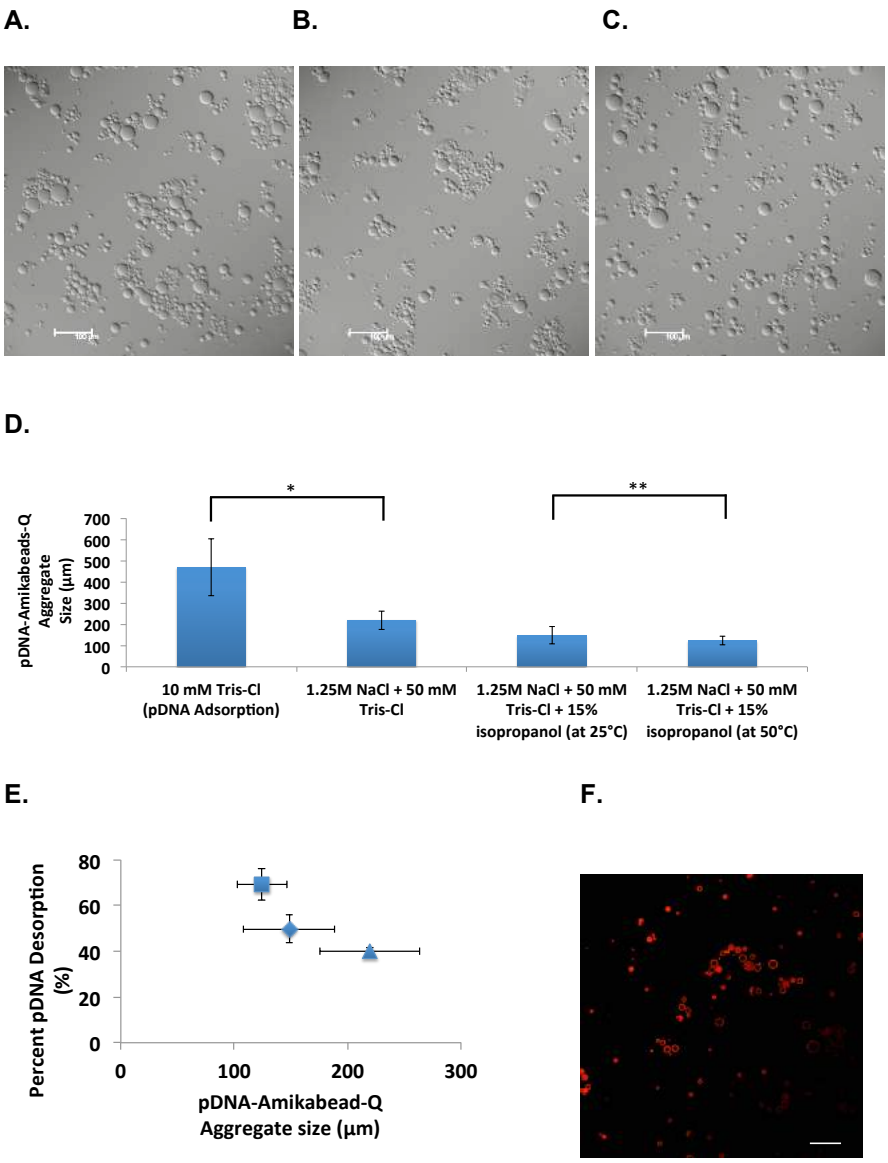

Figure 5-13. Amikabead aggregate size after desorption. Phase contrast images (10X zoom) of Amikabeads-Q loaded with 280,000 ng of pDNA/mg of beads treated with different desorption media **(a)** Tris-Cl buffer with 1.3 M salt (50 mM Tris-Cl, 1.25 M NaCl, pH 8.5) **(b)** Tris-Cl buffer with 1.3 M salt (50 mM Tris-Cl, 1.25 M NaCl, pH 8.5) supplemented with15% isopropanol in absence and **(c)** presence of elevated temperature (50^{o}C) for 36 hours. **(d)** Average aggregate size of pDNA-Amikabeads-Q measured before and after treatment with different elution media. Average sizes of aggregates decreased following pDNA desorption (*$p<0.001$). Equilibration with 15% isopropanol at elevated temepratures (50^{o}C) significantly decreased the aggregate size (**$p<0.05$), whch was consistent with highest amounts of pDNA desorption seen under these elution conditions. **(e)** pDNA-Amikabead-Q aggregate size decreased with increasing desorption of the biomacromolecule from the microbead surface using different desorption buffers. Triangle: Tris-Cl buffer with 1.3 M salt (50 mM Tris-Cl, 1.25 M NaCl, pH 8.5) ; Diamond: Tris-Cl buffer with 1.3 M salt (50 mM Tris-Cl, 1.25 M NaCl, pH 8.5) supplemented with 15% isopropanol in absence and Square: in presence of elevated temperature (50^{o}C) **(f)** Undesorbed pDNA was found to be bound to the surface of Amikabeads-Q after desorption. Scale bar = 100 µm.

Sizes of pDNA-Amikabead-Q aggregates following equilibration with different elution bufferes were further investigated. (**Figure 5-13 A-D**). It was observed that, in general, the size of pDNA-Amikabead-Q aggregate decreased with increasing desorption of the biomacromolecule from the bead surface (**Figure 5-13E**). Plasmid DNA that was not desorbed remained bound to the surface of Amikabeads (**Figure 5-13F**). It is important to note that this colloidal aggregation behavior may be moot in cases of well-packed chromatographic columns that may employ Amikabeads as the stationary (solid) phase for biomolecule (e.g. pDNA) separations.

In situ capture of DNA from Mammalian Cells

Cationic microparticles and membranes have been previously used for on-site capture of genomic DNA for polymerase chain reactions [230]. For example, Cao et al. [231] reported chitosan coated beads that could extract DNA from lysed whole blood sample for PCR analyses. Here, we investigated if Amikabeads-P and -Q could be employed for extracting DNA directly from mammalian cells. PC3 human prostate cancer cells were incubated with different amounts of Amikabeads-P and -Q in order to investigate their effect on viability following cell lysis; we hypothesized that direct lysis mediated by the microbeads can facilitate extraction of DNA from cells. Amikabeads-P (500 µg, 24 hour incubation) resulted in loss of viability of ~80% of the cell population, as determined by the MTT assay (**Figure 5-14A**, diamonds). The LC_{50} (amount required to reduce cell viability to 50%) value of Amikabeads-P was approximately 400 µg for PC3 prostate cancer cells under these experimental conditions.

A.

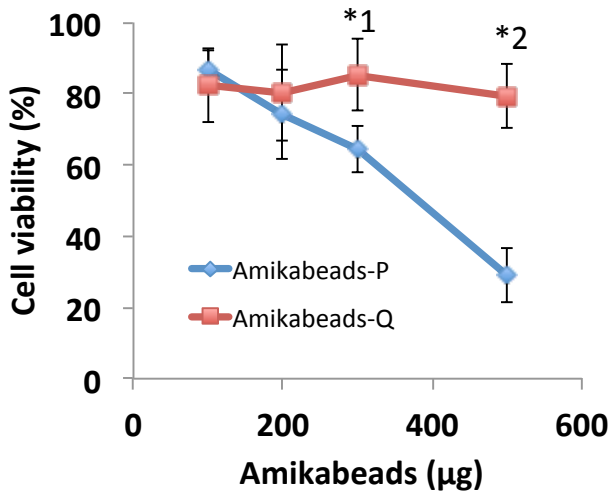

B.

C.

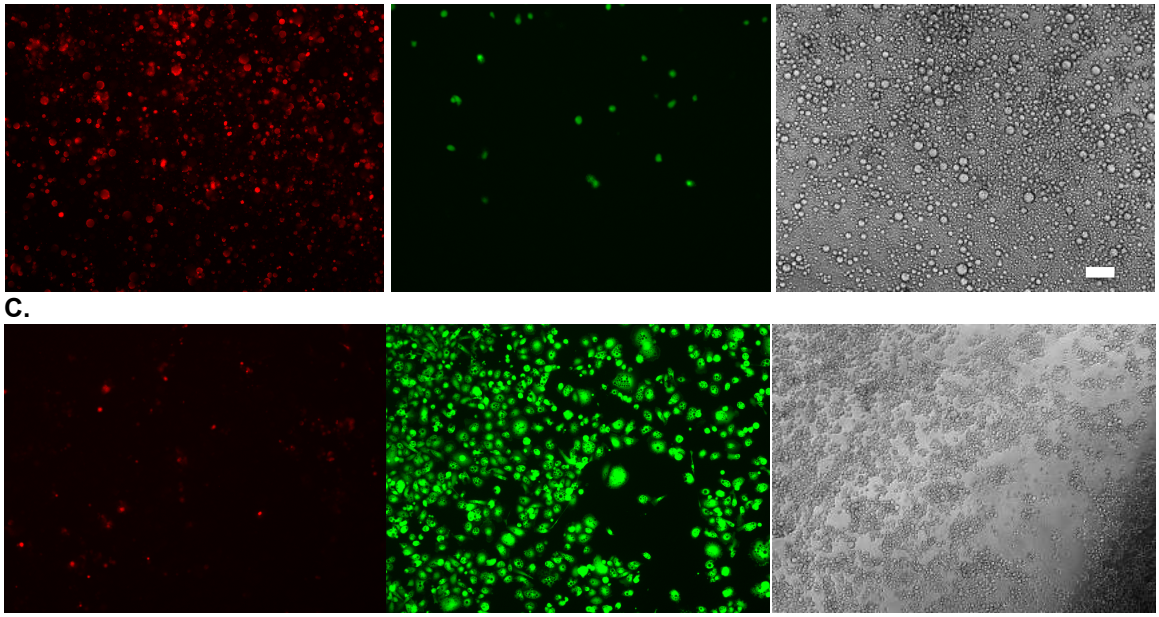

Figure 5-14. Whole cell DNA isolation with Amikabeads. (A) Cell viability of PC3 human prostate cancer cells after exposure to different amounts of unmodified and quaternized Amikabeads for 24 hours as determined using the MTT assay (n=2). *1 – statistical significance p=0.003 between cell viability of cells exposed to 300 µg Amikabeads-P and Q. *2 – statistical significance p=0.00002 between cell viability of cells exposed to 500 µg Amikabeads-P and Q. Amikabeads-P (approximate diameter: ~12. ± 4 µm) and Amikabeads-Q (approximate diameter: ~11 ± 6 µm). Students' t-test was used to determine statistical significance. **(B)** Amikabeads-P (500 µg; approximate diameter: ~12 ± 4 µm) and **(c)** 500 µg Amikabeads-Q (approximate diameter: ~11 ± 6 µm) were exposed to 10,000 PC3 prostate cancer cells for 24 hours followed by live (green)-dead (red) staining. Scale bar = 100 µm. Green fluorescence emission of Calcein inside the live cells was detected using 38 HE filter set (Excitation: 470/40; Emission: 525/50) and red fluorescence of nucleic acid bound-EthD-1 was detected using a 43 HE filter set (Excitation: 550/25; Emission: 605/70).

In contrast, unlike Amikabeads-P, Amikabeads-Q did not induce significant cell death in PC3 cells even when amounts as high as 500 µg were employed (**Figure 5-14B**, squares). These results from the MTT assay were further confirmed using Live/Dead® analyses, in concert with fluorescence microscopy (**Figures 5-14 A-B and Figures 5-15**).

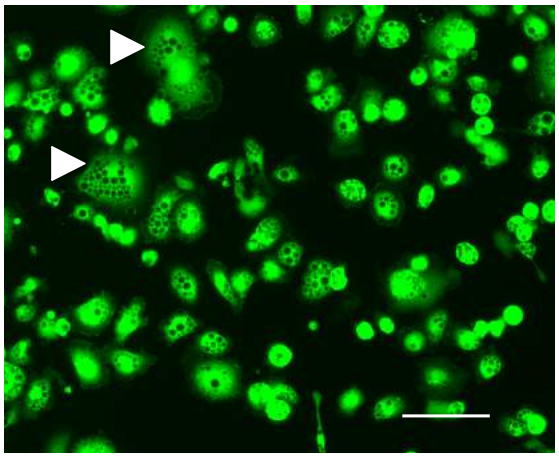

Figure 5-15. Amikabeads-Q were not toxic to PC3 prostate cancer cells. Amikabeads-Q (500 µg; approximate diameter: 11 ± 6 µm) were exposed to 10,000 PC3 prostate cancer cells for 24 hours, followed by staining with Calcein AM. The beads likely on the surface of the PC3 prostate cancer cells can be seen as dark spheres. Green fluorescence emission of calcein inside the live cells was detected using 38 HE filter set (Excitation: 470/40; Emission: 525/50). Scale bar= 100 µm

Cells treated with Amikabeads-P demonstrated significantly higher levels of red fluorescence compared to those with Amikabeads-Q, since cell lysis by the former results in damage and exposure of cellular DNA to the red-fluorescent ethidium homodimer-I dye. In all cases, the microbeads were seen in close proximity with the cells (**Figure 5-14C and 5-15**). Incubation of Amikabeads-P and -Q with PC3 cells in absence of serum proteins for 6 hours did not change the toxicity of parental (P) or quaternized (Q) Amikabeads (**Figure 5-16**), indicating that serum proteins have minimal or no role in determining Amikabead cytotoxicity under the conditions employed.

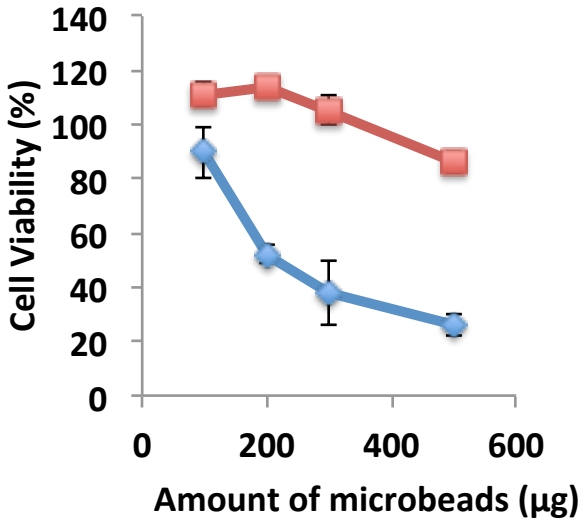

Figure 5-16. Cell viability of PC3 prostate cancer cells after treatment with Amikabeads-P and –Q. Beads were treated (Average diameters: Amikabeads-P: 12 ± 4 µm Amikabeads-Q: 11 ± 6 µm) for 6 hours in serum-free media, followed by 18 hours in serum containing RPMI media as determined using the MTT assay. Statistical test (Students' t-test) was used to test the statistical difference between the unmodified and quaternized Amikabeads. At all concentrations, the parental Amikabeads-P (squares) were significantly more toxic than the quaternized Amikabeads-Q (diamonds) ($p<0.05$).

The above results are along the lines of previous reports in literature that indicate reduced cytotoxicity of cationic polymers after quaternization [232-235]. For example, Brownlie et al. showed that quaternization of amines in polyethyleneimine (PEI) reduced its cytotoxicity by almost 4 fold in A431 lung cancer cells [234]. Previous reports in literature [222] indicate that conversion of primary amines to quaternary amines (e.g. in case of Amikagel-P to Amikagel-Q) results in increasing hydrophilicity of the resulting derivative. This, in turn, results in increased hydration of these molecules, which is thought to be responsible for their lower hemolytic activities [222, 235]. The relatively mild negative charge on the surface of mammalian cells [236] is likely not sufficient to overcome the hydration of Amikabeads-Q (in contrast to strong Coulombic interactions of the microbeads with the strongly anionic plasmid DNA). This can likely indicate minimal interactions between the cells and Amikabeads-Q, and therefore explain the low cytotoxicity of these microbeads towards PC3 cells. However, given the lower hydration of primary amines compared to quaternary amines [222], it is more likely for Amikabeads-P to interact with cell membranes, leading to their disruption, and eventual cell lysis. Thus, although

quaternization of Amikabeads-P led to microbeads with significantly lower toxicities, Amikabeads-P were employed for directly sequestering cellular DNA following lysis of mammalian cells.

Fluorescence microscopy indicated in situ capture of cellular DNA in case of PC3 cells treated with 12 ± 4 μm Amikabeads-P for 24 h (**Figure 5-17A**). As seen in **Figure 5-17A**, Amikabeads-P were able to simultaneously lyse cells, extract DNA molecules, and bind them. This activity of Amikabeads-P may have application in point-of-care testing [237], on-chip nucleic acid extraction and detection [238], and on-site/on-chip whole cell lysis and DNA/RNA capture for PCR reactions [239]. Amikabeads-P, in absence of bound DNA, did not demonstrate any red fluorescence, which is along expected lines (**Figure 5-17B**).

A. **B.**

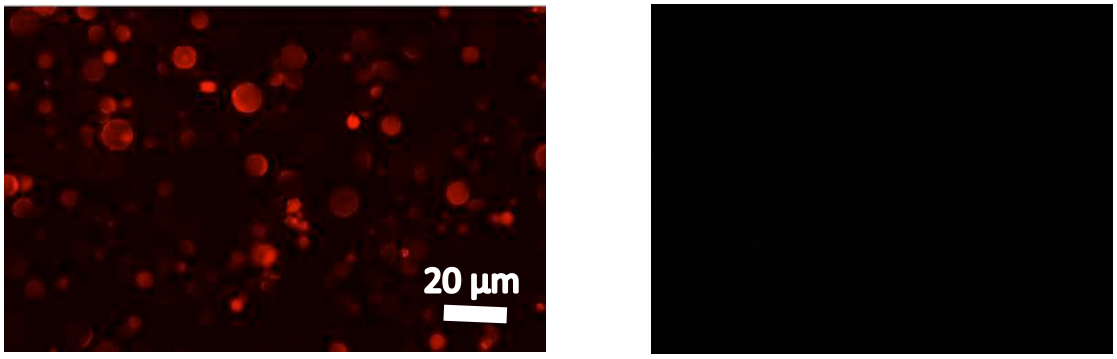

Figure 5-17. In situ DNA capture using Amikabeads-P from mammalian cells. (A) 500 μg Amikabeads-P (approximate diameter: ~12 ± 4 μm) were exposed to 10,000 PC3 prostate cancer cells for 24 hours followed staining with the nucleic acid binding dye, ethidium homodimer-1. Nucleic acids adsorbed to the beads were stained red. **(B)** No red fluorescence was observed with ethidium homodimer-1 stained Amikabeads in the absence of bound DNA. Scale bar = 20 μm.

5.4. CONCLUSION

We have developed a novel anion-exchange resin material based on hydrogel microbeads ('Amikabeads') generated from amikacin and poly(ethylene glycol) diglycidyl ether, with an eye towards applications in biotechnology. Parental Amikabeads-P demonstrated a Q_{max} of 44.5 μg pDNA / mg of the microbeads as determined by fitting a Langmuir isotherm to experimental batch adsorption data. Near-complete recovery of pDNA was possible from Amikabeads-P using high salt concentrations, indicating electrostatic binding between the biomolecule and the microbeads.

Quaternization of amines present in parental Amikabeads resulted in the formation of microbeads (Amikabeads-Q), which demonstrated Q_{max} values approximately 7-fold higher than those for Amikagels-P under the conditions employed. Desorption of the pDNA from these beads was not as efficient as Amikabeads-P, although recovery could be significantly improved by using isopropanol as an organic modifier. Amikabeads-P were able to extract and bind cellular DNA following lysis of mammalian cells, indicating their use for in situ DNA extraction; Amikabeads-Q however, were not able to lyse cells and demonstrated lower cytotoxicities. Our results indicate that Amikabeads are a versatile platform, with multiple easily conjugable groups for several applications in DNA biotechnology ranging from purification to cellular DNA recovery.

CHAPTER 6: SENSITIZING CANCER CELLS TO TRAIL-INDUCED DEATH BY MICELLAR DELIVERY OF MITOXANTRONE

6.1. INTRODUCTION

Tumor necrosis factor alpha-related apoptosis inducing ligand (TRAIL) has generated considerable interest as a targeted cancer therapeutic due its ability to selectively induce cell death in various cancers, with minimal toxicity to normal cells [240]. However, many tumors are inherently resistant or acquire resistance to TRAIL [76]. Mechanisms of TRAIL resistance include overproduction of cellular FLICE inhibitory protein (c-FLIP) which, as a mimic of caspase-8, leads to binding and inactivation of death inducing signaling complex (DISC) [241], overproduction of decoy receptors on cancer cell surface, mutational inactivation of the death receptor gene, dysfunction in the formation of the DISC complex [242], overexpression of Bcl-2 [243], and deficiency of caspase 8 [76]. Strategies that can effectively sensitize resistant cells to TRAIL-induced death could provide a path to new therapeutic options.

Mitoxantrone is an anthracenedione that binds DNA and acts as a topoisomerase II inhibitor, leading to DNA fragmentation. Mitoxantrone intercalation within DNA causes DNA damage, induces expression of the p53 protein, and ultimately results in cellular apoptosis [244]. Mitoxantrone has been shown to be involved in the production of free radicals (reactive oxygen species or ROS), although to a lower extent than doxorubicin [245-247]. Mitoxantrone has also been shown to cause caspase-3 activation in immortalized NIH-3T3 cells [248]. Recent studies on parallel screening of a panel of anti-neoplastic drugs in our laboratory led to the identification of several FDA-approved candidates, including mitoxantrone [25], as sensitizers of a variety of cancer cells to TRAIL-induced death [154].

Nanoscale micelles [249-257] and liposomes [258-259] can be effective for enhanced delivery of poorly water-soluble therapeutics to cancer cells. The efficacy of these vectors is reflected in the FDA approval of the anti-cancer drug formulation Doxil (liposomal formulation of doxorubicin) [260-261]. Several other micellar drug formulations, including Genexol-PM [262], NK105 and NC-6004 [263],

are in different phases of clinical trials. PEG (2000)-DSPE i.e. 1,2–Distearoyl-sn-glycero-3-phosphoethanolamine–N-(methoxy(polyethylene glycol)-2000), an FDA approved [264], biodegradable polymer [265-266], is an important component of liposomes owing to its ability to sterically stabilize liposomes, resulting in long-circulating particles in-vivo. The relatively low critical micelle concentration (CMC) (0.5-1 μM) of PEG-DSPE results in its self assembly into stable 10- to 20-nm micelles [267]; CMC is the concentration of surfactant molecules in an aqueous solution that is required to initiate micelle formation. These micelles have been employed for delivery of therapeutic agents to a variety of cancers [265, 268-270], and their small size is thought to enable deep tumor penetration [268].

In this chapter, we generated and characterized PEG-DSPE micelles loaded with mitoxantrone, and investigated their ability to sensitize prostate and breast cancer cells to TRAIL-induced death. Further, we investigated the influence of different terminal groups on the hydrophilic PEG shell of PEG-DSPE micelles-particularly methoxy, amine and carboxylic acid-on mitoxantrone loading, stability, size, zeta potential, single agent cytotoxicity and synergistic cytotoxicity with TRAIL. To our knowledge, this is the first report of micellar delivery of mitoxantrone for sensitization of cancer cells to TRAIL induced death.

6.2. MATERIALS AND METHODS

Materials

1,2 –Distearoyl-sn-glycero-3-phosphoethanolamine–N-(methoxy(polyethylene glycol)-2000)(ammonium salt) (CH_3O-PEG-DSPE) and 1,2-distearoyl-sn-glycero-3-phosphoethanolamine-N-(amino(polyethylene glycol)-2000) (ammonium salt) (NH_2-PEG-DSPE) were purchased from Avanti Polar Lipids (Alabaster, AL, USA) and used without further purification. Mitoxantrone was purchased from Ontario Chemicals Inc. (Guelph, Ontario, Canada) and was verified for purity using ^{1}H NMR. Mitoxantrone.2HCl, 4-(2-hydroxyethyl)-1-piperazineethanesulfonic acid (HEPES), succinic anhydride and 4-dimethylaminopyridine (DMAP) were purchased from Sigma-Aldrich Inc. (St. Louis, MO). Float-A-Lyzer 8-10K Dialysis membranes were purchased from Spectrum Labs (Rancho Dominguez, CA). Cell culture media -

RPMI 1640 with L-glutamine, Pen-Strep solution: 10000-units/mL penicillin and 10000-µg/mL streptomycin in 0.85% NaCl, and fetal bovine serum (FBS), were purchased from Hyclone (Logan, UT). The MTT assay kit was purchased from ATCC (Manassas, VA). TRAIL (TNF-a Related Apoptosis Inducing Ligand) was purchased from R&D systems (Minneapolis, MN) and suspended in 1 mL of 1X PBS to a concentration of 10 µg/mL. Disposable PD-10 desalting columns, packed with Sephadex™ G-25 medium, were purchased from GE Healthcare (Piscataway, NJ).

Synthesis of HOOC-PEG-DSPE

Amine-terminated PEG-DSPE (NH_2-PEG (2000)-DSPE, 20 mg, 0.007 mmoles), succinic anhydride (10 mg, 0.01 mmoles) and 4-dimethylaminopyridine (DMAP) (5 mg, 0.041 mmoles) were stirred at room temperature for 24 hours in 5 mL of anhydrous tetrahydrofuran (THF). After removing THF under vacuum, the residue was dialyzed against nanopure water and the product was freeze dried. Yield: 60%. ^{1}H NMR ($CDCl_3$, 400 MHz, δ, ppm): 5.19 (1H, -CONH-), 4.38 (1H, -OCH-), 4.20 (2H, OCH_2), 3.94 (2H, OCH_2), 3.2-3.7 (184H, OCH_2CH_2O, OCH_2CH_2NHCO), 2.63 (2H, $NHCOCH_2CH_2COOH$), 2.50 (2H, $NHCOCH_2CH_2COOH$), 2.23 (4H, CH_2CH_2COO), 1.23 (60H, CH_2), 0.86 (6H, CH_3). (**Fig. 6-1)**

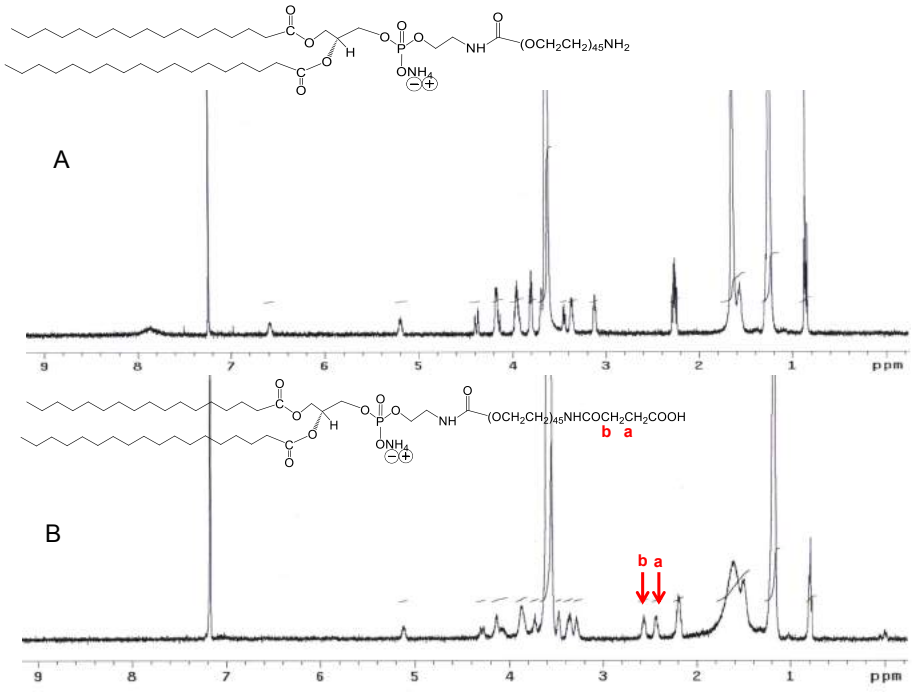

Figure 6-1. ^{1}H NMR spectra of micelles. (A) Amine-terminated PEG-DSPE micelles (M2) in $CDCl_3$, **(B)** Modified Carboxyl-terminated PEG-DSPE micelles (M3) in $CDCl_3$.

Micelle preparation and Mitoxantrone Loading

Methoxy-terminated PEG-DSPE (CH_3O-PEG(2000)-DSPE, 10 mg, 0.0035 mmoles, M1) , amine-terminated PEG-DSPE (NH_2-PEG(2000)-DSPE, 10 mg, 0.0035 mmoles, M2), carboxyl-terminated PEG-DSPE (HOOC-PEG(2000)-DSPE, 10 mg, 0.0034 mmoles, M3) polymers and mitoxantrone (1 mg, 0.0022 mmoles) were weighed and mixed in methanol. In brief, 10 mg of each polymer was mixed with mitoxantrone in methanol. Once mixed, the methanol was removed under vacuum using a rotavapor, leaving a dried crust of mitoxantrone and the lipid polymer behind. After drying overnight to remove all traces of methanol, 1 mL of HEPES buffer (10 mM, pH 7.4) was added to the system with continuous stirring for 30 minutes, followed by ultrasonication for 20 minutes to yield uniform sized drug-encapsulated micelles, M4, M5 and M6 with methoxy, amine and carboxyl terminated micelles, respectively. Detailed compositions of the micelles, M1 – M6 and their properties are given in **Table 1**. Drug-loaded micelles M4, M5 and

M6 were then subjected to size exclusion chromatography using disposable PD-10 desalting column to separate mitoxantrone-loaded micelles from the free drug. Eluates of 1 mL each were collected and measured for mitoxantrone content using absorption spectroscopy. (**Fig. 6-2**).

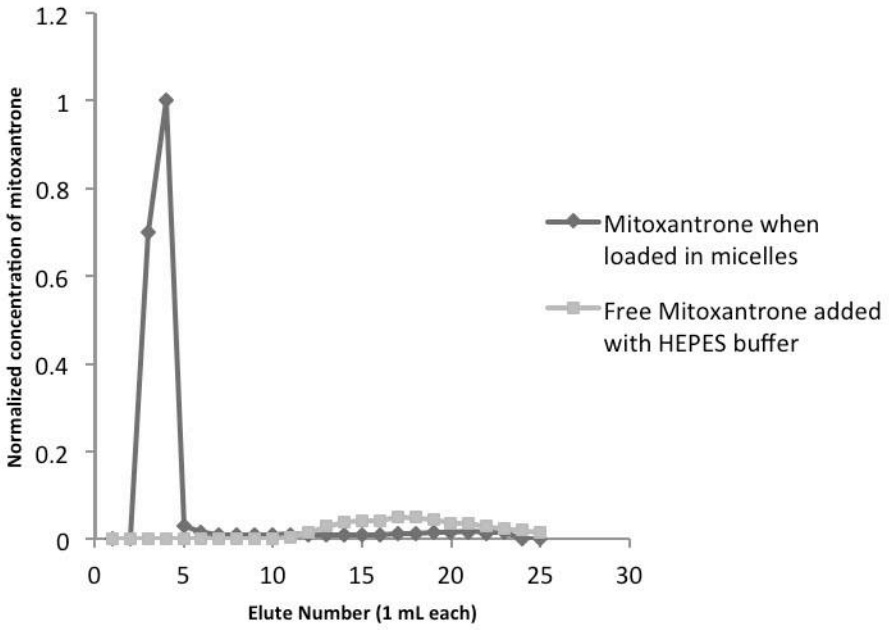

Figure. 6-2. **Elution profile of free (unencapsulated) mitoxantrone and mitoxantrone in PEG-DSPE micelles through PD-10 column**. Black diamonds represent the elution profile of mitoxantrone loaded in micelles (M4) and grey squares represent the elution profile of the free mitoxantrone.

Micelle characterization

Size and Zeta potential determination

The hydrodynamic diameters of micelles M1 – M6 (**Fig. 6-3**) were characterized by dynamic light scattering (DLS) using the Zetasizer Nanosystems Nano-ZS (Malvern Instruments, Mission Viejo, CA) at a concentration of 0.1-mg/mL concentration of respective PEG-DSPE polymer. Dilution of PEG-DSPE micelles to 0.1 mg/mL corresponds to a polymer concentration of approximately 35 μM, which is higher than the CMC (0.5 – 1 μM) of these micelles [267]. Zeta potential measurements of all micelles were carried out using the Zetasizer. Micelle formulations were diluted to 0.1mg/mL polymer concentration for these measurements.

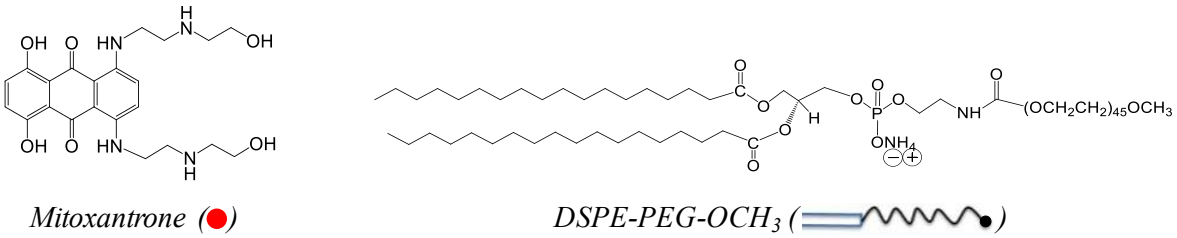

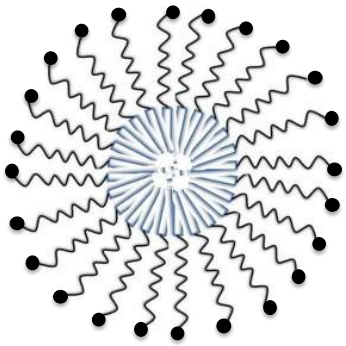

● – terminal groups on PEG

(Empty micelles)

CH_3O – M1
NH_2 – M2
COOH – M3

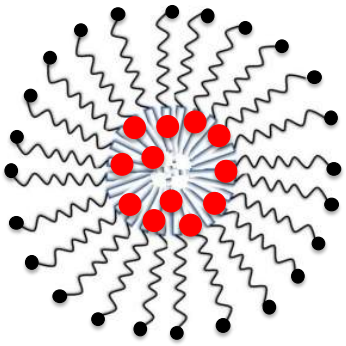

● – terminal groups on PEG

(Mitoxantrone loaded micelles)

CH_3O – M4
NH_2 – M5
COOH – M6

Figure 6-3. Schematic of micelles used in the study. M1 - M3 and M4 – M6 micelles, mitoxantrone and CH_3O-PEG-DSPE micelles were employed in the study. Red circles represent mitoxantrone.

NMR spectroscopy

Micelles generated in HEPES buffer were dialyzed against nanopure water for 24 hours and lyophilized. Lyophilized micelles were resuspended in Dimethyl sulfoxide (DMSO) or D_2O. Next, ^{1}H-NMR measurements were carried out to investigate mitoxantrone encapsulation. ^{1}H-NMR spectrum was obtained with a Varian 400 spectrometer (Varian, Palo Alto, CA) operating at 400 MHz in the Fourier transform mode. Control spectra of mitoxantrone in DMSO, empty micelles in

DMSO and empty micelles in D_2O were obtained in order to confirm mitoxantrone encapsulation. Previous studies have demonstrated that protons of paclitaxel and doxorubicin, encapsulated within PEG-DSPE micelles, exhibit minimal mobility, and are therefore absent in ^1H NMR spectra [265, 271]. The absence of the chemical shifts of mitoxantrone in ^1H NMR spectra of drug-loaded micelles in aqueous solutions was used as an indicator of encapsulation.

Determination of drug loading

The light absorption profile of mitoxantrone in DMSO was used to measure its loading in micelles. The absorbance of known concentrations of mitoxantrone in DMSO was used to generate a standard calibration curve. The peak intensity of mitoxantrone at 682 nm (wavelength for maximum absorbance of mitoxantrone) measured using Shimadzu UV-3600 UV-VIS-NIR Spectrophotometer was used in these calculations. The concentration of mitoxantrone loaded in micelles was determined by disrupting the micelles in THF and resuspending them in DMSO to measure absorbance at 682 nm. The corresponding concentration of the drug in micelles was calculated based on the standard curve.

Stability measurements

Mitoxantrone-loaded micelles were stored in 10 mM HEPES buffer at 4^oC and periodically tested for stability as a function of time. A 10-µL sample of the micelle dispersion was diluted to 1 mL in 10 mM HEPES buffer (final polymer concentration 0.1 mg/mL) and the absorbance was measured at 669 nm in order to determine the amount of drug released, if any. The size of the micelles was also determined as a function of time. Stability studies were also carried out by suspending the micelles in cell culture media (RPMI 1640 supplemented with 10% fetal bovine serum (FBS) and 1% Penicillin/Streptomycin: 10000 units/mL penicillin and 10000 µg/mL streptomycin in 0.85% NaCl) at 37^oC for 24 hours and measuring their absorbance as described above.

In-vitro drug release

In order to determine the release properties of mitoxantrone from micelles, 1 mL micelle sample (M4) was added into the 8- to 10-kD cut off Float-A-Lyzer dialysis tubing (Spectrum Labs, Rancho Dominguez, CA) at 37^{o}C and dialyzed against 200 mL 10-mM HEPES buffer at pH 7.4, 200 mL of 1X PBS buffer at pH 7.4 (150 mM equivalent salt concentration) and 200 mL of 1X PBS buffer at pH 7.4 supplemented with 10% FBS respectively. The concentration of mitoxantrone was measured at regular intervals for a period of 48 hours by carefully removing a 10-µL sample from within the dialysis tubing and determining mitoxantrone concentration. The absorbance immediately upon set up (time=0 min) was denoted as 100% mitoxantrone and subsequent absorbance readings were calculated with respect to this value. Drug release was studied for up to 48 hours. Release characteristics of the free mitoxantrone drug in 10-mM pH 7.4 HEPES buffer from the dialysis tubing was also determined and used for comparison with that observed with the micelles.

Confocal microscopy

Cell uptake of mitoxantrone.2HCl free drug and mitoxantrone loaded in micelles (M4) were imaged by laser scanning confocal microscopy using a Leica SP5 Confocal Microscope (Leica Microsystems, Wetzlar, Germany) and Nikon C2 laser scanning confocal system with a TE2000 inverted microscope. PC3 human prostate cancer cells (4×10^4) were grown on autoclaved 1-cm diameter circular coverslips for 24 hours before treatment. Cells were treated with mitoxantrone.2HCl and mitoxantrone in micelles (M4) at a final drug concentration of 6.6 and 13.3 µM, and imaged at four different time points to visualize their sub-cellular localization.

Prior to imaging, cells were fixed in 2% paraformaldehyde solution for 30 minutes followed by three washes with 1X PBS. Cells were mounted on the glass slide with glycerol based mounting medium (90% glycerol in PBS) and imaged using Leica 63X, NA1.4 oil immersion lens or Nikon 60X, NA 1.3 oil immersion lens. Cells were stained with DAPI in order to visualize the nucleus. Cells were fixed as described previously at 30 minutes, 1 hour, 2 hours and 3 hours after treatment with 6.6 and 13.3 µM of mitoxantrone and mitoxantrone-loaded micelles.

Cells were excited at 633 nm (He/Ne laser) (Leica microscope)/637 nm (Nikon microscope) and emission was collected using a 670-nm long pass filter to visualize mitoxantrone. Image J software (NIH, Bethesda, MD) was used to evaluate the cellular fluorescence of mitoxantrone. The raw fluorescence intensity of mitoxantrone was acquired and corrected to account for background fluorescence as calculated by the software.

Cell culture and cytotoxicity analysis

Cell culture

PC3 human prostate cancer cells, MDA-MB-231 breast cancer cells [272] (purchased from ATCC at Manassas, VA) and T24 bladder cancer cells [273] (obtained as part of an existing collaboration with Professor Christina Voekel-Johnson at Medical University of South Carolina, Charleston, SC) were cultured in RPMI 1640 medium supplemented with 10% (v/v) FBS and 1% (v/v) penicillin and streptomycin (Pen-Strep solution: 10000 units/mL penicillin and 10000 µg/mL streptomycin in 0.85% NaCl).

Evaluation of single-agent mitoxantrone

The effect of treatment with free mitoxantrone and micelle-encapsulated mitoxantrone (M4-M6 in **Fig. 1**) on cell viability was investigated. Cancer cells (8,400 /well in a 96-well plate) were plated with 150 µL of cell culture medium and allowed to adhere for 24 hours before the addition of free or micelle-encapsulated drug. The efficacy of micelle-encapsulated mitoxantrone (free base form) was compared to mitoxantrone.2HCl (salt form) that was used as the free drug only in cytotoxicity and imaging experiments. (Note: To avoid confusion between mitoxantrone free base and mitoxantrone.2HCl, the free drug in both forms is subsequently referred to as 'free mitoxantrone').

Empty micelles (M1 – M3 in **Fig. 6-3**) and HEPES buffer were used as controls in the cytotoxicity studies. After 24 hours of administering the drug formulations, cell viability was determined using the MTT (3-(4,5-Dimethylthiazol-2-yl)-2,5-diphenyltetrazolium bromide) cell proliferation assay [274]. The MTT dye reports for cellular metabolic activity and can be used as an indicator of cellular viability and proliferation using methods similar to those described in our

previous studies [154]. **Fig. 6-4 (Top panel)** shows a schematic of the single-agent treatments investigated.

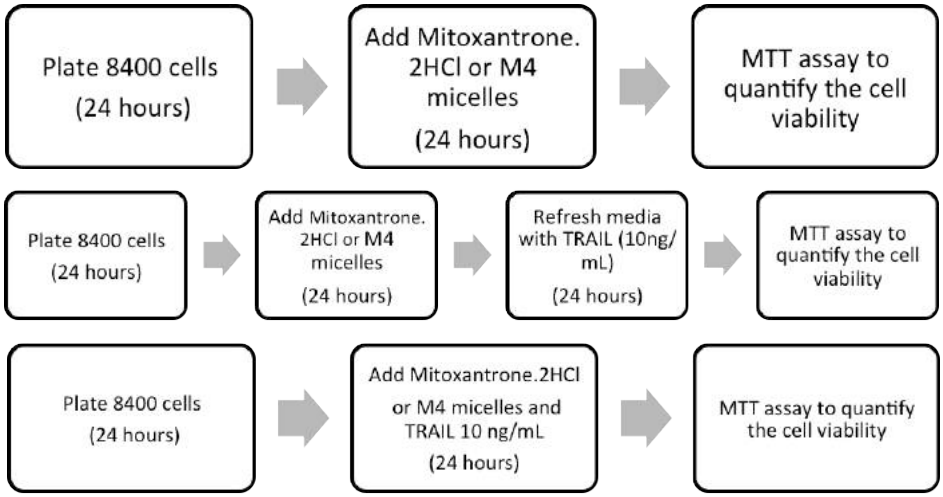

Figure 6-4. Schematic of treatments:
Top panel – Single agent cytotoxic treatments
Middle panel – Sequential drug-TRAIL treatments
Bottom panel – Simultaneous drug-TRAIL treatments

Sequential treatment with mitoxantrone and TRAIL

Cells were first treated with free mitoxantrone or mitoxantrone-loaded micelles (M4-M6) for 24 hours as described above. Then, the cell culture media was replaced with fresh media, followed by treatment with 10 ng/mL TRAIL for an additional 24 hours. Cell viability was determined using the MTT assay following TRAIL treatment. Total treatment time in the case of sequential mitoxantrone-TRAIL treatments was 48 hours as opposed to 24 hours for single-agent (mitoxantrone alone or TRAIL alone) treatments. Cells treated with TRAIL alone and TRAIL treatment in combination with empty PEG-DSPE micelles (M1 – M3 in **Fig. 6-3**) were used as controls. **Fig. 6-4 (middle panel)** shows a schematic of the sequential treatments.

Simultaneous treatment of mitoxantrone and TRAIL

Cells were simultaneously treated with 10 ng/mL of TRAIL and free mitoxantrone or mitoxantrone-loaded M4 – M6 micelles. After 24 hours of incubation with the two treatments, cell viability was determined using the MTT assay as described above (**Fig. 6-4 bottom panel**).

6.3. RESULTS AND DISCUSSION

Encapsulation of mitoxantrone in micelles

Fig. 6-3 shows the structures of mitoxantrone and DSPE-PEG and a schematic of the different micelles employed in this study. Drug-loaded CH_3O-PEG-DSPE (M4), NH_2-PEG-DSPE (M5), and HOOC-PEG-DSPE (M6) micelles were generated using a PEG-DSPE polymer concentration of 10 mg/mL. **Fig. 6-2** shows the characteristic elution profile of free mitoxantrone compared to representative M4 micelles from PD-10 column. As expected, micelles with the encapsulated drug elute faster because of their larger size.

Micelle properties are shown in **Table 6-1**. As seen in the table, different micelles were saturated at various concentrations of mitoxantrone during the preparation process. The phosphate group of the DSPE in the micelle is negatively charged at pH 7.4 [258]. Mitoxantrone, in turn, has two ionizable amines with pK_a values of 8.3-8.6 [275] which are positively charged at pH 7.4. Electrostatic interactions between these moieties can accelerate encapsulation and intercalation of mitoxantrone [276-279].

Table 6-1. Physical characteristics of micelles employed in the current study. The corresponding PEG-DSPE concentration was 0.1 mg/mL in all Size and Zeta potential studies shown as Mean ± SD.

Polymeric micelles	Micelles	Drug loading[a]	Size diameter (nm)	Zeta potential (mV)	
CH_3O- PEG-DSPE only (Empty)	M1	--	11.8 ± 3.2	-12.1 ± 1.9 *3	*
Mitoxantrone loaded CH_3O- PEG-DSPE	M4	67.0% ± 3.75% *1	13.3 ± 4.0	-4.0 ± 1.7	
NH_2 - PEG-DSPE only (Empty)	M2	--	12.0 ± 3.0	-5.5 ± 1.6	*
Mitoxantrone loaded NH_2 - PEG-DSPE	M5	45.6 ± 6.11%	11.3 ± 3.3	7.3 ± 2.0	
HOOC - PEG-DSPE only (Empty)	M3	--	13.9 ± 3.0	-41.0 ± 7.5 *4	*
HOOC - PEG-DSPE Mitoxantrone loaded	M6	66.0 ± 3.88 % *2	14.7 ± 3.8	-20.5 ± 5.1	

a: Weight percentage of the drug loaded into the micelles when 1 mg drug was mixed with 10 mg of the respective PEG-DSPE polymer.
*1: Statistical significance ($p<0.05$) between loading percentage of M4 and M5 micelles.
*2: Statistical significance ($p<0.05$) between loading percentage of M5 and M6 micelles.
**3: Statistical significance ($p<0.01$) between zeta potential values of (M1- M2) and (M1-M3) micelles.
*4: Statistical significance ($p<0.05$) between zeta potential values of M2 and M3 micelles.
The zeta potential across all three micelles (M1-M4, M2-M5, M3-M6) was more positive after mitoxantrone loading (statistical significance ($p<0.05$)).
Zeta potential across three micelles after drug loading (M4-M5 (**), M4-M6 (**) and M5-M6 (**)) was significantly different ($p<0.01$)

Although we have not verified this experimentally, the positive charge on the secondary amines on mitoxantrone may enhance interactions with the phosphate group at the core-shell junction of DSPE-PEG micelles. In addition, it is likely that the hydrophobic portion of the drug partitions into the hydrophobic DSPE core. Similar interactions have been suggested between doxorubicin and PEG-DSPE where the aminoglycoside moiety of doxorubicin is thought to extend into the PEG layer while the anthracycline component interacts with the hydrophobic core [268].

The CH_3O-PEG-DSPE and HOOC-PEG-DSPE micelles were saturated with approximately equivalent amounts of mitoxantrone/10 mg polymer to form M4 and M6, whereas the NH_2-PEG-DSPE amine-terminated micelles (M5) were saturated with smaller amounts of the drug ($p <$

0.05). This reduction could be due to the repulsion of the terminal amine of the NH_2-micelle and the amine group in mitoxantrone during loading. It is also possible that terminal amines on the DSPE-PEG molecule compete with mitoxantrone for interactions with the phosphate on the DSPE molecule. However, similar loading efficiencies for M4 and M6 micelles suggest that their phosphate entity remains available for mitoxantrone binding irrespective of these terminal groups. The drug loading percentages in **Table 6-1** are indicative of the saturation (maximum) concentration of mitoxantrone that can be loaded in the respective micelles.

Micelle size and zeta potential

The diameters of all micelles before (M1 – M3) and after mitoxantrone loading (M4 – M6) were determined to be less than 20 nm, indicating that micelle size is unaltered by drug loading (**Table 6-1 and Fig. 6-5**). It has been observed previously that loading drugs within PEG-DSPE micelles leads to a minimal changes, if any, in their hydrodynamic size [265, 268, 280].

A. **B.**

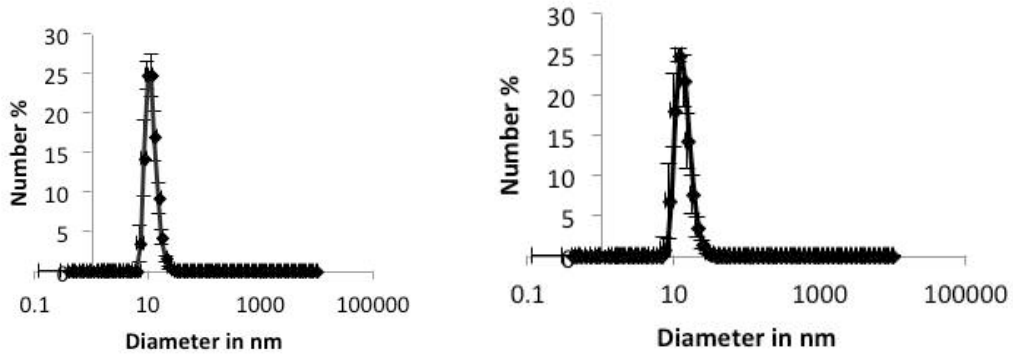

Figure 6-5. DLS profile of micelles. **(A)** Empty methoxy terminated PEG-DSPE micelles (M1) and **(B)** Mitoxantrone-loaded methoxy terminated PEG-DSPE micelle (M4). (PEG-DSPE concentration in both species was 0.1 mg/mL).

All three micelles were stable for up to two months in HEPES buffer (10 mM, pH 7.4) based on size and drug release analyses (data not shown). No precipitation of the drug was observed during storage.

The zeta potentials of the micelles with and without encapsulated mitoxantrone were measured to determine whether drug loading and the micelle terminal groups affect the micellar surface charge properties (**Table 6-1**). Carboxyl-terminated micelles exhibited the highest

negative zeta potential of approximately -40 mV. Empty methoxy micelles (M1) and amine micelles (M2) were found to possess significantly lower, but negative zeta potential values compared to the empty carboxyl terminus PEG-DSPE (M3) micelle ($p<0.05$)(not shown in the table). The ionizable phosphate group of DSPE is primarily responsible for the negative zeta potential observed in all empty micelles.

Following mitoxantrone loading, all micelles demonstrated a reduction in their negative zeta potential values with statistical significance ($p<0.05$) for (M1 vs. M4) (M2 vs. M5) and (M3 vs. M6) (**Table 6-1**). For example, empty NH_2-PEG-DSPE micelles showed a slightly negative zeta potential that reversed polarity following mitoxantrone loading ($p<0.05$). The positively charged moieties on mitoxantrone can shield some of the negative charge of the DSPE phosphates, thereby reducing the micelle's negative zeta potential. This reduction in the negative zeta potential value, observed across all the three micelle species, can be used as another indicator of mitoxantrone encapsulation. Similar phenomena have been observed for other drugs loaded within PEG-DSPE micelles [281].

Spectral characterization of mitoxantrone-loaded micelles

Free mitoxantrone dissolved in HEPES buffer showed an absorbance spectrum with two maxima, one at 610 nm and the other 660 nm, corresponding to the dimer and monomer forms of the drug, respectively [282] [278]. These absorption peaks showed a bathochromic shift (redshift) when mitoxantrone was encapsulated within PEG-DSPE micelles. As shown in **Fig. 6-6**, the absorption maxima for the monomer shifted from 660 nm in HEPES buffer (black dots) to 669 ± 1 nm when loaded within micelles (dotted line). The dimer peak exhibited a smaller red shift. At equivalent drug concentrations, an increase in the overall absorption intensity profile of the drug was observed following encapsulation (**Fig. 6-6**). This is consistent with other observations in literature on mitoxantrone absorbance in CTAB and SDS micelles [283-284], and is likely since some drugs exhibit lower absorption in aqueous media compared to that in hydrophobic environments. No shift in absorption maxima were noticed when mitoxantrone was dissolved in presence of PEG (2000) alone.

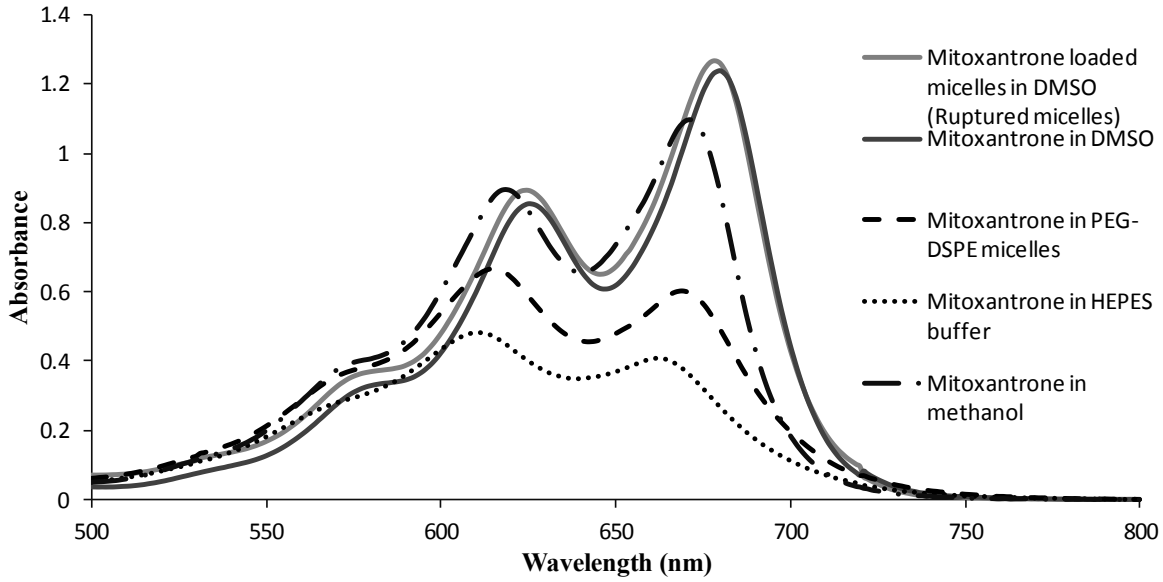

Figure 6-6. Absorption spectra of free mitoxantrone in various modalities. Absorption spectra of free (unencapsulated) mitoxantrone (35μM) in 10 mM pH 7.4 HEPES buffer (dotted line), 0.5 mg/ml PEG(2000)-DSPE micelles M4 (**- -**), methanol (−·−·−), and DMSO (black and grey solid lines). Black and grey solid lines indicate the absorption profile of 35 μM of free mitoxantrone and M4 micelles in DMSO respectively.

The positions of mitoxantrone monomer and dimer maximal absorption peaks are different for the free drug and encapsulated drug due to differences in the local microenvironment.

It has been previously reported that the absorbance peak of mitoxantrone is sensitive to its surrounding environment. Enache et al. [278, 283] reported that the wavelength of maximal absorbance of mitoxantrone depends on the dielectric constant of the surrounding medium. In case of mitoxantrone encapsulated within micelles, we observed a shift in the monomer peak to 669 ± 1 nm. This peak position was similar to that observed for mitoxantrone in methanol (**Fig. 2**). This suggests that the environment surrounding mitoxantrone may be similar to that in methanol, which is less hydrophobic than the lipid core of DSPE. This could likely indicate that mitoxantrone localizes at the interface of the DSPE-PEG with the hydrophobic part of the drug interacting with the lipid core, and the protonated amines interacting with the anionic phosphates of DSPE at the interface. This is consistent with other reports in the literature [284], which discuss the orientation of mitoxantrone in SDS micelles. It was suggested the chromophore ring in mitoxantrone is

immersed in the micelle core and positively charged exterior interacts with the polar head groups of the SDS. Although this is likely to be consistent in DSPE-PEG micelles, it is important to mention the difficulty of exactly pinpointing the location of mitoxantrone, due to the dynamic nature of the micelles as well as the drug.

As an additional study, we determined the absorption spectra of mitoxantrone in 1, 4-dioxane (**Fig 6-7**). Hydrophobic hydrocarbon cores typically possess dielectric constants around 2 to 5, which is similar to that of 1,4 dioxane [285].

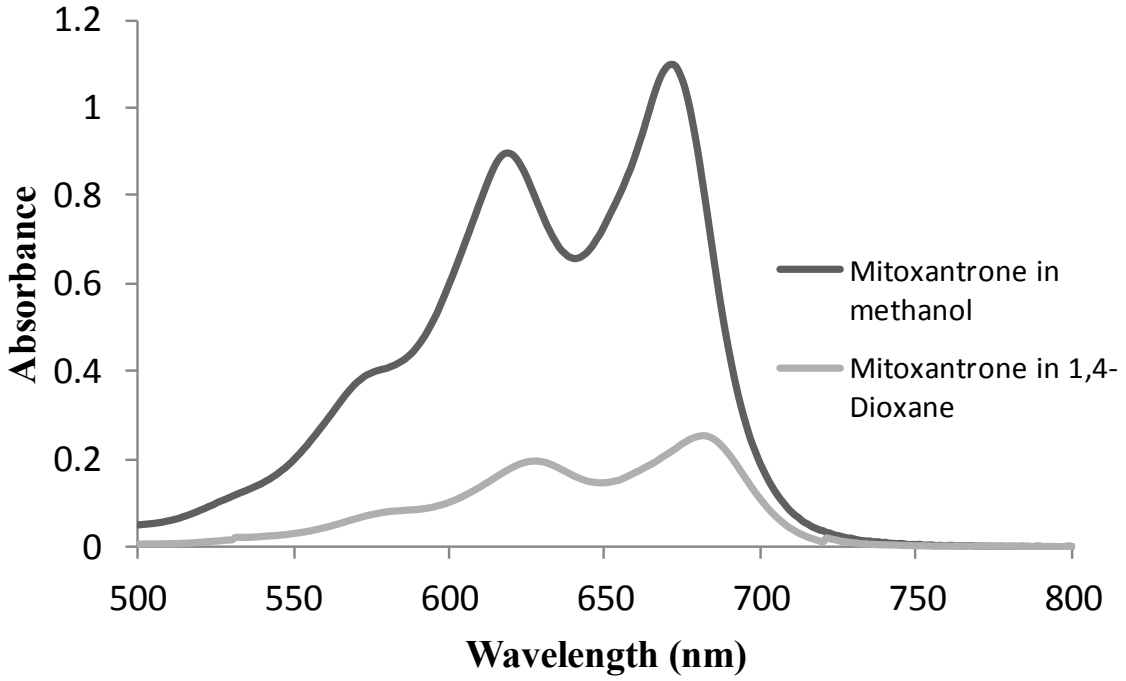

Figure 6-7. Absorption spectra of free (unencapsulated) mitoxantrone in various solvents. Absorption spectra of free (unencapsulated) mitoxantrone (35μM) in methanol (Black line) and 1,4-Dioxane (Grey line).

We found that the absorption spectra of the drug in 1, 4-dioxane is significantly different from its absorption spectra in methanol or PEG-DSPE micelles, which is likely an additional indicator that mitoxantrone might be predisposed to locate near the core-shell junction.

NMR measurements

Mitoxantrone-loaded micelles in HEPES buffer were dialyzed against nanopure water for 24 hours and freeze dried. ^{1}H-NMR measurements were carried out on freeze-dried micelles to investigate mitoxantrone encapsulation. **Fig. 6-8** shows the ^{1}H-NMR spectrum of mitoxantrone-loaded micelles (M4) measured in D_2O (a), free mitoxantrone in DMSO (b), and micelle-encapsulated mitoxantrone in DMSO (c).

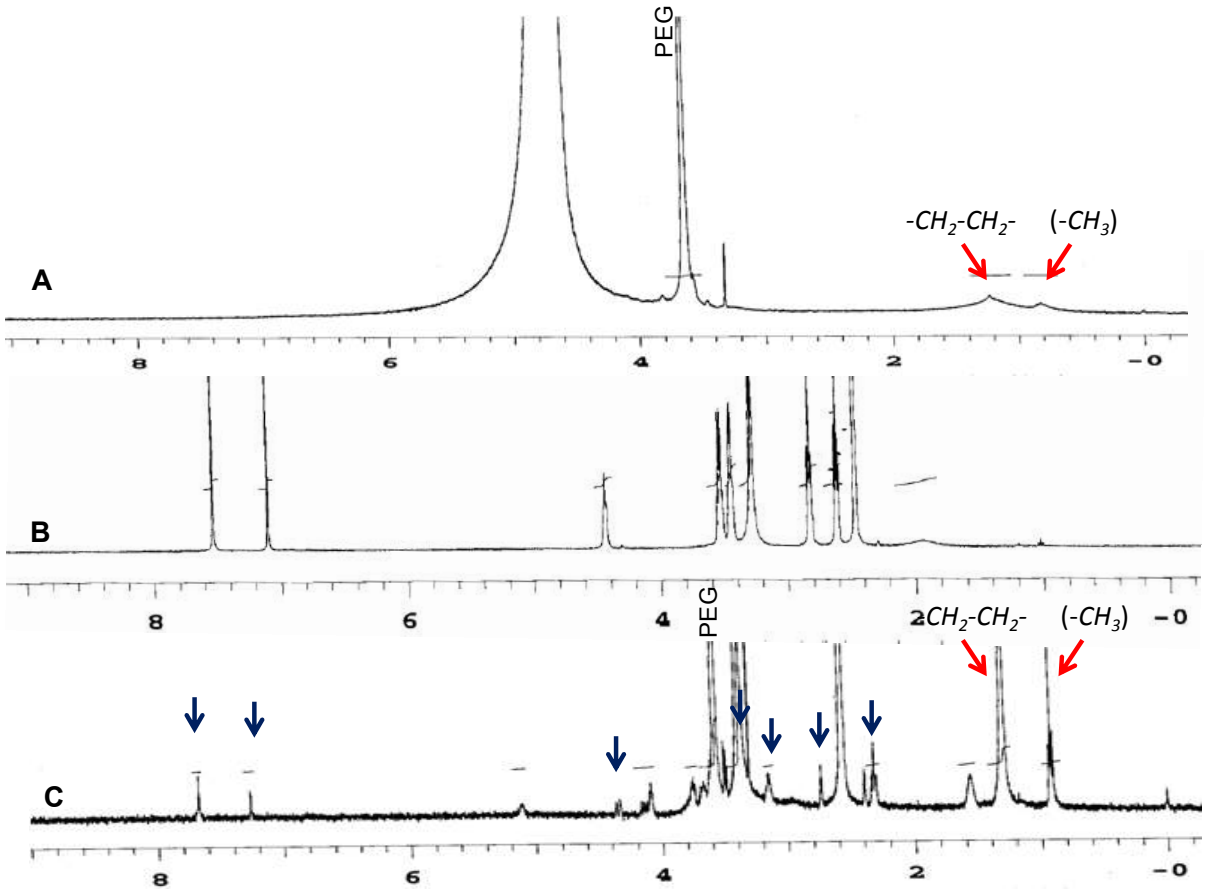

Figure 6-8. **^{1}H NMR spectra of micelles before and after rupture**. ^{1}H NMR spectra of **(A)** mitoxantrone-loaded M4 micelle in D_2O, **(B)** free mitoxantrone in DMSO, and (C) mitoxantrone-loaded M4 (ruptured) micelle in DMSO.

In D_2O, spectral peaks corresponding to PEG (-CH_2-CH_2-O-) can be seen from 3.5-3.8 ppm and peaks corresponding to distearoyl can be seen at 1.2 ppm (-CH_2-CH_2-) and 0.8 ppm (-CH_2-CH_3). The distearoyl peaks are broad and intensity is reduced compared to its intensity in DMSO. This is due to restricted mobility of the hydrophobic distearoyl chains in the micelle cores. The ^{1}H-NMR spectra of micelle-encapsulated mitoxantrone in D_2O did not show peaks corresponding to mitoxantrone, likely due to its core-shell location in the micelles, causing restricted proton mobility. This is consistent with previous NMR observations of drug encapsulation within PEG-DSPE micelles (e.g. for paclitaxel [265]). However, spectral peaks corresponding to mitoxantrone and polymer were observed in ^{1}H-NMR spectra recorded in DMSO, due to disruption of micelles by DMSO and release of mitoxantrone in the solvent. Comparison of spectra of free mitoxantrone, empty PEG-DSPE micelles and mitoxantrone loaded PEG-DSPE micelles in DMSO with mitoxantrone-loaded micelles in D_2O indicated that mitoxantrone was encapsulated within micelles (**Fig. 6-8**).

Micelle stability

As may be expected, mitoxantrone is sensitive to its surrounding environment, which allows for investigations into time-dependent stability of the micelle-encapsulated drug by following changes in absorbance profiles. While free mitoxantrone possesses absorbance peaks at 610 nm (dimer) and 660 nm (monomer), mitoxantrone inside micelles demonstrates peaks at 614 ± 1 nm and 669 ± 1 nm. These differences in absorbance profiles can be monitored to determine stability. We periodically determined the absorbance profile of micelle-encapsulated mitoxantrone (M4-M6) stored at 4^{o}C in 10-mM pH 7.4 HEPES by methods previously described. We observed minimal absorbance peak shifts and size changes of the drug-encapsulated micelles for over two months, which indicates stability under these storage conditions.

Fig. 6-9 A,B shows time-dependent changes in the absorption profile of 35 μM free mitoxantrone and mitoxantrone in micelles (M4) for over 24 hours in RPMI 1640 cell culture media supplemented with 10% FBS and 1% penstrep antibiotic at 37^{o}C. It was observed that the drug, in both formulations, shows reduced absorbance after 24 hours.

A. **B.**

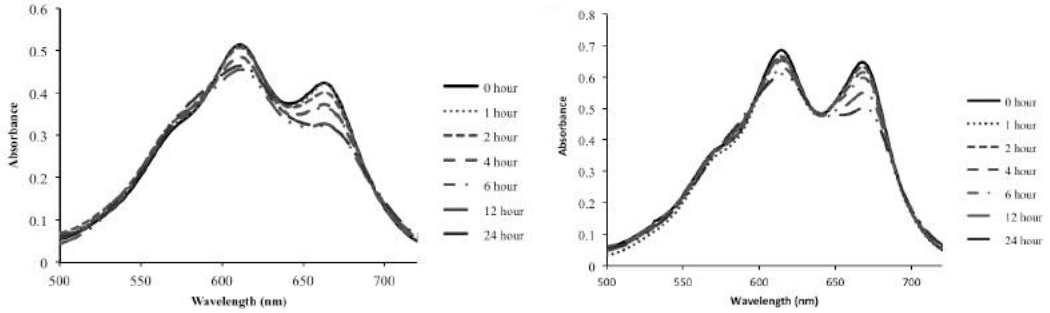

Figure 6-9. Absorbance profiles indicating stability of mitoxantrone in micelles. Absorbance profiles indicating stability of **(A)** 35 μM mitoxantrone and **(B)** M4 micelles containing 35 μM mitoxantrone in RPMI 1640 cell culture media supplemented with 10% fetal bovine serum (FBS) and 1% Penicillin/Streptomycin (10,000 units/mL) at 37^{o}C over 24 hours. Note that the absorbance intensity of mitoxantrone in micelles is higher than the free mitoxantrone at equivalent concentrations at all times. Data shown are representative of two independent experiments (n=2).

These similar changes in the absorption profile could indicate dimerization of the drug when left for prolonged intervals in the cell culture media. However, it should be noted that mitoxantrone monomer peak stays at 669 ± 1 nm in the case of micelles in RPMI media. We also calculated time-dependent change in the ratio of dimer/monomer peak absorbance for both species. As shown in **Table 6-2, (**free mitoxantrone in RPMI media has a higher percentage of dimers than mitoxantrone in M4 micelles suspended in RPMI. Comparing the time-dependent changes in the ratio, we observe that there is a slow change in the dimer/monomer mitoxantrone population in both species. However, the M4 micelle absorbance curve does not resemble that of the free drug. Over 24 hours, only ~25% decrease is observed in the M4 micelle monomer peak absorbance, which remains at 669 ± 1 nm, a characteristic of the drug retained in micelles.

Table 6-2. The absorbance intensities of peaks of free mitoxantrone (dimer: 610 nm and monomer: 660 nm) and M4 micelles (dimer: 614 ± 1 nm and monomer: 669 ± 1 nm) measured in RPMI 1640 cell culture media during time dependent stability studies.

Species	Dimer peak Absorbance	Monomer peak Absorbance	Ratio Dimer/Monomer
Free drug 0 hour	0.516	0.425	1.21
Free drug 1 hour	0.515	0.422	1.22
Free drug 2 hour	0.508	0.403	1.26
Free drug 4 hour	0.486	0.373	1.30
Free drug 6 hour	0.484	0.367	1.32
Free drug 12 hour	0.456	0.328	1.39
Free drug 24 hour	0.465	0.324	1.44

Species	Dimer peak Absorbance	Monomer peak Absorbance	Ratio Dimer/Monomer
M4 micelles 0 hour	0.687	0.648	1.06
M4 micelles 1 hour	0.663	0.634	1.05
M4 micelles 2 hour	0.666	0.632	1.05
M4 micelles 4 hour	0.656	0.615	1.07
M4 micelles 6 hour	0.653	0.598	1.09
M4 micelles 12 hour	0.629	0.552	1.14
M4 micelles 24 hour	0.610	0.502	1.21

It has been previously observed that Amphotericin B-containing PEG-DSPE micelles were stable for only 45 minutes [286]. However, this was not observed in case of mitoxantrone loaded micelles (M4): An absorbance change of less than 3% was observed over the first hour after suspension in RPMI 1640 (**Table 6-2**). We also measured the size of the micelles in RPMI media and found that micelle size changes minimally in RPMI media over time (**Fig. 6-10**). Analyzing the changes in the absorption profile of mitoxantrone, we observe them to be minimal over a 6-hour time period (~ 10% reduction, **Fig 6-9B**) which is acceptable for micellar delivery of the drug to cells [287].

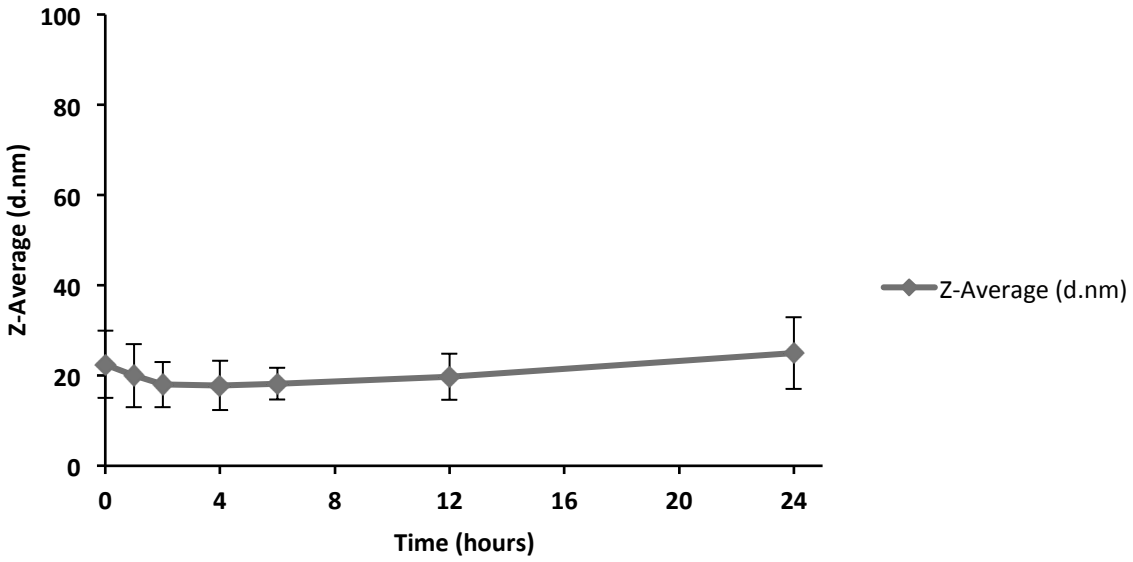

Figure 6-10. Time-dependent change in the Z-average (diameter in nm) of M4 micelles. Time-dependent change in the Z-average (diameter in nm) of M4 micelles containing 35μM mitoxantrone in RPMI cell culture media. The error bars denote the polydispersity in nanometers. The Z-size average has a +/- 5.4% change in the 24 hours in RPMI cell culture media. Data shown is representative of two independent experiments.

In-vitro drug release

Release of mitoxantrone from micelles was investigated under various conditions by monitoring release of the drug from an 8- to 10-kD Float-A-Lyzer membrane. The release profile was compared to diffusion of the free drug under similar experimental conditions. As shown in **Fig. 6-11**, over 48 hours approximately 7%, 20% and 25% of initially encapsulated mitoxantrone was

released from the micelles at pH 7.4 in 10-mM HEPES buffer, 150-mM phosphate buffered saline (PBS) and 150-mM phosphate buffered saline supplemented with 10% FBS, respectively.

Higher salt concentration of 150 mM in case of 1X PBS (physiological salt concentration) led to an increase in drug release ($p<0.05$) compared to release in 10-mM HEPES buffer. This could be due to the shielding of ionic charge at higher salt concentration leading to lower retention of the mitoxantrone in the micelle and, therefore, higher release. Nevertheless, the release was only approximately 20% of the initially encapsulated mitoxantrone over a period of 48 hours. Introduction of FBS to M4 micelles in PBS resulted in a statistically significant ($p<0.05$) increase in mitoxantrone release at 4, 6 and 12 hours compared to micelles in PBS alone. Approximately 25% of the encapsulated drug was released after 48 hours in the presence of FBS (**Fig. 6-11**). As may be expected, the diffusion of free mitoxantrone from the dialysis tubing was significantly more rapid; approximately 85% of the drug diffused out of the dialysis membrane in 48 hours in 10 mM pH 7.4 HEPES buffer.

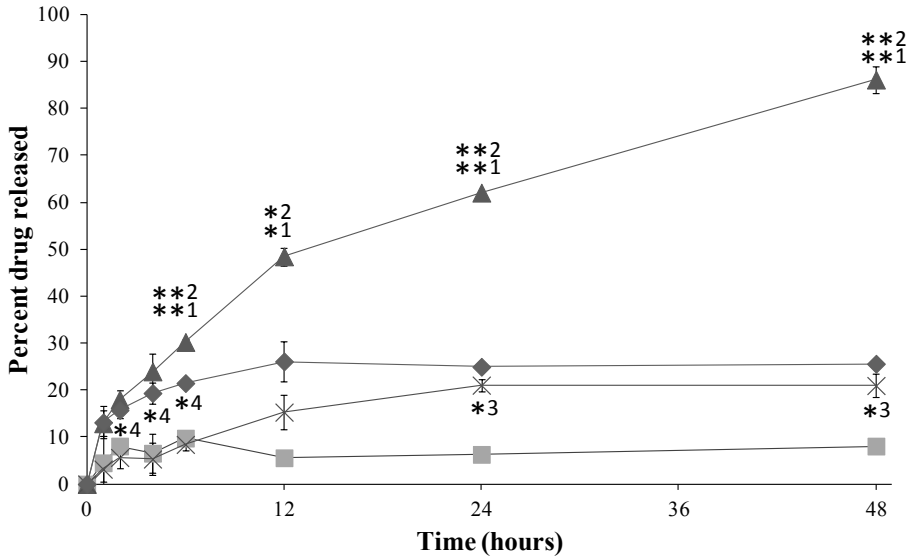

Figure 6-11. Kinetics of mitoxantrone release from micelles. Kinetics of mitoxantrone release from micelles (M4) in 1X PBS pH 7.4 (150 mM equivalent salt concentration) supplemented with 10% fetal bovine serum (grey diamonds), 1X PBS pH 7.4 (crosses) at 37°C and 10 mM HEPES buffer pH 7.4 (grey squares). Diffusion of the free (unencapsulated) mitoxantrone in the dialysis-based study in 10 mM HEPES buffer at pH 7.4 is shown by dark grey triangles. $*^1$ indicate statistical significance between grey diamonds and triangles, $*^2$ indicate statistical significance between grey triangles and grey crosses and $*^3$ indicate statistical significance between grey crosses and grey squares. $*^4$ indicate statistical significance between grey crosses and grey diamonds.

Cellular uptake

Free mitoxantrone and mitoxantrone-loaded micelles (M4) were administered to PC3 prostate cancer cells and imaged at different time points using confocal fluorescence microscopy in order to investigate cellular uptake. Our results indicate that mitoxantrone was internalized by the cells in both free and micellar formulations**. Fig. 6-12 A-D and Fig. 6-13** show confocal microscopic images of drug fluorescence at 3 hours following administration of 13.3 μM mitoxantrone loaded micelles (M4) and free mitoxantrone respectively.

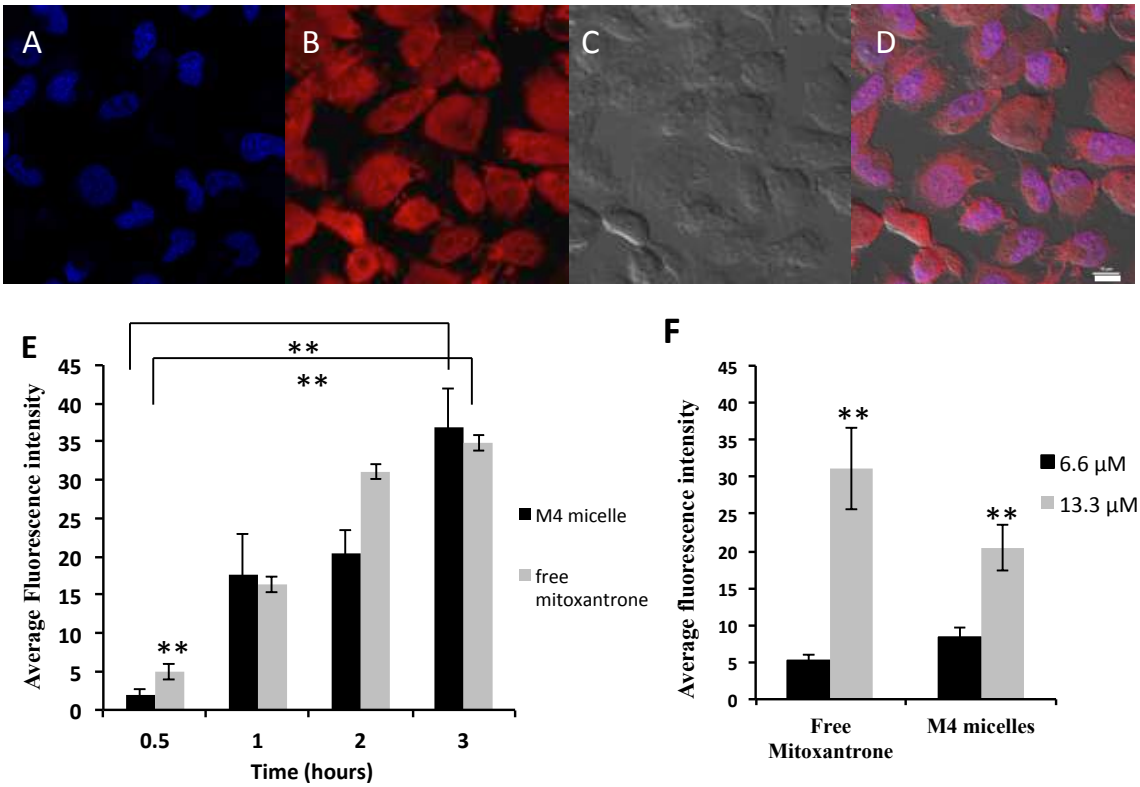

Figure 6-12. Cell uptake of mitoxantrone micelles into PC3 cancer cells. **(a-c)** Confocal microscopy image showing internalization of mitoxantrone (13.3 µM)-loaded micelles (M4) in PC3 prostate cancer cells after 3 hours of treatment. The nucleus was stained with DAPI **(A)** (stained blue; excitation: 358 nm, emission: 461 nm). Mitoxantrone **(B)** was excited with 637 nm laser and emission was detected in the far red region (670 nm) with long pass filter (red false color was used to indicate mitoxantrone emission). Image **(C)** shows the phase contrast image and Image **(D)** shows the overlay image of a,b and c. Scale Bar : 10 µm

E. Average mitoxantrone fluorescence calculated over 10 different representative PC3 prostate cancer cells following treatment with 13.3 µM of free mitoxantrone (grey bars) and M4 micelles (black bars) at different time intervals. Minimal intracellular drug fluorescence was observed in case of M4 micelles ($p<0.01$) compared to the free drug in the first 30 minutes following treatment. Higher fluorescence was noticed after 3 hours of addition than 0.5 hours for both M4 micelles ($p<0.01$) and free mitoxantrone ($p<0.01$).

F. Concentration-dependent fluorescence observed in cells after exposure to different concentrations of free mitoxantrone and M4 micelles after 2 hours. Significant differences were observed between the two doses (both free drug and M4 micelles). ($p<0.01$)

The drug, detected by its characteristic far-red emission, was observed to be present in the whole cell in case of both free mitoxantrone and micellar formulations. This is similar to the observations by Smith et al. who reported preferential accumulation of mitoxantrone drug molecules within the cytoplasm, nuclear membrane, and nucleoli in drug-resistant murine cancer cells [288]. In our experiments, quantification of intracellular fluorescence indicated that in the initial 30 minutes following administration, lower fluorescence intensity was observed in the case of M4 micelles

compared to that observed with free mitoxantrone ($p<0.01$) (**Fig. 6-12E**). This could be due to the slow release of drug from the micelles in vitro. Further, a time- (**Fig. 6-12E**) and concentration-dependent (**Fig. 6-12F**) difference in the fluorescence of mitoxantrone ($p<0.01$) was observed in both treatments (free mitoxantrone and mitoxantrone-loaded M4 micelles). As may be expected, higher fluorescence intensities were observed at longer time points ($p<0.01$ between 0.5 and 3.0 hours; **Fig. 6-12E**).

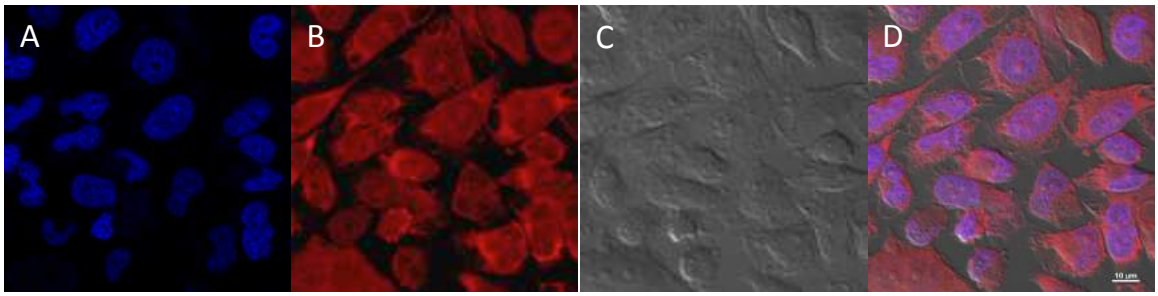

Figure 6-13. Cell uptake of free mitoxantrone into PC3 cancer cells. Confocal microscopy image showing the internalization of free (unencapsulated) mitoxantrone (13.3 μM) by PC3 human prostate cancer cells 3 hours following treatment. The nucleus was stained with DAPI **(A)** (blue; ex: 358 nm em: 461 nm). Mitoxantrone **(B)** was excited with 637 nm laser and emission was recorded in the far-red region at 670 nm with long pass filter. A false red color was employed to indicate mitoxantrone emission. Image **(C)** shows the phase contrast image and Image (d) shows the overlay image of a,b and c. Scale Bar : 10 μm.

Control equivalent concentrations of HEPES buffer alone and M1 PEG-DSPE micelles (without mitoxantrone) did not show intracellular fluorescence due to absence of the drug in these cases (data not shown). Previous studies with mitoxantrone indicated similar intracellular behaviour at these equivalent concentrations [246, 288-289]. For example, Sophie et al. [246] showed that cytosolic accumulation of mitoxantrone resulted in significant increase in breast cancer cell death. As shown in **Fig. 6-12E**, we observed similar integrated intracellular fluorescence intensity for the free and micelle-encapsulated drug after 1 hour.

A recent study on the internalization kinetics of the PEG-DSPE micelle loaded with doxorubicin indicated that PEG-DSPE micelles disassemble at the cell membrane lipid bilayer, resulting in release of doxorubicin at the cell surface [290]. PEG-phospholipid micelles have a hydrophobic core that is very similar to the phospholipids in the lipid bilayer, thus creating a strong driving force for the micelle core to 'open' at the cell surface due to hydrophobic

interactions between these moieties. Similar intracellular fluorescence intensity after 1-hour incubation with free and micelle-encapsulated (M4) mitoxantrone (**Fig. 6-12E**) could be an indication that the PEG-DSPE micelles release mitoxantrone at the cell surface followed by mitoxantrone entry into the cell by a flip-flop mechanism [291] across the lipid bilayer, or by its passive diffusion through the membrane.

Loss of cancer cell viability

Single agent (mitoxantrone alone; free drug vs. drug in micelles (M4))

The loss of cell viability following treatment with micelle-encapsulated mitoxantrone compared with that induced by free drug was studied in three different cancer cell lines: PC3 and T24 bladder cancer cells and MDA-MB-231 human breast cancer cells. **Fig. 6-4** shows a schematic of the different treatments. Both, free mitoxantrone and drug-loaded micelle (M4) induced a dose-dependent loss in viability of PC3 cells (**Fig. 6-14 A-B, grey triangles**).

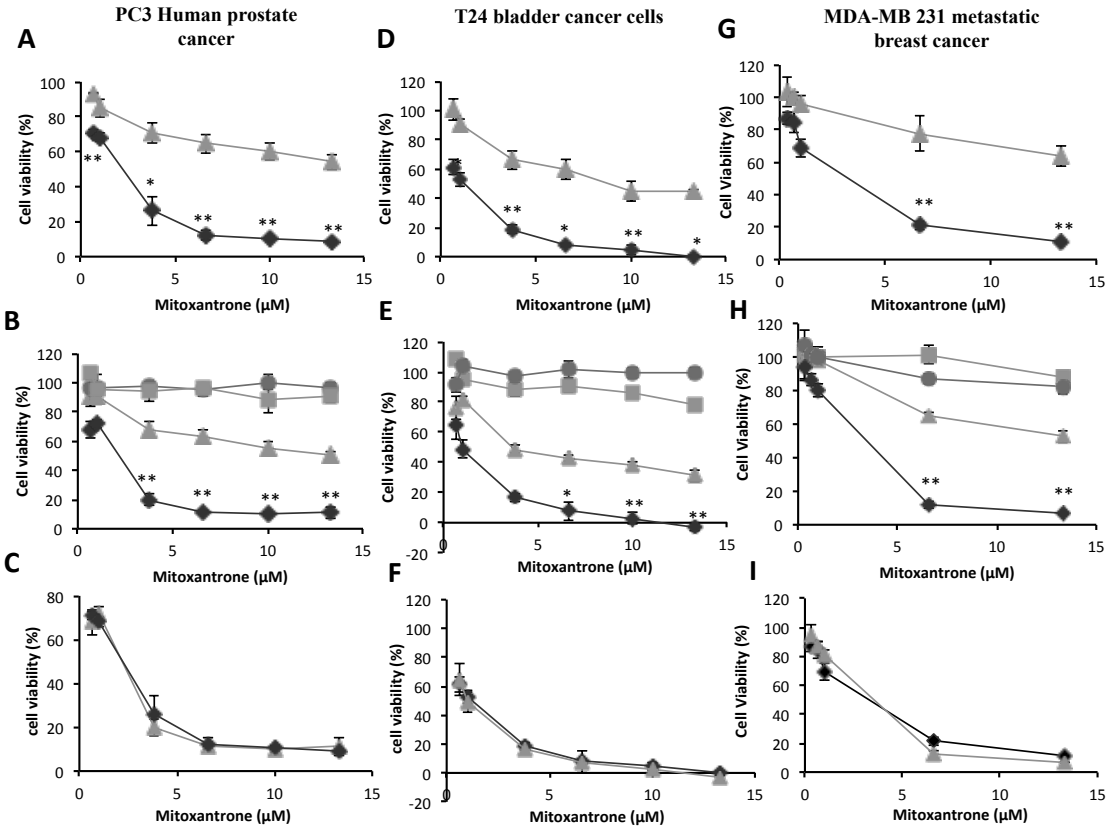

Figure 6-14. Efficacy of free mitoxantrone and mitoxantrone-loaded micelles in different cancer cells. Efficacy of free mitoxantrone and mitoxantrone-loaded micelles in **(A-C) PC3, (D-F) T24 bladder cancer cells** and **(G-I) MDA-MB 231** breast cancer cells is shown. Lines connecting data points are for visualization alone.

A,D,G. Single-agent cytotoxicity of free mitoxantrone (grey triangles) compared to cytotoxicity induced by sequential treatment of mitoxantrone and TRAIL (10 ng/mL)(black diamonds). Statistically significant differences between cell viability following single-agent and sequential mitoxantrone-TRAIL combination treatments are indicated by asterisks.

PC3 prostate cancer, T24 bladder cancer and MDA-MB-231 breast cancer cell viability after single-agent TRAIL treatment (24 h) was (94.55 ± 4.2%),(99.48 ± 7.17%) and(91.2 ± 5.7%) respectively.

B,E,H. Cytotoxicity of mitoxantrone-loaded micelles (M4) (grey triangles) as compared to cytotoxicity of sequential treatment of M4 micelles and 10 ng/mL TRAIL (black diamonds). Statistically significant differences between cell viability among single-agent and sequential treatments for the M4 micelles are shown by asterisks.

C,F,I. Comparison of sequential combination treatments of free mitoxantrone (black diamonds) and mitoxantrone encapsulated M4 micelles (grey triangles)is shown.

M4 micelles and the free mitoxantrone at equivalent drug concentrations caused similar levels of cytotoxicity, as shown in (**Fig. 6-14 A-B, grey triangles**). Negligible decrease in cell viability was observed in the case of empty micelles (**Fig. 6-15 A**).

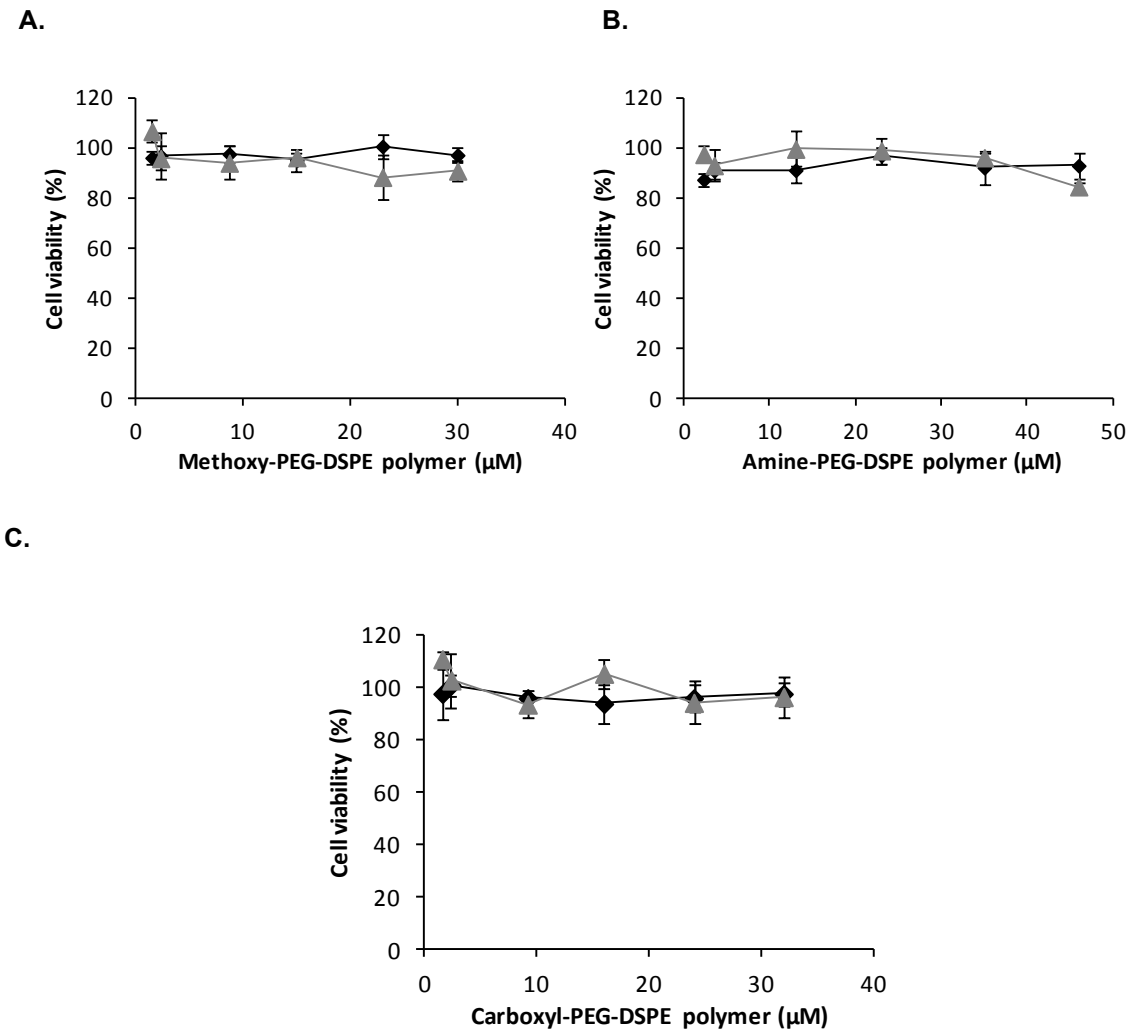

Figure 6-15: **Impact of empty micelles on cell viability**. Cell viability (%) in PC3 prostate cancer cells after single-agent treatment with M1 micelle **(A)** M2 micelle **(B)** M3 micelle **(C)** is shown in black diamonds. Sequential treatment of various polymers and 10 ng/mL of TRAIL are shown in grey triangles. Cell viability was estimated using the MTT cell viability assay. Lines connecting the data points are for visualization purpose only.

These results are well correlated with previous observations of cellular uptake of the drug (**Fig. 6-12 A-D and Fig. 6-13**). Free mitoxantrone and micelle-encapsulated mitoxantrone resulted in similar levels of intracellular fluorescence intensity within 1 hour of administration (**Fig. 6-12E**), suggesting equivalent accumulation of drug in the cells for both treatments. This is reflected in similar decreases in cell viability: Free mitoxantrone and drug-containing M4 micelles showed near-identical LC_{50} (equivalent drug concentration that induces a 50% decrease in cell viability) of approximately 13.3 μM (**Table 6-3**). Encapsulation of mitoxantrone in M4 micelles

resulted in enhanced levels of T24 bladder cancer cell death compared to free mitoxantrone (**Fig. 6-14 D-E; grey triangles**; $p<0.05$). The LC_{50} value of mitoxantrone in M4 micelles was 3.8 μM compared to 9 μM for the free mitoxantrone treatment.

Table 6-3. LC_{50} values of mitoxantrone (free drug or encapsulated in M4 micelles) in the different cancer cell lines investigated and reported as Mean ± SD. LC_{50} = concentration of drug required to induce loss of viability in 50% of cell population.

	PC3 cells		T24 cells		MDA-MB-231 cells	
Treatment	**Free drug**	**Drug in micelles (M4)**	**Free drug**	**Drug in micelles (M4)**	**Free drug**	**Drug in micelles (M4)**
Single-agent treatments (without TRAIL)	**> 13.3 μM (15 ± 2.0)**	**13.3 ± 1.9 μM**	**9 ± 1.7 μM**	**3.8 ± 0.5 μM**	**>> 13.3 μM (16.5 ± 2.0)**	**13.3 ± 1 μM**
Sequential treatments with 10 ng /mL TRAIL	**2.2 ± 0.7 μM**	**2.1 ± 0.4 μM**	**1.3 ± 0.6 μM**	**0.9 ± 0.3 μM**	**3.3 ± 0.5 μM**	**3.5 ± 0.3 μM**

Treatment with empty M1 micelles resulted in negligible loss of T24 viability (data not shown).

Differences in efficacy of micellar formulations compared to free drugs have been previously reported [292] and attributed to the delivery of drug as packets to the cells rather than in the free diffused form[293].

The MDA-MB-231 breast cancer cell line was more resistant to both, free and encapsulated mitoxantrone (**Fig. 6-14 G-H**; **grey triangles**). A 25-35% loss of viability was observed at 6.6 μM concentration of the drug, and 40-50% loss was seen beyond 13.3 μM concentration range. Empty micelles produced only a 10% reduction in viability at the highest concentration tested (micelle concentration equivalent to that required to deliver 13.3 μM mitoxantrone) (data not shown).

Combination Treatments: micellar delivery of mitoxantrone to sensitize cancer cells to TRAIL

Sequential treatments with TRAIL

Following micelle characterization and an investigation into the single-agent efficacy of free and encapsulated mitoxantrone, we conducted experiments designed to test whether micelle-encapsulated mitoxantrone was able to sensitize cancer cells to TRAIL-induced loss of cancer cell viability. We chose to employ a 10-ng/mL TRAIL concentration in these and previous [154] studies, since we are particularly interested in identifying combination treatments that are effective at lower TRAIL concentrations than previous studies[294-295] which employed a ten-fold higher concentration of the cytokine.

As a single-agent treatment, 10 ng/mL TRAIL induced ~5-10% cell death in PC3, T24 and MDA-MB-231 cells (**Fig. 6-16**), indicating resistance of these cells to TRAIL-induced death.

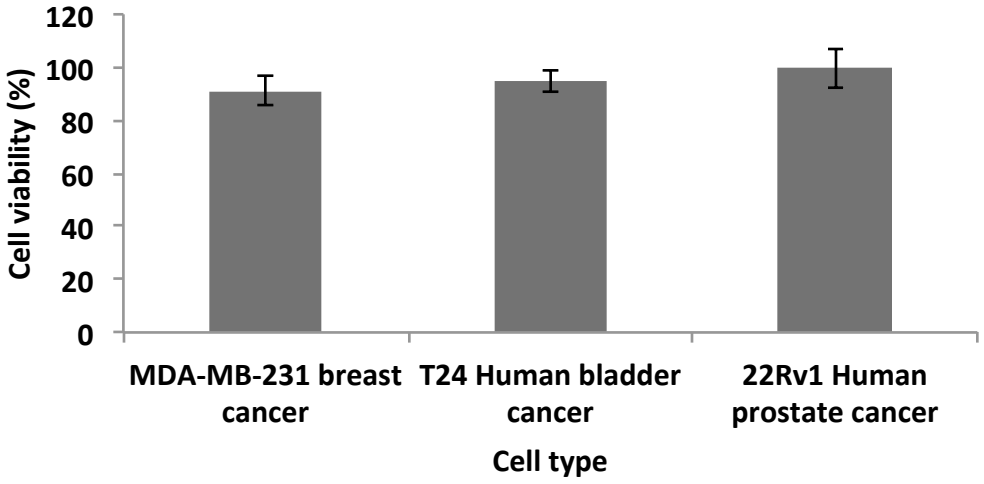

Figure 6-16: **Impact of TRAIL treatment alone on cell viability.** Cell viability (%) after single-agent treatment with 10 ng/mL of TRAIL for 24 hours in various cell lines. Cell viability was estimated using the MTT cell viability assay.

In addition, empty micelles (without mitoxantrone) did not induce cell death in combination with TRAIL, indicating that the micelles by themselves did not play a role in TRAIL sensitization. However, micelle-encapsulated mitoxantrone (M4) and free mitoxantrone were able to sensitize PC3 prostate cancer cells to TRAIL-induced death (**Fig. 6-14 A-B; black diamonds**). The

highest levels of synergy were observed at equivalent mitoxantrone concentrations of 3.8 μM and 6.6 μM in M4 micelles followed by 10 ng/mL TRAIL in PC3 prostate cancer cells. Single-agent TRAIL induced ~10% cell death and single-agent mitoxantrone in micelles (M4) at the two concentrations resulted in ~30% and ~35% cell death. However, the combination treatment resulted in ~75% ($p<0.05$) and ~85% ($p<0.05$) cell death at the respective M4 concentrations. These results are indicative of synergy between micelle-encapsulated mitoxantrone and TRAIL; the extent of cell death induced by the combination treatment (e.g. 75% at 3.8 μM) is greater than the sum (additive effect) of the two individual treatments (e.g. 10% for TRAIL alone + 30% for micelle-encapsulated mitoxantrone).

Table 6-3 shows LC_{50} values in the three cancer cell lines for free and micelle-encapsulated mitoxantrone (M4) in combination with TRAIL. Both free and micelle-encapsulated mitoxantrone were able to augment the effects of TRAIL in all these cells, leading to synergistic enhancement of cancer cell death. Although encapsulation in M4 micelles resulted in an increase in the efficacy of single-agent mitoxantrone in T24 cells, no such enhancement by encapsulation was seen in the case of the mitoxantrone-TRAIL combination in this cell line (**Fig. 6-14 D-E; black diamonds**). A similar sensitization profile was observed when M4 micelles were used to pretreat MDA-MB-231 breast cancer cells (**Figs. 6-14 G-H; black diamonds**).

Potential mechanisms involved in the synergy could include upregulation of death receptors following mitoxantrone treatment, downregulation of c-FLIP, a caspase 8 inhibitor, mitochondrial depolarization and ROS production induced by mitoxantrone. These collectively can help overcome cancer cell resistance to TRAIL-induced death. The total amount of chemotherapeutic drug needed to achieve same amount of cell death is reduced in case of synergistic combinations. This, in turn, can help reduce dose-dependent side effects associated with chemotherapeutic drugs. In addition, due to the selectivity of TRAIL for malignant cells, the combination of micelle-encapsulated mitoxantrone and TRAIL is an attractive synergistic treatment for ablation of cancer cells.

Comparison of sequential and simultaneous treatments of micelle-encapsulated mitoxantrone in combination with TRAIL

In addition to sequential treatments, cells were treated simultaneously with the free or micelle-encapsulated mitoxantrone (M4) and TRAIL in order to investigate whether this method of dosing had a different effect on cancer cell viability. Compared to the sequential treatments, simultaneous dosing with TRAIL and mitoxantrone resulted in reduced synergy (**Fig. 6-17**) between the drug-TRAIL combinations, (**Fig. 6-14 A-I**). These trends were observed for both free and micelle-encapsulated mitoxantrone and are consistent with our previous observations [154, 296]. One explanation for this observation could be that a finite period of time is required for sensitization to take place, and for cellular resistance mechanisms to TRAIL-mediated death to be overcome. It may also be the case that hitherto unknown interactions between micelles and TRAIL attenuate the latter's lethality when simultaneous treatments are applied. Taken together, our results demonstrate that sequential treatment with micellar mitoxantrone and TRAIL results in enhanced cell kill compared to simultaneous treatment with the same agents.

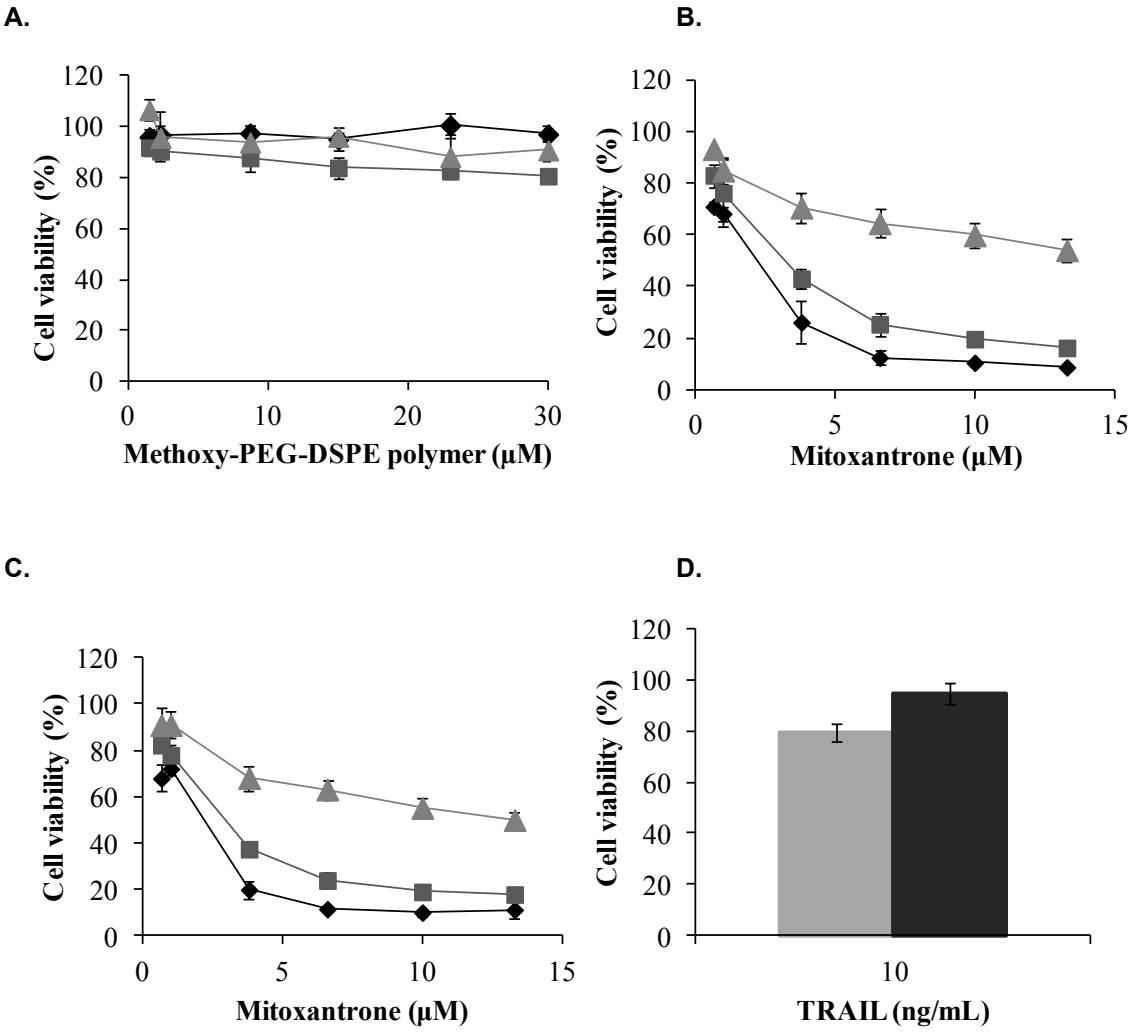

Figure 6-17. Comparison of different treatment modalities in PC3 human prostate cancer cells. Lines connecting data points are for visualization alone.

A. Single-agent treatment cytotoxicity of M1 micelles (grey triangles), simultaneous treatment of M1 micelles with TRAIL 10 ng/mL (grey squares) and sequential treatment of M1 micelles and TRAIL 10 ng/mL (black diamonds). Data points represent the concentration of PEG-DSPE associated with mitoxantrone in various treatments (30 µM polymer concentration was the highest used).

B. Single-agent treatment cytotoxicity of free mitoxantrone (grey triangles), simultaneous treatment of free mitoxantrone with 10 ng/mL TRAIL (grey squares) and sequential treatment of free mitoxantrone and 10 ng/mL TRAIL (black diamonds).

C. Single-agent treatment cytotoxicity of M4 micelles (grey triangles), simultaneous treatment of M4 micelles with 10 ng/mL TRAIL (grey squares) and sequential treatment of M4 micelles and 10 ng/mL TRAIL (black diamonds).

D. Control: Cytotoxicity of 10 ng/mL TRAIL (sequential treatments) (black bar) and cytotoxicity of 10 ng/mL TRAIL (simultaneous treatments) (grey bar). Experimental details provided in text.

Influence of terminal groups on micellar efficacy (single agent and sequential treatments)

In addition to the neutral (methoxy-terminated) micelles described previously, we employed empty (M2) and mitoxantrone-loaded (M5) amine-terminated micelles, as well as empty (M3) and mitoxantrone-loaded (M6) carboxyl-terminated micelles in order to investigate the effect of micelle surface chemistry on treatment efficacy. As shown in **Fig. 6-18**, the nature of the exterior micellar charge did not affect the efficacy of mitoxantrone-mediated cancer cell death, either as a single-agent treatment or in combination with TRAIL when administered as a sequential treatment. The synergy with TRAIL was maintained for all micelle types (M4-M6) (**Fig. 6-14B Fig. 6-18 B,D**). Empty micelles M2 and M3 (**Fig. 6-3**) showed no significant cytotoxicity (**Fig 6-15 B-C).**

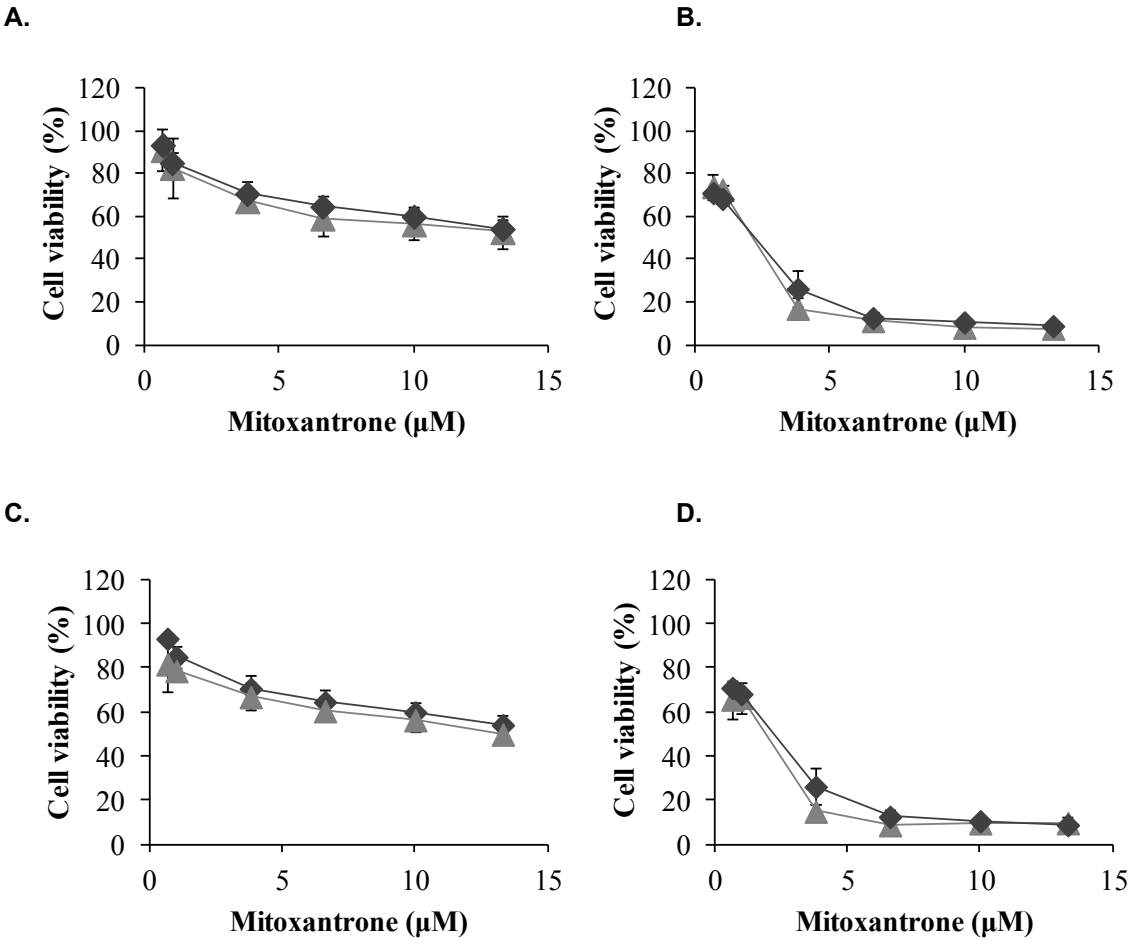

Figure 6-18. **Influence of micelle terminal groups on cytotoxicity on loss of PC3 human prostate cancer cell viability.** Lines connecting data points are for visualization alone.
A-B. Amine terminated micelles: **A**. Loss of cell viability following single agent treatment with free mitoxantrone (black diamonds) compared to mitoxantrone-loaded, amine-terminated M5 micelles (grey triangles) **B.** Loss of viability following sequential treatment of free mitoxantrone and 10 ng/mL TRAIL (black diamonds) compared to mitoxantrone-loaded, amine-terminated M5 micelles + 10 ng/mL TRAIL (grey triangles).
C-D. Carboxyl terminated micelles: **C.** Loss of viability following single agent treatment with free mitoxantrone (black diamonds) compared to mitoxantrone-loaded, carboxyl-terminated M6 micelles (grey triangles). **D.** Loss of viability following sequential treatment of free mitoxantrone and 10 ng/mL TRAIL (black diamonds) compared to mitoxantrone-loaded and carboxyl-terminated M6 micelles + 10 ng/mL TRAIL (grey triangles).

The lack of efficacy differences among the three micelle species may stem from micelle disassembly at the cell surface due to the previously-described interactions between phospholipids of these two entities [290, 297-298]. It has been suggested that due to the overall negative charge on the cell surface exterior, internalization of negatively charged species could

be hindered compared to the favorable electrostatic interactions between cells and positively charged counterparts [299]. However, it is possible that the energetics of attraction between the hydrophobic DSPE core of the micelle and the phospholipid bilayer outweigh the energetics of the repulsion between cells and the micelle. In addition, the flexibility of the outer PEG layer can facilitate interactions with the cell membrane.

6.4. CONCLUSION

We have successfully encapsulated mitoxantrone within PEG-DSPE micelles and have used the micellar form for ablation of prostate and breast cancer cells, both as a single-agent treatment and in synergistic combination with TRAIL. The efficacies of the micelle-based single-agent and synergistic treatments were similar to those observed with free mitoxantrone, indicating that encapsulation did not compromise efficacy of the drug. The advantages of encapsulation, compared to free-circulating mitoxantrone, arise from the extended longevity in the blood compartment of the micelle-enclosed form. Micelles with different surface functional groups – methoxy, amine, and carboxylic acid – demonstrated similar levels of drug loading of mitoxantrone and cancer cell ablation efficacy. Successful encapsulation, stability and efficacy of mitoxantrone-containing micelles opens up the door for sequential targeting of cancer with nanoparticles decorated with biomolecules for targeting, followed by delivery of TRAIL for targeted synergistic ablation of tumors in vivo.

CHAPTER 7: ADDITIONAL DEVELOPED METHODS: HIGH-THROUGHPUT FABRICATION OF SCALABLE POLYMERIC SCAFFOLDS FOR NOVEL PDNA LIGAND SCREENING

7.1. INTRODUCTION

Cells in human body associate with neighboring cells and tissues in three dimensions, but the laboratory cell culture techniques used to mimic the same in-vivo processes rely on two dimensional cell culture plates [34, 85]. Cells grown on these 2D plates do not mimic the human body [33]. They lack extensive cell-cell contact, nutrient and metabolite gradient, complex waste disposal system that exists in the body [21, 111]. Hence it is necessary that appropriate systems be used to capture the 3D nature of human body in the petridish in the research lab.

Macroporous scaffolds provide a 3D substrate with extensive surface area that matches the 3D environment the cells in the body reside in [300]. For example, these macroporous scaffolds can be designed to be extensively interconnected, mimicking the bone trabecular structure [301]. Bone trabeculae are characterized with a highly porous structure filled with bone marrow. Multiple macroporous materials have been used to create bone mimics that can capture stem cell growth and differentiation on them etc [300, 302-303]. Macroporous monoliths or scaffolds also find their use in industrial plasmid DNA chromatography [304]. Their macroporous structure provides higher surface area for reactivity, high permeability, large number of channels, without the issue of big pressure drops that occur with smaller microbead resin columns [305]. Traditional monolithic cultures are prepared via cryo-gelation/cryo-polymerization. Briefly, scaffold monomers are mixed with specific initiators (example: photoinitiators [306]) in an aqueous porogen system that is incubated below $0^{o}C$, above the freezing temperature of the monomers. Freezing of water (porogen) causes monomers to accumulate in highly concentrated pockets allowing robust reaction upon initiation. Temperature is increased to retrieve the macroporous monolithic column after sufficient polymerization [307].

These macroporous materials can also be made by using a porogen such as salt/glucose or sucrose etc, which are insoluble in polymer slurry, but are soluble in aqueous solvents [302]. The

polymer pre-gel is mixed with insoluble salt crystals and casted on a special device. Polymerization is initiated either by a catalyst or an enzyme added to the pre-gel mixture. Heat and light are also used to initiate polymerization. Once the polymerization and gelation are complete, the porogen is leached out using aqueous solvents such as water, leaving behind a macroporous scaffold.

A significant challenge in this approach is the absence of a device that can be used to create these systems in high throughput and easily retrieve them. We found existing technologies to be tedious and poor in yield. A critical problem exists in easy recovery of the polymeric macroporous scaffolds after their preparation. Hence, we wished to design and develop devices and methods for preparation of user desired polymeric scaffold materials (macroporous or non-macroporous) in high-throughput and their easy retrieval out of the device. This brief chapter describes the technique developed to generate macroporous amikagel ('Amikalith') in high-throughput for multiple biomedical applications such as plasmid DNA binding and cell culture. The chapter also describes the methodology for conjugation novel ligand doxorubicin to Amikagels and Amikaliths for enhanced pDNA binding. The high-throughput device described in chapter 2 was used to generate macroporous columns with NaCl porogen.

7.2. MATERIALS AND METHODS

Materials

Amikacin hydrate was purchased from TOKU-E (Bellingham, WA). Poly(ethylene glycol) diglycidyl ether (PEGDE) was purchased from Sigma-Aldrich Inc. (St Louis, MO). NaCl crystals were purchased from Avantor Performance Materials (Center Valley, PA). Doxorubicin was purchased from Ontario Chemicals (Guelph, Ontario). Qiagen Giga kits for pDNA extraction were purchased from Qiagen Inc. (Alameda, CA). 27 G needles were purchased from Becton, Dickinson and Company (Franklin Lakes, NJ). Chloroform was purchased from Acros Organics (Morris Plains, NJ). Different acrylic geometries were designed and cut using a Universal Laser Systems CO_2 laser cutter.

Preparation of Amikaliths I and II

For each monolith type, a pregel solution was formed by dissolving amikacin hydrate (100 mg, 0.17 mmoles) in dimethyl sulfoxide (DMSO) followed by the addition of poly(ethylene glycol) diglycidyl ether (PEGDE) in a mole ratio of 1:2. Amikacin hydrate and PEGDE were each dissolved in 0.5 mL DMSO. Both mixtures were combined and vortexed to form a uniform pregel solution.

Amikaliths II and I were formed using unfused salt and fused salt crystals respectively. NaCl crystals with an average initial diameter of 520 ± 170 μm were used in all experiments. Both acrylic device components were wrapped in a layer of paraffin wax tape and joined together to form an array of cylindrical gaps. A single side of the device was provided with a layer of parafilm to serve as a base for the hollow wells. To form Amikaliths I, cylindrical device wells were filled to the brim with NaCl crystals. The porogen in each well was treated with 10 μL of the pregel solution. The entire device-salt-pregel setup was incubated at 40^{o}C for 48 hours. Following incubation, the device was cracked open and salt-gel columns were removed using a 27 G needle. Columns were subjected to three washes in nanopure water, resulting in the final Amikalith I structure.

In preparation of Amikaliths II, a monolayer of salt crystals was deposited into a parafilm-wrapped container. The open container was placed in a 37^{o}C incubator with 95% humidity for one hour to achieve uniform wetting of the salt crystals. During this time, the device was prepared with parafilm wrappings. Immediately following one hour, the container was removed from the incubator and the wetted crystals were packed into the wells of the prepared acrylic device. After addition of the wetted crystals, excess salt was swept away until the thickness of the salt columns was equal to that of the device height. The salt filled device was left undisturbed at room temperature for 12 hours to allow the packed crystals to fuse and harden. The device was then cracked open and salt fused columns were carefully removed. Recovered salt columns were wetted with 10 μL of the Amikagel pregel solution. Gelation was initiated by incubating the monoliths at 40^{o}C for 24 hours after which the salt was dissolved in washes of nanopure water.

Amikalith II Swelling Ratio

Swelling ratio of Amikaliths II was calculated using the following equation obtained from Park et al. They define the swelling ratio of a hydrogel as the increase in weight caused by absorption of water:

$$\text{Swelling Ratio} = (W_s - W_d) / W_d$$

The weight of the dried Amikalith W_d was obtained after incubating the gel at 40ºC for 24 hours, while the weight of the saturated Amikalith W_s was taken upon swelling the gel in nanopure water. Three Amikaliths composed of 30 µL of pregel solution were chosen for swelling ratio measurements.

Amikalith II Surface Area using BET Analysis

Total surface area of macroporous Amikaliths II was calculated using a Brunauer-Emmett-Teller (BET) adsorption isotherm. Amikaliths II were prepared by submerging in increasing gradients of acetone. Once subjected to 100% acetone, the monoliths were dried and BET analysis was used to calculate total surface area per gram.

Scanning Electron Microscopy of Amikaliths I and II

Amikalith and PLGA surface morphologies were visualized using a field emission scanning electron microscope (FE-SEM; Philips FEI XL-30 SEM) at a voltage of 25 kV. Carbon tape attached to the aluminum stub was used to anchor scaffolds in place during preparation and imaging. Columns were sputter-coated with Au-Pt particles for 120 s (E1030 ion sputter). An accelerating voltage of 20 kV was used during SEM imaging.

pDNA Binding to Amikaliths II and I

Final Amikalith scaffolds used in plasmid DNA adsorption and desorption possessed a cylindrical shape characterized with a diameter of 2.5 mm and a thickness of 4.5 mm. Binding profiles were generated by incubating Amikaliths I and II with 15,000-60,000 ng of pDNA in 10 mM Tris-Cl buffer, pH 8.5 for 5 hours at room temperature (25ºC). Each Amikalith was deposited into a single

microtube containing a pDNA-buffer suspension with a total volume of 1 mL. Initial efforts to bind pDNA to Amikaliths using a rotisserie shaker yielded poor results. Rotation of the microtube containing the Amikalith in a pDNA-buffer suspension did not provide adequate mixing to allow pDNA to enter into the inner structure of the monolith. A force sufficient to push the pDNA through the Amikalith was needed. For this reason, a jerk motion was desired. Microtubes (2.0 ml) containing the suspension and a single Amikalith each were organized in a hammock-like fashion with both ends of the hammock clipped to a single side of the shaker. Each full rotation made by the shaker caused the microtube base of the hammock to reach a peak height, which quickly succumbed to gravity, producing the desired swing motion to thrust the pDNA in each microtube through its respective Amikalith structure.

Plasmid DNA concentration in the supernatant was measured using a NanoDrop Spectrophotometer after 5 hours of mixing. Mass balance was used to calculate the amount of pDNA adsorbed onto the matrix surface. The data obtained was used to form adsorption isotherm profiles for both Amikalith types. Following surface adsorption measurements, Amikaliths were submerged in acetone for 30 minutes and again in a second acetone wash for 15 minutes to sufficiently dehydrate the monoliths. Acetone was completely removed and Amikaliths were incubated at 40ºC for 24 hours. Dried Amikaliths were weighed and the weights were incorporated into binding profiles to normalize pDNA bound per unit volume of Amikalith. The data were fitted to a Langmuir isotherm in order to calculate the maximum binding capacity (Qmax) of Amikaliths I and II.

Conjugation of doxorubicin to Amikabeads and Amikaliths: Towards novel ligands for pDNA binding

Preparation doxorubicin Drug Solution

Doxorubicin (100mg, 543g/mol) was dissolved in 10mL of Dimethyl sulfoxide (DMSO) followed by addition of 50uL of triethylamine (TEA). The stock mixture of doxorubicin, DMSO and TEA (10mg/mL) was stored in a 20mL glass via at 4^{o}C for future use.

Conjugation of doxorubicin with crosslinker

Stock mixture was retrieved from 4^{o}C and preheated at 37^{o}C for 5 minutes. 1 mL of the 10 mg/mL of the stock mixture was mixed with 1, 4-Cyclohexanediol diglycidyl ether (CHDDE) in a mole ratio of 1:3. 5 mole equivalents of TEA was added to the mixture in a 20 mL glass vial and the final volume was brought upto 2 mL in DMSO. The glass container was covered by aluminum foil for minimizing any photobleaching and the mixture was stirred with magnetic beads for 8 hours at 320 rpm at room temperature to link one end of the crosslinker with the doxorubicin.

Formation of doxorubicin conjugated Amikabeads/Amikaliths

1mg of Amikabeads/ individual Amikalith unit was collected and washed with DMSO. Supernatant was decanted and Amikabeads/Amikaliths were transferred to the prepared doxorubicin-linker solution. The solution stirred at 320rpm for 8 hours at 25^{0}C. After reaction, the beads were thoroughly washed with DMSO and the diameter of conjugated doxo-beads were measured using an inverted microscope.

7.3. RESULTS AND DISCUSSION

Design of Acrylic Geometry for Amikagel Monolith Generation and Recovery

Current macroporous scaffold generation methods suffer from several drawbacks that we addressed while designing the high-throughput device. The device makes use of the molding technique in which a polymer pregel is added to a solid template which supports subsequent gelation [308]. While this is a well-established technique for gel formation, existing mold templates do not allow for easy removal of the 3D hydrogel following polymerization. For example, PLGA scaffolds may be formed by depositing the gel precursor into a polydimethylsiloxide (PDMS) mold and heating the construct to initiate polymerization. However, the mold provides no inherent means of releasing the final scaffold and tweezers are needed to remove the gel [309]. This presents the potential to damage the final structure. Similarly, a method of producing macroporous PLGA sheet and cylindrical scaffolds reports that a porogen-containing polymer

slurry is cast into a glass mold. Once semi-solidified, the sheet morphology required 1.5 h of air drying to remove from the mold [310].

In order to address these shortcomings, we developed a device to allow for the high-throughput fabrication and easy recovery of Amikalith scaffolds. **Figure 2-5** shows the final device design that consists of two mirror components with semi-circular teeth that may be linked to generate a central array of cylindrical wells. As described before, the greatest design strength and distinguishing factor was the incorporation of a central break line in the design that allowed very easy recovery. Both device sections were wrapped with a layer of paraffin wax tape for easy assembly and disassembly. A single layer of parafilm was applied to the bottom side of the device to close off the wells at one end. We were able to create the acrylic geometries in multiple shapes such as cylinder and cuboid (**Fig. 7-1 A-C**).

A. **B.** **C.**

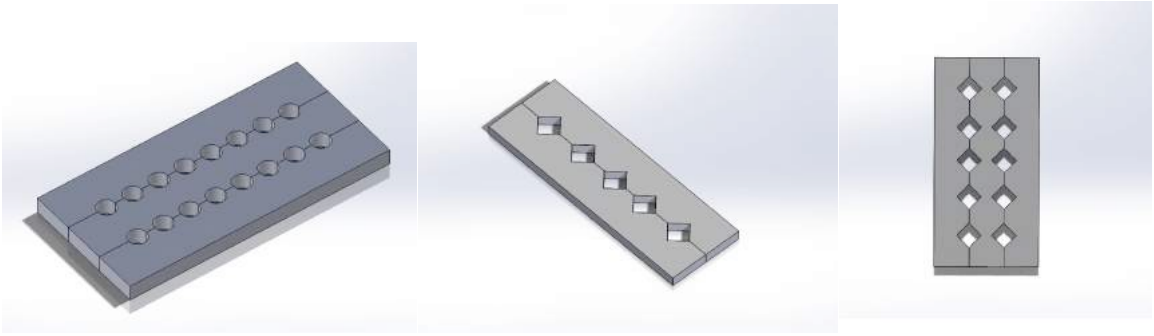

Figure 7-1. Various geometries of the polymeric scaffold generation device. Device components are all formed from laser cut acrylic sheets. (A.) Cylindrical monoliths are possible and were used to form Amikaliths for pDNA binding and elution. (B-C) Cube-shaped scaffolds are also possible using the same technology. Additional middle inset pieces may be included to increase the throughput of each device.

Synthesis of Amikaliths I and II

Amikaliths I and II were formed using unfused salt and fused salt crystals respectively. The specially developed device served as a support for unfused salt crystals and prevented columns from collapsing during sample preparation (Amikaliths I, II) and incubation (Amikalith I). Salt crystals underwent separate preparation stages in order to form Amikaliths I and II. Amikaliths I

were formed as a first proof of concept. No alterations were made to the salt crystals prior to pregel addition and gelation. In order to form the non-interconnected porous network of Amikaliths I, dry salt was poured into the wells of the device whereupon the porogen was wetted with the pregel mixture and columns were incubated at 40ºC. It was hypothesized that fusion of the salt crystals prior to the addition of pregel would facilitate the formation of interconnected pores in the final gel monolith. To validate this, Amikaliths II were prepared by packing the device wells with crystals that were previously exposed to 95% humidity at 37ºC for 1 hour (**Figure 7-2A**). The wetted NaCl crystals were allowed 12 hours to dry undisturbed in the device wells after which the device was cracked opened and the partially-fused salt columns were removed. Pregel was then added to the stand alone salt columns. Following incubation at 40ºC, all columns were subjected to three washes in nanopure water to completely dissolve the porogen, leaving behind a macroporous scaffold. The increased incubation time of Amikaliths I (48 hours) compared to Amikaliths II (24 hours) was to ensure complete gelation throughout the entire monolith contained in the device. **Figure 7-2B** outlines the fabrication processes for Amikaliths I and II.

A.

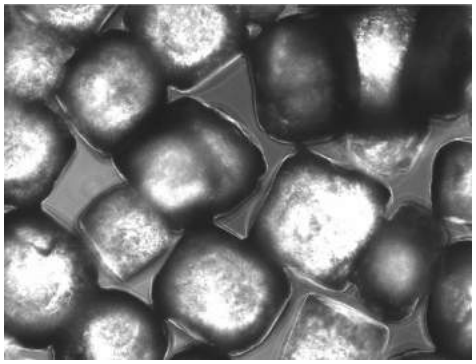

B.

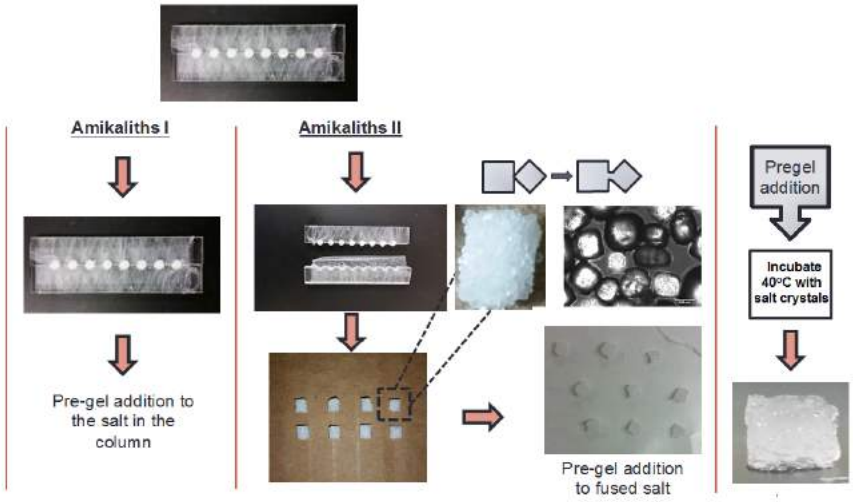

Figure 7-2. Salt fusion method to generate macroporous Amikaliths. (A) Monolayer of salt after exposure to 37ºC, 95% humidity for one hour. Salt crystals are visibly fused in order to bridge gaps between the crystals in order to facilitate formation of Amikaliths II. **(B)** The process of preparing each Amikalith type. Unfused salt crystals used to form Amikaliths I must be kept in the acrylic device during gelation while fused salt columns used for Amikaliths II may be removed before addition of pregel without collapsing.

Characterization of Amikaliths

No significant difference was observed in the pore sizes of salt unfused Amikaliths I (279 ± 83 µm) and salt fused Amikaliths II (280 ± 54 µm). Both monoliths provide pore diameters sufficiently large to allow for the adsorption of plasmid DNA macromolecules within the internal structure of the monoliths. Amikaliths I prepared using salt alone did not show any interconnections between the pores as observed in **Fig. 7-3A** image. It is likely that dry salt crystals with no prior fusion become completely encapsulated by pregel during its addition. Gelation occurs between the

spaces among the salt crystals, leading to separated pores following porogen leaching. In contrast, Amikalith II pores appear highly interconnected (**Fig. 7-3B**). Amikaliths II also display numerous bumps protruding from the surface.

A.

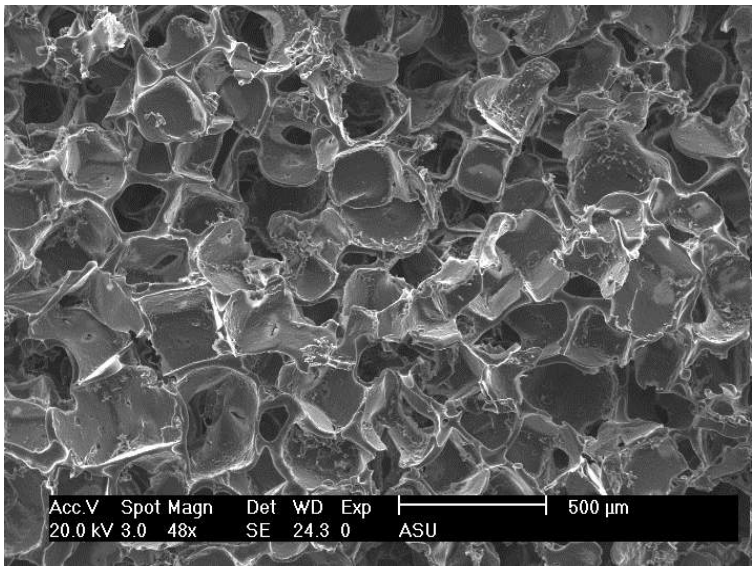

B.

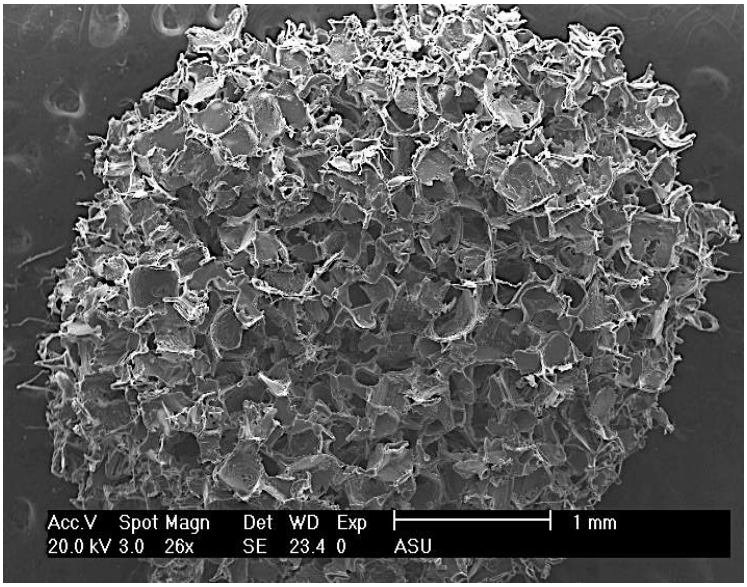

Figure 7-3. SEM images of Amikalith I (A) and Amikalith II (B). Amikaliths display macroscale pores following salt leaching. Amikalith I pores appear as separate compartments while Amikalith II pores appear interconnected (collapsed due to sample dehydration) and possess uneven surface topography, increasing surface area for pDNA binding.

As stated earlier, Amikaliths with a total pregel volume of 30 µL were selected for swelling ratio characterization. Larger volume and consequently heavier Amikaliths were chosen for swelling ratio studies to minimize variance in the measurements caused by scale sensitivity. Salt fused Amikaliths displayed a swelling ratio of 11.3 ± 2.1. BET analysis performed using 32 Amikalith structures revealed a surface area of approximately 1.5 m^2/g, which is comparable to the Amikabead surface area of approximately 2.0 m^2/g [83].

Plasmid DNA Binding to Amikaliths I and II

We hypothesized that a monolith structure with interconnected pores would offer a higher plasmid DNA binding potential compared to a matrix of non-interconnected pores. To validate this, plasmid DNA binding with unfused salt Amikaliths (I) and fused salt Amikaliths (II) was investigated. Amikaliths were incubated with 15,000-60,000 ng of pDNA for 5 hours. Because of the fragility of the Amikaliths, we looked to minimize the time required to adsorb pDNA to the structure surface. A total binding time of 5 hours was found to be a sufficient to reach the maximum binding capacity of the Amikaliths while preserving structural integrity of the columns. **Figure 7-4** shows the maximum binding capacity (Qmax) values for pDNA binding to Amikaliths I and II. Experimental data was fitted using a Langmuir isotherm. Qmax values were calculated by creating linearized adsorption isotherms for pDNA binding to Amikaliths I and II (n=3). Amikaliths II bound significantly higher pDNA (25.9 ± 6.1 µg pDNA / mg of Amikalith) compared to Amikaliths I (9.1 ± 3.5 µg pDNA / mg of Amikalith) ($p < 0.02$). It is likely that the interconnected pore structure allowed for significantly higher pDNA binding compared to the non-interconnected Amikaliths. T24 cells and Bj5ta human foreskin fibroblasts cultured on Amikaliths showed high viability indicating its use as novel cell culture platforms.

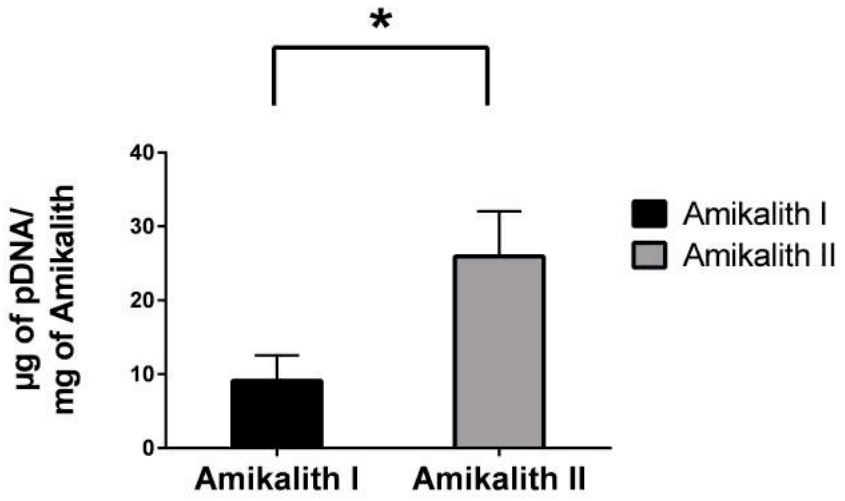

Figure 7-4. pDNA binding to Amikaliths. pDNA adsorption results show that Amikaliths II have a significantly higher binding capacity compared to Amikaliths I ($p < 0.02$*).

Doxorubicin Conjugation to Amikabeads and Amikaliths

The presence of numerous easily conjugable groups on Amikabeads and Amikaliths allows for incorporation and conjugation of multiple novel ligands on the surface. Doxorubicin is a very well known anticancer drug, which works by binding to the DNA double helix and prevents cell duplication [311]. We hypothesized that conjugation of DNA binding drugs such as doxorubicin, mitoxantrone to the surface of Amikaliths could allow for the exploitation of the DNA binding anti-neoplastic agents towards pDNA chromatography. Doxorubicin and mitoxantrone exploit either hydrophobic or a combination of hydrophobic and electrostatic interactions to bind DNA [277, 312-313]. Hence a resin with multiple copies of displayed doxorubicin or mitoxantrone can provide multi-modal capabilities to the resin for selective binding. These also provide an opportunity for screening of DNA binding ligands that have been used elsewhere for DNA interactions. Here, we provide the method developed to conjugate anticancer drug doxorubicin to the surface of Amikabeads. As shown in **Fig. 7-5**, excess 1,4 cyclohexanedimethanol diglycidyl ether was used to link one doxorubicin/Mitoxantrone to one of the epoxy ends of the cross-linker. Next, Amikabeads/Amikaliths were added to the solution and the other end of the epoxy was conjugated to the amines on the beads. **Fig. 7-6 A-C** shows the drug conjugated Amikabeads

and Amikaliths after the conjugation process. The process also gave rise to non-clumped beads after the final conjugation step (**Fig. 7-7 A-B**).

A.

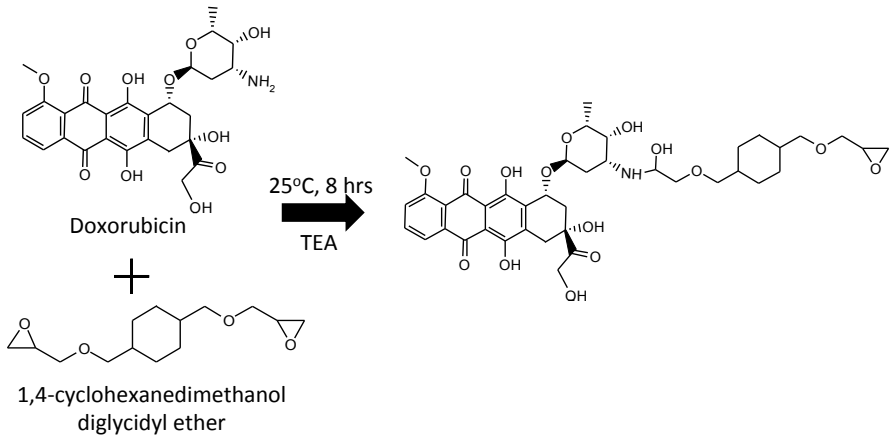

B.

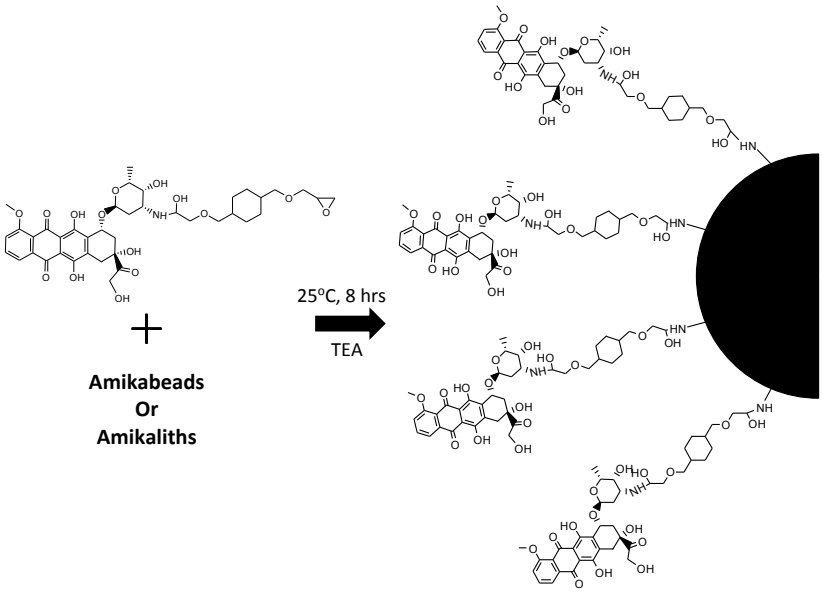

Figure 7-5. Doxorubicin conjugation to Amikabeads/Amikaliths. (A) Doxorubicin was stirred with 1,4-cyclohexanedimethanol diglycidyl ether with Triethylamine (1:3:5) in DMSO for 8 hours at 25°C. **(B)** Next, the Amikabeads/Amikaliths were added to the mixture for 8 hours followed by extensive washing steps to remove unreacted doxorubicin.

A. **B.**

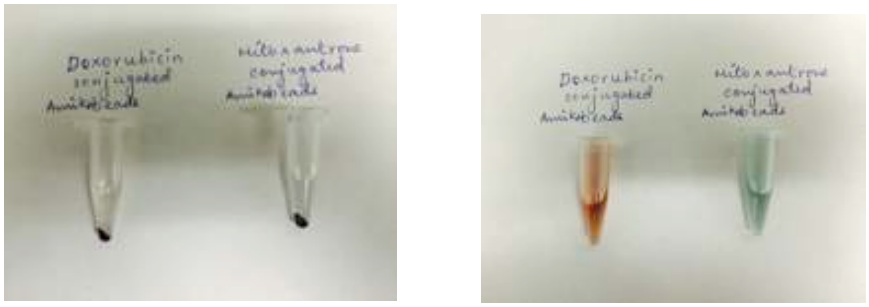

C.

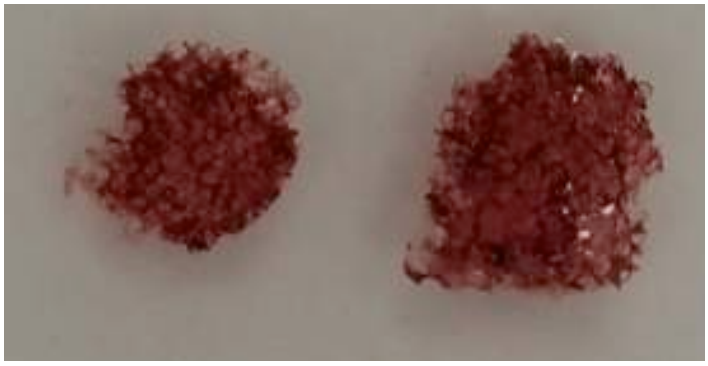

Figure. 7-6 Novel pDNA ligand conjugation to Amikabeads and Amikaliths. (A-B) Doxorubicin and Mitoxantrone conjugated Amikabeads **(C)** Doxorubicin conjugated monoliths.

Reversing the protocol by adding excess crosslinker to the beads at the first step did not yield good results. As shown in supporting information, big chunks of cross-linked beads were found when the cross-linker was added to the beads as the first step. Tuning the mole ratio of cross-linker: Amikabeads did not help either (**Fig. 7-7A**). Hence, it was hypothesized that working backwards, doxorubicin could be conjugated to one end of the epoxy end of the crosslinker, which could then be added to the intact beads (**Fig. 7-7B**). We propose this is as a better mechanism of conjugating any ligand to the surface of the any microbead or monolith surface.

A. **B.**

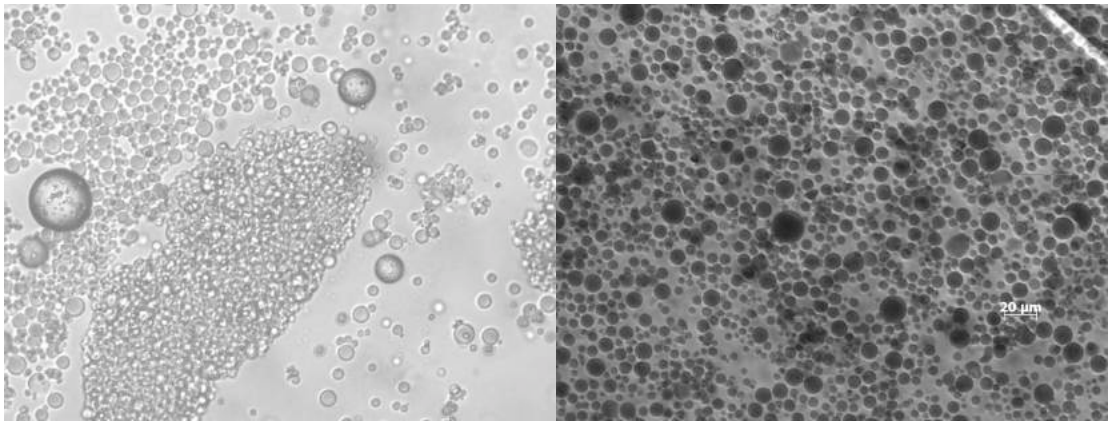

Figure. 7-7 Strategies to achieve non-aggregated ligand conjugated Amikabeads. (A) Reacting beads with 1,4-CHDDE initially before conjugating the drug yielded very poor results. Beads were seen to extensively clump. **(B)** Conjugating 1,4-CHDDE to doxorubicin followed by addition of the intermediate to the beads gave rise to minimal clumping and uniform conjugation.

Conjugation of anticancer drugs to the surface of Amikaliths could give rise to novel materials that can be used for plasmid DNA binding. These DNA binding anticancer drugs could provide multi-modal affinity to the resin to allow increased pDNA binding.

7.4. CONCLUSION

We present an novel methodology involving a novel, scalable, easy-to-use device to generate user defined 3D macroporous polymeric scaffolds in a high-throughput format for their use in substrates for plasmid DNA chromatography, cell culture, stem cell differentiation etc. The device's uniqueness comes from its smart design with parafilm coating, in-situ porogen fusion, in-situ polymerization and gelation and breakaway piece design that allow for easy recovery of formed matrices after gelation/polymerization. The unique design of the device has been tested numerous times to demonstrate its reproducibility. Amikaliths were generated in high throughput and conjugated with DNA binding anticancer drugs. Plasmid DNA was bound to the Amikaliths, which were found to be similar to Amikabeads in their plasmid DNA binding ability.

CHAPTER 8: CONCLUSIONS AND FUTURE PERSPECTIVES

8.1. SUMMARY OF FINDINGS

A complete cancer cure cannot be achieved till the problems of tumor dormancy and relapse are solved. Fundamental biological understanding of the underlying processes that control the tumor dormancy and relapse phases can help guide the design and development of targeted novel drugs and biologics. In parallel, development of novel high-throughput platforms that can capture the dormant phase of cancer in high-throughput will allow for rapid screening of drugs that work to ablate the target. Drug libraries in pharmaceutical companies can contain many thousands of molecules that need to be screened against a specific target [11]. High-throughput models allow for the establishment of massive parallel screens for that purpose. Despite decades of work in cancer, fundamental understanding of underlying phenomena regulating dormancy and relapse are still unclear. This dissertation work focuses on design and development of novel aminoglycoside based hydrogels that capture tumor dormancy and relapse in high-throughput for rational drug discovery and delivery. In this dissertation, we establish novel tumor dormancy and relapse model based on T24 bladder cancer cells and also utilize the high-throughput model for rational drug discovery and delivery. Further, we experimentally show novel strategies to accelerate the ablation of dormant tumors by modulating intracellular cation levels. Accelerating therapy will not only save the time required to achieve an appropriate outcome, but also provide cost benefits to the patient and the healthcare infrastructure etc.

Results in chapter 2 describe the design and development of novel aminoglycoside based hydrogel (‘Amikagel’) platform for high-throughput 3D tumor microenvironment generation. Multiple important physico-chemical properties such as mechanical stiffness, adhesivity, gelation kinetics, pore size and surface roughness of the hydrogel were tunable based on the monomer ratios used. Different formulation of Amikagels resulted in differential cell adhesivity and mechanical stiffness that further impacted the 3DTM formation on the hydrogel surface. We believe Amikagel to be the first hydrogel prepared using

aminoglycoside amikacin as a starting material towards its use in high-throughput 3D cell culture. Availability of multiple easily conjugable groups such as amino and hydroxyl groups allow for conjugation of other ligands on the Amikagel surface towards further biological studies. T24 bladder cancer cells were noted to undergo complete tumor dormancy on Amikagel substrate likely due to formation of extensive cell-cell contacts in a 3D format. High N-cadherin expression on cell surface has been shown to lead cells into cell cycle arrest via p27 CDK inhibitor modulation. Dormant 3DTMs generated on Amikagel surface were almost completely arrested in the G0/G1 phase of cell cycle (~95%), low in metabolite consumption and were also highly resistant to conventional chemotherapeutics such as mitoxantrone and docetaxel (even at high concentrations of 100 μM). Amikagels also allowed for generation of fibroblast co-culture 3DTMs with likely hypoxic and necrotic central core that were also resistant to conventional anticancer drugs.

Results obtained in chapter 3 define a new strategy for dormant cancer cell ablation. Dormant cancer cells had slight but significantly higher per cell protein content due to their arrest in the G0/G1 phase of cell cycle. We hypothesized that by targeting the protein production pathway, we can likely sensitize these dormant cells to ER stress mediated death. Targeting the ER to induce ER stress for apoptosis is a very widely explored area of research. Multiple drugs such as cycloheximide (translation inhibitor), thapsigargin (SERCA calcium channel inhibitor- chaperone inhibitor), brefeldin A (inhibitor of protein transport from ER to Golgi), bortezomib (proteasome inhibitor) have been used and studied to ablate the actively dividing cancer cells by targeting ER [64]. In dormant melanoma cancer cells, Ranganathan et al.[37, 67] found key adaptations in the ER that allowed dormant cells to mitigate chemotherapeutics and deal with ER stress. We found that inducing ER stress via thapsigargin mediated SERCA inhibition (calcium dependent chaperone inhibition) in concert with proteasome inhibition significantly sensitized the dormant cancer cells to death. The dormant bladder cancer cells were also very susceptible to proteasome inhibition alone, indicating an active proteasome is essential to maintain the dormant phenotype. However, the combination of both the drugs (bortezomib and thapsigargin) was significantly better in inducing total ablation of the dormant tumors compared to

individual drugs. We also showed that the dormant cancer cell death could be significantly accelerated by exogenous delivery of calcium cation under chronic ER stress. Under chronic ER stress, mitochondrial depolarization drives the apoptotic dormant cancer cell death that is initiated by two main pathways. Multifunctional transcriptional factor CHOP produced as a response to chronic ER stress, causes transcriptional activation of multiple pro-apoptotic proteins such as Bax and Bak that work to puncture the outer mitochondrial membrane. In addition, the calcium from cytoplasm and the ER are pumped into the mitochondrial matrix, depolarizing the potential difference thereby causing mitochondrial lysis. Our results strongly indicated that exogenous delivery of calcium cation could significantly accelerate the apoptotic dormant cancer cell death by increased mitochondrial depolarization under chronic ER stress induced by bortezomib and thapsigargin. Makridakis et al. [51] found active proteasome function in both metastatic and non-metastatic variant of T24 bladder cancer cells, further lending credence to our finding of dormant cancer sensitization via proteasome inhibition and chronic ER stress. Delivery of calcium to accelerate chronic ER stress mediated dormant cancer cell death is one of the most novel findings in this dissertation. This approach can be applied to multiple other cancers where ER stress pathways have shown promise in cancer ablation (Example: multiple myeloma).

Relapse from tumor dormancy occurs after an indefinite period of time and strategies to understand and prevent the phenomena are of urgent need. Results obtained in chapter 4 demonstrate that the chemo-mechanical modulation of Amikagel could result in relapse from tumor dormancy. Transfer of dormant T24 3D-DTMs to a pliant Amikagel (less stiff, more adhesive gel) resulted in selective separation and relapse of N-cadherin poor metastatic fraction of the bladder cancer cells. Specific engineering of Amikagel adhesivity resulted in selective migration and isolation of only the metastatic cancer cell fraction in the heterogeneous population. The N-cadherin rich population was seen to remain behind in the mother 3DTM. As described, N-cadherin downregulation and absence has been identified as an extremely poor prognostic indicator of metastases and death in bladder cancer patients. Selective isolation and separation of the metastatic fraction of the cancer cells makes Amikagel platform further unique and very important for future biological uses. Transfer of the dormant 3D-DTMs to 2D tissue culture plastic

did not cause selective isolation like that observed on Amikagels. Our results strongly indicate the need of engineering of the adhesivity of the surface to isolate only the most metastatic cell types. While highly adhesive surfaces cause complete cell migration and relapse (2D tissue culture plates), high non-adhesivity results in no migration and escape at all (AM3 Amikagel). Engineering adhesivity of the hydrogel in high-throughput can quickly identify the best formulation required to isolate the most metastatic cell fraction of the population. Such an approach would significantly lower the time required to isolate the most metastatic cell fractions. For example, a previous research by Nicholson et al.[171] demonstrated a lengthy procedure of isolation and enrichment of highly metastatic fraction of T24 cells by sequential injection into mice over 30-40 weeks. T24 cells were injected into six-week– old NCr nu/nu mice and were allowed to form metastases. The first generation metastatic cells were collected and reintroduced into mice to further enrich the metastatic population and so on. Three generations of enrichment took almost 30-40 weeks. Our engineered adhesivity strategy of metastatic cancer cell isolation can drastically cut down the time required to do so. Cells expressing differential N-cadherin on their surface can also be separated using this platform technology.

We used the high-throughput relapse platform to further identify drugs that not only can inhibit relapse from tumor dormancy, but also those that might accidently promote it. Docetaxel, a well-known microtubule inhibitor is also a cdc42 inhibitor that prevents the formation of actin rich filopodial extensions. Addition of docetaxel prior to chemo-mechanical modulation completely prevented the relapse from T24 3D-DTM. ROCK inhibitor on the other hand promoted the relapse likely due to Rac1 activation [181]. ROCK inhibitor did not change the cell cycle profile of the treated 3D-DTMs.

8.2. OTHER DEVELOPED TECHNOLOGIES

Natural binding affinity of aminoglycosides towards nucleic acids was exploited to design novel chromatographic resins for plasmid DNA binding and desorption. Amikagel was converted into microbead (‘Amikabead’) formulation via emulsion polymerization. Additional Span-80 was added after each batch process to reduce batch-to-batch size variations in the microbead

preparation. The pDNA binding affinity of parental Amikabeads was significantly improved by quaternization of the amines using glycidyl trimethyl ammonium groups. While 1M salt was sufficient to desorb almost all the adsorbed pDNA from the parental Amikabeads, it was not sufficient to desorb pDNA from the quaternized Amikabeads. We noted that additional of 15% isopropanol coupled with a temperature of 50^{o}C was required to desorb ~70% of adsorbed plasmid DNA from the Amikabeads. Mild hydrophobicity of the isopropanol (balance between increase in hydrophobicity and decrease in dielectric constant) likely played an important role in enhancing desorption of the plasmid DNA.

Additional methods were developed to generate macroporous amikagels ('Amikaliths') in high-throughput for plasmid DNA binding and novel substrates for cell culture. Novel high-throughput devices were prepared for rapid generation and recovery of multiple macroporous scaffolds in large numbers. Central break line in the acrylic devices was found to be highly useful and aided easy recovery of the macroporous gels. Additional insets allowed further improvements in the throughput of the system. As described, Amikabeads and Amikalith surfaces are rich in several easily conjugable groups such as amines and hydroxyls. This provides an opportunity to conjugate several ligands and spacers on the Amikagel surface for improving the specificity of the resin towards pDNA binding resin. Method to conjugate two such novel ligands is shown. Doxorubicin and mitoxantrone, bind DNA via a mixture of electrostatic and hydrophobic interactions were conjugated to the surface of Amikabeads and Amikaliths via an easy technique. Easy conjugation of multi-modal ligands on the surface of Amikagel will likely significantly advance the use of Amikabeads towards pDNA binding and desorption.

The dissertation also describes the development of mitoxantrone-loaded PEG-DSPE micelles for mitoxantrone delivery to prostate, bladder and breast cancer cells for TRAIL sensitization. TRAIL (TNF-related apoptosis-inducing ligand) induces apoptosis in cancer cells by specifically binding to the surface expressed death receptors. However, multiple resistance adaptations in the cancer cells reduce the efficacy of TRAIL therapies. We previously identified mitoxantrone as a novel TRAIL sensitizer in cancer cells [105]. We developed novel nanoparticle (micelle) based delivery vehicles of mitoxantrone to improve the pharmacokinetics of the drug.

Sequential delivery of the mitoxantrone loaded micelles followed by TRAIL delivery was seen to be better than simultaneous delivery of the micelles and TRAIL. Modification of the end group of the micelles from methoxy to positive amino and negatively charged carboxyl group did not have any impact on the efficacy of mitoxantrone TRAIL sensitization likely due to the mechanism of micelle unimers fusion with the cell membrane during the drug delivery.

8.3. FUTURE PERSPECTIVES

Future Direction 1 – Exosome Diagnostics - Diagnosis and continuous monitoring of tumor dormancy and relapse by studying the cell derived exosomal content

Exosomes are small lipid bilayer containing membrane vesicles that are secreted by a number of different cells in the body [314]. They are typically 40-100 nm and are secreted into the intracellular milieu. There has been an explosion of new findings regarding exosomes that cement their integral role in cell-cell communication [314-319]. Exosomes released from cancer cells have been shown to modulate distant metastatic sites to prepare them for cancer cell arrival [320]. Cancer cell exosomes were seen to induce the preparation of pre-metastatic niche in lungs and liver for eventual cancer cell arrival [320-321]. Exosomal content is cell type dependent and can be composed of lipid, DNA, mRNA, microRNAs and protein. Some of the most commonly identified proteins in exosomes are proteins such as β-actin, β-catenin, cofillin, tubulins and other heat shock proteins. Some of these proteins such as loss of β-catenin has been strongly implicated in bladder cancer progression and poor patient prognosis [322]. Often the exosomal content is a clear snapshot of the cell at any particular time-point. Melo et al. [323] showed that compared to exosomes derived from healthy cells, exosomes from cancer cells had disproportionately higher amount of mature miRNAs. Exosomal miRNA expression levels were significantly higher in serum exosomes isolated from 25 glioblastoma multiforme patients compared to the age and sex matched healthy volunteers. Serum exosomal levels of *miR-17-5p* and *miR-21* were found to be significantly higher in pancreatic adenocarcinoma patients compared to the healthy ones [324]. High levels of HSP90 protein were found in exosomes isolated from lung cancer patients compared to

the healthy patients [325]. These exosomal attributes further strengthen their utilization towards development of novel diagnostic tools that can track and monitor the disease [326]

Multiple factors such as high stability of exosomal content, rich and varied content, shedding of exosomes via urine, easy exosome isolation make them a good candidate for monitoring cancer growth, dormancy status and metastases [327]. Exosomal content secreted from a dormant cancer cell likely to be very different from a relapsed, actively dividing cell. Monitoring the content of exosomes shed through urine to diagnose tumor dormancy versus relapse can make the disease highly manageable. Rapid detection of relapse from tumor dormancy via urine paper tests can significantly reduce the fear associated with relapse from the cancer disease. T24 cells have already been shown to secrete exosomes into the extracellular media. Franzen et al. [328] found significant sensitization and epithelial to mesenchymal transition in primary urothelial cells when they were exposed to exosomes isolated from conditioned media of T24 and UMUC3 cells. Increased expression of several mesenchymal markers such as snail, α-smooth muscle actin, S100A4 and decreased expression of epithelial markers such as E-cadherin was observed in the urothelial cells. Further, they showed that exosomes isolated from bladder cancer patient could also cause the EMT in urothelial cells [328]. Their study also provides direct proof that T24 cells produce exosomes that have functional role in advancing the disease. After isolation of exosomes from the supernatants of dormant T24 and relapsed T24 cells, quantitative proteomic and RNA sequencing will allow for elucidation of differences in the cargoes of the two phenotypes of the cell line [329-330]. Identification of differences in exosomal cargoes will allow for design of novel easy to use, test strips that can detect and monitor the progression of the disease.

Future Direction 2 - High-throughput amikagel based microfluidic platforms to 1) identify triggers of relapse from tumor dormancy, and 2) rapidly isolate metastatic cancer cell fractions

This dissertation has been instrumental in establishing a novel chemo-mechanically tunable hydrogel platform that can capture multiple facets of tumor dormancy and relapse in high-throughput. A significant advantage of temperature-controlled gelation of Amikagel is the

possibility of using it as substrate in microfluidic devices etc. Pre-gel solutions can be easily flown into the microfluidic devices followed by T24 bladder cancer cells to form tumor spheroids within the microfluidic chambers. Microfluidic devices also allow generation of rapid combinatorial assays for high throughput drug screens etc [239, 331]. Kim et al. [296] developed a novel microfluidic platform for cell based large scale combinatorial drug assays. The microfluidic platform consisted of pneumatic valves that allowed accurate fluid control for rapid generation of diverse drug gradients. Kim et al. established the use of the technology by demonstrating TRAIL sensitization of PC3 prostate cancer cells by sequentially treating cells with anticancer drug doxorubicin. Using the microfluidic platform, they could rapidly develop 64 different mixtures of TRAIL and doxorubicin to identify the most effective concentration. Microfluidic platform developed for tumor dormancy and relapse could have multiple useful applications such as –

- As described, relapse from tumor dormancy and tumor progression happen due to not yet fully understood reasons. Our high throughput platform can allow for elucidation of critical factors that can drive a dormant tumor towards relapse and metastases. Utilizing our synthetic engineered adhesive amikagel substrates, we have isolated highly dormant cancer cell fractions from the heterogeneous mixture of T24 cell populations. A microfluidic platform cultured with these dormant cancer cells can allow for exposure of multiple triggers such as toxins (nicotine) [332], UV rays [333], stress factors [334], chemotherapeutic drugs [335], phthalates [336] etc, that can initiate relapse from tumor dormancy. The microfluidic platform can allow for exposure and identification of these triggers in high-throughput. Elucidation of bio-physico-chemical triggers that lead to relapse from tumor dormancy can allow design and development of strategies to avoid the spread of the disease.
- Identification of strategies to quickly isolate the most metastatic cancer cell fractions help in development of targeted drugs against those specific cells. We have shown a synthetic engineered adhesivity approach to isolate metastatic cells from a population of heterogeneous cancer cells. Exposing the heterogeneous cell spheroid to multiple different chemo-mechanical substrates could allow for development of biomaterial

strategies to quickly isolate the most metastatic cell types within one microfluidic system. Separately, placement of the heterogeneous 3DTM on a hydrogel with chemo-mechanical gradient can allow for migrational selection of most metastatic cell types, leaving behind a truly dormant cell population.

Other Future Directions –

1. **Whole cell RNA sequencing for novel phenotype specific drug discovery**

   Whole cell RNA extraction from 2D cells, dormant cells, mother 3D-DTM and relapsed cells would allow for sequencing and identification of specific set of genes that are upregulated in a each phenotype. Transient phenotype specific RNA expression can lead to fundamental biological understanding of underlying phenomena that governs each state of the cell. These will likely spur the identification of novel drug targets against tumor dormancy and relapse.

2. **Conjugation of multiple DNA binding anticancer drugs on Amikabead/Amikalith surface for novel pseudoaffinity resins**

   Amikabead/Amikalith provide a surface with ample easily conjugable groups such as hydroxyls and amines that can be rapidly conjugated to multiple DNA binding ligands. We developed an easy to use method to link model drugs mitoxantrone and doxorubicin to the surface of Amikabeads and Amikaliths respectively. Similar strategy could be used to conjugate multiple other DNA intercalating anticancer drugs such as daunorubicin, pixantrone, amonafide etc. Significant amount of research has gone into developing DNA binding anticancer drugs with specialized activities such as pure intercalators (flavones, ellipticines), groove binders (streptonigrin), mixed groove binders and intercalators (amonafide, anthracyclines, mitoxantrone, pixantrone) and covalent intercalators (psorospermin) etc [337]. Advances made in designing novel DNA binding ligands for anti-cancer activity can be directly applied to designing novel ligands and ligand combinations that can selectively bind and extract desired plasmid DNA from whole bacterial broths.

THESIS CONTRIBUTION - This dissertation describes multiple inventions regarding design and development of aminoglycoside based hydrogels for applications in high-throughput cell culture models of tumor dormancy, relapse (for drug discovery and development) and novel chromatographic resins for plasmid DNA biotechnology:

1. The first demonstration and development of amikacin aminoglycoside based hydrogel with tunable chemo-mechanical properties of mechanical stiffness and adhesivity.
2. Aminoglycoside based hydrogels for high-throughput 3D cell culture platforms of prostate, bladder, breast and pancreatic cancer cell types.
3. Novel high-throughput in-vitro platform of tumor dormancy, relapse and micrometastases in a 96 well plate format
4. Identification of chronic ER stress as a novel pathway to induce apoptosis in dormant bladder cancer 3DTMs.
5. Acceleration of chronic ER stress induced apoptosis by exogenous delivery of calcium to the cell cytoplasm.
6. Identification of synthetic material strategies for rapid isolation and separation of metastatic cell fractions from a heterogeneous cancer cell population.
7. Design and development of novel aminoglycoside based microbeads and macroporous gels for pDNA binding and recovery.

In addition, this dissertation also describes generation of novel acrylic devices for high-throughput generation of user desired polymeric scaffolds and micellar mitoxantrone drug delivery of TRAIL sensitizer to sensitize multiple cancer cell lines to TRAIL mediated cell death:

8. Micellar delivery of anticancer drug mitoxantrone towards TRAIL sensitization of bladder, prostate and breast cancer cell lines in-vitro.

9. Design and development of high-throughput acrylic based devices for rapid and high-throughput generation of user desired macroporous and non-macroporous polymeric scaffolds.

REFERENCES

1. Pestka, S., Inhibitors of ribosome functions. *Annual Reviews in Microbiology* **1971,** *25* (1), 487-562.

2. Reynolds, A.; Hamilton-Miller, J.; Brumfitt, W., Newer aminoglycosides—amikacin and tobramycin: an in-vitro comparison with kanamycin and gentamicin. *Br med J* **1974,** *3* (5934), 778-780.

3. Taber, H. W.; Mueller, J.; Miller, P.; Arrow, A., Bacterial uptake of aminoglycoside antibiotics. *Microbiological reviews* **1987,** *51* (4), 439.

4. Fourmy, D.; Recht, M. I.; Puglisi, J. D., Binding of neomycin-class aminoglycoside antibiotics to the A-site of 16 S rRNA. *Journal of molecular biology* **1998,** *277* (2), 347-362.

5. Rege, K.; Hu, S. H.; Moore, J. A.; Dordick, J. S.; Cramer, S. M., Chemoenzymatic synthesis and high-throughput screening of an aminoglycoside-polyamine library: identification of high-affinity displacers and DNA-binding ligands. *Journal of the American Chemical Society* **2004,** *126* (39), 12306-12315.

6. Moore, R. D.; Lietman, P. S.; Smith, C. R., Clinical response to aminoglycoside therapy: importance of the ratio of peak concentration to minimal inhibitory concentration. *Journal of Infectious Diseases* **1987,** *155* (1), 93-99.

7. Kunz-Schughart, L. A.; Freyer, J. P.; Hofstaedter, F.; Ebner, R., The Use of 3-D Cultures for High-Throughput Screening: The Multicellular Spheroid Model. *Journal of Biomolecular Screening* **2004,** *9* (4), 273-285.

8. Szymański, P.; Markowicz, M.; Mikiciuk-Olasik, E., Adaptation of high-throughput screening in drug discovery—toxicological screening tests. *International journal of molecular sciences* **2011,** *13* (1), 427-452.

9. Hughes, J.; Rees, S.; Kalindjian, S.; Philpott, K., Principles of early drug discovery. *British journal of pharmacology* **2011,** *162* (6), 1239-1249.

10. Macarron, R.; Banks, M. N.; Bojanic, D.; Burns, D. J.; Cirovic, D. A.; Garyantes, T.; Green, D. V.; Hertzberg, R. P.; Janzen, W. P.; Paslay, J. W., Impact of high-throughput screening in biomedical research. *Nat. Rev. Drug Discov.* **2011,** *10* (3), 188-195.

11. VC Guido, R.; Oliva, G.; D Andricopulo, A., Modern drug discovery technologies: opportunities and challenges in lead discovery. *Combinatorial chemistry & high throughput screening* **2011,** *14* (10), 830-839.

12. LaBarbera, D. V.; Reid, B. G.; Yoo, B. H., The multicellular tumor spheroid model for high-throughput cancer drug discovery. *Expert Opinion on Drug Discovery* **2012,** *7* (9), 819-830.

13. Tung, Y.-C.; Hsiao, A. Y.; Allen, S. G.; Torisawa, Y.-s.; Ho, M.; Takayama, S., High-throughput 3D spheroid culture and drug testing using a 384 hanging drop array. *Analyst* **2011,** *136* (3), 473-478.

14. Dickey, C. A.; Eriksen, J.; Kamal, A.; Burrows, F.; Kasibhatla, S.; Eckman, C. B.; Hutton, M.; Petrucelli, L., Development of a high throughput drug screening assay for the detection of changes in tau levels-proof of concept with Hsp90 inhibitors. *Current Alzheimer Research* **2005,** *2* (2), 231-238.

15. Galietta, L. V.; Jayaraman, S.; Verkman, A., Cell-based assay for high-throughput quantitative screening of CFTR chloride transport agonists. *American Journal of Physiology-Cell Physiology* **2001,** *281* (5), C1734-C1742.

16. Xu, X.; Farach-Carson, M. C.; Jia, X., Three-dimensional in vitro tumor models for cancer research and drug evaluation. *Biotechnology advances* **2014,** *32* (7), 1256-1268.

17. Edmondson, R.; Broglie, J. J.; Adcock, A. F.; Yang, L., Three-dimensional cell culture systems and their applications in drug discovery and cell-based biosensors. *Assay and drug development technologies* **2014,** *12* (4), 207-218.

18. Bhadriraju, K.; Chen, C. S., Engineering cellular microenvironments to improve cell-based drug testing. *Drug discovery today* **2002,** *7* (11), 612-620.

19. Birgersdotter, A.; Sandberg, R.; Ernberg, I. In *Gene expression perturbation in vitro—a growing case for three-dimensional (3D) culture systems*, Seminars in cancer biology, Elsevier: **2005**; pp 405-412.

20. Timmins, N.; Nielsen, L., Generation of Multicellular Tumor Spheroids by the Hanging-Drop Method. In *Tissue Engineering*, Hauser, H.; Fussenegger, M., Eds. Humana Press: **2007**; Chapter 8, pp 141-151.

21. Bin Kim, J.; Stein, R.; O'Hare, M. J., Three-dimensional in vitro tissue culture models of breast cancer - a review. *Breast Cancer Research and Treatment* **2004,** *85* (3), 281-291.

22. Weirether, F. J.; Walker, J. S.; Lincoln, R. E., A precise method for replicating suspension cultures of mammalian cells. *Applied microbiology* **1968,** *16* (6), 841-844.

23. Hughes, C. S.; Postovit, L. M.; Lajoie, G. A., Matrigel: a complex protein mixture required for optimal growth of cell culture. *Proteomics* **2010,** *10* (9), 1886-1890.

24. Pickl, M.; Ries, C., Comparison of 3D and 2D tumor models reveals enhanced HER2 activation in 3D associated with an increased response to trastuzumab. *Oncogene* **2009,** *28* (3), 461-468.

25. Petrylak, D. P., Chemotherapy for advanced hormone refractory prostate cancer. *Urology* **1999,** *54* (6A), 30-35.

26. Röcken, M., Early tumor dissemination, but late metastasis: insights into tumor dormancy. *The Journal of clinical investigation* **2010,** *120* (6), 1800.

27. Wells, A.; Griffith, L.; Wells, J. Z.; Taylor, D. P., The dormancy dilemma: quiescence versus balanced proliferation. *Cancer research* **2013,** *73* (13), 3811-3816.

28. Mehlen, P.; Puisieux, A., Metastasis: a question of life or death. *Nature Reviews Cancer* **2006,** *6* (6), 449-458.

29. Scully, O. J.; Bay, B.-H.; Yip, G.; Yu, Y., Breast cancer metastasis. *Cancer Genomics-Proteomics* **2012,** *9* (5), 311-320.

30. Páez, D.; Labonte, M. J.; Bohanes, P.; Zhang, W.; Benhanim, L.; Ning, Y.; Wakatsuki, T.; Loupakis, F.; Lenz, H.-J., Cancer dormancy: a model of early dissemination and late cancer recurrence. *Clinical Cancer Research* **2012,** *18* (3), 645-653.

31. Shiozawa, Y.; Pedersen, E. A.; Patel, L. R.; Ziegler, A. M.; Havens, A. M.; Jung, Y.; Wang, J.; Zalucha, S.; Loberg, R. D.; Pienta, K. J., GAS6/AXL axis regulates prostate cancer invasion, proliferation, and survival in the bone marrow niche. *Neoplasia (New York, NY)* **2010,** *12* (2), 116.

32. Aguirre-Ghiso, J. A., Models, mechanisms and clinical evidence for cancer dormancy. *Nature Reviews Cancer* **2007,** *7* (11), 834-846.

33. Elliott, N. T.; Yuan, F., A Review of Three-Dimensional In Vitro Tissue Models for Drug Discovery and Transport Studies. *J. Pharm. Sci.* **2011,** *100* (1), 59-74.

34. Derda, R.; Laromaine, A.; Mammoto, A.; Tang, S. K. Y.; Mammoto, T.; Ingber, D. E.; Whitesides, G. M., Paper-supported 3D cell culture for tissue-based bioassays. *Proceedings of the National Academy of Sciences* **2009,** *106* (44), 18457-18462.

35. Wenzel, C.; Riefke, B.; Gründemann, S.; Krebs, A.; Christian, S.; Prinz, F.; Osterland, M.; Golfier, S.; Räse, S.; Ansari, N., 3D high-content screening for the identification of compounds that target cells in dormant tumor spheroid regions. *Experimental cell research* **2014,** *323* (1), 131-143.

36. Hsiao, A. Y.-C., 3D spheroid culture systems for metastatic prostate cancer dormancy studies and anti-cancer therapeutics development. **2011**.

37. Ranganathan, A. C.; Adam, A. P.; Zhang, L.; Aguirre-Ghiso, J. A., Tumor cell dormancy induced by p38SAPK and ER-stress signaling: an adaptive advantage for metastatic cells? *Cancer biology & therapy* **2006,** *5* (7), 729-735.

38. Barkan, D.; Green, J. E.; Chambers, A. F., Extracellular matrix: a gatekeeper in the transition from dormancy to metastatic growth. *European Journal of Cancer* **2010,** *46* (7), 1181-1188.

39. Yong, F.; Yihong, W.; Yulei, W.; Yan, M.; Junlan, Z.; Honglei, J.; Jingxia, L.; Dongyun, Z.; Yonghui, Y.; Xue-Ru, W., A new tumour suppression mechanism by p27Kip1: EGFR down-regulation mediated by JNK/c-Jun pathway inhibition. *Biochemical Journal* **2014,** *463* (3), 383-392.

40. Aguirre-Ghiso, J. A.; Estrada, Y.; Liu, D.; Ossowski, L., ERKMAPK activity as a determinant of tumor growth and dormancy; regulation by p38SAPK. *Cancer research* **2003,** *63* (7), 1684-1695.

41. Aguirre-Ghiso, J. A.; Liu, D.; Mignatti, A.; Kovalski, K.; Ossowski, L., Urokinase receptor and fibronectin regulate the ERKMAPK to p38MAPK activity ratios that determine carcinoma cell proliferation or dormancy in vivo. *Molecular Biology of the Cell* **2001,** *12* (4), 863-879.

42. Barkan, D.; Kleinman, H.; Simmons, J. L.; Asmussen, H.; Kamaraju, A. K.; Hoenorhoff, M. J.; Liu, Z.-y.; Costes, S. V.; Cho, E. H.; Lockett, S., Inhibition of metastatic outgrowth from single dormant tumor cells by targeting the cytoskeleton. *Cancer research* **2008,** *68* (15), 6241-6250.

43. Pillai, M. S.; Sapna, S.; Shivakumar, K., p38 MAPK regulates G1-S transition in hypoxic cardiac fibroblasts. *The international journal of biochemistry & cell biology* **2011,** *43* (6), 919-927.

44. Thornton, T. M.; Rincon, M., Non-classical p38 map kinase functions: cell cycle checkpoints and survival. *Int J Biol Sci* **2009,** *5* (1), 44-51.

45. Siegel, R.; Ma, J.; Zou, Z.; Jemal, A., Cancer statistics, 2014. *CA: a cancer journal for clinicians* **2014,** *64* (1), 9-29.

46. Siegel, R. L.; Miller, K. D.; Jemal, A., Cancer statistics, 2015. *CA: a cancer journal for clinicians* **2015,** *65* (1), 5-29.

47. Gildea, J. J.; Golden, W. L.; Harding, M. A.; Theodorescu, D., Genetic and phenotypic changes associated with the acquisition of tumorigenicity in human bladder cancer. *Genes, Chromosomes and Cancer* **2000,** *27* (3), 252-263.

48. Jin, H.; Yu, Y.; Hu, Y.; Lu, C.; Li, J.; Gu, J.; Zhang, L.; Huang, H.; Zhang, D.; Wu, X.-R., Divergent behaviors and underlying mechanisms of cell migration and invasion in non-metastatic T24 and its metastatic derivative T24T bladder cancer cell lines. *Oncotarget* **2015,** *6* (1), 522.

49. Qu, H.; Ma, B.; Yuan, H.-F.; Wang, Z.-Y.; Guo, S.-J.; Zhang, J., Effect of salinomycin on metastasis and invasion of bladder cancer cell line T24. *Asian Pacific journal of tropical medicine* **2015,** *8* (7), 578-582.

50. Laidler, P.; Gil, D.; Pituch-Noworolska, A.; Ciołczyk, D.; Ksiazek, D.; Przybyło, M.; Lityńska, A., Expression of beta1-integrins and N-cadherin in bladder cancer and melanoma cell lines. *Acta biochimica Polonica* **1999,** *47* (4), 1159-1170.

51. Makridakis, M.; Gagos, S.; Petrolekas, A.; Roubelakis, M. G.; Bitsika, V.; Stravodimos, K.; Pavlakis, K.; Anagnou, N. P.; Coleman, J.; Vlahou, A., Chromosomal and proteome analysis of a new T24‐based cell line model for aggressive bladder cancer. *Proteomics* **2009,** *9* (2), 287-298.

52. Kottke, T.; Boisgerault, N.; Diaz, R. M.; Donnelly, O.; Rommelfanger-Konkol, D.; Pulido, J.; Thompson, J.; Mukhopadhyay, D.; Kaspar, R.; Coffey, M., Detecting and targeting tumor relapse by its resistance to innate effectors at early recurrence. *Nature medicine* **2013**.

53. Hamasaki, T.; Hattori, T.; Kimura, G.; Nakazawa, N., Tumor progression and expression of matrix metalloproteinase-2 (MMP-2) mRNA by human urinary bladder cancer cells. *Urological research* **1998,** *26* (6), 371-376.

54. Lascombe, I.; Clairotte, A.; Fauconnet, S.; Bernardini, S.; Wallerand, H.; Kantelip, B.; Bittard, H., N-cadherin as a novel prognostic marker of progression in superficial urothelial tumors. *Clinical cancer research* **2006,** *12* (9), 2780-2787.

55. Rieger-Christ, K. M.; Cain, J. W.; Braasch, J. W.; Dugan, J. M.; Silverman, M. L.; Bouyounes, B.; Libertino, J. A.; Summerhayes, I. C., Expression of classic cadherins type I in urothelial neoplastic progression. *Human pathology* **2001,** *32* (1), 18-23.

56. Asano, K.; Duntsch, C. D.; Zhou, Q.; Weimar, J. D.; Bordelon, D.; Robertson, J. H.; Pourmotabbed, T., Correlation of N-cadherin expression in high grade gliomas with tissue invasion. *Journal of neuro-oncology* **2004,** *70* (1), 3-15.

57. Zhan, D. q.; Wei, S.; Liu, C.; Liang, B. y.; Ji, G. b.; Chen, X. p.; Xiong, M.; Huang, Z. y., Reduced N‐cadherin expression is associated with metastatic potential and poor surgical outcomes of hepatocellular carcinoma. *Journal of gastroenterology and hepatology* **2012,** *27* (1), 173-180.

58. Jäger, T.; Becker, M.; Eisenhardt, A.; Tilki, D.; Tötsch, M.; Schmid, K. W.; Romics, I.; Rübben, H.; Ergün, S.; Szarvas, T., The prognostic value of cadherin switch in bladder cancer. *Oncology reports* **2010,** *23* (4), 1125-1132.

59. Palade, G. E., The endoplasmic reticulum. *The Journal of biophysical and biochemical cytology* **1956,** *2* (4), 85-98.

60. Arias, I. M.; Doyle, D.; Schimke, R. T., Studies on the synthesis and degradation of proteins of the endoplasmic reticulum of rat liver. *Journal of Biological Chemistry* **1969,** *244* (12), 3303-3315.

61. Helenius, A.; Trombetta, E. S.; Hebert, D. N.; Simons, J. F., Calnexin, calreticulin and the folding of glycoproteins. *Trends in cell biology* **1997,** *7* (5), 193-200.

62. Bergeron, J. J.; Brenner, M. B.; Thomas, D. Y.; Williams, D. B., Calnexin: a membrane-bound chaperone of the endoplasmic reticulum. *Trends in biochemical sciences* **1994,** *19* (3), 124-128.

63. Lee, A.-H.; Iwakoshi, N. N.; Anderson, K. C.; Glimcher, L. H., Proteasome inhibitors disrupt the unfolded protein response in myeloma cells. *Proceedings of the National Academy of Sciences* **2003,** *100* (17), 9946-9951.

64. Schonthal, A., Targeting endoplasmic reticulum stress for cancer therapy. *Frontiers in bioscience (Scholar edition)* **2011,** *4*, 412-431.

65. Nishitoh, H., CHOP is a multifunctional transcription factor in the ER stress response. *Journal of biochemistry* **2012,** *151* (3), 217-219.

66. Görlach, A.; Klappa, P.; Kietzmann, D. T., The endoplasmic reticulum: folding, calcium homeostasis, signaling, and redox control. *Antioxidants & redox signaling* **2006,** *8* (9-10), 1391-1418.

67. Ranganathan, A. C.; Zhang, L.; Adam, A. P.; Aguirre-Ghiso, J. A., Functional coupling of p38-induced up-regulation of BiP and activation of RNA-dependent protein kinase–like endoplasmic reticulum kinase to drug resistance of dormant carcinoma cells. *Cancer research* **2006,** *66* (3), 1702-1711.

68. Shen, J.; Chen, X.; Hendershot, L.; Prywes, R., ER stress regulation of ATF6 localization by dissociation of BiP/GRP78 binding and unmasking of Golgi localization signals. *Developmental cell* **2002,** *3* (1), 99-111.

69. Lin, J. H.; Li, H.; Yasumura, D.; Cohen, H. R.; Zhang, C.; Panning, B.; Shokat, K. M.; LaVail, M. M.; Walter, P., IRE1 signaling affects cell fate during the unfolded protein response. *science* **2007,** *318* (5852), 944-949.

70. Yoshida, H.; Matsui, T.; Yamamoto, A.; Okada, T.; Mori, K., XBP1 mRNA is induced by ATF6 and spliced by IRE1 in response to ER stress to produce a highly active transcription factor. *Cell* **2001,** *107* (7), 881-891.

71. Harding, H. P.; Zhang, Y.; Bertolotti, A.; Zeng, H.; Ron, D., Perk is essential for translational regulation and cell survival during the unfolded protein response. *Molecular cell* **2000,** *5* (5), 897-904.

72. Wu, J.; Kaufman, R., From acute ER stress to physiological roles of the unfolded protein response. *Cell Death & Differentiation* **2006,** *13* (3), 374-384.

73. Baumgartner, H. K.; Gerasimenko, J. V.; Thorne, C.; Ferdek, P.; Pozzan, T.; Tepikin, A. V.; Petersen, O. H.; Sutton, R.; Watson, A. J.; Gerasimenko, O. V., Calcium elevation in

mitochondria is the main Ca2+ requirement for mitochondrial permeability transition pore (mPTP) opening. *Journal of Biological Chemistry* **2009,** *284* (31), 20796-20803.

74. Deniaud, A.; Maillier, E.; Poncet, D.; Kroemer, G.; Lemaire, C.; Brenner, C., Endoplasmic reticulum stress induces calcium-dependent permeability transition, mitochondrial outer membrane permeabilization and apoptosis. *Oncogene* **2008,** *27* (3), 285-299.

75. Silke, J.; Ekert, P. G.; Day, C. L.; Hawkins, C. J.; Baca, M.; Chew, J.; Pakusch, M.; Verhagen, A. M.; Vaux, D. L., Direct inhibition of caspase 3 is dispensable for the anti-apoptotic activity of XIAP. *Embo Journal* **2001,** *20* (12), 3114-3123.

76. Zhang, L. D.; Fang, B. L., Mechanisms of resistance to TRAIL-induced apoptosis in cancer. *Cancer Gene Therapy* **2005,** *12* (3), 228-237.

77. Srinivasula, S. M.; Hegde, R.; Saleh, A.; Datta, P.; Shiozaki, E.; Chai, J.; Lee, R.-A.; Robbins, P. D.; Fernandes-Alnemri, T.; Shi, Y., A conserved XIAP-interaction motif in caspase-9 and Smac/DIABLO regulates caspase activity and apoptosis. *Nature* **2001,** *410* (6824), 112-116.

78. Zou, H.; Li, Y.; Liu, X.; Wang, X., An APAF-1· cytochrome c multimeric complex is a functional apoptosome that activates procaspase-9. *Journal of Biological Chemistry* **1999,** *274* (17), 11549-11556.

79. Zorov, D. B.; Juhaszova, M.; Sollott, S. J., Mitochondrial ROS-induced ROS release: an update and review. *Biochimica et Biophysica Acta (BBA)-Bioenergetics* **2006,** *1757* (5), 509-517.

80. Potta, T.; Zhen, Z.; Grandhi, T. S. P.; Christensen, M. D.; Ramos, J.; Breneman, C. M.; Rege, K., Discovery of antibiotics-derived polymers for gene delivery using combinatorial synthesis and cheminformatics modeling. *Biomaterials* **2014,** *35* (6), 1977-1988.

81. Miryala, B.; Feng, Y.; Omer, A.; Potta, T.; Rege, K., Quaternization enhances the transgene expression efficacy of aminoglycoside-derived polymers. *International journal of pharmaceutics* **2015,** *489* (1), 18-29.

82. Miryala, B.; Zhen, Z.; Potta, T.; Breneman, C. M.; Rege, K., Parallel Synthesis and Quantitative Structure–Activity Relationship (QSAR) Modeling of Aminoglycoside-Derived Lipopolymers for Transgene Expression. *ACS Biomaterials Science & Engineering* **2015,** *1* (8), 656-668.

83. Grandhi, T. S. P.; Mallik, A.; Lin, N.; Miryala, B.; Potta, T.; Tian, Y.; Rege, K., Aminoglycoside antibiotic-derived Anion-exchange Microbeads for Plasmid DNA Binding and In situ DNA Capture. *ACS applied materials & interfaces* **2014**.

84. Diogo, M.; Queiroz, J.; Prazeres, D., Chromatography of plasmid DNA. *Journal of Chromatography A* **2005,** *1069* (1), 3-22.

85. Szot, C. S.; Buchanan, C. F.; Freeman, J. W.; Rylander, M. N., 3D in vitro bioengineered tumors based on collagen I hydrogels. *Biomaterials* **2011,** *32* (31), 7905-7912.

86. Sainz, B.; TenCate, V.; Uprichard, S. L., Three-dimensional Huh7 cell culture system for the study of Hepatitis C virus infection. *Virology Journal* **2009,** *6*.

87. Griffith, L. G.; Swartz, M. A., Capturing complex 3D tissue physiology in vitro. *Nature Reviews Molecular Cell Biology* **2006,** *7* (3), 211-224.

88. Yamada, K. M.; Cukierman, E., Modeling Tissue Morphogenesis and Cancer in 3D. *Cell* **2007,** *130* (4), 601-610.

89. Cukierman, E.; Pankov, R.; Yamada, K. M., Cell interactions with three-dimensional matrices. *Current Opinion in Cell Biology* **2002,** *14* (5), 633-639.

90. Li, H. Y.; Chang, S. P.; Yuan, C. C.; Chao, H. T.; Ng, H. T.; Sung, Y. J., Establishment of an efficient method to quantify embryo attachment to endometrial epithelial cell monolayers. *In Vitro Cellular & Developmental Biology-Animal* **2002,** *38* (9), 505-511.

91. Kunz-Schughart, L. A.; Kreutz, M.; Knuechel, R., Multicellular spheroids: a three-dimensional in vitro culture system to study tumour biology. *International Journal of Experimental Pathology* **1998,** *79* (1), 1-23.

92. Vinci, M.; Gowan, S.; Boxall, F.; Patterson, L.; Zimmermann, M.; Court, W.; Lomas, C.; Mendiola, M.; Hardisson, D.; Eccles, S. A., Advances in establishment and analysis of three-dimensional tumor spheroid-based functional assays for target validation and drug evaluation. *Bmc Biology* **2012,** *10*.

93. Kelm, J. M.; Djonov, V.; Ittner, L. M.; Fluri, D.; Born, W.; Hoerstrup, S. P.; Fussenegger, M., Design of custom-shaped vascularized tissues using microtissue spheroids as minimal building units. *Tissue Engineering* **2006,** *12* (8), 2151-2160.

94. Mehta, G.; Hsiao, A. Y.; Ingram, M.; Luker, G. D.; Takayama, S., Opportunities and challenges for use of tumor spheroids as models to test drug delivery and efficacy. *Journal of Controlled Release* **2012,** *164* (2), 192-204.

95. Liang, Y.; Jeong, J.; DeVolder, R. J.; Cha, C.; Wang, F.; Tong, Y. W.; Kong, H., A cell-instructive hydrogel to regulate malignancy of 3D tumor spheroids with matrix rigidity. *Biomaterials* **2011,** *32* (35), 9308-9315.

96. Loessner, D.; Stok, K. S.; Lutolf, M. P.; Hutmacher, D. W.; Clements, J. A.; Rizzi, S. C., Bioengineered 3D platform to explore cell–ECM interactions and drug resistance of epithelial ovarian cancer cells. *Biomaterials* **2010,** *31* (32), 8494-8506.

97. Oliviero, O.; Ventre, M.; Netti, P. A., Functional porous hydrogels to study angiogenesis under the effect of controlled release of vascular endothelial growth factor. *Acta Biomater.* **2012,** *8* (9), 3294-3301.

98. Porter, A. M.; Klinge, C. M.; Gobin, A. S., Covalently grafted VEGF165 in hydrogel models upregulates the cellular pathways associated with angiogenesis. *American Journal of Physiology - Cell Physiology* **2011,** *301* (5), C1086-C1092.

99. Lin, R.-Z.; Chang, H.-Y., Recent advances in three-dimensional multicellular spheroid culture for biomedical research. *Biotechnology Journal* **2008,** *3* (9-10), 1172-1184.

100. Kelm, J. M.; Fussenegger, M., Microscale tissue engineering using gravity-enforced cell assembly. *Trends in biotechnology* **2004,** *22* (4), 195-202.

101. Kelm, J. M.; Timmins, N. E.; Brown, C. J.; Fussenegger, M.; Nielsen, L. K., Method for generation of homogeneous multicellular tumor spheroids applicable to a wide variety of cell types. *Biotechnology and Bioengineering* **2003,** *83* (2), 173-180.

102. Härmä, V.; Virtanen, J.; Mäkelä, R.; Happonen, A.; Mpindi, J.-P.; Knuuttila, M.; Kohonen, P.; Lötjönen, J.; Kallioniemi, O.; Nees, M., A Comprehensive Panel of Three-Dimensional Models

for Studies of Prostate Cancer Growth, Invasion and Drug Responses. *PLoS ONE* **2010,** *5* (5), e10431.

103. Webber, M. M.; Trakul, N.; Thraves, P. S.; Bello-DeOcampo, D.; Chu, W. W.; Storto, P. D.; Huard, T. K.; Rhim, J. S.; Williams, D. E., A human prostatic stromal myofibroblast cell line WPMY-1: a model for stromal-epithelial interactions in prostatic neoplasia. *Carcinogenesis* **1999,** *20* (7), 1185-1192.

104. Carlsson, J.; Yuhas, J. M., LIQUID-OVERLAY CULTURE OF CELLULAR SPHEROIDS. *Recent Results in Cancer Research* **1984,** *95*, 1-23.

105. Taylor, D.; Parsons, C.; Han, H.; Jayaraman, A.; Rege, K., Parallel screening of FDA-approved antineoplastic drugs for identifying sensitizers of TRAIL-induced apoptosis in cancer cells. *BMC cancer* **2011,** *11* (1), 470.

106. Cheng, T.-L.; Chuang, K.-H.; Chen, B.-M.; Roffler, S. R., Analytical measurement of PEGylated molecules. *Bioconjugate chemistry* **2012,** *23* (5), 881-899.

107. Al-Sabha, T. a. N., Spectrophotometric determination of amikacin sulphate via charge transfer complex formation reaction using tetracyanoethylene and 2, 3-dichloro-5, 6-dicyano-1, 4-benzoquinone reagents. *Arabian Journal for Science and Engineering* **2010,** *35* (2 A), 27-40.

108. Park, H.; Guo, X.; Temenoff, J. S.; Tabata, Y.; Caplan, A. I.; Kasper, F. K.; Mikos, A. G., Effect of swelling ratio of injectable hydrogel composites on chondrogenic differentiation of encapsulated rabbit marrow mesenchymal stem cells in vitro. *Biomacromolecules* **2009,** *10* (3), 541-546.

109. Patankar, N. A., On the Modeling of Hydrophobic Contact Angles on Rough Surfaces. *Langmuir* **2003,** *19* (4), 1249-1253.

110. Zhu, J., Bioactive modification of poly (ethylene glycol) hydrogels for tissue engineering. *Biomaterials* **2010,** *31* (17), 4639-4656.

111. Mueller-Klieser, W., Tumor biology and experimental therapeutics. *Critical Reviews in Oncology Hematology* **2000,** *36* (2-3), 123-139.

112. Skardal, A.; Sarker, S. F.; Crabbé, A.; Nickerson, C. A.; Prestwich, G. D., The generation of 3-D tissue models based on hyaluronan hydrogel-coated microcarriers within a rotating wall vessel bioreactor. *Biomaterials* **2010,** *31* (32), 8426-8435.

113. Cheng, G.; Tse, J.; Jain, R. K.; Munn, L. L., Micro-Environmental Mechanical Stress Controls Tumor Spheroid Size and Morphology by Suppressing Proliferation and Inducing Apoptosis in Cancer Cells. *PLoS ONE* **2009,** *4* (2), e4632.

114. Fennema, E.; Rivron, N.; Rouwkema, J.; van Blitterswijk, C.; de Boer, J., Spheroid culture as a tool for creating 3D complex tissues. *Trends in biotechnology* **2013,** *31* (2), 108-115.

115. Moll, R.; Achtstätter, T.; Becht, E.; Balcarova-Ständer, J.; Ittensohn, M.; Franke, W., Cytokeratins in normal and malignant transitional epithelium. Maintenance of expression of urothelial differentiation features in transitional cell carcinomas and bladder carcinoma cell culture lines. *The American journal of pathology* **1988,** *132* (1), 123.

116. Syrigos, K. N.; Krausz, T.; Waxman, J.; Pandha, H.; Rowlinson‐Busza, G.; Verne, J.; Epenetos, A. A.; Pignatelli, M., E‐cadherin expression in bladder cancer using formalin‐fixed,

paraffin‐embedded tissues: Correlation with histopathological grade, tumour stage and survival. *International journal of cancer* **1995,** *64* (6), 367-370.

117. Lipponen, P.; Eskelinen, M., Reduced expression of E-cadherin is related to invasive disease and frequent recurrence in bladder cancer. *Journal of cancer research and clinical oncology* **1995,** *121* (5), 303-308.

118. Mialhe, A.; Levacher, G.; Champelovier, P.; MARTEL, V.; SERRES, M.; KNUDSEN, K.; SEIGNEURIN, D., Expression of E-, P-, N-cadherins and catenins in human bladder carcinoma cell lines. *The Journal of urology* **2000,** *164* (3), 826-835.

119. Levenberg, S.; Yarden, A.; Kam, Z.; Geiger, B., p27 is involved in N-cadherin-mediated contact inhibition of cell growth and S-phase entry. *Oncogene* **1999,** *18* (4), 869-876.

120. Beacham, D. A.; Amatangelo, M. D.; Cukierman, E., Preparation of Extracellular Matrices Produced by Cultured and Primary Fibroblasts. In *Current Protocols in Cell Biology*, John Wiley & Sons, Inc.: **2001**.

121. Nishida, T.; Yasumoto, K.; Otori, T.; Desaki, J., The network structure of corneal fibroblasts in the rat as revealed by scanning electron microscopy. *Investigative Ophthalmology & Visual Science* **1988,** *29* (12), 1887-1890.

122. Whatcott, C.; Han, H.; Posner, R. G.; Von Hoff, D. D., Tumor-stromal interactions in pancreatic cancer. *Critical Reviews™ in Oncogenesis* **2013,** *18* (1-2).

123. Zheng, X.; Wise, S.; Cristini, V., Nonlinear simulation of tumor necrosis, neo-vascularization and tissue invasion via an adaptive finite-element/level-set method. *Bulletin of mathematical biology* **2005,** *67* (2), 211-259.

124. Du, Y.; Chia, S.-m.; Han, R.; Chang, S.; Tang, H.; Yu, H., 3D hepatocyte monolayer on hybrid RGD/galactose substratum. *Biomaterials* **2006,** *27* (33), 5669-5680.

125. Grandhi, T. S. P.; Potta, T.; Taylor, D. J.; Tian, Y.; Johnson, R. H.; Meldrum, D. R.; Rege, K., Sensitizing cancer cells to TRAIL-induced death by micellar delivery of mitoxantrone. *Nanomedicine* **2013,** (0), 1-14.

126. MARGOLIS, D., Prostate Cancer Intervention. *Clinical Interventional Oncology: Expert Consult-Online and Print* **2013**, 197.

127. Bubendorf, L.; Schöpfer, A.; Wagner, U.; Sauter, G.; Moch, H.; Willi, N.; Gasser, T. C.; Mihatsch, M. J., Metastatic patterns of prostate cancer: an autopsy study of 1,589 patients. *Human pathology* **2000,** *31* (5), 578-583.

128. Tamada, T.; Sone, T.; Jo, Y.; Imai, S.; Kajihara, Y.; Fukunaga, M., Three-dimensional trabecular bone architecture of the lumbar spine in bone metastasis from prostate cancer: comparison with degenerative sclerosis. *Skeletal radiology* **2005,** *34* (3), 149-155.

129. Coleman, R. E.; Guise, T. A.; Lipton, A.; Roodman, G. D.; Berenson, J. R.; Body, J.-J.; Boyce, B. F.; Calvi, L. M.; Hadji, P.; McCloskey, E. V., Advancing treatment for metastatic bone cancer: consensus recommendations from the Second Cambridge Conference. *Clinical cancer research* **2008,** *14* (20), 6387-6395.

130. Loberg, R. D.; Logothetis, C. J.; Keller, E. T.; Pienta, K. J., Pathogenesis and treatment of prostate cancer bone metastases: targeting the lethal phenotype. *Journal of Clinical Oncology* **2005,** *23* (32), 8232-8241.

131. Persidis, A., Cancer multidrug resistance. *Nature biotechnology* **1999,** *17* (1), 94-95.

132. Gewirtz, D. A., A critical evaluation of the mechanisms of action proposed for the antitumor effects of the anthracycline antibiotics Adriamycin and daunorubicin. *Biochemical Pharmacology* **1999,** *57* (7), 727-741.

133. Fox, E. J., Mechanism of action of mitoxantrone. *Neurology* **2004,** *63* (12), S15-S18.

134. Wu, H.-C.; Hebert, C. G.; Hung, C.-W.; Quan, D. N.; Carter, K. K.; Bentley, W. E., Tuning cell cycle of insect cells for enhanced protein production. *Journal of biotechnology* **2013,** *168* (1), 55-61.

135. Milo, R., What is the total number of protein molecules per cell volume? A call to rethink some published values. *Bioessays* **2013,** *35* (12), 1050-1055.

136. Lytton, J.; Westlin, M.; Hanley, M. R., Thapsigargin inhibits the sarcoplasmic or endoplasmic reticulum Ca-ATPase family of calcium pumps. *Journal of Biological Chemistry* **1991,** *266* (26), 17067-17071.

137. Ganley, I. G.; Wong, P.-M.; Gammoh, N.; Jiang, X., Distinct autophagosomal-lysosomal fusion mechanism revealed by thapsigargin-induced autophagy arrest. *Molecular cell* **2011,** *42* (6), 731-743.

138. Ogata, M.; Hino, S.-i.; Saito, A.; Morikawa, K.; Kondo, S.; Kanemoto, S.; Murakami, T.; Taniguchi, M.; Tanii, I.; Yoshinaga, K., Autophagy is activated for cell survival after endoplasmic reticulum stress. *Molecular and cellular biology* **2006,** *26* (24), 9220-9231.

139. Ruschak, A. M.; Slassi, M.; Kay, L. E.; Schimmer, A. D., Novel proteasome inhibitors to overcome bortezomib resistance. *Journal of the National Cancer Institute* **2011,** *103* (13), 1007-1017.

140. Adams, J., The proteasome: structure, function, and role in the cell. *Cancer treatment reviews* **2003,** *29*, 3-9.

141. Hideshima, T.; Bradner, J. E.; Wong, J.; Chauhan, D.; Richardson, P.; Schreiber, S. L.; Anderson, K. C., Small-molecule inhibition of proteasome and aggresome function induces synergistic antitumor activity in multiple myeloma. *Proceedings of the National Academy of Sciences of the United States of America* **2005,** *102* (24), 8567-8572.

142. Jagannath, S.; Barlogie, B.; Berenson, J. R.; Singhal, S.; Alexanian, R.; Srkalovic, G.; Orlowski, R. Z.; Richardson, P. G.; Anderson, J.; Nix, D., Bortezomib in recurrent and/or refractory multiple myeloma. *Cancer* **2005,** *103* (6), 1195-1200.

143. Kane, R. C.; Dagher, R.; Farrell, A.; Ko, C.-W.; Sridhara, R.; Justice, R.; Pazdur, R., Bortezomib for the treatment of mantle cell lymphoma. *Clinical Cancer Research* **2007,** *13* (18), 5291-5294.

144. Kane, R. C.; Bross, P. F.; Farrell, A. T.; Pazdur, R., Velcade®: US FDA approval for the treatment of multiple myeloma progressing on prior therapy. *The oncologist* **2003,** *8* (6), 508-513.

145. Parlati, F.; Lee, S. J.; Aujay, M.; Suzuki, E.; Levitsky, K.; Lorens, J. B.; Micklem, D. R.; Ruurs, P.; Sylvain, C.; Lu, Y., Carfilzomib can induce tumor cell death through selective inhibition of the chymotrypsin-like activity of the proteasome. *Blood* **2009,** *114* (16), 3439-3447.

146. Herndon, T. M.; Deisseroth, A.; Kaminskas, E.; Kane, R. C.; Koti, K. M.; Rothmann, M. D.; Habtemariam, B.; Bullock, J.; Bray, J. D.; Hawes, J., US Food and Drug Administration approval: carfilzomib for the treatment of multiple myeloma. *Clinical Cancer Research* **2013,** *19* (17), 4559-4563.

147. Bernales, S.; McDonald, K. L.; Walter, P., Autophagy counterbalances endoplasmic reticulum expansion during the unfolded protein response. *PLoS Biol* **2006,** *4* (12), e423.

148. Blommaart, E. F.; Krause, U.; Schellens, J. P.; Vreeling-Sindelarova, H.; Meijer, A. J., The phosphatidylinositol 3-kinase inhibitors wortmannin and LY294002 inhibit autophagy in isolated rat hepatocytes. *European Journal of Biochemistry* **1997,** *243* (1-2), 240-246.

149. Sambrook, J. F., The involvement of calcium in transport of secretory proteins from the endoplasmic reticulum. *Cell* **1990,** *61* (2), 197-199.

150. Ashley, J. D.; Stefanick, J. F.; Schroeder, V. A.; Suckow, M. A.; Kiziltepe, T.; Bilgicer, B., Liposomal bortezomib nanoparticles via boronic ester prodrug formulation for improved therapeutic efficacy in vivo. *Journal of medicinal chemistry* **2014,** *57* (12), 5282-5292.

151. Malhotra, J. D.; Kaufman, R. J., ER stress and its functional link to mitochondria: role in cell survival and death. *Cold Spring Harbor perspectives in biology* **2011,** *3* (9), a004424.

152. Green, D. R.; Amarante-Mendes, G. P., The point of no return: mitochondria, caspases, and the commitment to cell death. In *Apoptosis: Mechanisms and Role in Disease*, Springer: **1998**, pp 45-61.

153. Morishima, N.; Nakanishi, K.; Takenouchi, H.; Shibata, T.; Yasuhiko, Y., An endoplasmic reticulum stress-specific caspase cascade in apoptosis cytochrome c-independent activation of caspase-9 by caspase-12. *Journal of Biological Chemistry* **2002,** *277* (37), 34287-34294.

154. Taylor, D. J.; Parsons, C. E.; Han, H. Y.; Jayaraman, A.; Rege, K., Parallel screening of FDA-approved antineoplastic drugs for identifying sensitizers of TRAIL-induced apoptosis in cancer cells. *Bmc Cancer* **2011,** *11*.

155. Chang, H. Y.; Yang, X., Proteases for cell suicide: functions and regulation of caspases. *Microbiology and molecular biology reviews* **2000,** *64* (4), 821-846.

156. Benham, C.; Davis, J.; Randall, A., Vanilloid and TRP channels: a family of lipid-gated cation channels. *Neuropharmacology* **2002,** *42* (7), 873-888.

157. Berridge, M. J.; Lipp, P.; Bootman, M. D., The versatility and universality of calcium signalling. *Nature reviews Molecular cell biology* **2000,** *1* (1), 11-21.

158. Jousset, H.; Frieden, M.; Demaurex, N., STIM1 knockdown reveals that store-operated Ca2+ channels located close to sarco/endoplasmic Ca2+ ATPases (SERCA) pumps silently refill the endoplasmic reticulum. *Journal of Biological Chemistry* **2007,** *282* (15), 11456-11464.

159. Armengol, X.; Estelrich, J., Physical stability of different liposome compositions obtained by extrusion method. *Journal of microencapsulation* **1995,** *12* (5), 525-535.

160. Jones, M.; Nicholas, A., The effect of blood serum on the size and stability of phospholipid liposomes. *Biochimica et Biophysica Acta (BBA)-Biomembranes* **1991,** *1065* (2), 145-152.

161. Senior, J.; Gregoriadis, G., Stability of small unilamellar liposomes in serum and clearance from the circulation: the effect of the phospholipid and cholesterol components. *Life sciences* **1982,** *30* (24), 2123-2136.

162. Meyerhoff, A., US Food and Drug Administration approval of AmBisome (liposomal amphotericin B) for treatment of visceral leishmaniasis. *Clinical infectious diseases* **1999,** *28* (1), 42-48.

163. Doan, N. T. Q.; Paulsen, E. S.; Sehgal, P.; Møller, J. V.; Nissen, P.; Denmeade, S. R.; Isaacs, J. T.; Dionne, C. A.; Christensen, S. B., Targeting thapsigargin towards tumors. *Steroids* **2015,** *97*, 2-7.

164. Costa, A. K.; Schieble, T. M.; Heffel, D. F.; Trudell, J. R., Toxicity of calcium Ionophore A23187 in monolayers of hypoxic hepatocytes. *Toxicology and applied pharmacology* **1987,** *87* (1), 43-47.

165. Indraccolo, S.; Stievano, L.; Minuzzo, S.; Tosello, V.; Esposito, G.; Piovan, E.; Zamarchi, R.; Chieco-Bianchi, L.; Amadori, A., Interruption of tumor dormancy by a transient angiogenic burst within the tumor microenvironment. *Proceedings of the National Academy of Sciences of the United States of America* **2006,** *103* (11), 4216-4221.

166. Gimbrone, M. A.; Leapman, S. B.; Cotran, R. S.; Folkman, J., Tumor dormancy in vivo by prevention of neovascularization. *The Journal of experimental medicine* **1972,** *136* (2), 261-276.

167. Ghajar, C. M.; Peinado, H.; Mori, H.; Matei, I. R.; Evason, K. J.; Brazier, H.; Almeida, D.; Koller, A.; Hajjar, K. A.; Stainier, D. Y., The perivascular niche regulates breast tumour dormancy. *Nature cell biology* **2013,** *15* (7), 807-817.

168. Aitken, K. J.; Bägli, D. J., The bladder extracellular matrix. Part I: architecture, development and disease. *Nature Reviews Urology* **2009,** *6* (11), 596-611.

169. Szarvas, T.; vom Dorp, F.; Ergün, S.; Rübben, H., Matrix metalloproteinases and their clinical relevance in urinary bladder cancer. *Nature Reviews Urology* **2011,** *8* (5), 241-254.

170. Liu, Y.-a.; Liang, B.-y.; Guan, Y.; You, J.; Zhu, L.; Chen, X.-p.; Huang, Z.-y., Loss of N-cadherin is associated with loss of E-cadherin expression and poor outcomes of liver resection in hepatocellular carcinoma. *Journal of Surgical Research* **2015,** *194* (1), 167-176.

171. Nicholson, B. E.; Frierson, H. F.; Conaway, M. R.; Seraj, J. M.; Harding, M. A.; Hampton, G. M.; Theodorescu, D., Profiling the evolution of human metastatic bladder cancer. *Cancer Research* **2004,** *64* (21), 7813-7821.

172. Shah, A. M. Bioengineered surfaces and hydrogels for specific cell capture and release from whole blood. Massachusetts Institute of Technology, **2008**.

173. Chen, W. T., Method and compositions for isolating metastatic cancer cells, and use in measuring metastatic potentatial of a cancer thereof. Google Patents: **2003**.

174. Myung, J. H.; Launiere, C. A.; Eddington, D. T.; Hong, S., Enhanced tumor cell isolation by a biomimetic combination of E-selectin and anti-EpCAM: implications for the effective separation of circulating tumor cells (CTCs). *Langmuir* **2010,** *26* (11), 8589-8596.

175. Chen, C.; Chen, L.; Chen, W. T., Blood test prototypes and methods for the detection of circulating tumor and endothelial cells. Google Patents: **2006**.

176. Wang, S.-h.; Lin, S.-Y., Tumor dormancy: potential therapeutic target in tumor recurrence and metastasis prevention. *Experimental Hematology & Oncology* **2013,** *2* (1), 29.

177. Li, Y.; Yang, X.; Su, L.-J.; Flaig, T. W., Pazopanib synergizes with docetaxel in the treatment of bladder cancer cells. *Urology* **2011,** *78* (1), 233. e7-233. e13.

178. Kogashiwa, Y.; Sakurai, H.; Kimura, T.; Kohno, N., Docetaxel suppresses invasiveness of head and neck cancer cells in vitro. *Cancer science* **2010,** *101* (6), 1382-1386.

179. Zins, K.; Lucas, T.; Reichl, P.; Abraham, D.; Aharinejad, S., A Rac1/Cdc42 GTPase-Specific Small Molecule Inhibitor Suppresses Growth of Primary Human Prostate Cancer Xenografts and Prolongs Survival in Mice. *PloS one* **2013,** *8* (9), e74924.

180. Liu, S.; Goldstein, R. H.; Scepansky, E. M.; Rosenblatt, M., Inhibition of rho-associated kinase signaling prevents breast cancer metastasis to human bone. *Cancer research* **2009,** *69* (22), 8742-8751.

181. Yang, S.; Kim, H.; Aspenstrom, P., ROCK Inhibition Activates MCF-7 Cells. *PLoS ONE* **2014,** *9* (2), e88489.

182. Comunale, F.; Causeret, M.; Favard, C.; Cau, J.; Taulet, N.; Charrasse, S.; Gauthier‐Rouvière, C., Rac1 and RhoA GTPases have antagonistic functions during N‐cadherin‐dependent cell—cell contact formation in C2C12 myoblasts. *Biology of the Cell* **2007,** *99* (9), 503-517.

183. Banerjee, R.; Huang, L., Plasmid DNA–Mediated Gene Therapy. In *Burger's Medicinal Chemistry and Drug Discovery*, John Wiley & Sons, Inc.: **2003**.

184. Horn, N. A.; Meek, J. A.; Budahazi, G.; Marquet, M., Cancer gene therapy using plasmid DNA: purification of DNA for human clinical trials. *Human Gene Therapy* **1995,** *6* (5), 565-573.

185. Anderson, W. F., Gene therapy for genetic diseases. *Human gene therapy* **1994,** *5* (3), 281-282.

186. Alton, E.; Middleton, P. G.; Caplen, N. J.; Smith, S. N.; Steel, D. M.; Munkonge, F.; Jeffery, P.; Geddes, D.; Hart, S.; Williamson, R., Non–invasive liposome–mediated gene delivery can correct the ion transport defect in cystic fibrosis mutant mice. *Nature genetics* **1993,** *5* (2), 135-142.

187. Tighe, H.; Corr, M.; Roman, M.; Raz, E., Gene vaccination: plasmid DNA is more than just a blueprint. *Immunology today* **1998,** *19* (2), 89-97.

188. Boussif, O.; Lezoualc'h, F.; Zanta, M. A.; Mergny, M. D.; Scherman, D.; Demeneix, B.; Behr, J.-P., A versatile vector for gene and oligonucleotide transfer into cells in culture and in vivo: polyethylenimine. *Proceedings of the National Academy of Sciences* **1995,** *92* (16), 7297-7301.

189. Voordouw, G.; Kam, Z.; Borochov, N.; Eisenberg, H., Isolation and physical studies of the intact supercoiled: The open circular and the linear forms of coie1-plasmid DNA. *Biophysical chemistry* **1978,** *8* (2), 171-189.

190. Cohen, S. N.; Chang, A. C.; Hsu, L., Nonchromosomal antibiotic resistance in bacteria: genetic transformation of Escherichia coli by R-factor DNA. *Proceedings of the National Academy of Sciences* **1972,** *69* (8), 2110-2114.

191. Elmer, J. J.; Christensen, M. D.; Rege, K., Applying horizontal gene transfer phenomena to enhance non-viral gene therapy. *J Control Release* **2013,** *172* (1), 246-57.

192. Corr, M.; Lee, D. J.; Carson, D. A.; Tighe, H., Gene vaccination with naked plasmid DNA: mechanism of CTL priming. *The Journal of experimental medicine* **1996,** *184* (4), 1555-1560.

193. Hermanson, G.; Whitlow, V.; Parker, S.; Tonsky, K.; Rusalov, D.; Ferrari, M.; Lalor, P.; Komai, M.; Mere, R.; Bell, M., A cationic lipid-formulated plasmid DNA vaccine confers sustained antibody-mediated protection against aerosolized anthrax spores. *Proceedings of the National Academy of Sciences of the United States of America* **2004,** *101* (37), 13601-13606.

194. Budahazi, G.; Horn, N.; Marquet, M.; Meek, J., Production of pharmaceutical-grade plasmid DNA. Google Patents: **1996**.

195. Prazeres, D. M. F.; Schluep, T.; Cooney, C., Preparative purification of supercoiled plasmid DNA using anion-exchange chromatography. *Journal of Chromatography A* **1998,** *806* (1), 31-45.

196. Sousa, F.; Prazeres, D. M.; Queiroz, J. A., Affinity chromatography approaches to overcome the challenges of purifying plasmid DNA. *Trends in biotechnology* **2008,** *26* (9), 518-525.

197. Diogo, M.; Queiroz, J.; Prazeres, D., Studies on the retention of plasmid DNA and Escherichia coli nucleic acids by hydrophobic interaction chromatography. *Bioseparation* **2001,** *10* (4-5), 211-220.

198. Limonta, M.; Márquez, G.; Rey, I.; Pupo, M.; Ruiz, O.; Amador-Canizares, Y.; Duenas-Carrera, S., Plasmid DNA recovery using size-exclusion and perfusion chromatography. **2008**.

199. Lao, U. L.; Kostal, J.; Mulchandani, A.; Chen, W., Affinity purification of plasmid DNA by temperature-triggered precipitation. *Nature protocols* **2007,** *2* (5), 1263-1268.

200. Sousa, F.; Matos, T.; Prazeres, D.; Queiroz, J., Specific recognition of supercoiled plasmid DNA in arginine affinity chromatography. *Analytical biochemistry* **2008,** *374* (2), 432-434.

201. Woodgate, J.; Palfrey, D.; Nagel, D. A.; Hine, A. V.; Slater, N. K., Protein‐mediated isolation of plasmid DNA by a zinc finger‐glutathione S‐transferase affinity linker. *Biotechnology and bioengineering* **2002,** *79* (4), 450-456.

202. Lundeberg, J.; Wahlberg, J.; Uhlén, M., Affinity purification of specific DNA fragments using a lac repressor fusion protein. *Gene Analysis Techniques* **1990,** *7* (3), 47-52.

203. Wils, P.; Escriou, V.; Warnery, A.; Lacroix, F.; Lagneaux, D.; Ollivier, M.; Crouzet, J.; Mayaux, J.; Scherman, D., Efficient purification of plasmid DNA for gene transfer using triple-helix affinity chromatography. *Gene Therapy* **1997,** *4* (4).

204. Diogo, M.; Ribeiro, S.; Queiroz, J.; Monteiro, G.; Perrin, P.; Tordo, N.; Prazeres, D., Scale-up of hydrophobic interaction chromatography for the purification of a DNA vaccine against rabies. *Biotechnology letters* **2000,** *22* (17), 1397-1400.

205. To, B.; Lenhoff, A. M., Hydrophobic interaction chromatography of proteins: I. The effects of protein and adsorbent properties on retention and recovery. *Journal of Chromatography A* **2007,** *1141* (2), 191-205.

206. Eon-Duval, A.; Burke, G., Purification of pharmaceutical-grade plasmid DNA by anion-exchange chromatography in an RNase-free process. *Journal of chromatography B* **2004,** *804* (2), 327-335.

207. Rege, K.; Ladiwala, A.; Hu, S.; Breneman, C. M.; Dordick, J. S.; Cramer, S. M., Investigation of DNA-binding properties of an aminoglycoside-polyamine library using quantitative structure-activity relationship (QSAR) models. *J Chem Inf Model* **2005,** *45* (6), 1854-63.

208. Tokuyama, H.; Yazaki, N., Preparation of poly (< i> N</i>-isopropylacrylamide) hydrogel beads by circulation polymerization. *Reactive and Functional Polymers* **2010,** *70* (12), 967-971.

209. Deveikytė, R.; Makuška, R., Quaternization of chitosan and partial destruction of the quaternized derivatives making them suitable for electrospinning. *chemija* **2013,** *24* (4), 325-334.

210. Tiller, J. C.; Liao, C.-J.; Lewis, K.; Klibanov, A. M., Designing surfaces that kill bacteria on contact. *Proceedings of the National Academy of Sciences* **2001,** *98* (11), 5981-5985.

211. Glazer, A. N.; Peck, K.; Mathies, R. A., A stable double-stranded DNA-ethidium homodimer complex: application to picogram fluorescence detection of DNA in agarose gels. *Proceedings of the National Academy of Sciences* **1990,** *87* (10), 3851-3855.

212. Kotra, L. P.; Haddad, J.; Mobashery, S., Aminoglycosides: perspectives on mechanisms of action and resistance and strategies to counter resistance. *Antimicrobial agents and chemotherapy* **2000,** *44* (12), 3249-3256.

213. Mehta, R.; Champney, W. S., 30S ribosomal subunit assembly is a target for inhibition by aminoglycosides in Escherichia coli. *Antimicrobial agents and chemotherapy* **2002,** *46* (5), 1546-1549.

214. Arya, D. P.; Coffee, R. L.; Willis, B.; Abramovitch, A. I., Aminoglycoside-nucleic acid interactions: remarkable stabilization of DNA and RNA triple helices by neomycin. *Journal of the American Chemical Society* **2001,** *123* (23), 5385-5395.

215. MARKS, M. I., In vitro antibacterial activity of amikacin, a new aminoglycoside, against clinical bacterial isolates from children. *The Journal of Clinical Pharmacology* **1975,** *15* (4), 246-251.

216. Rodríguez, M.; Oses, J.; Ziani, K.; Mate, J. I., Combined effect of plasticizers and surfactants on the physical properties of starch based edible films. *Food Research International* **2006,** *39* (8), 840-846.

217. Zeng, W.; Huang, J.; Hu, X.; Xiao, W.; Rong, M.; Yuan, Z.; Luo, Z., Ionically cross-linked chitosan microspheres for controlled release of bioactive nerve growth factor. *International journal of pharmaceutics* **2011,** *421* (2), 283-290.

218. Bodamer, G. W.; Kunin, R., Behavior of Ion Exchange Resins in Solvents other than Water-Swelling and Exchange Characteristics. *Industrial & Engineering Chemistry* **1953,** *45* (11), 2577-2580.

219. Tiihonen, J.; Markkanen, I.; Laatikainen, M.; Paatero, E., Elasticity of ion‐exchange resin beads in solvent mixtures. *Journal of applied polymer science* **2001,** *82* (5), 1256-1264.

220. McCaldin, D., The chemistry of ninhydrin. *Chemical Reviews* **1960,** *60* (1), 39-51.

221. Kean, T.; Roth, S.; Thanou, M., Trimethylated chitosans as non-viral gene delivery vectors: cytotoxicity and transfection efficiency. *Journal of Controlled Release* **2005,** *103* (3), 643-653.

222. Palermo, E. F.; Lee, D.-K.; Ramamoorthy, A.; Kuroda, K., Role of cationic group structure in membrane binding and disruption by amphiphilic copolymers. *The Journal of Physical Chemistry B* **2010,** *115* (2), 366-375.

223. Koga, Y.; Westh, P.; Nishikawa, K.; Subramanian, S., Is a methyl group always hydrophobic? Hydrophilicity of trimethylamine-N-oxide, tetramethyl urea and tetramethylammonium ion. *The Journal of Physical Chemistry B* **2011,** *115* (12), 2995-3002.

224. Karlström, A. E.; Hober, S., Chromatographic methods for protein purification. **2006**.

225. Tseng, W.-C.; Ho, F.-L., Enhanced purification of plasmid DNA using Q-Sepharose by modulation of alcohol concentrations. *Journal of Chromatography B* **2003,** *791* (1), 263-272.

226. Chang, C.-S.; Ni, H.-S.; Suen, S.-Y.; Tseng, W.-C.; Chiu, H.-C.; Chou, C. P., Preparation of inorganic–organic anion-exchange membranes and their application in plasmid DNA and RNA separation. *Journal of Membrane Science* **2008,** *311* (1), 336-348.

227. Tseng, W.-C.; Ho, F.-L.; Fang, T.-Y.; Suen, S.-Y., Effect of alcohol on purification of plasmid DNA using ion-exchange membrane. *Journal of membrane science* **2004,** *233* (1), 161-167.

228. Iuliano, S.; Fisher, J.; Chen, M.; Kelly, W., Rapid analysis of a plasmid by hydrophobic-interaction chromatography with a non-porous resin. *Journal of Chromatography A* **2002,** *972* (1), 77-86.

229. Latulippe, D. R.; Ager, K.; Zydney, A. L., Flux-dependent transmission of supercoiled plasmid DNA through ultrafiltration membranes. *Journal of membrane science* **2007,** *294* (1), 169-177.

230. Huang, H.-C.; Barua, S.; Kay, D. B.; Rege, K., Simultaneous enhancement of photothermal stability and gene delivery efficacy of gold nanorods using polyelectrolytes. *Acs Nano* **2009,** *3* (10), 2941-2952.

231. Cao, W.; Easley, C. J.; Ferrance, J. P.; Landers, J. P., Chitosan as a polymer for pH-induced DNA capture in a totally aqueous system. *Analytical chemistry* **2006,** *78* (20), 7222-7228.

232. Lee, J. H.; Lim, Y.-b.; Choi, J. S.; Choi, M.-u.; Yang, C.-h.; Park, J.-s., Quaternized polyamidoamine dendrimers as novel gene delivery system: relationship between degree of quaternization and their influences. *BULLETIN-KOREAN CHEMICAL SOCIETY* **2003,** *24* (11), 1637-1640.

233. Lee, J. H.; Lim, Y.-b.; Choi, J. S.; Lee, Y.; Kim, T.-i.; Kim, H. J.; Yoon, J. K.; Kim, K.; Park, J.-s., Polyplexes assembled with internally quaternized PAMAM-OH dendrimer and plasmid DNA have a neutral surface and gene delivery potency. *Bioconjugate chemistry* **2003,** *14* (6), 1214-1221.

234. Brownlie, A.; Uchegbu, I.; Schätzlein, A., PEI-based vesicle-polymer hybrid gene delivery system with improved biocompatibility. *International journal of pharmaceutics* **2004,** *274* (1), 41-52.

235. Palermo, E. F.; Kuroda, K., Chemical structure of cationic groups in amphiphilic polymethacrylates modulates the antimicrobial and hemolytic activities. *Biomacromolecules* **2009,** *10* (6), 1416-1428.

236. Lodish, H., *Molecular cell biology*. Macmillan: **2008**.

237. Niemz, A.; Ferguson, T. M.; Boyle, D. S., Point-of-care nucleic acid testing for infectious diseases. *Trends in biotechnology* **2011,** *29* (5), 240-250.

238. Wu, J.; Kodzius, R.; Cao, W.; Wen, W., Extraction, amplification and detection of DNA in microfluidic chip-based assays. *Microchimica Acta* **2013**, 1-21.

239. Kim, J.; Johnson, M.; Hill, P.; Gale, B. K., Microfluidic sample preparation: cell lysis and nucleic acid purification. *Integrative Biology* **2009,** *1* (10), 574-586.

240. Almasan, A.; Ashkenazi, A., Apo2L/TRAIL: apoptosis signaling, biology, and potential for cancer therapy. *Cytokine & Growth Factor Reviews* **2003,** *14* (3-4), 337-348.

241. Tepper, C. G.; Seldin, M. F., Modulation of caspase-8 and FLICE-inhibitory protein expression as a potential mechanism of Epstein-Barr virus tumorigenesis in Burkitt's lymphoma. *Blood* **1999,** *94* (5), 1727-1737.

242. Daniel, P. T.; Wieder, T.; Sturm, I.; Schulze-Osthoff, K., The kiss of death: promises and failures of death receptors and ligands in cancer therapy. *Leukemia* **2001,** *15* (7), 1022-1032.

243. Fulda, S.; Meyer, E.; Debatin, K. M., Inhibition of TRAIL-induced apoptosis by Bcl-2 overexpression. *Oncogene* **2002,** *21* (15), 2283-2294.

244. Symes, J. C.; Kurin, M.; Fleshner, N. E.; Medin, J. A., Fas-mediated killing of primary prostate cancer cells is increased by mitoxantrone and docetaxel. *Molecular Cancer Therapeutics* **2008,** *7* (9), 3018-3028.

245. Novak, R. F.; Kharasch, E. D., MITOXANTRONE - PROPENSITY FOR FREE-RADICAL FORMATION AND LIPID-PEROXIDATION - IMPLICATIONS FOR CARDIOTOXICITY. *Investigational New Drugs* **1985,** *3* (2), 95-99.

246. Vibet, S.; Maheo, K.; Gore, J.; Dubois, P.; Bougnoux, P.; Chourpa, I., Differential subcellular distribution of mitoxantrone in relation to chemosensitization in two human breast cancer cell lines. *Drug Metabolism and Disposition* **2007,** *35* (5), 822-828.

247. Duthie, S. J.; Grant, M. H., THE ROLE OF REDUCTIVE AND OXIDATIVE-METABOLISM IN THE TOXICITY OF MITOXANTRONE, ADRIAMYCIN AND MENADIONE IN HUMAN-LIVER DERIVED HEP-G2 HEPATOMA-CELLS. *British Journal of Cancer* **1989,** *60* (4), 566-571.

248. Koceva-Chyla, A.; Jedrzejczak, M.; Skierski, J.; Kania, K.; Jozwiak, Z., Mechanisms of induction of apoptosis by anthraquinone anticancer drugs aclarubicin and mitoxantrone in comparison with doxorubicin: Relation to drug cytotoxicity and caspase-3 activation. *Apoptosis* **2005,** *10* (6), 1497-1514.

249. Gaucher, G.; Dufresne, M. H.; Sant, V. P.; Kang, N.; Maysinger, D.; Leroux, J. C., Block copolymer micelles: preparation, characterization and application in drug delivery. *Journal of Controlled Release* **2005,** *109* (1-3), 169-188.

250. Kim, S.; Shi, Y. Z.; Kim, J. Y.; Park, K.; Cheng, J. X., Overcoming the barriers in micellar drug delivery: loading efficiency, in vivo stability, and micelle-cell interaction. *Expert Opin. Drug Deliv.* **2010,** *7* (1), 49-62.

251. Torchilin, V. P., Structure and design of polymeric surfactant-based drug delivery systems. *Journal of Controlled Release* **2001,** *73* (2-3), 137-172.

252. Kataoka, K.; Kwon, G. S.; Yokoyama, M.; Okano, T.; Sakurai, Y., BLOCK-COPOLYMER MICELLES AS VEHICLES FOR DRUG DELIVERY. *Journal of Controlled Release* **1993,** *24* (1-3), 119-132.

253. Torchilin, V. P., Micellar nanocarriers: Pharmaceutical perspectives. *Pharmaceutical Research* **2007,** *24* (1), 1-16.

254. Torchilin, V. P., Targeted pharmaceutical nanocarriers for cancer therapy and Imaging. *Aaps Journal* **2007,** *9* (2), E128-E147.

255. Dabholkar, R. D.; Sawant, R. M.; Mongayt, D. A.; Devarajan, P. V.; Torchilin, V. P., Polyethylene glycol-phosphatidylethanolamine conjugate (PEG-PE)-based mixed micelles: Some properties, loading with paclitaxel, and modulation of P-glycoprotein-mediated efflux. *International Journal of Pharmaceutics* **2006,** *315* (1-2), 148-157.

256. Lukyanov, A. N.; Torchilin, V. P., Micelles from lipid derivatives of water-soluble polymers as delivery systems for poorly soluble drugs. *Advanced Drug Delivery Reviews* **2004,** *56* (9), 1273-1289.

257. Torchilin, V. P., Targeted polymeric micelles for delivery of poorly soluble drugs. *Cellular and Molecular Life Sciences* **2004,** *61* (19-20), 2549-2559.

258. Woodle, M. C.; Lasic, D. D., STERICALLY STABILIZED LIPOSOMES. *Biochimica Et Biophysica Acta* **1992,** *1113* (2), 171-199.

259. Papahadjopoulos, D.; Allen, T. M.; Gabizon, A.; Mayhew, E.; Matthay, K.; Huang, S. K.; Lee, K. D.; Woodle, M. C.; Lasic, D. D.; Redemann, C.; Martin, F. J., STERICALLY STABILIZED LIPOSOMES - IMPROVEMENTS IN PHARMACOKINETICS AND ANTITUMOR THERAPEUTIC EFFICACY. *Proceedings of the National Academy of Sciences of the United States of America* **1991,** *88* (24), 11460-11464.

260. Gabizon, A.; Catane, R.; Uziely, B.; Kaufman, B.; Safra, T.; Cohen, R.; Martin, F.; Huang, A.; Barenholz, Y., PROLONGED CIRCULATION TIME AND ENHANCED ACCUMULATION IN MALIGNANT EXUDATES OF DOXORUBICIN ENCAPSULATED IN POLYETHYLENE-GLYCOL COATED LIPOSOMES. *Cancer Research* **1994,** *54* (4), 987-992.

261. O'Brien, M. E. R.; Wigler, N.; Inbar, M.; Rosso, R.; Grischke, E.; Santoro, A.; Catane, R.; Kieback, D. G.; Tomczak, P.; Ackland, S. P.; Orlandi, F.; Mellars, L.; Alland, L.; Tendler, C.; Grp, C. B. C. S., Reduced cardiotoxicity and comparable efficacy in a phase III trial of pegylated liposomal doxorubicin HCl (CAELYX (TM)/Doxil (R)) versus conventional doxorubicin for first-line treatment of metastatic breast cancer. *Annals of Oncology* **2004,** *15* (3), 440-449.

262. Saif, M. W.; Podoltsev, N. A.; Rubin, M. S.; Figueroa, J. A.; Lee, M. Y.; Kwon, J.; Rowen, E.; Yu, J.; Kerr, R. O., Phase II Clinical Trial of Paclitaxel Loaded Polymeric Micelle in Patients with Advanced Pancreatic Cancer. *Cancer Invest.* **2010,** *28* (2), 186-194.

263. Oerlemans, C.; Bult, W.; Bos, M.; Storm, G.; Nijsen, J. F. W.; Hennink, W. E., Polymeric Micelles in Anticancer Therapy: Targeting, Imaging and Triggered Release. *Pharmaceutical Research* **2010,** *27* (12), 2569-2589.

264. Shi, J. J.; Xiao, Z. Y.; Kamaly, N.; Farokhzad, O. C., Self-Assembled Targeted Nanoparticles: Evolution of Technologies and Bench to Bedside Translation. *Accounts of Chemical Research* **2011,** *44* (10), 1123-1134.

265. Gill, K. K.; Nazzal, S.; Kaddoumi, A., Paclitaxel loaded PEG(5000)-DSPE micelles as pulmonary delivery platform: Formulation characterization, tissue distribution, plasma pharmacokinetics, and toxicological evaluation. *European Journal of Pharmaceutics and Biopharmaceutics* **2011,** *79* (2), 276-284.

266. Davidsen, J.; Vermehren, C.; Frokjaer, S.; Mouritsen, O. G.; Jorgensen, K., Drug delivery by phospholipase A(2) degradable liposomes. *International Journal of Pharmaceutics* **2001,** *214* (1-2), 67-69.

267. Ashok, B.; Arleth, L.; Hjelm, R. P.; Rubinstein, I.; Onyuksel, H., In vitro characterization of PEGylated phospholipid micelles for improved drug solubilization: Effects of PEG chain length and PC incorporation. *J. Pharm. Sci.* **2004,** *93* (10), 2476-2487.

268. Tang, N.; Du, G. J.; Wang, N.; Liu, C. C.; Hang, H. Y.; Liang, W., Improving penetration in tumors with nanoassemblies of phospholipids and doxorubicin. *Journal of the National Cancer Institute* **2007,** *99* (13), 1004-1015.

269. Gao, Y.; Chen, L. L.; Gu, W. W.; Xi, Y.; Lin, L. P.; Li, Y. P., Targeted Nanoassembly Loaded with Docetaxel Improves Intracellular Drug Delivery and Efficacy in Murine Breast Cancer Model. *Molecular Pharmaceutics* **2008,** *5* (6), 1044-1054.

270. Chandran, T.; Katragadda, U.; Teng, Q.; Tan, C., Design and evaluation of micellar nanocarriers for 17-allyamino-17-demethoxygeldanamycin (17-AAG). *International Journal of Pharmaceutics* **2010,** *392* (1-2), 170-177.

271. Wang, Y. G.; Wang, R. Q.; Lu, X. Y.; Lu, W. L.; Zhang, C. L.; Liang, W., Pegylated Phospholipids-Based Self-Assembly with Water-Soluble Drugs. *Pharmaceutical Research* **2010,** *27* (2), 361-370.

272. Cailleau, R.; Young, R.; Olive, M.; Reeves, W. J., BREAST TUMOR-CELL LINES FROM PLEURAL EFFUSIONS. *Journal of the National Cancer Institute* **1974,** *53* (3), 661-674.

273. Voelkel-Johnson, C., TRAIL-mediated signaling in prostate, bladder and renal cancer. *Nature Reviews Urology* **2011,** *8* (8), 417-427.

274. Hansen, M. B.; Nielsen, S. E.; Berg, K., Re-examination and further development of a precise and rapid dye method for measuring cell growth/cell kill. *Journal of Immunological Methods* **1989,** *119* (2), 203-210.

275. Raghunand, N.; Mahoney, B. P.; Gillies, R. J., Tumor acidity, ion trapping and chemotherapeutics I. pH-dependent partition coefficients predict importance of ion trapping on pharmacokinetics of weakly basic chemotherapeutic agents. *Biochemical Pharmacology* **2003,** *66* (7), 1219-1229.

276. Ma, Y. H.; Zhou, L.; Zheng, H. Q.; Xing, L.; Li, C. G.; Cui, J. H.; Che, S. A., pH-responsive mitoxantrone (MX) delivery using mesoporous silica nanoparticles (MSN). *J. Mater. Chem.* **2011,** *21* (26), 9483-9486.

277. Wang, Z. Q.; Chen, S.; Lu, Y. N.; Ni, K. Y.; He, H., Molecular Modeling of the Interaction Between Mitoxantrone and B-DNA. *Acta Chim. Sin.* **2010,** *68* (6), 551-556.

278. Enache, M.; Volanschi, E., Spectral Studies on the Molecular Interaction of Anticancer Drug Mitoxantrone with CTAB Micelles. *J. Pharm. Sci.* **2011,** *100* (2), 558-565.

279. Law, S. L.; Chang, P.; Lin, C. H., CHARACTERISTICS OF MITOXANTRONE LOADING ON LIPOSOMES. *International Journal of Pharmaceutics* **1991,** *70* (1-2), 1-7.

280. Han, X.; Liu, J.; Liu, M.; Xie, C.; Zhan, C. Y.; Gu, B.; Liu, Y.; Feng, L. L.; Lu, W. Y., 9-NC-loaded folate-conjugated polymer micelles as tumor targeted drug delivery system: Preparation and evaluation in vitro. *International Journal of Pharmaceutics* **2009,** *372* (1-2), 125-131.

281. Han, X.; Liu, J.; Liu, M.; Xie, C.; Zhan, C.; Gu, B.; Liu, Y.; Feng, L.; Lu, W., 9-NC-loaded folate-conjugated polymer micelles as tumor targeted drug delivery system: Preparation and evaluation in vitro. *International Journal of Pharmaceutics* **2009,** *372* (1–2), 125-131.

282. Lee, B. S.; Dutta, P. K., OPTICAL SPECTROSCOPIC STUDIES OF THE ANTITUMOR DRUG 1,4-DIHYDROXY-5,8-BIS 2- (2-HYDROXYETHYL)AMINO ETHYL AMINO -9,10-ANTHRA CENEDIONE (MITOXANTRONE). *Journal of Physical Chemistry* **1989,** *93* (15), 5665-5672.

283. Enache, M.; Volanschi, E., SPECTRAL CHARACTERIZATION OF SELF-ASSOCIATION OF ANTITUMOR DRUG MITOXANTRONE. *Rev. Roum. Chim.* **2010,** *55* (4), 255-+.

284. Enache, M.; Anghelache, I.; Volanschi, E., Coupled spectral and electrochemical evaluation of the anticancer drug mitoxantrone-sodium dodecyl sulfate interaction. *International Journal of Pharmaceutics* **2010,** *390* (2), 100-106.

285. Chapman, D., Phospholipid bilayers physical principles and models. Gregor Cevc and Derek Marsh (Eds), John Wiley and Sons Ltd. xvi + 442 pages, £73.35 (1987). *Cell Biochemistry and Function* **1988,** *6* (2), 147-148.

286. Vakil, R.; S. Kwon, G., Effect of Cholesterol on the Release of Amphotericin B from PEG-Phospholipid Micelles. *Molecular Pharmaceutics* **2007,** *5* (1), 98-104.

287. Torchilin, V. P., Fluorescence microscopy to follow the targeting of liposomes and micelles to cells and their intracellular fate. *Advanced Drug Delivery Reviews* **2005,** *57* (1), 95-109.

288. Smith, P. J.; Sykes, H. R.; Fox, M. E.; Furlong, I. J., SUBCELLULAR-DISTRIBUTION OF THE ANTICANCER DRUG MITOXANTRONE IN HUMAN AND DRUG-RESISTANT MURINE CELLS ANALYZED BY FLOW-CYTOMETRY AND CONFOCAL MICROSCOPY AND ITS RELATIONSHIP TO THE INDUCTION OF DNA DAMAGE. *Cancer Research* **1992,** *52* (14), 4000-4008.

289. Shen, F.; Bailey, B. J.; Chu, S. Y.; Bence, A. K.; Xue, X. J.; Erickson, P.; Safa, A. R.; Beck, W. T.; Erickson, L. C., Dynamic Assessment of Mitoxantrone Resistance and Modulation of Multidrug Resistance by Valspodar (PSC833) in Multidrug Resistance Human Cancer Cells. *Journal of Pharmacology and Experimental Therapeutics* **2009,** *330* (2), 423-429.

290. Wang, J.; Wang, Y.; Liang, W., Delivery of drugs to cell membranes by encapsulation in PEG–PE micelles. *Journal of Controlled Release* (0).

291. Regev, R.; Yeheskely-Hayon, D.; Katzir, H.; Eytan, G. D., Transport of anthracyclines and mitoxantrone across membranes by a flip-flop mechanism. *Biochemical Pharmacology* **2005,** *70* (1), 161-169.

292. Lu, X. Y.; Zhang, F. Y.; Qin, L.; Xiao, F. Y.; Liang, W., Polymeric micelles as a drug delivery system enhance cytotoxicity of vinorelbine through more intercellular accumulation. *Drug Delivery* **2010,** *17* (4), 255-262.

293. Mohanty, C.; Acharya, S.; Mohanty, A. K.; Dilnawaz, F.; Sahoo, S. K., Curcumin-encapsulated MePEG/PCL diblock copolymeric micelles: a novel controlled delivery vehicle for cancer therapy. *Nanomedicine* **2010,** *5* (3), 433-449.

294. Vaculova, A.; Kaminskyy, V.; Jalalvand, E.; Surova, O.; Zhivotovsky, B., Doxorubicin and etoposide sensitize small cell lung carcinoma cells expressing caspase-8 to TRAIL. *Molecular Cancer* **2010,** *9*.

295. Ravi, R.; Bedi, A., Sensitization of tumor cells to Apo2 ligand/TRAIL-induced apoptosis by inhibition of casein kinase II. *Cancer Research* **2002,** *62* (15), 4180-4185.

296. Kim, J.; Taylor, D.; Agrawal, N.; Wang, H.; Kim, H.; Han, A.; Rege, K.; Jayaraman, A., A programmable microfluidic cell array for combinatorial drug screening. *Lab on a Chip* **2012,** *12* (10), 1813-1822.

297. Chen, H. T.; Kim, S. W.; Li, L.; Wang, S. Y.; Park, K.; Cheng, J. X., Release of hydrophobic molecules from polymer micelles into cell membranes revealed by Forster resonance energy transfer imaging. *Proceedings of the National Academy of Sciences of the United States of America* **2008,** *105* (18), 6596-6601.

298. Chen, H.; Kim, S.; He, W.; Wang, H.; Low, P. S.; Park, K.; Cheng, J. X., Fast release of lipophilic agents from circulating PEG-PDLLA micelles revealed by in vivo Forster resonance energy transfer imaging. *Langmuir* **2008,** *24* (10), 5213-5217.

299. Torchilin, V. P., Recent approaches to intracellular delivery of drugs and DNA and organelle targeting. *Annual Review of Biomedical Engineering* **2006,** *8*, 343-375.

300. Keskar, V.; Marion, N. W.; Mao, J. J.; Gemeinhart, R. A., In vitro evaluation of macroporous hydrogels to facilitate stem cell infiltration, growth, and mineralization. *Tissue engineering Part A* **2009,** *15* (7), 1695-1707.

301. Syková, E.; Jendelová, P.; Urdzíková, L.; Lesný, P.; Hejčl, A., Bone marrow stem cells and polymer hydrogels—two strategies for spinal cord injury repair. *Cellular and molecular neurobiology* **2006,** *26* (7-8), 1111-1127.

302. Murphy, W. L.; Dennis, R. G.; Kileny, J. L.; Mooney, D. J., Salt fusion: an approach to improve pore interconnectivity within tissue engineering scaffolds. *Tissue engineering* **2002,** *8* (1), 43-52.

303. Liu, X.; Ma, P. X., Polymeric scaffolds for bone tissue engineering. *Annals of biomedical engineering* **2004,** *32* (3), 477-486.

304. Smrekar, F.; Podgornik, A.; Ciringer, M.; Kontrec, S.; Raspor, P.; Štrancar, A.; Peterka, M., Preparation of pharmaceutical-grade plasmid DNA using methacrylate monolithic columns. *Vaccine* **2010,** *28* (8), 2039-2045.

305. Svec, F.; Fréchet, J. M., Continuous rods of macroporous polymer as high-performance liquid chromatography separation media. *Analytical Chemistry* **1992,** *64* (7), 820-822.

306. Yin, R.; Wang, K.; Lu, Y.; Nie, J., Macroporous Crosslinked Polymers with Controlled Structure Fabricated via Low Temperature Phase‐Separation Photopolymerization. *Macromolecular Materials and Engineering* **2015,** *300* (3), 291-298.

307. Aoki, H.; Tanaka, N.; Kubo, T.; Hosoya, K., Polymer‐based monolithic columns in capillary format tailored by using controlled in situ polymerization. *Journal of separation science* **2009,** *32* (3), 341-358.

308. Khademhosseini, A.; Langer, R., Microengineered hydrogels for tissue engineering. *Biomaterials* **2007,** *28* (34), 5087-5092.

309. Vozzi, G.; Flaim, C.; Ahluwalia, A.; Bhatia, S., Fabrication of PLGA scaffolds using soft lithography and microsyringe deposition. *Biomaterials* **2003,** *24* (14), 2533-2540.

310. Lin, H. R.; Kuo, C. J.; Yang, C.-Y.; Shaw, S. Y.; Wu, Y. J., Preparation of macroporous biodegradable PLGA scaffolds for cell attachment with the use of mixed salts as porogen additives. *Journal of biomedical materials research* **2002,** *63* (3), 271-279.

311. Jain, R. K.; Stylianopoulos, T., Delivering nanomedicine to solid tumors. *Nat. Rev. Clin. Oncol.* **2010,** *7* (11), 653-664.

312. Alberts, D. S.; Peng, Y. M.; Bowden, G. T.; Dalton, W. S.; Mackel, C., Pharmacology of mitoxantrone: mode of action and pharmacokinetics. *Investigational new drugs* **1985,** *3* (2), 101-107.

313. Baginski, M.; Fogolari, F.; Briggs, J. M., Electrostatic and non-electrostatic contributions to the binding free energies of anthracycline antibiotics to DNA. *Journal of molecular biology* **1997,** *274* (2), 253-267.

314. Simons, M.; Raposo, G., Exosomes–vesicular carriers for intercellular communication. *Current opinion in cell biology* **2009,** *21* (4), 575-581.

315. Fevrier, B.; Raposo, G., Exosomes: endosomal-derived vesicles shipping extracellular messages. *Current opinion in cell biology* **2004,** *16* (4), 415-421.

316. Pisitkun, T.; Shen, R.-F.; Knepper, M. A., Identification and proteomic profiling of exosomes in human urine. *Proceedings of the National Academy of Sciences of the United States of America* **2004,** *101* (36), 13368-13373.

317. Théry, C.; Amigorena, S.; Raposo, G.; Clayton, A., Isolation and characterization of exosomes from cell culture supernatants and biological fluids. *Current protocols in cell biology* **2006**, 3.22. 1-3.22. 29.

318. Peinado, H.; Alečković, M.; Lavotshkin, S.; Matei, I.; Costa-Silva, B.; Moreno-Bueno, G.; Hergueta-Redondo, M.; Williams, C.; García-Santos, G.; Ghajar, C. M., Melanoma exosomes educate bone marrow progenitor cells toward a pro-metastatic phenotype through MET. *Nature medicine* **2012,** *18* (6), 883-891.

319. Théry, C.; Boussac, M.; Véron, P.; Ricciardi-Castagnoli, P.; Raposo, G.; Garin, J.; Amigorena, S., Proteomic analysis of dendritic cell-derived exosomes: a secreted subcellular compartment distinct from apoptotic vesicles. *The Journal of Immunology* **2001,** *166* (12), 7309-7318.

320. Hoshino, A.; Costa-Silva, B.; Shen, T.-L.; Rodrigues, G.; Hashimoto, A.; Mark, M. T.; Molina, H.; Kohsaka, S.; Di Giannatale, A.; Ceder, S., Tumour exosome integrins determine organotropic metastasis. *Nature* **2015,** *527* (7578), 329-335.

321. Zhang, Y.; Wang, X.-F., A niche role for cancer exosomes in metastasis. *Nature cell biology* **2015,** *17* (6), 709-711.

322. Del Muro, X. G.; Torregrosa, A.; Munoz, J.; Castellsague, X.; Condom, E.; Vigues, F.; Arance, A.; Fabra, A.; Germa, J., Prognostic value of the expression of E-cadherin and β-catenin in bladder cancer. *European Journal of Cancer* **2000,** *36* (3), 357-362.

323. Melo, S. A.; Sugimoto, H.; O'Connell, J. T.; Kato, N.; Villanueva, A.; Vidal, A.; Qiu, L.; Vitkin, E.; Perelman, L. T.; Melo, C. A., Cancer exosomes perform cell-independent microRNA biogenesis and promote tumorigenesis. *Cancer cell* **2014,** *26* (5), 707-721.

324. Munson, P.; Shukla, A., Exosomes: Potential in Cancer Diagnosis and Therapy. *Medicines* **2015,** *2* (4), 310-327.

325. Jakobsen, K. R.; Paulsen, B. S.; Bæk, R.; Varming, K.; Sorensen, B. S.; Jørgensen, M. M., Exosomal proteins as potential diagnostic markers in advanced non-small cell lung carcinoma. *Journal of extracellular vesicles* **2015,** *4*.

326. Yu, S.; Cao, H.; Shen, B.; Feng, J., Tumor-derived exosomes in cancer progression and treatment failure. *Oncotarget* **2015,** *6* (35), 37151-37168.

327. Taylor, D. D.; Gercel-Taylor, C., Exosome platform for diagnosis and monitoring of traumatic brain injury. *Philosophical Transactions of the Royal Society of London B: Biological Sciences* **2014,** *369* (1652), 20130503.

328. Franzen, C.; Blackwell, R.; Todorovic, V.; Greco, K.; Foreman, K.; Flanigan, R.; Kuo, P.; Gupta, G., Urothelial cells undergo epithelial-to-mesenchymal transition after exposure to muscle invasive bladder cancer exosomes. *Oncogenesis* **2015,** *4* (8), e163.

329. Zhao, X.; Wu, Y.; Duan, J.; Ma, Y.; Shen, Z.; Wei, L.; Cui, X.; Zhang, J.; Xie, Y.; Liu, J., Quantitative Proteomic Analysis of Exosome Protein Content Changes Induced by Hepatitis B Virus in Huh-7 Cells Using SILAC Labeling and LC–MS/MS. *J. Proteome Res.* **2014,** *13* (12), 5391-5402.

330. Huang, X.; Yuan, T.; Tschannen, M.; Sun, Z.; Jacob, H.; Du, M.; Liang, M.; Dittmar, R. L.; Liu, Y.; Liang, M., Characterization of human plasma-derived exosomal RNAs by deep sequencing. *BMC genomics* **2013,** *14* (1), 1.

331. Huang, G. Y.; Zhou, L. H.; Zhang, Q. C.; Chen, Y. M.; Sun, W.; Xu, F.; Lu, T. J., Microfluidic hydrogels for tissue engineering. *Biofabrication* **2011,** *3* (1).

332. Hoffmann, D.; Hecht, S. S., Nicotine-derived N-nitrosamines and tobacco-related cancer: current status and future directions. *Cancer research* **1985,** *45* (3), 935-944.

333. Armstrong, B. K.; Kricker, A., The epidemiology of UV induced skin cancer. *Journal of Photochemistry and Photobiology B: Biology* **2001,** *63* (1), 8-18.

334. Khansari, N.; Shakiba, Y.; Mahmoudi, M., Chronic inflammation and oxidative stress as a major cause of age-related diseases and cancer. *Recent patents on inflammation & allergy drug discovery* **2009,** *3* (1), 73-80.

335. Chan, K. S., Molecular Pathways: Targeting Cancer Stem Cells Awakened by Chemotherapy to Abrogate Tumor Repopulation. *Clinical Cancer Research* **2015**, clincanres. 0183.2015.

336. Kluwe, W.; McConnell, E.; Huff, J.; Haseman, J.; Douglas, J.; Hartwell, W., Carcinogenicity testing of phthalate esters and related compounds by the National Toxicology Program and the National Cancer Institute. *Environmental health perspectives* **1982,** *45*, 129.

337. Fellows, I. M.; Hurley, L.; Schwaebe, M. K.; Whitten, J. P., Methods for preparation and use of psorospermin analogs. Google Patents: **2002**.